



# Expériences d'écoulement de fluides à seuil en milieu poreux comme nouvelle méthode de porosimétrie

Antonio Rodriguez de Castro

## ► To cite this version:

Antonio Rodriguez de Castro. Expériences d'écoulement de fluides à seuil en milieu poreux comme nouvelle méthode de porosimétrie. Mécanique des matériaux [physics.class-ph]. Ecole nationale supérieure d'arts et métiers - ENSAM, 2014. Français. NNT : 2014ENAM0021 . pastel-01068908

HAL Id: pastel-01068908

<https://pastel.hal.science/pastel-01068908>

Submitted on 26 Sep 2014

**HAL** is a multi-disciplinary open access archive for the deposit and dissemination of scientific research documents, whether they are published or not. The documents may come from teaching and research institutions in France or abroad, or from public or private research centers.

L'archive ouverte pluridisciplinaire **HAL**, est destinée au dépôt et à la diffusion de documents scientifiques de niveau recherche, publiés ou non, émanant des établissements d'enseignement et de recherche français ou étrangers, des laboratoires publics ou privés.

École doctorale n° 432 : Sciences des Métiers de l'Ingénieur

## Doctorat ParisTech

### THÈSE

pour obtenir le grade de docteur délivré par

**l'École Nationale Supérieure d'Arts et Métiers**

**Spécialité " Mécanique-matériaux "**

*présentée et soutenue publiquement par*

**Antonio RODRÍGUEZ DE CASTRO**

le 17 juillet 2014

**Flow experiments of yield stress fluids  
in porous media as a new porosimetry method**

Directeur de thèse : **Azita AHMADI-SÉNICHIAULT**

Co-directeur de thèse : **Abdelaziz OMARI**

Co-encadrement de la thèse : **Denis BRUNEAU**

#### Jury

**M. Henri BERTIN**, Directeur de Recherche, CNRS, I2M – TREFLE

**M. Harold AURADOU**, Directeur de Recherche, CNRS, FAST, Orsay

**M. Seyed Majid HASSANIZADEH**, Professor, Utrecht University - The Netherlands

**Mme Azita AHMADI-SÉNICHIAULT**, Professeur, I2M – TREFLE, Arts et Métiers ParisTech

**M. Abdelhak AMBARI**, Professeur, LAMPA, Arts et Métiers ParisTech

**M. Dominique BERNARD**, Directeur de Recherche, CNRS, ICMCB

**M. Abdelaziz OMARI**, Professeur, I2M – TREFLE, INP Bordeaux

**Mme Sabine SAVIN**, Docteur-Ingénieur, TOTAL – CSTJF, Pau

**M. Denis BRUNEAU**, Maître de Conférences, I2M – TREFLE, Arts et Métiers ParisTech

Président

Rapporteur

Rapporteur

Examinateur

Examinateur

Examinateur

Examinateur

Examinateur

Invité

T  
H  
È  
S  
E



*A la memoria de mi amigo Roberto Revilla Martínez...*

# Acknowledgments

---

As this thesis comes to an end, I remember with gratitude all the people who have made this work possible, more pleasant and most rewarding.

First of all, I must express my deepest appreciation to my supervisors, Azita Ahmadi-Sénichault and Abdelaziz Omari. Thank you, Azita, for trusting me, for materializing my wish to carry out a thesis on this topic and for all the opportunities I have received from you. Thank you with all my heart for the frankness with which you have always spoken to me and for your continuous support that have permitted to successfully overcome the obstacles of a project which was as atypical as fascinating. Also, an important lesson I have learnt during this period, and maybe the most valuable one, is that optimism makes your life happier and leads to better results. Thank you, Aziz, for teaching me this priceless doctrine. I am equally grateful for the scientific rigor you have transmitted to me and for your availability in a number of key moments of this thesis. Thank you both for your energy, your time and your scientific and moral guidance.

Back in time to the moment when I decided to come and study in France, Denis Bruneau played a decisive role as responsible for international relations. Later, he was supervisor of my Master's thesis and advisor of my PhD thesis. Thank you, Denis, for your determinant role in these transcendental moments.

Much of the work presented here is owed to Sabine Savin (TOTAL), who always supported my thesis, expressed her interest in the subject and welcomed me to CSTJF laboratory in Pau. I am sincerely grateful to her for this support, for the chance to work at CSTJF and for helping to give an industrial prospect to this project.

I would like to thank Harold Auradou and Seyed Majid Hassanzadeh for accepting to review my manuscript and for your pertinent remarks. Also, I express my gratitude to the members of the jury for accepting to examine my work and for your interest.

During my stay in Pau (TOTAL), I had the opportunity to meet a great variety of wonderful people. Special thanks go to Luis-Fernando Madariaga, who was my mentor at CSTJF laboratory, helped me a lot with my experiments, and with whom I learnt a lot about petroleum industry procedures and core analysis. Thank you, Luis, for your time, your kindness, your knowledge and your friendship. Also, I would like to thank Hélène Berthet for those enlightening discussions on microtomography and for obtaining the valuable 3D microtomographies presented in this thesis. Moreover, I express my gratitude to Gerald Hamon, Vincent-Arnaud Thebault, Ghislain Pujol, Manuel Chamerois, Benoît Gaubert and the other participants in our rewarding scientific exchanges.

The origin of this thesis was a collaborative project with Professor Abdelhak Ambari's team (LAMPA, Arts et Métiers) in Angers. I feel very lucky to have been given the opportunity to

work in such an exciting topic. Moreover, I would like to thank Angers team for their warm welcome during my stay in their laboratory and the exchanges during my thesis. Thank you, Abdelhak Ambari, Stéphane Champmartin, Antoine Despeyroux and Aimad Oukhlef. A special mention goes to Guillaume Malvaul, with whom I have had the chance to work more closely and to whom I wish a career full of success and happiness.

I want to express my gratitude to all these experts with whom I have had the opportunity to discuss and learn. Henri Bertin, for his valuable advice and opinion on diverse aspects of porous media. Fernando Leal Calderon (ENSCBP) for sharing his knowledge of micro emulsions. Dominique Bernard (ICMCB) for sharing his knowledge of microtomography. Hugues Bodiguel, who welcomed me to LOF laboratory (Rhodia) and taught me key concepts of micro models. Julien Beaumont (LOF, Rhodia) for your training in microfluidic chips fabrication. Thank you all for your availability.

I must express my great appreciation to all these technicians and engineers who have provided me with a valuable experimental assistance. In Bordeaux: Audrey Duphil (I2M – TREFLE) for your technical learnings, training and support, Léa Pigot (ENSEGID) for kindly accepting to assist with mercury porosimetry tests and core cutting, Julien Monteil (ENSCBP) for your training in rheometry and Couette machine. In Pau (TOTAL): Françoise Bouganne and Pauline Capdeville for your contribution with mercury porosimetry tests, Pierre Faurissoix and Regis Brugidou for your support and guidance with the experimental setup.

Yang Wu, Olivier Doublet, Raphaël Augé and José Luis Miranda, thank you for your work and assistance during your respective internships. I wish you further success in your future endeavors.

Special thanks to the different entities that have financed this research project in an adverse economic context: La Caixa Foundation (Spain), Arts et Métiers ParisTech and TOTAL S.A.

Of course, I also want to give all my gratitude to my family, and particularly to my parents, whose love and support have been a constant motivation and whose wisdom has been a reference.

Sincere thanks to those persons who have accompanied me during these years and who have made my time in France one of the happiest periods of my life. Estefania del Campo, for all these wonderful memories, for your support and for the great time and fun we have shared. Mehrez Agnaou, for being such a good friend and person. Ernesto Velázquez, Claudia Rouault and Fabien Rouault, for all these unforgettable moments and gourmet meals. Mehdi, Tom, Lina, Stéphanie, Youssef, Louis, Sandra, Cécile, Tan, Vladimir, Maimouna, José Luis, Franck, and the other PhD candidates and permanent staff of the laboratory. Thanks to all the fabulous friends I have made here in Bordeaux.

Last but not least, thanks to all those persons that are not mentioned here but whose help has been most valuable for the development of this thesis: Secretarial and Administrative staff...



# Contents

<b>1. General Introduction .....</b>	<b>1</b>
<b>2. Background.....</b>	<b>5</b>
<b>2.1. Porous media and characterization of their Pore Size Distribution (PSD) .....</b>	<b>5</b>
2.1.1. Introduction.....	5
2.1.2. Characterization of porous media at the macroscopic and pore scale .....	6
2.1.3. Pore space modelling .....	10
2.1.4. Mercury Intrusion Porosimetry (MIP) .....	15
2.1.5. Health, environmental and legal issues related to MIP: international context.....	18
2.1.6. Other methods to characterize PSDs of porous media .....	20
2.1.7. Reference porous media .....	24
<b>2.2. Complex fluids .....</b>	<b>24</b>
2.2.1. Classification of non-Newtonian fluids and main models .....	24
2.2.2. Some comments on yield stress .....	31
2.2.3. Complex fluids: link between microstructure and rheology .....	36
2.2.4. Rheology of polymer solutions.....	38
2.2.5. Some examples of yield stress fluids .....	41
<b>2.3. Flow of yield stress fluids through porous media .....</b>	<b>44</b>
2.3.1. Laminar flow of Herschel-Bulkley fluids through a straight cylindrical capillary and through a bundle of capillaries.....	45
2.3.2. Predicting the flow rate as a function of the pressure gradient for the flow of yield stress fluids through porous media.....	48
2.3.3. Flow of polymer solutions in porous media .....	50
<b>2.4. Obtaining the PSD of a porous medium from the injection of a yield stress fluid.....</b>	<b>54</b>
2.4.1. Theoretical principles .....	54
2.4.2. Available methods .....	55
<b>3. The Yield Stress fluids Method (YSM).....</b>	<b>57</b>
<b>3.1. The basis of the YSM: Physical principle.....</b>	<b>57</b>
<b>3.2. PSD determination.....</b>	<b>58</b>
<b>3.3. Numerical validation of YSM .....</b>	<b>60</b>
3.3.1. Numerical experiments .....	60
3.3.2. PSD determination.....	60
3.3.3. Sensitivity analysis: fluid properties, measurement parameters and errors.....	62
3.3.4. Comparison of YSM with available methods based on yield stress fluids injection .....	71
<b>3.4. Design of experiments .....</b>	<b>72</b>
<b>4. Laboratory experiments .....</b>	<b>75</b>
<b>4.1. Preliminary laboratory experiments .....</b>	<b>75</b>
4.1.1. Materials.....	75
4.1.2. Rheograms of the injected fluids.....	76

4.1.3. Experimental setup and procedures.....	78
4.1.4. Measurements of pressure gradient as a function of flow rate .....	80
4.1.5. Results and comparison with MIP .....	80
4.1.6. Conclusions.....	82
<b>4.2. Sensitivity of the obtained PSD to polymer concentration.....</b>	<b>84</b>
4.2.1. Materials.....	84
4.2.2. Rheograms of the fluids.....	84
4.2.3. Experimental setup and procedure .....	86
4.2.4. Measurements of pressure gradient as a function of flow rate .....	86
4.2.5. Apparent viscosity compared to effective viscosity .....	87
4.2.6. PSDs obtained with YSM.....	91
<b>4.3. Sensitivity of the obtained PSD to the type of porous medium.....</b>	<b>93</b>
4.3.1. Materials.....	93
4.3.2. Rheograms of the injected fluids.....	95
4.3.3. Experimental setup and procedure .....	97
4.3.4. Measurements of pressure gradient as a function of flow rate .....	99
4.3.5. Apparent viscosity compared to effective viscosity .....	101
4.3.6. PSDs obtained with YSM.....	102
<b>4.4. Complementary laboratory measurements .....</b>	<b>104</b>
4.4.1. Dispersion tests in porous media .....	105
4.4.2. Effluent density measurements during saturation with xanthan gum solution.....	107
4.4.3. Effluent viscosity measurements during saturation with xanthan gum solution.....	109
4.4.4. Evolution of the viscosity of the effluent during the different stages of a typical test .....	111
<b>4.5. Modified YSM for laboratory experiments.....</b>	<b>114</b>
<b>4.6. Conclusions .....</b>	<b>116</b>
<b>5. Comparison of YSM with other porosimetry methods .....</b>	<b>119</b>
<b>5.1. Results obtained by Mercury Intrusion Porosimetry (MIP) and comparison with those of YSM .....</b>	<b>119</b>
5.1.1. PSDs obtained by MIP.....	119
5.1.2. Different representations of a PSD obtained with MIP .....	121
5.1.3. Comparison of the PSDs obtained by YSM and MIP.....	124
5.1.4. Capillary pressure <i>versus</i> saturation for MIP and YSM.....	124
5.1.5. Are the samples of porous media analyzed with YSM reusable?.....	130
<b>5.2. 3D microtomography .....</b>	<b>131</b>
5.2.1. Analysis of single 2D images obtained with microtomography.....	131
5.2.2. Comparison of the PSDs obtained with microtomography to those obtained with MIP .....	134
5.2.3. Analysis of 3D images obtained with microtomography.....	136
5.2.4. Capillary pressure <i>versus</i> saturation for microtomography, MIP and YSM.....	138
<b>6. Discussion, conclusions and prospects .....</b>	<b>139</b>
<b>6.1. Discussion .....</b>	<b>139</b>
6.1.1. Concerning the modelling of the pore space .....	139
6.1.2. Concerning the rheology of the fluids used in the experiments .....	140
6.1.3. Concerning the apparent viscosity of the used fluids.....	141
6.1.4. Concerning the pore size determined by each method: are they directly comparable? .....	143

<b>6.2. Conclusions .....</b>	<b>145</b>
<b>6.3. Prospects.....</b>	<b>147</b>
<b>7. References .....</b>	<b>149</b>
<b>Annex A: <math>Q(\nabla P)</math> measurements .....</b>	<b>159</b>
<b>Annex B: PSDs obtained with the modified YSM for laboratory experiments.....</b>	<b>165</b>
<b>Annex C: Quasi mono disperse oil-in-water emulsions. ....</b>	<b>169</b>
<b>Formulation .....</b>	<b>169</b>
<b>Preparation.....</b>	<b>169</b>
<b>Characterization of the size of the oil droplets .....</b>	<b>170</b>
<b>Rheology.....</b>	<b>170</b>



# Nomenclature

A	Cross area of the porous medium [m <sup>2</sup> ]
C	Concentration [ppm]
C*	Overlap concentration [ppm]
C**	Concentration of aggregation [ppm]
C <sub>0</sub>	Original concentration [ppm]
C <sub>inj</sub>	Injected concentration [ppm]
C <sub>p</sub>	Polymer concentration [ppm]
C <sub>s</sub>	NaCl concentration [ppm]
Ca	Capillary number [-]
d <sub>p</sub>	Equivalent cylindrical pore diameter for packed spheres [m]
d <sub>m</sub>	Mean diameter of the beads in a packing of glass beads [m]
D	Density of the effluent [-]
̄̄D	Shear rate tensor [s <sup>-1</sup> ]
D <sub>0</sub>	Density of the fluid saturating the porous medium [-]
D <sub>c</sub>	Molecular diffusion coefficient [m <sup>2</sup> /s]
D <sub>f</sub>	Density of the injected fluid [-]
e	Equivalent hydrodynamic thickness of the adsorbed polymer layer [m]
F	Shape factor [-]
G	Young's shear modulus [Pa]
k	Consistency [Pa s <sup>n</sup> ]
k <sub>cr</sub>	Fitting parameter in Cross model [s <sup>n</sup> ]
K	Absolute permeability [D]
K <sub>a</sub>	Air permeability [D]
L	Length of the porous medium [m]
L <sub>p</sub>	Average length of the path followed by a fluid particle traversing the porous medium [m]
m <sub>p</sub>	Consistency in power law model [Pa s <sup>n<sub>p</sub></sup> ]
M	Molecular weight
n	Flow index [-]
n <sub>cr</sub>	Fitting parameter in Cross model [-]
n <sub>app</sub>	Apparent flow index in the porous medium [-]
n <sub>i</sub>	Number of pores with radius r <sub>i</sub> [-]
n <sub>p</sub>	Flow index in power law model [-]
N+1	Number of experimental Q(∇P) measures [-]
NP	Number of pores [-]
p(r)	Probability in terms of relative frequency [%]
p <sub>v</sub> (r)	Probability in terms of relative volume [%]
P	Pressure [Pa]
P <sub>c</sub>	Capillary pressure [Pa]
P <sub>L</sub>	Laplace pressure [Pa]
Pe	Péclet number [-]

$\Delta P$	Pressure drop [Pa]
$\nabla P$	Pressure gradient [Pa m <sup>-1</sup> ]
$q(\nabla P_j, r)$	Elementary flow rate of a Herschel-Bulkley fluid through a capillary of radius $r$ under a pressure gradient $\nabla P_j$ [m <sup>3</sup> s <sup>-1</sup> ]
$\bar{q}(\nabla P_j)$	Average flow in a pore for a bundle of capillaries corresponding to a pressure gradient $\nabla P_j$ [m <sup>3</sup> s <sup>-1</sup> ]
$Q$	Total flow rate [m <sup>3</sup> s <sup>-1</sup> ]
$r$	Radius of a capillary [m]
$r_c$	Critical radius [m]
$r_i$	i-est pore radius class [m]
$\bar{r}$	Average pore radius [m]
$\bar{r}_a$	Average pore radius after adsorption [m]
$R$	Radius of the porous medium [m]
$R_K$	Permeability reduction [-]
$R_M$	Resistance factor [-]
$R^*$	Minimum droplet size in an emulsion [m]
$S$	Saturation of non-wetting phase[%]
$S_g$	Specific surface area: surface per unit volume of grain [m <sup>-1</sup> ]
$t$	Time [s]
$T$	Tortuosity factor [-]
$V$	Axial velocity [m s <sup>-1</sup> ]
$\bar{v}$	Velocity vector [m s <sup>-1</sup> ]
$V_D$	Darcy's velocity [m s <sup>-1</sup> ]
$x$	Radial coordinate [m]
$\bar{x}$	Position vector [m]
$z$	Longitudinal coordinate [m]
$\alpha$	Shift parameter for pore size classes [-]
$\beta$	Empirical shift parameter for apparent shear rate [-]
$\gamma$	Shear strain [-]
$\dot{\gamma}$	Shear rate [s <sup>-1</sup> ]
$\dot{\gamma}_{app}$	Apparent shear rate of the fluid in the porous medium [s <sup>-1</sup> ]
$\dot{\gamma}_{min}$	Minimum apparent shear rate in the porous medium [s <sup>-1</sup> ]
$\dot{\gamma}_{max}$	Maximum apparent shear rate in the porous medium [s <sup>-1</sup> ]
$\delta$	Weighting parameter for Carreau fit [-]
$\epsilon$	Porosity [-]
$\epsilon_{eff}$	Effective porosity [-]
$1/\lambda$	Onset of shear-thinning behavior in Carreau model [s <sup>-1</sup> ]
$1/\lambda_{app}$	Apparent onset of shear-thinning behavior in the porous medium [s <sup>-1</sup> ]
$\mu$	Solution viscosity [Pa s]
$[\mu]$	Intrinsic viscosity [Reciprocal concentration]

$\mu_0$	Plateau viscosity at low shear rates in Carreau model [Pa s]
$\mu_{0app}$	Apparent plateau viscosity at low shear rates in the porous medium[Pa s]
$\mu_{0cr}$	Apparent plateau viscosity at low shear rates in Cross model [Pa s]
$\mu_{0p}$	Apparent plateau viscosity at low shear rates in truncated power law model [Pa s]
$\mu_\infty$	Plateau viscosity at high shear rates in Carreau model [Pa s]
$\mu_{\infty cr}$	Apparent plateau viscosity at high shear rates in Cross model [Pa s]
$\mu_{\infty app}$	Apparent plateau viscosity at high shear rates in the porous medium [Pa s]
$\mu_{\infty p}$	Apparent plateau viscosity at high shear rates in truncated power law model[Pa s]
$\mu_{app}$	Apparent viscosity of the fluid in the porous medium [Pa s]
$\mu_B$	Bingham viscosity [Pa s]
$\mu_C$	Casson viscosity
$\mu_{emulsion}$	Apparent viscosity of the emulsion [Pa s]
$\mu_s$	Solvent viscosity [Pa s]
$\mu_r$	Relative viscosity [-]
$\xi$	Structural parameter for thixotropy [-]
$\theta$	Contact angle [ $^\circ$ ]
$\vartheta$	Average interstitial velocity [ $m s^{-1}$ ]
$\sigma$	Surface tension [ $N m^{-1}$ ]
$\tau$	Shear stress [Pa]
$\bar{\tau}$	Shear stress tensor [Pa]
$\tau_0$	Yield stress [Pa]
$\tau_{0B}$	Yield stress in Bingham model [Pa]
$\tau_0^C$	Yield stress in Casson model [Pa]
$\varphi$	Relaxation time [s]
$\chi$	Dispersivity [m]
$\psi$	Longitudinal dispersion coefficient [ $m^2 s^{-1}$ ]



# 1. General Introduction

---

Porous media are inherent in many industrial applications such as oil recovery, soil remediation, CO<sub>2</sub> underground storage, liquid separation and geothermal energy. Highly irregular cavities and tortuous interconnected pathways surrounded by a solid skeleton extend throughout the hollow at the interior of the medium, so macroscopic properties such as porosity or permeability are not sufficient to characterize the local shape and dimension of the pore space. Although the void space is continuous, it is usually discretized as being a succession of individual pores, which is a useful idealization to quantify local characteristics. Indeed, the size of the pores and their relative distribution determine numerous transport properties of porous media so they are of vital importance. A practical and commonly used approach lies in modelling the pore space as a combination of capillaries whose radii are distributed following a specific distribution, known as Pore Size Distribution (PSD). PSD influences the distribution of fluids and capillary pressures inside the material, its permeability, particles retention, solute dispersion, etc.

Some properties that are intimately linked to the PSD, e.g. capillary pressure curves, are used as inputs to reservoir simulation software and provide valuable information for management and decision making. Likewise, several methods used in Enhanced Oil Recovery (EOR) are based on flooding with chemicals such as polymer solutions, foams or emulsions with the purpose of reducing the mobility ratio of displacing fluid to the displaced fluid. This results in reduction of viscous fingering and therefore in improved sweep efficiency in the reservoir (Sheng 2011). The PSD of the reservoir rock influences the propagation of the fluid front and is often determinant to choose the most appropriate technique.

As a consequence of the interest in PSD of porous media, engineers and researchers have developed a multitude of techniques for its characterization, each of them having particular advantages and drawbacks. Recent advances provide improved spatial and temporal resolution for microtomography. At present, multiphase flow and displacement can be quantified with this non-destructive technique, regardless of whether the images contain diverse phases. Even dynamic processes can be imaged. However, several obstacles have not yet been overcome. Resolution ( $\sim 1 \mu\text{m}$ ) and reliable segmentation of the images are some of the limiting factors. Besides, acquisition time is long and not all materials can be characterized. Other methods are convenient to obtain PSD of macroporous materials ( $> 50 \text{ nm}$ ) but they are often time-consuming and require meticulous preparation. This is the case of water-desorption calorimetry, which allows determination of PSDs typically ranging from 50 nm to a  $10 \mu\text{m}$  from interpretation of water desorption isotherm.

Nowadays, mercury porosimetry is the most widespread technique to determine pore size distributions of porous media. Some of its strengths are the broad range of analyzable pore sizes ( $\sim 1 \text{ nm} - 500 \mu\text{m}$ ), the relatively short duration of the tests ( $\sim 3\text{h}$ ) and the benefits and popularity of a well-established method which is the reference when characterizing PSDs. However, this technique presents several drawbacks including toxicity of the employed fluid

and low performance with unconsolidated porous media. Despite the existence of other less toxic porosimetry methods, none of them is efficient enough to replace mercury porosimetry. Furthermore, the new international legislation that will be put in place following the ratification of the Minamata Convention on Mercury in October 2013 is intended to ban or severely restrict mercury porosimetry, forasmuch as it is one of the main sources of mercury use. Moreover, it is always advisable to replace a toxic technique as this one with a new environmentally-friendly technique which in addition does not threaten the user's health. It is for that reason that the IUPAC (International Union of Pure and Applied Chemistry) recently appealed to the international scientific community (Rouquerol *et al.* 2012) emphasizing the interest and the need to develop new effective and non-toxic porosimetry methods.

The most likely outcome of the decline of mercury porosimetry is that 3D microtomography takes its place as the dominant technique to obtain PSD. However, there is an absence of alternatives during the years ahead until microtomography reaches full development... and even then, because this method may remain unaffordable for most research centers and is not applicable to all types of porous samples. In this context, the objective of the present thesis is to answer the following question: is it possible to develop a simple, efficient and nontoxic method to characterize porous media in terms of their Pore Size Distribution?

To answer this question, the starting point is the work of Ambari *et al.* (1990), who proposed the theoretical basis of a new method to obtain the PSD by injecting yield stress fluids through porous media while measuring the flow rate  $Q$  at several pressure gradients  $\nabla P$ . On the grounds of these theoretical considerations, an intuitive approach to calculate PSD from  $Q(\nabla P)$  is presented in this work. It relies on considering the extra increment of  $Q$  when  $\nabla P$  is increased, as a consequence of the pores of smaller radius newly incorporated to the flow. The underlying principle of such behavior is the rheology of yield stress fluids in porous media. The procedure is first tested and validated on numerically generated experiments. Then, it is applied to exploit data coming from laboratory experiments and the resulting PSDs are compared with those provided by mercury porosimetry and in some cases also with results from 3D micro tomographies.

The performances that are pursued with this new technique are diverse. Obviously, the first requisite will be nontoxicity in contrast to mercury porosimetry. In addition, we seek a simple and inexpensive method which allows rapid characterization of a large spectrum of porous media without needing any exclusive equipment. Furthermore, it is also preferred that the analyzed cores can be subsequently analyzed by other means, so the tests should be nondestructive. Moreover, the characterized pore dimensions must be associated with macroscopic properties of interest. This method is expected to be especially useful in EOR due to the nature of the experiments, which involve injection of commonly used flooding materials.

Other important goals of the present work are to identify and assess the most critical questions regarding the experimental feasibility of the method, determine its strengths, its weaknesses, and propose ways to improve its performance without scarifying any of the main criteria. In

this respect, the evaluation of some issues linked to interactions of complex fluids with porous media, such as retention or differences between bulk and apparent rheology, will be decisive.

The flow through porous media of non-Newtonian fluids in general, and of yield stress fluids in particular, is of special interest in applications such as EOR, soil remediation, filtration, propagation of blood through a kidney etc. Unfortunately, its modelling, simulation and experimental implementation is highly complex. As a consequence, even though it is currently the subject of an active research and great progress has been achieved, there is still no concluding macroscopic model and numerical simulations are not able to predict experimental measures in numerous cases. Furthermore, there is a lack of experimental work on this subject as reported by several authors (Chevalier *et al.* 2013), who also pointed out the difficulty to find reliable data bases. For that reason, a complementary objective of this thesis is to provide rigorous procedures as well as experimental results which may be compared with numerical simulations and macroscopic models.

The following chapter of this work will provide an overview of the topics related to this investigation, including a bibliographic survey of porosimetry methods, complex fluids and their flow in porous media. Chapter 3 is devoted to the presentation of the principles of Yield Stress fluids Method (YSM) and its numerical validation on “*in silico*” experiments. Laboratory experiments aiming to verify the experimental feasibility, the performance, the results in terms of PSD and the key issues related to YSM are presented in Chapter 4. Both natural and synthetic porous media are tested. In Chapter 5, the results obtained by YSM will be compared with those deduced from mercury porosimetry and microtomography. Finally, a discussion on some fundamental aspects of YSM is proposed in Chapter 6 together with the conclusions of this work and some prospects for future work.



## 2. Background

---

This chapter is divided in four parts. It begins with a bibliographic review of porous media, focusing on characterization of the pore space geometry. Then, some aspects of the rheology of non-Newtonian fluids and their flow through porous media are introduced, with special dedication to the type of fluids used in the experiments that will be presented later. Finally, the theoretical ideas underlying the method developed in this work are summarized.

---

### **2.1. Porous media and characterization of their Pore Size Distribution (PSD)**

In this section, porous media are defined and classified according to different criteria. Then, the principal properties of these media as well as different models of the pore space are presented. After that, the principles of the reference technique to obtain the Pore Size Distribution (PSD) of porous media, i.e. Mercury Intrusion Porosimetry (MIP), are explained. Also, an outlook of the current international context of MIP is analyzed in this section. Finally, other methods to characterize PSD are presented, insisting on the lack of reference materials to compare the measures obtained with different instruments and techniques.

#### **2.1.1. Introduction**

A porous medium is a type of matter composed of a solid matrix containing void spaces known as pores. In the scope of this work, the pore space is the region of the volume of these materials that is not occupied by solid matter and through which a fluid can flow. Hence, this definition excludes the empty sections that are utterly surrounded by solid because they do not contribute to flow.

Porous media are involved in many domains of vital importance such as oil and gas production from reservoirs, contaminant remediation and hydrogeology. Due to their internal structure and their high surface to volume ratio inducing high performance in heat and mass transfer processes, they are used in numerous industrial processes namely those involved in fuel cells fabrication, paper pulp drying, filtration, etc. Therefore, continuously growing research efforts are devoted to study porous media structure and especially the flow of Newtonian fluids as well as complex fluids therein.

Porous media may be classified in a number of manners. In fact, with the exception of metals and ceramics that are fired at high temperatures, all the earth's solid contents are to some extent porous (Schüth *et al.* 2002). Regarding their origin they can be divided in natural porous media and synthetic porous media. Among the natural porous media a distinction may be made between “in-vivo” porous media such as biological tissues and “ex-vivo” porous media such as rocks. Some examples of synthetic porous media are porous glasses and sintered silicates. Another distinction can be made between consolidated (rigid, macroscopic

solid matrix) and unconsolidated (loosely packed assemblages of solid particles) porous media. In that respect, the process of changing accumulated unconsolidated sediments into a rock is called lithification. Grains are compacted by the overburden sediments and cemented by deposition (from interstitial water) of silica, calcite, clays, iron oxide, and other minerals, between the grains (Tiab and Donaldson 2004).

Porous materials may be formed by different routes (Rouquerol *et al.* 1994): as an inherent feature of crystalline structures (zeolites, some clay materials...), by loose packing and subsequent consolidation of small particles (some inorganic gels, ceramics...), as a subtractive (certain elements of an original structure are selectively removed to create pores) or by natural processes of cell division and self-organization (plant and animal tissues).

### **2.1.2. Characterization of porous media at the macroscopic and pore scale**

Different scales can be considered when describing or observing porous media and the flow within. At the microscopic scale, also known as pore scale, the characteristic dimensions are of the same order as those of the pores or grains. Therefore, parameters such as packing arrangements or pore wall roughness are measured by means of imaging techniques (tomography, SEM microscopy, etc.). The macroscopic scale corresponds to the dimensions of a porous medium core. Properties such as permeability or porosity are analyzed at the macroscopic scale to be used, for instance, as an input to computer models to predict flow of fluids. Other larger or intermediate scales can be considered in petroleum engineering or hydrogeology (Tiab and Donaldson 2004). The passage from one scale to another is achieved through homogenization methods (Bensoussan *et al.* 1978) or volume averaging methods (Quintard and Whitaker 1994). The interest of characterizing a porous medium at the pore level is to understand, model and control (in some cases) its behavior at the macroscopic scale (Dullien 1991). For example, it allows simulating transport and distribution of fluids within the pore space.

We will begin by presenting some important properties of porous media at the macroscopic scale:

**Porosity ( $\varepsilon$ ):** porosity is one of the most important properties that characterize a porous medium from a macroscopic point of view. It is defined as the ratio of pore volume to overall volume occupied by solid. If the non-conducting isolated voids are taken into account, total porosity can be defined as the ratio of volume of pores and voids to overall volume. Porosity may be calculated from the difference of the weight of a porous medium before and after saturation with water or by measuring the volume of water entering the sample during saturation. It has to be noted that the air present in the porous medium should be evacuated or replaced by a more water-miscible gas previous to its saturation with water in order to avoid air trapping. That may be achieved by means of a vacuum pump or by saturating the porous sample with CO<sub>2</sub> (more soluble in water than air). Once a sufficiently low pressure is reached, the porous medium is saturated with water at relatively high pressure (typically 10 bars) to guarantee complete saturation of the pore space. Other methods also lead to the measure of

porosity. For example, porosity can be calculated from the difference of weight of a porous medium before and after saturation with mercury in the case of mercury porosimetry. The factors governing the magnitude of porosity as well as several classifications of porosity may be found elsewhere (Tiab and Donaldson 2004).

**Permeability ( $\bar{\bar{K}}$ ):** like porosity, permeability is a macroscopic property of a porous medium. It indicates the ability of the porous medium to conduct fluids. Even if permeability is a tensor, only the case of isotropic porous media with  $\bar{\bar{K}} = K\bar{\bar{I}}$  will be considered, where  $\bar{\bar{I}}$  is the identity tensor and  $K$  is the absolute permeability of the porous medium. For simplicity  $K$  will be simply called permeability hereinafter. The French engineer Henri Darcy developed the equation linking the flow rate with the pressure gradient through a porous medium in the case of the steady laminar flow of a Newtonian fluid (Darcy 1856), which has become one of the key relations and probably the most famous law for fluid transport in porous media. In the simplest case of a homogeneous isotropic porous medium, Darcy's law can be written as follows:

$$Q = \frac{KA|\nabla P|}{\mu} \quad (2.1)$$

where  $A$  is the cross area of the porous medium,  $\mu$  is the dynamic viscosity of the fluid,  $|\nabla P|$  is the magnitude of the pressure gradient through the porous medium and  $Q$  is the volumetric flow rate. Permeability may be measured by injecting a Newtonian fluid (typically water) through a sample of the porous medium at several flow rates and measuring the generated pressure loss for each flow rate. The slope of the flow rate as a function of the pressure loss is proportional to permeability. However, different methods to measure  $K$  may lead to different values. Ahmed *et al.* (1991) reviewed the permeability measurement techniques and their interrelationships.

**Specific surface area:** specific surface area is the surface of pores per unit volume. The nature of the considered volume may lead to different definitions of specific surface area: surface per unit grain volume ( $S_g$ ), per unit solid volume or per unit pore volume. That property of porous media is important for adsorption, chemical reactions, catalysis, etc.

The structure of the pore space is complex with tortuous and interconnected pathways. The sources that cause difficulties in modelling the geometry of the pore space are:

**Tortuosity:** tortuosity factor  $T$  can be defined as the ratio of the average length of the path followed by a fluid particle traversing the porous medium,  $L_p$ , to the length of the porous medium  $L$  along the major flow or diffusion axis (Epstein 1989). Given that  $L_p > L$ , tortuosity factor  $T = (L_p/L)^2$  is greater than 1. In fact, the path followed by fluid particles through the porous media is unknown. However, the length of this path is needed to calculate the pressure gradient corresponding to a given pressure difference between the ends of a porous sample. Several experimental methods to measure tortuosity are available. One of these methods consists in measuring the diffusion factor (from Fick's first law) corresponding to a

nonreactive species both in the case of pure water and in the case of a core of the porous medium (Sweerts 1991). Other experimental methods are based on electrical resistivity measurements (Paterson 1983; Walsh and Brace 1984) or on the use of ultrasounds propagation (Moussatov *et al.* 2001). However, these measures are time-consuming and the required equipment is quite specific. In contrast, the measurement of porosity is not complicated. For that reason, and knowing that measured tortuosity factors are highly correlated with porosity, it is more efficient in some cases to use theoretical or empirical relations to estimate tortuosity factor. To this end, one may use theoretical or empirical relations. Theoretical relations link directly the value of tortuosity factor to the value of porosity by assuming a model structure of the pore space. These relations do not include any adjustable parameters and the estimated tortuosities do not generally fit well with the measured values. Empirical relations resemble theoretical ones, but they include an adjustable parameter and are defined for a type of porous media (e.g. chalk, kaolin) instead of a type of structure. Evidently, empirical relations fit better with experience (Boudreau 1996). Recently, Sun *et al.* (2013) presented a general model with a numerical tool to calculate tortuosity factor and compared it with a set of classical relations and experimental data, finding good agreement in the case of artificial materials but worse agreement in the case of natural materials.

All the properties of the porous media presented up to here are macroscopic properties. However, the present work will mainly treat the characterization of porous media at the pore level. That is for that reason that we will focus here on some of the particularities of porous media at the pore scale that render their characterization complex at this level.

**Converging-diverging geometry** of pores: indeed, the voids in porous media are not uniform. There are continuous changes in the dimension of the cross section, with some zones of convergence and others of divergence. As will be seen later, these changes in size of the cross section involve additional pressure losses related to viscoelasticity of fluids. One common way to characterize the converging-diverging geometry is defining an aspect ratio (or pore to throat size ratio) which relates the dimensions of the constrictions to that of the large sections.

**Form of the cross section:** it is not realistic to say that all pores have regular form. Even if such modelling is suitable for simplification of calculations, the reality is that in general the shape of the cross section of pores cannot be described by simple geometries.

**Pores connectivity:** in most cases pores are interconnected, so the flow in a pore is not independent of the one in other pores. The coordination number of a pore system can be defined as the average number of pore constrictions connecting with each pore volume. It is a measure of the connectivity of the network of pores and determines the number of different pathways or access routes between pores (Wardlaw and McKellar 1981).

The **3D nature** of the pore space: the pore network spread in the three dimensions of space and not only in the direction in which the pressure difference is imposed or measured during a flow experiment.

The use of global porosity  $\varepsilon$  (pore volume/total volume) and permeability  $K$  of porous media does not provide any information about local dimension and shape of the void space. Despite being continuous, pore space is often modelled as a discrete succession of connected pore bodies and pore throats. However, and as will be seen in the next subsection, a simple and widely used representation of pore space consists in a bundle of straight parallel capillaries with various sizes following a probability density function  $p(r)$  often called **Pore Size Distribution (PSD)**. The shape of the PSD is determined by the geological history and composition of the material. Moreover, the PSD is linked to quantities such as capillary pressure, hydraulic conductivity, and solute dispersion (Nimmo 2004). Determination of the PSD is thus a routine task executed by means of several experimental methods, as will be presented in subsections 2.1.4 and 2.1.6.

It should be emphasized that the definition of PSD is very elusive. In fact, it depends on the particular method used for its determination. The general procedure used for the determination of a PSD consists in measuring some physical quantity *versus* another physical parameter that may be controlled by the operator during the experiment (Dullien 1991). The magnitude of one of these physical quantities (imposed or measured) should be related to a given magnitude of the “dimension of a pore” whereas the other physical quantity should be related to the occurrence of that “dimension” in the porous sample. For example, in mercury porosimetry, the volume of mercury penetrating a sample is measured as a function of the pressure imposed to the mercury. In that case, the magnitude of the imposed pressure is linked to a given pore dimension. The characterized “dimension of the pore” with mercury porosimetry is the diameter of the largest entrance or opening towards a certain portion of pore volume. In general, the resulting PSD is dependent on the sequence in which pores are encountered within the method used (Rouquerol *et al.* 1994) and on the mathematical model used to interpret the experimental data.

It is worth recalling here the recommendations for characterization of porous solids made by the International Union of Pure and Applied Chemistry (IUPAC) (Rouquerol *et al.* 1994):

- The complexity of the pore texture of materials is such that even on theoretical grounds the concepts which can be used to describe the texture usually entail the introduction of **simplifying assumptions**.
- No experimental method provides the absolute value of parameters such as porosity, surface area, pore-size, surface roughness : each gives a characteristic value which depends on the principles involved and the nature of the probe used (atom or molecule, radiation wavelength...). **One cannot speak of the PSD of a material** but, instead, of its mercury porosimetry PSD, its microtomography PSD, etc.

- The **selection** of a **method** of characterization must start from the **material and from its intended use**.
- The **method** chosen must indeed **assess a parameter related** as directly as possible **to phenomena involved in the application** of the porous material. In this respect, it may often be advisable to select a method involving physical phenomena similar or close to those involved during the practical application (i.e. adsorption or capillary condensation methods if the porous substance is to be used as a desiccant, or a freezing point depression method if one is interested in the frost resistance of a construction material ...) so that the parameters determined are appropriate.
- **Rather than to "check the validity"** of distinct methods, certified reference materials are needed to establish **how these methods differ** and, of course, to calibrate any individual equipment or technique.
- As a consequence, **one must not look for a "perfect agreement" between parameters provided by different methods**. Such an agreement, when it occurs, is not necessarily a proof of the validity of the derived quantities. Instead, one must be aware of the specific, limited and complementary significance of the information delivered by each method of characterization of a porous solid.

### **2.1.3. Pore space modelling**

Pore space is very complex, with tortuous and irregular forms. Different models exist for modelling pore space, some of them are very simple and others very sophisticated. None of them should be expected to provide the “absolute truth” about the pore space parameters such as pore size, grain shape, etc. The choice of one particular model depends on the particular application or property which is investigated. The different types of pores and some models for the pore structured are presented below.

#### **Different types of pores**

Rouquerol *et al.* (1994) classified pores (Figure 1) according to:

- Their availability to an external fluid:
  - o Closed pores (a) are isolated and do not participate in fluid flow and gas adsorption. However, they influence bulk density, mechanical strength, thermal conductivity and others macroscopic properties.
  - o Open pores, (b), (c), (d), (e) and (f), which have a continuous channel of communication with the external surface.
  - o Blind pores: they are open only at one end, (b) and (f).
  - o Through pores (e): open at two ends.

- Their shape: cylindrical, (e) and (f); ink-bottle shaped (b); funnel shaped (d) or slit-shaped. Rough surface (g) is not considered porous unless it has irregularities that are deeper than they are wide.

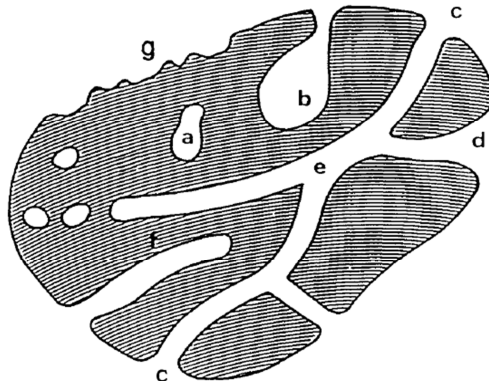


Figure 1: Schematic cross-section of a porous solid (Rouquerol *et al.* 1994).

### Pore structure models

Dullien (1991) claimed that any model of pore structure should aim to approximate the significant features of the real pore structure of a porous medium as closely as possible and necessary. However, the details of the pore structure which are irrelevant to the transport properties of the medium are to be omitted as they would unnecessarily increase the complexity of the model. In that respect, it should be kept in mind that in some cases, a peculiar behavior of the medium can be explained only with the help of certain pore structure features that for most other purposes are not relevant.

**Bundle-of-capillaries model:** in this simple model, pores are considered as being cylindrical. More precisely, the model consists in a solid cylindrical matrix containing a set of cylindrical voids crossing the matrix from one face to the other in the axial direction. In its simplest version, these cylinders are straight, parallel and have the same radius  $\bar{r}$ . Nevertheless **modifications** can be introduced in this model so as to take into account some complexities of the real porous medium:

- Pore size distribution: it is considered that the pore radii (cylinder radii) are not equal but distributed according to a probability density function (pore size distribution)  $p(r)$ .
- Tortuosity: in the simplest model, the average distance traveled by fluid particles ( $L_p$ ) is considered as being equal to the length of the matrix ( $L$ ). Nevertheless, pores are not straight but tortuous. This tortuosity may be represented by a tortuosity factor  $T$  which corrects the pore length:  $T = (L_p/L)^2$ .
- Variable cross-section: individual pores are assimilated to a set of straight capillaries connected in series and with different radii distributed according to a probability distribution so contractions and expansions can be reproduced. The length of each capillary in the series is constant.

Without considering tortuosity and variable cross-section, the only parameters characterizing a bundle of capillaries are its porosity  $\epsilon$ , the radii of its capillaries (PSD) and the total length  $L$  and radius  $R$  of the matrix (for a cylindrical matrix). In general,  $R$  and  $L$  correspond to the length and the radius of the porous sample being modeled. What is sought in practice is that the bundle has the same permeability or the same capillary pressure curve (capillary pressure as a function of saturation) as the real porous medium. It is obvious that the use of bundle-of-capillaries model is not able to roughly predict a number of transport phenomena. Nonetheless, it is a popular and widespread model. The bundle-of-capillaries model is used in many applications such as porosimetry methods (mercury porosimetry, contact porosimetry, liquid porosimetry, etc.). A complete review of these methods was presented by Sorbie (1991). However, it has to be noted that more complex models introduce additional structural features that cannot be easily measured.

**Network models:** an important flaw of the bundle-of capillaries-model is that it does not account for the fact that pores are interconnected in real media, forming a network of pores. Consequently, what “happens” in a pore is not independent of what “happens” in the others. Development of 2-D and 3-D networks along with the powerful mathematical theory of percolation (Yanuka 1992; Hunt and Ewing 2009) provided more suitable tools to treat complex phenomena in porous media.

The general approach consists in obtaining information about structural parameters from an image of the porous medium (thin section, tomography, etc.) in order to create a pore network as representative as possible of the real porous medium. As described by Øren and Bakke (2003) the main steps to generate a pore network from thin sections are:

- Image segmentation, treatment and analysis to obtain petrographic information (pore size, shape, etc.).
- 3D reconstruction of the porous medium microstructure based on modelling of the sedimentation and compaction of the grains (process-based model) or in matching stochastic functions of the image (statistical model).
- Analysis of the reconstructed microstructure to evaluate different structural parameters: pore bodies size distribution, pore throats size distribution, coordination number, shape factors corresponding to each pore, etc.
- The preceding structural parameters are used as input to a network model with simpler geometries than the reconstructed microstructure (triangular, circular or square pore sections as a function of the shape factors previously calculated). The network model is composed of larger pores (nodes or pore bodies) connected by smaller pores (pore throats).

A 3D image is directly obtained in the case of 3D microtomography as will be seen later, so the 3D reconstruction (second step) does not take place. Other possibilities to generate a pore

network directly from a 3D micro-tomography image are described elsewhere (Al-Kharusi and Blunt 2007). It has to be highlighted that pore throats determine the flow properties whereas pore bodies dominate the volumetric properties.

**Particles packing models:** regular or irregular packs are models in which pores are considered to be the voids between loosely packed granular particles of simple geometries (usually spheres). These models may be realistic for unconsolidated porous media (e.g. sand pack). See Dullien (1991) for more details.

**Fractal models and fractal analysis:** as explained by Hunt and Ewing (2009), the ability of fractal models to represent highly complex natural media with a small number of parameters is a strong argument in their favor. When dealing with a natural fractal porous medium, even if the range of fractal properties is restricted to one order of magnitude, the medium cannot be mapped to a regular network because the network has a fundamental scale and associated regularity. Fractal analysis applied to porous media will not be presented here but may be found elsewhere (Schüth *et al.* 2002).

### Estimation of pore sizes from petrophysical models

Petrophysical models aim to express permeability as a function of other measurable rock properties, which usually include pore or grain sizes. Therefore, if permeability is known, the expressions provided by these models may be used to estimate the pore or grain sizes.

Based on the bundle-of-capillaries model, Kozeny (1927) obtained from Hagen-Poiseuille law and Darcy's law that permeability  $K$  may be linked to porosity  $\varepsilon$  and average pore radius  $\bar{r}$  through:

$$\bar{r} = \sqrt{\frac{8K}{\varepsilon}} \quad (2.2)$$

As throats determine the pressure loss in porous media, the average pore radius obtained with Eq. (2.2) represents the average throat radius. In fact,  $\bar{r}$  is not directly measurable, but is related to the pore surface area to pore grain volume ratio  $S_g$  through:

$$S_g = \frac{2\varepsilon}{\bar{r}(1 - \varepsilon)} \quad (2.3)$$

Given that  $S_g$  can be measured with techniques such as nuclear magnetic resonance, Eq. (2.3) is usually formulated as:

$$K = \frac{\varepsilon^3}{2(1 - \varepsilon)^2 S_g^2} \quad (2.4)$$

Tortuosity T as well as a shape factor F associated to the tubes (2 for cylindrical pores) may be included in the preceding expression (Carman 1937; Nelson 1994; Nooruddin and Hossain 2012), giving:

$$K = \frac{\varepsilon^3}{FT(1 - \varepsilon)^2 S_g^2} \quad (2.5)$$

The average throat radius  $\bar{r}$  may be estimated from (2.2) and (2.4) as follows:

$$\bar{r} = 2 \sqrt{\frac{FTK}{\varepsilon}} \quad (2.6)$$

The **Kozeny-Carman** equation (Kozeny 1927; Carman 1937) assumes the pores to be voids between packed spheres of equal size  $d_p$ :

$$K = \frac{d_p^2 \varepsilon^3}{180(1 - \varepsilon)^2} \quad (2.7)$$

$d_p$  is the equivalent cylindrical pore diameter. For a distribution of n different grain shapes,  $d_p$  is defined as follows (Torskaya *et al.* 2014):

$$d_p = \frac{\sum_i^n f_i V_i}{\sum_i^n \frac{f_i V_i}{d_i}} \quad (2.8)$$

where  $f_i$  is the fraction by number of the  $i$ th grain shape with diameter  $d_i$  and volume  $V_i$ . Other aspects of Kozeny-Carman equation were discussed by Carrier (2003) including the shape factors accounting of the angularity of the individual solid grains. An excellent review of a number of petrophysical models to estimate K based on mineralogy, surface area, water saturation, etc. was published by Nelson (1994). Given that the present work focuses on PSD, two empirical models based on pores sizes are succinctly presented here:

**Winland's equation** (Kolodzie 1980; Pittman, 1992), where  $R_{35}$  is the pore radius in  $\mu\text{m}$  corresponding to 35% of the total mercury intrusion in mercury porosimetry and  $K_a$  is air permeability (mD):

$$\log R_{35} = 0.732 + 0.588 \log K_a - 0.864 \log \varepsilon \quad (2.9)$$

**Pittman's regressions** (Pittman 1992), where  $R_n$  is the pore radius corresponding to  $n\%$  of the total mercury intrusion in mercury porosimetry (Figure 2)

Saturation (%)	Equation
10	$K_a = 4.1 R_{10}^{2.00} \phi^{0.770}$
20	$K_a = 5.59 R_{20}^{1.93} \phi^{0.584}$
30	$K_a = 13.9 R_{30}^{1.82} \phi^{0.768}$
40	$K_a = 52.3 R_{40}^{1.72} \phi^{1.17}$
50	$K_a = 405 R_{50}^{1.60} \phi^{1.93}$
60	$K_a = 2,820 R_{60}^{1.54} \phi^{2.57}$
70	$K_a = 53,400 R_{70}^{1.59} \phi^{3.69}$

Figure 2: Predictive equations for air permeability (mD) based on regression equations by Pittman (1992), as a function of fractional porosity and pore throat radius ( $\mu\text{m}$ ) when mercury saturation varies. From Nelson (1994).

### 2.1.4. Mercury Intrusion Porosimetry (MIP)

**Mercury intrusion porosimetry (MIP)** consists in immersing a piece of porous medium in mercury and measuring the volume of the invading mercury *versus* the applied pressure, which gives the distribution of the capillary pressure as it represents the counterpart of the actually applied pressure (see Giesche 2006 for details). Moreover, knowing the mercury/solid interfacial tension  $\sigma$  and the contact angle  $\theta$  defined as in Figure 3, these data allow determination of PSD using a modified Laplace equation referred to as Washburn equation (Eq. 2.10). For that purpose the porous medium is usually modeled as a bundle of cylindrical capillaries. A value of  $0.485 \text{ N m}^{-1}$  at  $25^\circ\text{C}$  for the surface tension of mercury is commonly accepted.  $r_{\text{pore}}$  is the pore radius and  $\Delta P$  is the required pressure difference to penetrate the pore. Given that the sample is initially evacuated,  $\Delta P$  is very close to the applied pressure.

$$\Delta P = -\frac{2\sigma\cos\theta}{r_{\text{pore}}} \quad (2.10)$$

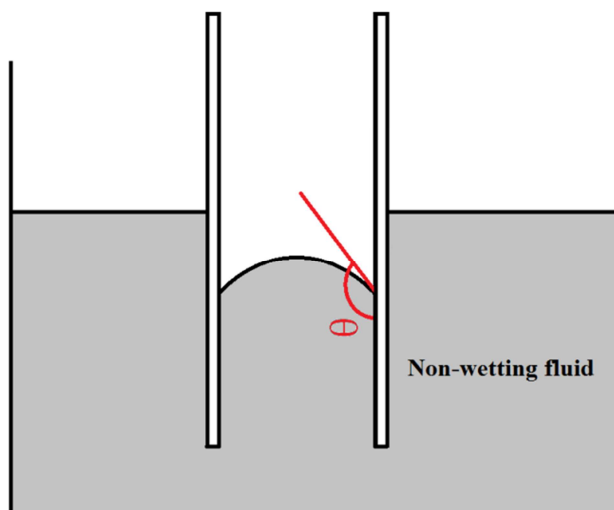


Figure 3: Contact angle  $\theta$  of a non-wetting fluid.

In a typical test, the sample of the porous medium has to be carefully prepared and then placed into a cell known as dilatometer. The first stage consists in evacuating the air and the residual moisture of the sample by means of a vacuum pump. Once the pressure is low enough, the mercury invades the dilatometer through a capillary, filling the cell without applying any pressure (excepting the one produced by the weight of the mercury). During the low-pressure phase of the test, the mercury contained in the capillary is pushed by a compressed air device whose pressure is progressively increased. By this way, smaller and smaller pores are penetrated. The volume of mercury that has entered the sample at each pressure is measured through changes in the capacitance between the column of mercury in the capillary and a coaxial metallic sheet. In a second step, higher pressures are applied through pressurized hydraulic oil in contact with the mercury in order to penetrate the smallest pores. Additionally, an extrusion of mercury (lowering of applied pressure) may be performed after the intrusion phase. In this phase, larger and larger pores are evacuated during the experiments. A number of international and national standards for MIP are available: ISO 15901-1:2005, British Standard 1992-11-15, etc.

MIP allows investigation of pore sizes ranging from 3.5 nm to 500  $\mu\text{m}$  (Giesche 2006), which is inconceivable to any other existent technique. Another advantage of MIP is the comparatively short time needed to carry out tests (typically 4h). However, the duration of the test increases considerably when a high sensitivity of the PSD is required (more measures are needed), when a better precision is sought (long equilibration time) or if a complete intrusion/extrusion loop is performed. The instruments can operate in a continuous or incremental mode (pressure is increased continuously or in a step-by-step manner). Nevertheless, incremental mode with equilibration times of more than 5 min is preferred in order to assure reliability of results. As can be observed in Figure 4, Micromeritics (1997) performed different analysis with the same material and different equilibration settings. The conclusion was that the obtained pore sizes may differ (40 % to 50 %) depending on these settings. In general, longer equilibration times give larger pores.

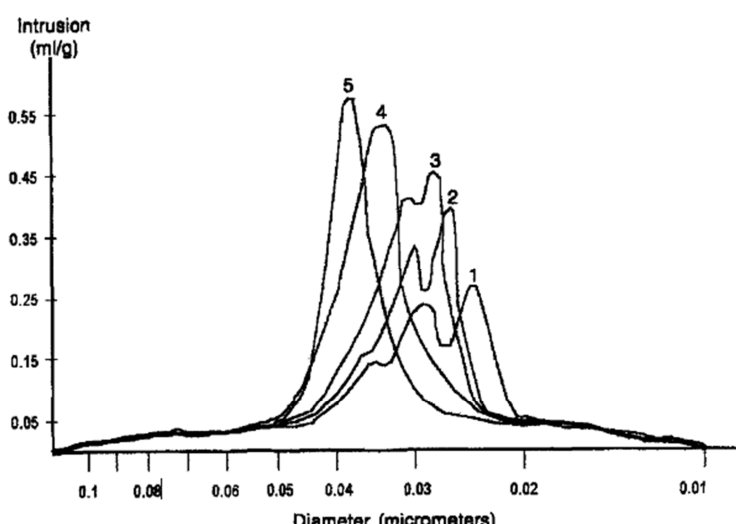


Figure 4: Differential intrusion against pore diameter for alumina extrudates using different equilibration settings. 1: pressure increased continuously, 2: 2 sec/measure, 3: 10 sec/measure, 4: 30 sec/measure, 5: 0.001  $\mu\text{L}/\text{g}$  sec (fixed injection rate). (Micromeritics 1997).

Modelling of pore space as a bundle of cylindrical capillaries leads to an overestimation of the occurrence of small pores. Indeed, the volume of the large pores situated downstream of constrictions, which are filled at higher pressures than those predicted with Washburn equation, is assigned to the smaller pores.

Also, it has to be highlighted that in many cases the contact angle is unknown or difficult to calculate (Adamson 1982). In fact, the contact angle is dependent on the composition of the material, its roughness, its modified composition when the contact with mercury is produced, etc. Furthermore, the contact angle for intrusion is different from the one for extrusion. The different manners to measure or estimate the contact angle are described elsewhere (Schüth *et al.* 2002) but its precise determination is practically impossible inasmuch as it changes even for the same material. In most cases, by tradition, its value is fixed between  $130^\circ$  and  $145^\circ$  independently of the material. It has to be noted that as a consequence of the user's choice for the contact angle, the corresponding PSD may be shifted by a factor of  $\cos(145^\circ)/\cos(130^\circ) = 1.27$ .

The PSD obtained from mercury intrusion relates to pore constrictions whereas the PSD obtained from extrusion measures relates to larger sections of the pores. A hysteresis phenomenon is observed (Figure 5) in the intrusion-extrusion cycle. Some partial explanations to this phenomenon are hysteresis of the contact angle, ink-bottle theory or pore connectivity. In fact, that hysteresis may be associated with pore connectivity through modelling. Nevertheless, during this modelling the user has to make several assumptions so the final result is somewhat arbitrary (Giesche 2006; Morrow 1990).

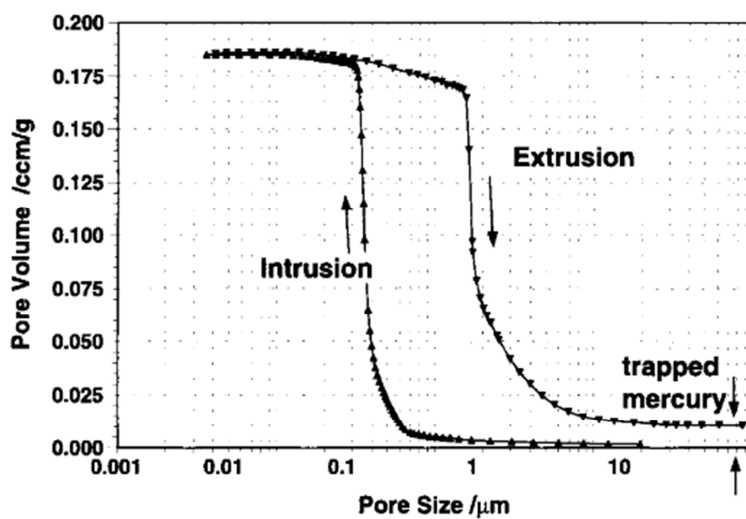
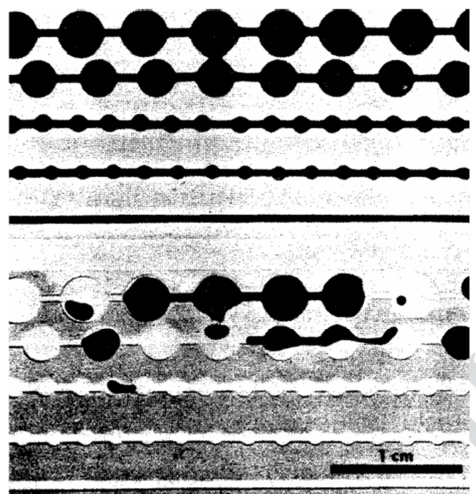


Figure 5: Typical intrusion/extrusion hysteresis observed in packed sphere structures (Schüth *et al.* 2002).

At the end of the intrusion-extrusion loop, some mercury remains trapped in the porous medium as not all the injected volume leaves the sample when the pressure is lowered. Consequently, the method is destructive and the porous samples are not reusable. As presented and proved by Wardlaw and McKellar (1981), four aspects affect the trapping of mercury during withdrawal from the porous medium: (1) pore and throat sizes and shapes and

pore to throat size ratio (Figure 6), (2) throat-to-pore coordination number, (3) random and non-random heterogeneities, (4) surface condition or roughness of pores and throats.



**Figure 6: Glass model of an artificial pore system. Trapped mercury is visible in black in the bottom picture after release of pressure. Wardlaw and McKellar (1981).**

As concluded by Giesche (2006) and Schüth *et al.* (2002), the PSD obtained from MIP are primarily useful in relative comparisons of similar materials, as the assumptions and experimental factors (contact angle, connectivity, compressibility, etc.) cancel out and therefore it is not quite as critical to have perfectly correct values in these cases.

Another factor that may be taken into account so as to increase precision of the results is compressibility. Not only the porous sample, but also the mercury and the penetrometer experience compression during a test. This involves an overestimation of the pore volume. The solution consists in performing a blank run together with mathematical corrections. Also, rapid compression (short equilibration times) at high pressures may lead to a temperature increase of as much as 50°C (Micromeritics 1997) that will affect the measure of small pores' volume. Therefore, an adequate control of temperature is required.

### **2.1.5. Health, environmental and legal issues related to MIP: international context**

Undoubtedly, the major shortcoming of MIP is the use of mercury, known to be a highly toxic fluid. The use of this fluid poses a health hazard as well as an environmental problem. The recommended limit of mercury vapor concentration in air is 0.02 mg/m<sup>3</sup> according to INRS (French National Institute of Health and Safety at Work, see INRS 2012). Blando and Singh (2004) provided information about safe handling of mercury. It has to be noted here that a great effort should be made in order to raise awareness of these concerns, especially in personnel and users that have manipulated mercury in the past when these risks for health and environment were not so well-known. Some professional diseases caused by mercury are: acute encephalopathy, intentional tremor, cerebellar ataxia, stomatitis, colic, diarrhea, azotemic nephritis and recurrent eczematous lesions (INRS 2003). An acute exposure to

mercury vapors may cause several psychiatric and neurological disturbances (World Health Organization 1976): loss of memory, insomnia, lack of self-control, irritability and excitability, anxiety, loss of self-confidence, drowsiness, and depression. In the most severe cases delirium with hallucinations, suicidal melancholia, or even manic-depressive psychoses have been described. Furthermore mercury is classed as mutagenic and carcinogenic and it may cause reproductive problems. Also, release of mercury to the environment may lead to accumulation in fish and shellfish with additional accumulation in their predators or consumers (biomagnification) as happened in Minamata (Japan) where almost 3000 persons suffered from diseases caused by mercury effluents to sea.

Several countries have already adopted national restrictions on mercury for measuring devices (Lassen *et al.* 2008; European Chemicals Agency 2011). **Norway** possesses currently the world's most progressive legislation on mercury in products: general prohibition on production, import, export, sale and use of mercury and articles containing mercury. In some cases, porosimeters may be used for "analysis and research" purposes, but import and sales are forbidden and suppliers have to apply for an exemption in order to place mercury on the market for analysis and research and in practice only a few applications are received. **Sweden** prohibits the placing on the market, use and export of mercury and goods containing mercury, including porosimeters: there are only two porosimeters exempted in the country and alternative methods dominate the market. **Denmark** prohibits import, sale and export of mercury and mercury-containing products. Mercury porosimetry may be exempted depending on the application. No particular problem has been reported with the introduction and application of these national restrictions. The **Netherlands** restrict production and import of mercury-containing products but an exemption exists for mercury porosimeters.

Besides, an **international** legally binding limitation on the use of mercury is being adopted following the signing of **Minamata Convention on Mercury** in October 2013 (UNEP 2013) by 139 governments. Some of the main resolutions of the United Nations treaty are listed below:

- Each Party shall not allow primary mercury mining that was not being conducted within its territory at the date of entry into force of the Convention for it.
- Any Party may submit a proposal to the Secretariat for listing a mercury-added product, which shall include information related to the availability, technical and economic feasibility and environmental and health risks and benefits of the non-mercury alternatives to the product.
- National plans will be drawn up within three years of the treaty entering into force to reduce - and if possible eliminate - mercury.
- Parties shall endeavor to cooperate to develop and improve information and research on the technical and economic availability of mercury-free products and processes and on best available techniques and best environmental practices to reduce and monitor emissions and releases of mercury and mercury compounds.
- The Conference of the Parties shall, by its second meeting and thereafter on a regular basis consider information on existing initiatives and progress made in relation to alternative technologies.

- The Convention also calls for additional research on issues related to mercury.

Concerning the last point, the pact tasks nations with reinforcing efforts to monitor and tally mercury releases from a slew of sources, as explained by Lubick and Malakoff (2013). States will be requested to firm up detailed figures on mercury emissions. That will result in an exigent tracking of mercury purchases as well as a surveillance of industries, which will be demanded to provide detailed pollution reports. Effectiveness of the measures adopted by the nations will be assessed within 6 years. On that occasion, researchers are expected to report on whether efforts to limit mercury pollution are sufficient or not.

Mercury porosimetry represents about 13% of the total mercury consumption in the EU (third largest consumer of mercury). A few years ago, the **General Environment Directorate of the European Commission** presented a report on the options for reducing mercury use in products and applications (Lassen *et al.* 2008). That report included an assessment of some existing alternatives for replacing mercury porosimetry. Also, it presented a comparison of the efficiency of different policies to limit mercury porosimetry. The conclusion was that the general ban of marketing of porosimeters for mercury in porosimetry would be the most appropriate policy.

Besides, **IUPAC** Working Group on Liquid Intrusion and Alternative Methods for the characterization of macroporous materials recently published a document (Rouquerol *et al.* 2012) with the intention of listing, examining, and comparing the methods presently used to characterize macroporous structures (pore width > 50 nm). The conclusion was that none of the current alternatives is in a position to replace the mercury porosimetry. Indeed, none of them can provide in 2–3 h comparable information over so broad a pore sizes range. Therefore, abandoning mercury porosimetry would result in a loss of efficiency of research and of routine work on macroporous materials. It is then of great interest to develop new alternative methods. In that respect, the aim of the present work is to propose an efficient nontoxic method to derive PSD from experiments of injection of a yield stress fluid in porous media.

### **2.1.6. Other methods to characterize PSDs of porous media**

Nowadays, Mercury Intrusion Porosimetry (MIP) is undeniably the reference technique to characterize porous media in terms of their PSD. In spite of the drawbacks that have been presented, MIP is a well-established method which has been used for decades. However, a number of different methods exist to obtain the PSDs of porous media, which may be complementary or alternative to MIP only in some applications. A distinction is made between imaging methods and invading fluid methods.

#### **Imaging methods**

Among these methods, **stereology** is a time consuming method which consists in deducing pore characteristics from imaging thin porous medium slices (Riche *et al.* 2012; Okabe and

Blunt 2005; Galaup *et al.* 2012). Treatment and correlation of many successive images is needed to provide statistically representative shapes and sizes of the pore space. Others disadvantages of the thin sectioning method include the extensive man hours required in polishing/slicing/digitalization, the destructive nature of the technique and the fact that the digitalization resolution within each slice is much superior to the slice thickness (Lindquist and Venkatarangan 2000). Being based on direct observations, this method provides, in a sense, more realistic values of the pore structural parameters than other less direct methods. On the other hand, such real values are of little use in predicting many of the practically important properties of porous media, such as permeability (Rouquerol *et al.* 1994).

More recently, great progress on direct measurement of the pore space topology has been achieved with **3D X-ray computed tomography** (Wildenschild 2012; Lindquist and Venkatarangan 2000; Prodanovic *et al.* 2006, 2007; Burlion *et al.* 2006). The experiments consist in scattering an X-ray beam through the porous sample (Figure 7), which is mounted on a rotation stage, and mapping the material's X-ray absorption. That is achieved by measuring the intensity of the beam after it passes through the sample in each direction. The attenuation phenomenon along the path followed by the X-ray beam is described by Beer-Lambert law. The procedure is repeated with many different orientations of the sample (by rotating it), resulting in a big set of radiograph of the sample from different angles. Then, a stack of 2D-images is obtained from these radiographs. Each of these 2D-images corresponds to a transversal section of the pore sample. Nevertheless, it has to be borne in mind that the 2D-images are actually volumetric, with a depth of 1 pixel. Finally, a 3D-image is obtained from combination of the 2D-views. The images obtained with 3D microtomography are undoubtedly eloquent and speaking, and allow visualization of closed pores. Nevertheless, this nondestructive technique has a resolution of typically 1  $\mu\text{m}$ , which makes impossible the visualization of pore constrictions in some cases and restricts its range of applicability to pores whose length is greater than that resolution. Furthermore, the porous samples analyzed with this technique should be tiny because, otherwise, the radiation would be completely absorbed. As a rule of thumb, the size of the pixel is 2,000 inferior to the diameter of the sample (for a cylindrical sample). Consequently, 1  $\mu\text{m}$  resolution is achieved with cylindrical samples whose diameter is 2 mm.

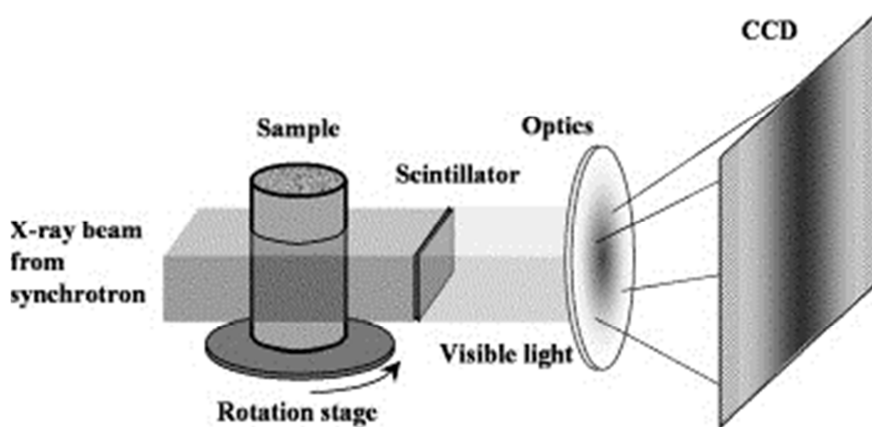
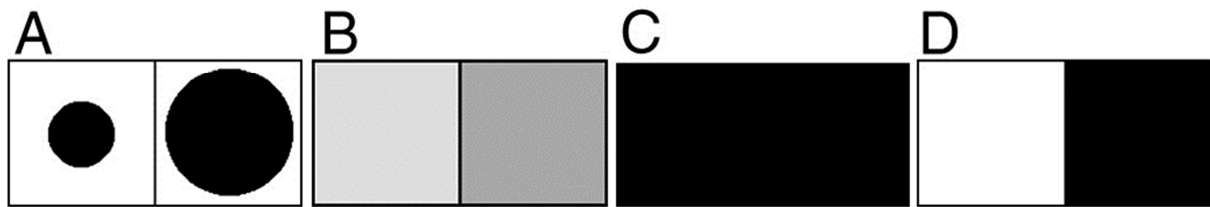


Figure 7: Sketch of the experimental setup for microtomography mapping. (Burlion *et al.* 2006).

A well-known problem regarding imaging techniques consists in the subjectivity associated to the choice of the grey level threshold needed to transform a raw image to a binary one in which one color represents void and the other color represents solid material. Filters are

usually applied to the raw image so as to enhance the definition of the edges (Sheppard *et al.* 2004). The most problematic voxels are those containing pores boundaries or pores whose size is smaller than the image resolution. Different choices of grey level threshold may lead to great differences in pore shape and size. This uncertainty yields to underestimation or overestimation of the pore boundaries and, as a consequence, to errors in the pores radii estimation. Even more, the boundary between two adjacent pores can be broken forming one large pore, or, on the contrary, fictitious boundaries can be created (Vergés *et al.* 2011) (Figure 8). Consequently, these two main limitations, resolution and choice of the grey level threshold, will strongly affect the obtained PSD.



**Figure 8: Partial volume effect.** A) Real configuration of two adjacent pores smaller than a pixel. B) Scanned image composed of two pixels with different grey-level. C) Binary segmented image that detects one large pore fusion instead of the two real ones. D) Binary segmentation that detects only the larger pore. (Vergés *et al.* 2011).

Finally, another difficulty lies in the fact that a preset network model is needed in order to define pore geometry. Regarding this definition of the pore geometry, several criteria are possible: spheres connected by channels, intersecting spheres, etc. The input of these networks include coordination number of pores, pore size distribution, pore throat distribution, pore body-to-pore throat aspect ratio, and pore body-to-pore body aspect ratio. Therefore, different networks may be obtained for the same sample as a consequence of the different possibilities to define pore bodies and pore throats (Prodanovic *et al.* 2006; Okabe and Blunt 2005, Sheppard *et al.* 2005). A recent work tackling the acquisition of microstructural parameters from a microtomographic image and their link to permeability was presented by Plougonven (2009). Also, an overview of the recent progress in microtomography was published by (Wildenschild 2012).

Other imaging methods exist but will not be treated here, such as **NMR methods** which seek to exploit the relaxation dynamics of the nuclear spin of fluid molecules to determine the pore size distribution (Padhy *et al.* 2007; Song 2007).

### **Invasive fluid methods**

Due to the limitations, representativeness and cost of the techniques mentioned above, methods of invading fluids are favored even if each of them has some specific shortcomings.

**Intrusion of non-wetting liquids other than mercury:** some candidates are Gallium, Indium, Wood's metal (bismuth alloy containing lead, tin, and cadmium) and Field's metal (eutectic alloy of bismuth, indium, and tin). Unfortunately, none of them gather these three necessary conditions (Rouquerol *et al.* 2012): non-wetting on many materials, liquid at room temperature, and safer to handle than mercury.

**Water intrusion in hydrophobic materials** (Gomez *et al.* 2000) is based on the same principle than MIP. However, only a few macroporous materials are strictly hydrophobic and determination of the contact angle is complicated.

**Liquid porosimetry** (Miller and Tyomkin 1994, Rouquerol *et al.* 2012) consists in draining a liquid (typically water) out of a saturated porous sample by applying increasing pressures and weighting the fluid leaving the sample at each pressure. Laplace's equation permits to associate a pore radius (bundle-of-capillaries model) to each pressure level. The principle is similar to that of MIP but the fluid is forced to leave the sample instead of forced to enter it. A suction/drainage cycle may be performed as described in the literature (Miller et Tyomkin 1994). This method is suitable for the determination of the pore size distribution in the range from 1 to 1000  $\mu\text{m}$ .

**Contact porosimetry** (Volkovich *et al.* 2001) is based on the laws of capillary equilibrium. The samples to be analyzed are stacked together and in close contact with some standard samples. Then, they are saturated with a wetting liquid (usually hydrocarbons). After that, a volume of liquid is evaporated through the open surface and the assembly is closed and stored until a new equilibrium is attained. After that, the stack is disassembled and the individual samples are weighted. Further evaporation is produced and the same procedure is repeated. Comparison with the standard samples allows determination of the PSD because at the state of capillary equilibrium (and under some hypothesis), the maximum pore size filled with the liquid is the same in all the samples in contact. Pores sizes ranging from  $10^{-2}$  to  $10^2 \mu\text{m}$  may be analyzed.

Several methods are based on **adsorption–desorption** from the **gas phase** in the pressure range associated with the phenomenon of capillary condensation. That phenomenon is generally accompanied by a hysteresis loop in the adsorption–desorption isotherm (Rouquerol *et al.* 2012). PSD is derived either by the application of procedures based on the Kelvin equation or by the application of density functional theory. **Water vapor adsorption methods** have shortcomings with respect to the analysis of coarse size pores due to the lack of capillary condensation (Kate and Gokhale 2006). **Low-pressure adsorption** of CO<sub>2</sub> is useful for characterizing microporosity (pore diameters < 2 nm), while **low-pressure adsorption** of nitrogen is useful for characterizing meso and macroporosity (pore sizes between 2 and 50 nm, and >50 nm, respectively) (Clarkson *et al.* 2013). Unfortunately, low-pressure adsorption has an upper pore diameter limit of about 300 nm. Furthermore, this technique requires drying of the porous media samples to remove volatiles prior to analysis.

Other methods to obtain PSD in porous media are: thermoporometry, SEM microscopy, ultrasounds, permeation methods, etc. An outstanding review of the methods to determine PSD was presented by Rouquerol *et al.* (2012).

### **2.1.7. Reference porous media**

Reference porous materials are standards used to check and compare the measures obtained with different instruments. Even if MIP is the most widespread porosimetry technique, there is not much variety in the choice of reference materials. Rouquerol *et al.* (2012) summarized the worldwide availability of these materials, concluding that they are really scarce. Other major problems are the lack of standard materials for porosimetry techniques other than MIP and gas adsorption and the inexistence in the market of simple homogeneous samples such as bundles of capillaries.

## **2.2. Complex fluids**

Complex fluids may be defined as condensed-phase materials whose mechanical properties are intermediate between ordinary liquids and ordinary solids. We will begin by classifying the types of non-Newtonian behaviors that can be representative of complex fluids as well as the most popular rheological laws. Afterwards, we will focus on several aspects of yield stress and the attached controversy. Also, some phenomenological interrelations between micro structure and rheology will be considered. At the end of the section some examples of yield stress fluids will be compared and the rheology of polymer solutions, which will be used in our experimental work, will be presented.

### **2.2.1. Classification of non-Newtonian fluids and main models**

Following Chhabra and Richardson (2008) “a non-Newtonian fluid is one whose flow curve (shear stress versus shear rate) is nonlinear or does not pass through the origin, i.e. where the apparent viscosity, shear stress divided by shear rate, is not constant at a given temperature and pressure but is dependent on flow conditions such as flow geometry, shear rate, etc. and sometimes even on the kinematic history of the fluid element under consideration”. Accordingly, non-Newtonian fluids may be classified into four main categories:

1. Fluids whose apparent viscosity is finite but dependent on the applied shear rate, i.e. shear stress divided by shear rate is not constant for every shear rate. This category may be divided into 2 subcategories:
  - a. **Shear-thickening fluids:** fluids whose apparent viscosity increases with shear rate.
  - b. **Shear-thinning fluids:** fluids whose apparent viscosity decreases with shear rate.
2. Fluids whose apparent viscosity is infinite below a threshold in terms of shear stress. That means that these fluids do not flow unless the stress they experience is greater than a yield value. They are known as **yield stress fluids**.
3. Fluids whose apparent viscosity depends on time: their apparent viscosity depends on the duration of the application of a given shear stress and/or on the previously applied

stresses. This behavior is known as **thixotropy** and the fluids exhibiting it are called **thixotropic fluids**.

4. Fluids exhibiting characteristics of both viscous fluids and elastic solids. They present both elastic energy storage and viscous energy loss, which entails that only a part of the strain is elastically recovered after deformation. They are known as **viscoelastic fluids**.

In this classification, non-Newtonian fluids are presented as having just one type of deviation from Newtonian behavior. However, very often non-Newtonian fluids exhibit a mix of these deviations. Therefore, they can be both thixotropic and rheo-thinning, viscoelastic and thixotropic, etc.

Only simple shear deformation of incompressible fluids will be considered here. In this case, the velocity vector  $\bar{v}$  has just one nonzero component  $v_i$  that depends only on the value of a coordinate  $j \neq i$ . The shear rate tensor in simple shear is of the form:

$$\bar{\bar{D}} = \begin{pmatrix} 0 & d & 0 \\ d & 0 & 0 \\ 0 & 0 & 0 \end{pmatrix}$$

with  $d = \frac{1}{2} \left( \frac{\partial v_i}{\partial x_j} \right)$  and  $\bar{x}$  being the position vector.

The corresponding shear stress tensor is:

$$\bar{\bar{\tau}} = \begin{pmatrix} 0 & -\tau & 0 \\ -\tau & 0 & 0 \\ 0 & 0 & 0 \end{pmatrix}$$

In the particular case of simple shear rate, a generalized shear rate may be defined as  $\dot{\gamma} = 2d = \frac{\partial v_i}{\partial x_j}$ . From now on, and for simplicity, we will refer to generalized shear rate simply as shear rate  $\dot{\gamma}$  and to  $\tau$  simply as shear stress, the apparent viscosity  $\mu$  being defined as  $\mu = \frac{\tau}{\dot{\gamma}}$ .

For Newtonian fluids  $\mu$  is constant at a given temperature and pressure and does not depend on time or on shear rate. Therefore:

$$\tau = \mu \dot{\gamma} \quad (2.11)$$

with  $\mu$  being the dynamic viscosity of the fluid.

Here below, some analytical rheological models for non-Newtonian fluids are presented. These models are rheological laws that link shear stress  $\tau$  to shear rate  $\dot{\gamma}$  or alternatively apparent viscosity to shear rate (**constitutive relations**). More information may be found in the reference book of Bird *et al.* (1977). The most usual relationships among these rheological laws are presented below.

## **Shear-thinning and shear-thickening fluids**

### **Power-law or Ostwald de Waele model**

In this empirical model,  $\tau$  and  $\dot{\gamma}$  are related through the power law

$$\tau = m_p \dot{\gamma}^{n_p} \quad (2.12)$$

giving:

$$\mu = m_p \dot{\gamma}^{n_p - 1} \quad (2.13)$$

$m_p$  is called consistency and  $n_p$  is called flow index.  $m_p$  and  $n_p$  are positive empirical parameters and are obtained by fitting experimental measures of shear stress or apparent viscosity as a function of shear rate. If  $n_p < 1$  the fluid behaves as shear-thinning and if  $n_p > 1$  the fluid exhibits shear-thickening behavior. The particular case  $n_p = 1$  corresponds to Newtonian fluids.

Power-law model is the simplest representation of shear-thinning/shear-thickening behavior and is the most employed model. However, it presents several drawbacks (Chhabra and Richardson 2008):  $m_p$  and  $n_p$  are usually dependent on the scanned range of shear rates and do not predict the limiting apparent viscosities at very low and very high shear rates.

### **Truncated power law**

Power-law model can be modified in order to allow prediction of the limiting values of viscosity at very low and very high shear rates, i.e.  $\mu_{0p}$  and  $\mu_{\infty p}$ .  $\mu_{0p}$  is the maximum plateau viscosity (at very low shear rates) and  $\mu_{\infty p}$  is the minimum plateau viscosity (at very high shear rates). The truncated power-law (López 2004) is a piecewise-defined function of the form:

$$\mu = \text{Max}\{\mu_{\infty p}; \text{Min}(m_p \dot{\gamma}^{n_p - 1}, \mu_{0p})\} \quad (2.14)$$

### **Carreau model (for shear-thinning fluids)**

In contrast to truncated power-law model, Carreau (1972) equation is based on molecular network theory. It includes an additional parameter with respect to truncated power-law,  $\lambda$ , that stands for the longest relaxation time. This model is often presented as:

$$\frac{\mu - \mu_{\infty}}{\mu_0 - \mu_{\infty}} = [1 + (\lambda \dot{\gamma})^2]^{\frac{n-1}{2}} \quad (2.15)$$

$\mu_\infty$ ,  $\mu_0$  and  $n$  being analogous to  $\mu_{\infty p}$ ,  $\mu_{0p}$ , and  $n_p$ . Newtonian case corresponds to  $\lambda = 0$  or  $n = 1$  or both.

### Cross model (for shear-thinning fluids)

It is another popular four parameter model presented by Cross (1965) which is expressed as:

$$\frac{\mu - \mu_{\infty cr}}{\mu_{0cr} - \mu_{\infty cr}} = \frac{1}{1 + k_{cr}\dot{\gamma}^{n_{cr}}} \quad (2.16)$$

with  $n_{cr}$  and  $k_{cr}$  being fitting parameters. It reduces to the power-law when  $\mu \ll \mu_{0cr}$  or  $\mu \gg \mu_{\infty cr}$ .

### Yield stress fluids

Yield stress fluids are materials that behave as a solid for  $\tau < \tau_0$ .

#### The Bingham model

This is the simplest empirical model to describe the rheological behavior of yield stress fluids. It is a piecewise-defined function as follows:

$$\begin{cases} \tau = \tau_{0B} + \mu_B \dot{\gamma} & \text{for } \tau \geq \tau_{0B} \\ \dot{\gamma} = 0 & \text{for } \tau \leq \tau_{0B} \end{cases} \quad (2.17)$$

where  $\mu_B$  is the Bingham viscosity and  $\tau_{0B}$  is the yield stress. The corresponding apparent viscosity is:

$$\begin{cases} \mu = \frac{\tau_{0B} + \mu_B \dot{\gamma}}{\dot{\gamma}} & \text{for } \tau \geq \tau_{0B} \\ \mu = \infty & \text{for } \tau \leq \tau_{0B} \end{cases} \quad (2.18)$$

Bingham viscosity is the slope of  $\tau(\dot{\gamma})$  beyond the yield stress:  $\mu_B = \frac{\tau - \tau_{0B}}{\dot{\gamma}}$  for  $\tau > \tau_{0B}$ . It is an empirical model in which  $\tau_0$  and  $\mu_B$  are generally obtained by fitting the measures of  $\tau$  as a function of  $\dot{\gamma}$ . Nevertheless, one can try to assess  $\tau_0$  in a more physically-meaning manner as will be explained later. Also, it has to be noted that no minimum value of  $\mu$  is included in the model, so  $\mu$  tends to 0 at very high shear rates.

### The Herschel-Bulkley model

As already mentioned, the elementary non-Newtonian behaviors presented above are usually combined so that, for example, a fluid may exhibit shear-thinning behavior and also have a yield stress. The empirical Herschel-Bulkley model combines yield stress  $\tau_0$  with shear-depending viscosity as:

$$\begin{cases} \tau = \tau_0 + k\dot{\gamma}^n & \text{for } \tau \geq \tau_0 \\ \dot{\gamma} = 0 & \text{for } \tau \leq \tau_0 \end{cases} \quad (2.19)$$

where  $k$  is named consistency and  $n$  is the flow index. In this case, the apparent viscosity is defined as:

$$\begin{cases} \mu = \frac{\tau_0}{\dot{\gamma}} + k\dot{\gamma}^{n-1} & \text{for } \tau \geq \tau_0 \\ \mu = \infty & \text{for } \tau \leq \tau_0 \end{cases} \quad (2.20)$$

$\tau_0$ ,  $k$  and  $n$  are generally obtained by fitting the data obtained by measuring  $\tau$  as a function of  $\dot{\gamma}$ . Furthermore, just as for the Bingham fluid, there is not a limiting value of viscosity at high shear rates.  $m$  and  $n$  depend on the range of shear rates considered. In fact, for sufficiently high shear rates, Herschel-Bulkley fluids may be approximated to Bingham fluids. Newtonian, Bingham and Herschel-Bulkley models are represented in Figure 9.

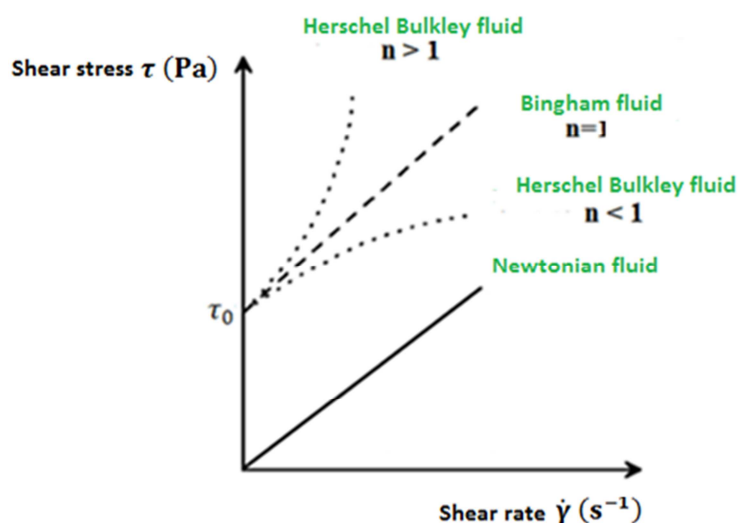


Figure 9: Newtonian, Bingham and Herschel-Bulkley models.

### The Casson model

This model is widespread when dealing with biological fluids or foodstuffs

$$\begin{cases} \tau^{1/2} = (\tau_0^C)^{1/2} + (\mu_C \dot{\gamma})^{1/2} & \text{for } \tau \geq \tau_0^C \\ \dot{\gamma} = 0 & \text{for } \tau \leq \tau_0^C \end{cases} \quad (2.21)$$

As in the preceding model, both shear-depending viscosity and yield stress are taken into account.

### **Thixotropic fluids**

According to Barnes *et al.* (1989) thixotropy can be defined as a decrease of the apparent viscosity in the course of time under constant shear stress or shear rate. This decrease may be followed by a gradual recovery when the stress or shear rate is removed. The same authors defined rheopexy as the opposite of thixotropy (increase of the apparent viscosity under constant shear stress or shear rate, followed by a gradual decrease when the stress or shear rate is removed).

Thixotropic behavior is very usual in many industrial applications, so its modelling has been the subject of significant efforts (Chhabra and Richardson 2008). Three distinct approaches may be adopted: continuum, micro-structural and structural kinetics. Continuum approaches consist in modifying non-thixotropic constitutive equations by making the parameters (yield stress, consistency, etc.) time-dependent. Nevertheless, it is not an easy task, because the model parameters are not always directly connected with structural changes resulting from thixotropy. Micro-structural models are theory-based. They involve definition of inter-particle forces, which have not always been studied in the case of engineering fluids. Finally, structural kinetics approaches are based on the definition of a parameter,  $\xi$ , which varies from zero (corresponding to the completely broken-down structure) to unity (corresponding to the complete build-up of structure). As explained by Chhabra and Richardson (2008), this family of models consists of two equations: the first equation connects the shear stress to shear rate for a fixed values of  $\xi$ . The second equation describes the variation of  $\xi$  with time, akin to a reversible chemical reaction. A widespread example of structural-kinetics approach is the Tiu-Boger model (Tiu and Boger 1974) is a modified Herschel-Bulkley model:

$$\tau = \xi(\tau_0 + k\dot{\gamma}^n) \quad (2.22)$$

The decay of the structural parameter  $\xi$  with time  $t$  was assumed to obey a second-order equation:

$$\frac{d\xi}{dt} = -k_1(\xi - \xi_e)^2 \quad (2.23)$$

Where  $\xi_e$  and  $k_1$  depend on shear rate and are determined experimentally by using the values of apparent viscosities (Tiu and Boger 1974; Rao 2007).  $\lambda_e$  represents the equilibrium shear rate for a given shear stress. The interested readers are referred to Tropea *et al.* (2007) for a more complete discussion on thixotropy.

### **Viscoelastic fluids**

Hooke's law expresses the proportionality between stress and deformation for a perfectly elastic material. In the case of simple shear, Hooke's law is written as:

$$\tau = G\gamma \quad (2.24)$$

where  $G$  is Young's shear modulus and  $\gamma$  is the strain. For real elastic materials, Eq. (2.24) is only valid for small deformations. When the applied stress is beyond the elastic limit, the material yields.

If the force deforming a perfectly elastic solid is inferior to the elastic limit, the solid will recover its original form on removal of that force. For perfectly viscous fluids, stress is proportional to strain rate (Eq. 2.11, known as Newton's law):  $\tau = \mu\dot{\gamma}$ . Whereas elastic solids deform when a stress is applied, viscous fluids flow. Viscoelastic materials present both elastic and viscous behaviors as they have some ability to store and recover mechanical energy.

### The Maxwell model for linear viscoelasticity

Models for linear viscoelasticity assume small deformation and small deformation rate. In that case, material functions do not depend on the magnitude of the stress, the magnitude of the deforming strain or the rate of application of the strain (Steffe 1996). A linear applied stress will produce a proportional strain response. The Maxwell model is usually presented through its mechanical analogue (Figure 10), which consists in a series combination of a spring and a dashpot. Spring represents an ideal elastic solid (following Hook's law) whereas dashpot represents an ideal viscous fluid (Newton's law). Given than the spring and the dashpot are connected in series, in shear flow the total shear rate  $\dot{\gamma}$  will be the sum of the shear rates of the spring  $\dot{\gamma}_1$  and the dashpot  $\dot{\gamma}_2$ :

$$\dot{\gamma} = \dot{\gamma}_1 + \dot{\gamma}_2 = \frac{\dot{\tau}}{G} + \frac{\tau}{\mu} \quad (2.25)$$

The previous expression may be rewritten as:

$$\tau + \varphi\dot{\tau} = \mu\dot{\gamma} \quad (2.26)$$

Where  $\varphi = \frac{\mu}{G}$  is known as relaxation time.

If a constant strain is applied  $\tau + \varphi\dot{\tau} = 0$  so  $\tau = \tau_m e^{-\frac{t}{\varphi}}$  where  $\tau_m$  is the maximum shear stress (at  $t = 0$ ). That reflects the fact that the spring will deform instantly (elastic deformation) and the dashpot will subsequently dissipate reducing the stored stress. Therefore, viscous response dominates in the Maxwell model and it conveniently represents liquid behavior. However, as real fluids exhibit complex behavior, that imposes the use of a relaxation time spectrum. The Maxwell model has been generalized for that end.

### The Voigt model for linear viscoelasticity

As in the Maxwell model, Voigt model is presented by means of its mechanical analogue. This time, the spring and the dashpot are connected in parallel (Figure 10) so the strain in both

elements is the same and the total stress is the sum of the stresses in the spring and the dashpot. In shear, this leads to:

$$\tau = G\gamma + \mu\dot{\gamma} \quad (2.27)$$

If a constant stress is instantaneously applied, the system will evolve until  $\tau = G\gamma$ , so no more flow will exist after a given time. This model is convenient to represent solid-like behavior.

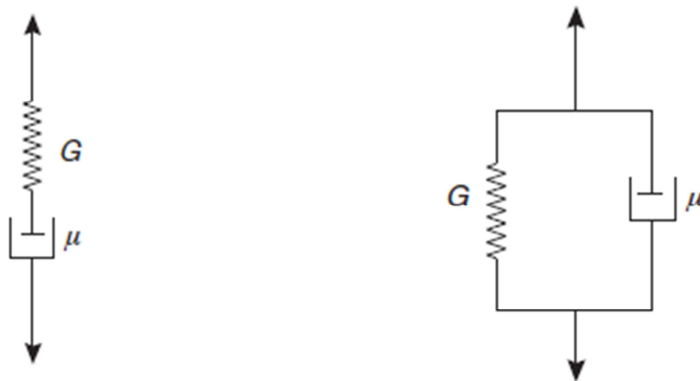


**Figure 10:** Schematic representation of Maxwell (left) and Voigt (right) model, from Chhabra and Richardson (2008).

It has to be noted that both Maxwell and Voigt models are crude and provide only qualitative representation of the viscoelastic behavior and more refined models are needed to approach commonly observed behaviors.

Models for non-linear viscoelasticity will not be tackled here (see Brinson and Brinson 2008 for information).

### **2.2.2. Some comments on yield stress**

As mentioned before, yield stress fluids do not flow unless they experience a stress exceeding the yield stress  $\tau_0$ . Under weaker stresses, they will only deform like an elastic solid, storing energy. This behavior may be explained by the presence of a 3D structure of sufficient rigidity to resist stresses whose value is weaker than  $\tau_0$ . However, that structure will break for stresses greater than  $\tau_0$  and the material will then behave like a viscous fluid (Chhabra and Richardson 2008; Steffe 1996). Unfortunately, that transition is difficult to describe and technically impossible to measure as will be exposed here below.

#### **The existence of yield stress: an endless debate?**

The existence of yield stress was challenged by Barnes and Walters (1985) and has been discussed for almost 30 years. In fact, it is a common occurrence at British Society of Rheology meetings, as well as in international conferences, that there is heated discussion as whether yield stress exists or not (Cheng 1986). As explained by Møller *et al.* (2009), supporters of the true yield stress argue that in some materials the viscosity increases very

sharply as the stress decreases towards the yield stress. However, the opponents claim that only a finite and constant viscosity (Newtonian plateau of viscosity) is observed below a certain stress. In their criticism of the yield stress, Barnes and Walters (1985) used the newly available rheometers of that time (stress-controlled rheometers) to show that at low enough shear rates, viscosity reaches a Newtonian plateau. They argued that any material flows providing enough observation time and sufficiently sensitive measuring equipment.

In stark contrast with Barnes and Walters (1985), Møller *et al.* (2009) showed experimentally that the Newtonian plateau is just the consequence of non-steady-state measurements (Figure 11). They demonstrated that for stresses below the yield stress, viscosity is “*a priori*” unbounded and increases continuously, though slowly, if enough time is allowed. They effectively observed an increase in viscosity even after  $10^4$  seconds. In other words, they found that viscosity is time dependent and tends to infinity below the yield stress.

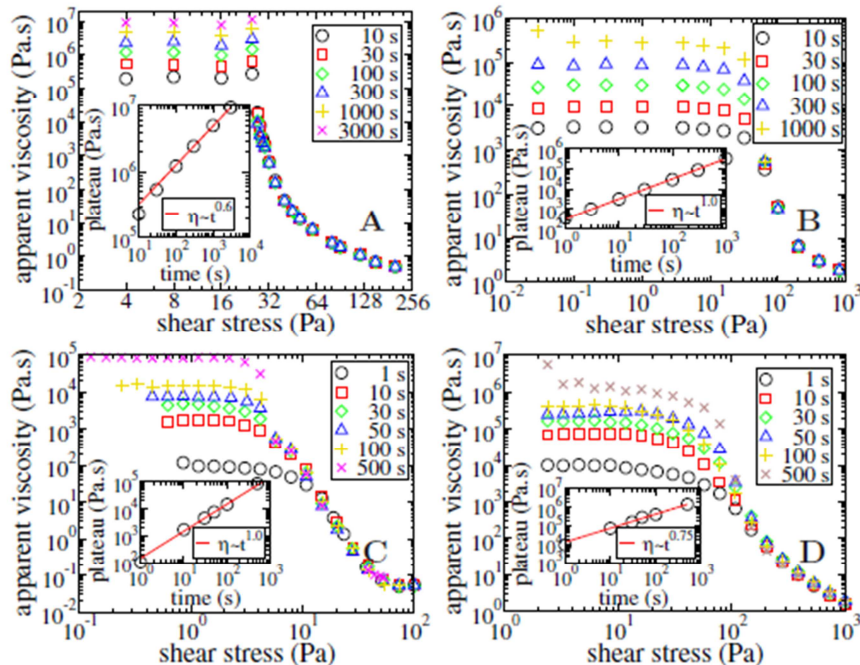


Figure 11: The values of the Newtonian plateaus increase with measurement time. The insets show that the plateaus increase as power laws with time with exponents in the range 0.6–1.0.  $\eta$  is the plateau viscosity A). 0.2% Carbopol sample. B) hair gel. C) foam. D) emulsion. From Møller *et al.* (2009).

Cheng (1986) published an enlightening article in which he explained that a further deformation will be observed for any stress provided that the observation time is long enough (Figure 12). One’s evaluation of the yield stress will differ depending on the length of the observation period and the moment at which observation begins. In fact, the choice of observation time should be related to the characteristic time of the flow process to which the result is to be applied.

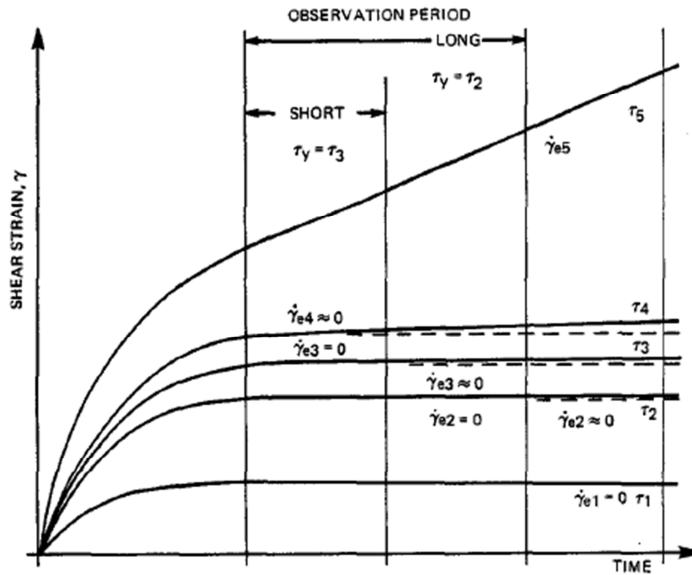


Figure 12: Yield stress (named  $\tau_y$  in this figure) depends on the length of observation period. From Cheng (1986).

Finally, opposing the existence of yield stress as a go-no go concept, Putz and Burghela (2009) reported an intermediate regime between elastic solid-like regime and purely viscous regime (power law stress-shear rate dependence) in the case of a physical gel (Carbopol). That intermediate regime consists in a solid-fluid phase coexistence characterized by a competition between destruction and reformation of the gel network.

### **The existence of yield stress: points of agreement**

At first sight, the conclusions that different researchers have drawn concerning the existence of yield stress may seem incompatible and irreconcilable. Nevertheless, a careful analysis shows that some agreement exists and may be summarized as follows:

- The yield stress of a fluid, if it ever exists, is tricky to quantify.
- Yield stress is an interesting concept with a large scope of applications.
- Steady-state is a subjective notion depending on the time scale, the tolerances, the moment at which the measurement starts, etc. Equilibrium at low shear rates is convenient but may not be necessary when dealing with applications of yield stress fluids.
- At least for a number of fluids, moderate measurement times (of strain or shear rate versus stress) will lead to a Newtonian plateau or to a bounded viscosity if a rheometer with sufficient resolution is used.
- Long but finite measurement times with a rheometer of sufficient resolution will evidence that there is always further deformation, even if the rate of deformation (shear rate) decrease with time.
- Given that the rate of deformation decreases with time at low stresses, the Newtonian plateau viscosity will increase with time.
- The existence of yield stress will never be proved because it would demand infinite measurement times.

- The nature of the structural transition occurring at yield stress is complex.

It seems that no unified theory exists concerning the nature of yield stress. Fundamentalists' repudiation of yield stress arises from the fact that it cannot be proved to be an inherent property of certain materials but depends on external and subjective factors. On the other hand, engineers and applied researchers believe in the usefulness of the yield stress in spite of its controversial determination. Indeed, yield stress is of practical interest in engineering and numerous materials closely approach the behavior of yield stress fluids. However, it is an idealized concept (Steffe 1996; Chhabra and Richardson 2008). Scott Blair (1933) defined yield stress as "that stress below which no flow can be observed under the conditions of experimentation". Then, any operational definition of yield stress should take into account both the technical limitations in its determination, and the characteristic time of the process to which it pertains (Chhabra and Richardson 2008). In the present work, an effort will be made in order to establish a yield stress determination protocol allowing comparative exploitation of our experiments.

### **Experimental determination of yield stress**

The rheological characterization of non-Newtonian fluids, and especially the experimental determination of the yield stress, is widely acknowledged to be far from straightforward (Chhabra and Richardson 2008; Møller *et al.* 2006). Møller *et al.* (2006) highlighted that the problems to determine the yield stress arise from a poor definition and from the fact that at low shear rates the shear localizes in a small region of the fluid while the remaining part behaves like a solid (shear localization). Besides, and as explained before, there is no way to know whether a given material has a true yield stress or not because the answer is related to the time scale of observation and only infinite time would show if strain ever stops or not.

Therefore, some authors prefer to refer to an "apparent yield stress", resulting from extrapolation of  $\tau(\dot{\gamma})$  to zero shear rate. A major inconvenience of this approach (Chhabra and Richardson 2008; Barnes and Walters 1985; Steffe 1996) is the fact that, as shown in Figure 13 (Barnes and Walters 1985), the obtained yield stress depends on the range of shear rates used for extrapolating as well as in the model of yield stress fluid. In fact, it is possible to fit different equations (power-law, Herschel-Bulkley, Casson, Bingham...) equally well to a given set of data, so the particular choice is based on convenience.

Another possibility consists in plotting apparent viscosity versus shear stress and taking  $\tau_0$  as the stress for which apparent viscosity attains its upper limit (or infinity in theory). That means that yield stress may be interpreted as an abrupt decrease in viscosity (several orders of magnitude) over a narrow range of shear rates or shear stresses. Accordingly, shear-thinning materials may be likened to yield stress fluids (Chhabra and Richardson 2008; Balhoff and Thompson 2006).

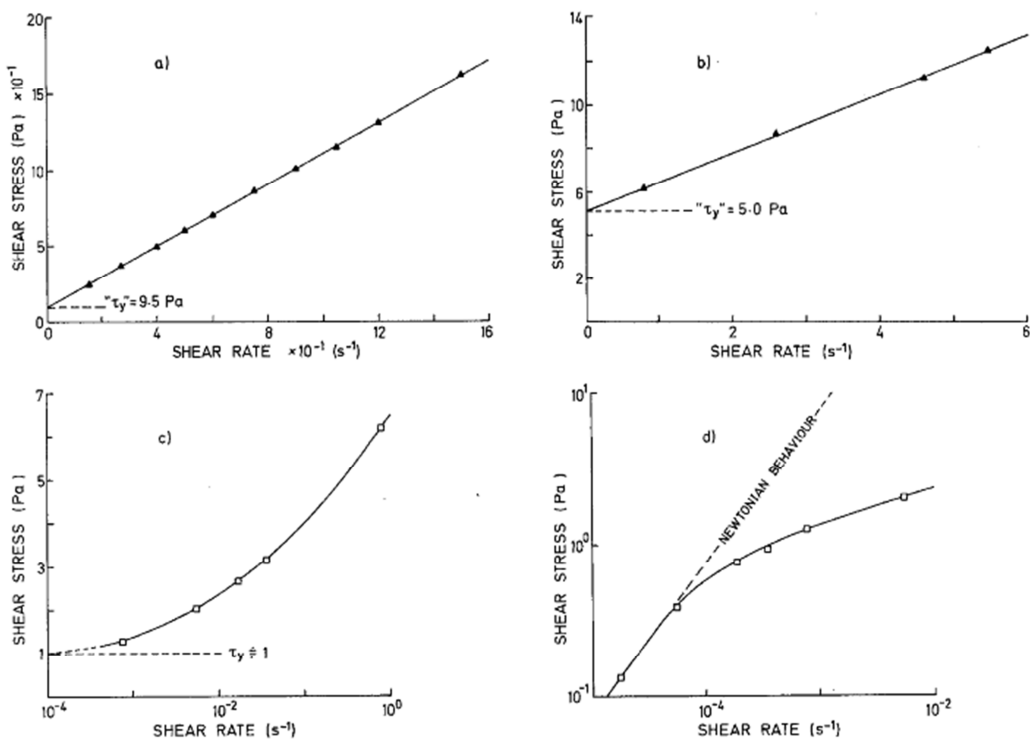


Figure 13: Viscosimetric data for a sample of PVA latex adhesive. Different ranges of shear rate lead to different values of the yield stress ( $\tau_y = \tau_0$ ) by extrapolation. a)  $10 - 150$  s $^{-1}$ , b)  $1 - 6$  s $^{-1}$ , c)  $10^{-3} - 1$  s $^{-1}$  and d)  $10^{-5} - 10^{-2}$  s $^{-1}$ . From Barnes and Walters (1985).

Due to their ability to produce very low shear rates, controlled-stress rheometers are more appropriate for investigating yield stress (Steffe 1996; Cheng 1986; Chhabra and Richardson 2008). The reason is that at low shear rates, the structure of the material may be preserved. Nonetheless, even with those rheometers, the determination of the “real” yield stress is subject to the general limitations of resolution and time scale presented before.

A number of techniques exist to measure the yield stress: stress decay, extrapolation, squeezing flow, etc. (Steffe 1996). Other than extrapolation, the vane method is quite popular (Nguyen and Boger 1983) because it minimizes wall slip and the structure of the material is not as disturbed as in the narrow gap geometries used in stress-controlled rheometers. Also, Balhoff et al. (2011) presented an inexpensive method delivering a more “objective” value of the apparent yield stress. In spite of these particular advantages, all methods present the same general limitations. It is worth remembering that an absolute yield stress is an elusive property (Steffe 1996).

### Dynamic versus static yield stress

Certain types of fluids present two different yield stresses: dynamic yield stress and static yield stress (Cheng 1986). The static yield stress is observed after prolonged storage of the fluid. During storage (at rest), a secondary weak structure builds-up and the fluid exhibits additional “resistance” to flow at low shear rates. However, that weak structure is very sensitive to shear rate, so it will be destroyed if a pre-shear is applied to the fluid and only the

dynamic yield stress corresponding to the shear-independent primary structure of the fluid will be measured. Evidently, static yield stress is greater than dynamic yield stress.

### **2.2.3. Complex fluids: link between microstructure and rheology**

Larson (1999) grouped complex fluids into classes as: polymers, glassy liquids, polymer gels, particulate gels, electro and magneto responsive suspensions, foams, emulsions, liquid crystals, liquid-crystalline polymers, surfactant solutions and block copolymers. He suggested that the main forces leading to microstructure formation are Van der Waals, electrostatic, hydrogen-bonding and hydrophobic interactions. In this subsection, some basic and qualitative concepts will be presented in order to help to understand how microstructural state is intimately linked to rheological behavior of complex fluids. But first of all, two assumptions will be made (Chhabra and Richardson 2008):

- Continuum description of the materials is assumed to be valid: micro-structural details are considered irrelevant when evaluating macroscopic characteristics.
- The material is considered homogeneous, so that the use of a space-averaged fluid property is justified.

Microstructure of complex fluids is usually transient and can be altered through application of low stresses. These changes in microstructure will lead to changes in macroscopic properties, such as viscosity. As a consequence, macroscopic behavior may be “customized” by means of additives able to change microstructure of the fluid.

Four general types of microstructures are considered here:

- Emulsion-like microstructures with a deformable discontinuous phase (droplets) immersed in a continuous phase.
- Dispersions of rigid particles in a liquid.
- Solutions of elastic coils or entangled macromolecules in a solvent.
- Suspension-like microstructures forming aggregates.

At rest, these structures are random as they are in a minimum energy state. If a low stress is applied, the microstructure will resist deformation, resulting in a high viscosity of the system: droplets in emulsions will prevent the flow of their neighbors, rigid rods randomly oriented will impede the displacement of other rods, aggregates will deform without breaking, etc. However, if the applied stress is strong enough, structural units will align or deform in the direction of flow, agglomerates will break and elastic polymer molecules will deform and disentangle. This is sketched in Figure 14. Therefore, progressive in stress will lead to progressive change in the internal structure, facilitating hence the flow of the system with, for example, a marked decrease of viscosity. For sufficiently high stresses, no more changes in structure are possible and viscosity attains a low limit. These changes in microstructure are

the basic source of the shear-thinning behavior as well as the limiting values for viscosity and the existence of yield stress.

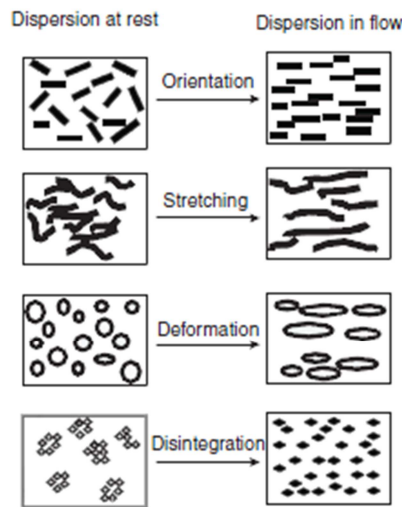


Figure 14: Schematics of ‘structures’ in rheologically complex systems under rest, from (Chhabra and Richardson 2008).

In some special cases, the particles which are disposed in layers under moderate shearing may form clusters at very high shear rates due to the particles being driven out of these layers and interacting. That entails an increase in viscosity and shear-thickening behavior.

### Connection between thixotropy, viscoelasticity and shear-thinning behavior

**Thixotropy** is a consequence of the **time** needed to complete the shear-induced **microstructural changes** in complex fluids. In fact, the microstructure of the fluid evolves in response to a change in the applied shear rate or stress. This results from competition between the processes of reordering or tearing apart by stress and flow-induced collision of particles (Tropea *et al.* 2007), and a new equilibrium state is reached. At this stage, if the stress or shear rate ceases, Brownian motion is able to reorganize the microstructural units towards more-favorable configurations. As a result, the structure is slowly rebuilt, and viscosity is increased. These destruction–reconstruction processes are reversible provided that the structural units are not destroyed during flow. It is worth reminding here that Brownian motion is the stochastic movement of the particles surrounded by a liquid (or gas) as a consequence of the thermal agitation of the molecules of the liquid. The random motion leads the structural units to favorable positions where they can “attach themselves” to other parts of the microstructure. Brownian motion-induced changes are much slower than shear-induced changes so destruction is faster than reconstruction. Finally, **rheopexy** or anti-thixotropy is observed in the case in which loosely attached structural unities are progressively detached due to Brownian motion.

**Linear viscoelasticity** is also a manifestation of the **time** required for the **microstructural changes** to take place. Effectively, if a fluid is sheared at high frequencies (short times) its structure does not have enough time to reorganize, so an elastic response is observed. However, if the fluid is sheared at low frequencies, its structure can adjust itself continuously,

i.e. it can flow showing viscous effects. As a consequence, if a whole range of shearing frequencies and times is considered, the material will show both effects (elastic and viscous) and will be classified as viscoelastic.

In some cases, the microstructure of the fluid undergoes **2 different changes** when sheared. A first change to adapt itself to respond to the flow (as linear viscoelastic materials), which takes **time**, and a second change produced by the flow itself, which takes additional **time**. These may correspond to the case of inelastic **thixotropic shear-thinning** fluids or **nonlinear viscoelastic** fluids. Therefore, the difference between thixotropic shear-thinning fluids and fluids presenting linear viscoelasticity is that in the first case the structure is destroyed whereas in the second case it is only elastically deformed but not essentially modified.

In conclusion, any structural change may take time, so all complex fluids are thixotropic to some extent. However, a fluid will be considered thixotropic only if the duration of its structural changes is of the same order as (or longer than) the duration of the measurements with a rheometer or the duration of the process. When these structural changes are shorter than the duration of the measurement or the process, the fluid will be considered viscoelastic. Finally, if the viscous effect is dominant with respect to the elastic effect for the whole range of times considered in the process, the fluid will be considered non-thixotropic shear-thinning.

### **Link between thixotropy and yield stress**

Møller *et al.* (2006) stated that yield stress and thixotropy are two effects coming from the same basic physics and that all the yield stress fluids they knew were also thixotropic. The main idea is that the build-up of the microstructure, which is typical of thixotropic materials, avoids the breakup of the microstructure below the yield stress so the fluid does not flow. Also, in contrast with the Herschel-Bulkley model predictions, viscosity jumps discontinuously from infinite to a low value at stresses slightly greater than the yield stress as a consequence of the dominance of the forces destructing the microstructure. In the same article, these authors presented a yield stress model including thixotropy.

Cheng (1986) explained that thixotropic fluids may exhibit an infinity of rheograms (shear stress as a function of shear rate), each one corresponding to a particular structural level. They also presented the determination of these rheograms. Also, an equilibrium rheogram may be obtained on which the structure is in equilibrium for each shear rate and the stress does not vary with time (Figure 15).

### **2.2.4. Rheology of polymer solutions**

The particular case of polymer solutions will be treated here because of their use in the experiments conducted in this work, which will be presented in the next chapters.

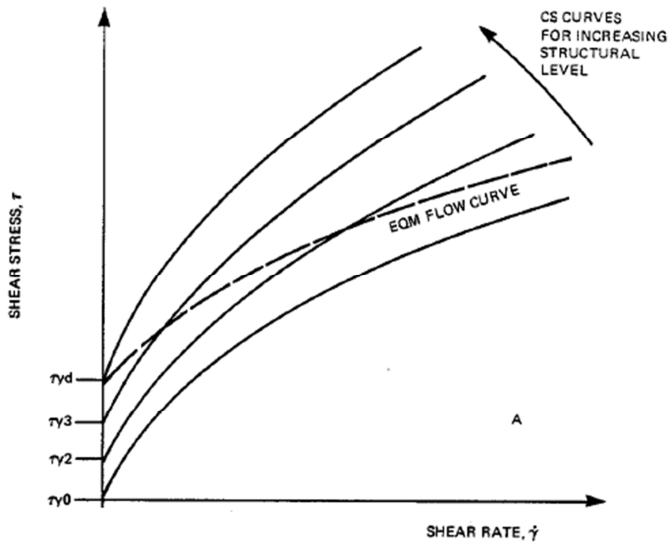


**Figure 15: Yield stress in a thixotropic fluid (Cheng 1986). CS=constant structure curve. EQM=equilibrium flow curve. ( $\tau_y = \tau_0$ ).**

### Molecular interactions as a function of polymer concentration

The relative viscosity  $\mu_r$  of a polymer solution is defined as the ratio of the solution viscosity  $\mu$  to the solvent viscosity  $\mu_s$ :

$$\mu_r = \frac{\mu}{\mu_s} \quad (2.28)$$

The relative viscosity of solutions depends on the polymer concentration  $C$  and may be expanded in a Taylor series (Bird *et al.* 1977):

$$\mu_r = 1 + [\mu]C + k'[\mu]^2C^2 + \dots \quad (2.29)$$

where the intrinsic viscosity  $[\mu]$  and the Huggins coefficient  $k'$  depend on the considered polymer/solvent couple and physicochemical conditions. From the previous expression, it follows that:

$$[\mu] = \lim_{C \rightarrow 0} \left( \frac{\mu - \mu_s}{C\mu_s} \right) \quad (2.30)$$

It has to be noted that  $[\mu]$  has the dimensions of a reciprocal concentration and represents the volume that isolate macromolecules occupy. In general,  $[\mu]$  is a function of the shear rate. At very low shear rates,  $[\mu]$  approaches a limiting value  $[\mu]_0$  which depends on the molecular weight of the polymer M and physicochemical conditions. The value of the Huggins coefficient  $k'$  is dependent on the magnitude of the monomer/solvent interaction as it represents the quality of the solvent for the considered polymer. For a good solvent, its value is  $\sim 0.3 - 0.4$  and for a poor solvent it may exceed 1.

From this point forward, we will focus on the case of linear polymers. In dilute state, the contribution of each macromolecule to viscosity is additive and the viscosity increases proportionally with concentration ( $\mu_r \cong 1 + [\mu]C$ ). At higher concentrations of the polymer solution such dependence becomes nonlinear. There exists a threshold concentration  $C^*$  above which the polymer macromolecules overlap and became entangled with each other. That concentration  $C^*$  is known as onset of entangled behavior or overlap concentration. The overlap concentration is of great interest given that it marks the transition between a dilute solution and a semi-dilute solution. Above this concentration, viscosity dependence on concentration is nonlinear. In particular, the zero shear viscosity  $\mu_0$  increases linearly with the molecular weight  $M$  below  $C^*$  while it scales typically as  $\propto M^{3.5}$  above  $C^*$  for flexible polymers of high molecular weight (Chhabra and Richardson 2008). It has to be borne in mind that this transition is progressive and does not happen at a precise concentration but rather at an interval of concentrations.

Above  $C^*$  the polymer coils interpenetrate each other producing entanglements and hindering the free movement of the polymeric chains. Gennes (1979) considered a single chain moving in a network of entangled chains. Given that the network cannot be crossed, the lateral movement of the individual chain is limited and the molecule is confined in a tube-like space by the mesh of constraints. Therefore, the polymer can only move in a wormlike fashion (back and forth movement) called “reptation” (Klein 1978). If the concentration is increased above  $C^*$ , the molecules in solution are contracted. For a given concentration called concentration of aggregation  $C^{**} (> C^*)$ , the molecules can no longer contract and form aggregates (Oliveira *et al.* 2013). Marrucci *et al.* (1999) presented an interesting review of the rheology of polymer melts and concentrated solutions.

Some concentrated polymeric solutions form physical gels. As defined by Larson (1999), physical gelation is the conversion of a liquid to a disordered solid by formation of a network of physical bonds between the molecules or particles composing the liquid. Physical gelation arises from intermolecular associations such as van der Waals forces, hydrogen bonding or electrostatic attraction. When the crosslinks are stable (for a given range of stresses and times), we say that the gel is strong. We say that the gel is weak when the bonds are not stable and can break and reform, (de Gennes 1979). Physical gelation has been shown to occur with formation of helical structures, micro crystallites and nodular domains. Polymeric physical gels are viscoelastic in general. Also, some concentrated solutions of rigid or semi rigid polymer may form liquid crystals (see Larson 1999 for details).

### **Rheological behavior of polymer solutions**

Polymer solutions are very diverse and it is not possible to define a general rheological behavior. The most important factors determining the rheological behavior of polymer solutions (Chhabra and Richardson 2008) are the molecular weight of the polymer, the structure and possible configurations of the macromolecule, its chemical composition, the polymer-solvent interactions, the volume fraction, the concentration and the physicochemical

conditions. The viscosity of the solution is strongly influenced by the architecture of polymer chains, i.e. rod-like (rigid or semi-rigid) or linear coils, and the degree of polymer branching.

The configuration of the polymer chains can be affected by the application of shear stresses or deformation rates, which may cause stretching, break-up of bonds, disentangling and uncoiling. All these effects produce shear-thinning behavior or thickening in the case of elongational flow. Besides, the viscoelasticity presented by a number of concentrated polymer solutions may be explained by the fact that whereas the network is deformed elastically, the entangled molecules can flow as explained before. Also, thixotropy is a consequence of the destruction and reconstruction of bonds and entanglements under flow and rest conditions.

### **2.2.5. Some examples of yield stress fluids**

Here, we will present several examples of complex fluids, with the objective of establishing the basis to compare their performances vis-à-vis the application considered in this work.

#### **Xanthan gum aqueous solutions**

Xanthan gum is a commonly used viscosifier (Garcia-Ochoa *et al.* 2000; Abidin *et al.* 2012) especially in manufacturing food grade products (Palaniraj and Jayaraman 2011), and is obtained through fermentation of Xanthomonas campestris bacteria (Wadhai and Dixit 2011; Garcia-Ochoa *et al.* 2000; Palaniraj and Jayaraman 2011). The use of xanthan gum solutions is also extended in polymer flooding technics for “Enhanced Oil Recovery”, EOR, (Abidin *et al.* 2012, Jones and Walters 1989) because they increase the “viscosity” of the fluid helping to prevent fingering, which has a negative effect on oil extraction.

Its chemical composition, structure and other physicochemical properties may be found elsewhere (Song *et al.* 2006). Several authors (Rocheford and Middlemann 1987) observed a gel-like behavior of xanthan gum solutions with a polymer concentration of 5 g/L. Iijima *et al.* (2007) proved that xanthan forms hydrogels when aqueous solutions are annealed at 40°C and subsequently cooled, and presented images of the network obtained by atomic force microscopy. The very weak flexibility of xanthan explains the liquid crystalline phase transition at high concentrations (Richardson and Ross-Murphy 1987).

Milas and Rinaudo (1983) studied the transition between isotropic phase and liquid crystal cholesteric phase, showing the sharp viscosity decrease when the cholesteric phase is formed. The values of C\* and C\*\* for xanthan gum solutions have been published by several authors (Southwick *et al.* 1981; Rodd *et al.* 2000, Oliveira *et al.* 2013), with important discrepancies in the reported values, probably dues to the measuring method, the different types of xanthan and the salt concentration. The presence of acetate and pyruvate groups determines that xanthan is a polyelectrolyte, and consequently its chain dimensions would be expected to change in response to changes in ionic strength (Richardson and Ross-Murphy 1987). In particular, the molecule is more rigid on addition of salt. Other features of xanthan’s rheology are its stability in extremes of temperature, pH, and NaCl (Whitcomb and Macosko 1978).

Xanthan gum solutions are one of the main examples of inelastic, shear thinning behavior (Sorbie 1991). Rochefort and Middleman (1987) studied salt, temperature and strain effects in oscillatory and steady shear behavior of xanthan solutions. Temperature, concentration and ionic strength effects were analyzed by Choppe *et al.* (2010). Jones and Walters (1989) compared xanthan gum solutions and polyacrylamide solutions (also used in EOR) in terms of their rheological behavior. In particular, they showed that polyacrylamide solutions and xanthan gum solutions having approximately the same shear-thinning viscosities present however radically different viscoelastic behaviors.

In fact, while polyacrylamide solutions are highly viscoelastic with clear extensional tension-thickening dominance over shear-thinning, xanthan gum solutions are only very weakly elastic and shear-thinning behavior prevails. It comes from the fact that the xanthan gum molecule is rigid and rodlike (Chauveteau 1982; Milas and Rinaudo 1983; Carnali 1991; Lopez *et al.* 2003) whereas polyacrylamide is flexible. Indeed, xanthan is one of the ‘stiffest’ molecules (Richardson and Ross-Murphy 1987). Furthermore, xanthan gum solutions were showed to produce much more stable flows than polyacrylamide solutions when flowing through tortuous geometries and constrictions, as those encountered in porous media. However, viscoelastic behavior is not nonexistent and becomes important at moderate and high concentrations (Song *et al.* 2006; Rochefort and Middleman 1987).

Its semi dilute aqueous solutions are known to develop a high viscosity level at low shear rates before displaying a drastic decrease when the applied shear rate is increased. Therefore, xanthan gum solutions have been reported to present an apparent yield stress (Song *et al.* 2006; Benmouffok-Benbelkacem *et al.* 2010, Khodja 2008; Carnali 1991; Whitcomb and Macosko 1978) even if strictly speaking, they should be referred to as pseudo-yield stress fluids. The Herschel-Bulkley model has been proved to describe the steady state flow of concentrated xanthan gum solutions (Song *et al.* 2006).

In solution state, an isolated xanthan macromolecule is more or less rigid and is of typically 1  $\mu\text{m}$  of contour length and a transverse size of approximately 2 nm (Mongruel and Cloitre 2003; Rodd *et al.* 2000; Iijima *et al.* 2007).

Concerning its flow through porous media, the nature and other aspects of adsorption on pore walls of xanthan gum macromolecules was studied by several authors (Dário *et al.* 2011; Chauveteau 1982; Sorbie 1991). It was found that xanthan adsorption in porous media is rather less important than that of polyacrylamide. This aspect will be further developed in the next section.

Finally, and as will also be explained later, xanthan gum solutions may present a depleted layer close to the pore wall due to a lesser concentration of polymer in that region. It produces an apparent wall slip which leads to a reduced average viscosity in the pores (Chauveteau 1982; Sorbie 1991). The size of that depleted layer has been reported to be of about 300 nm (Chauveteau 1982; Sorbie 1991).

### **Calibrated oil-in-water emulsions**

Emulsions consist of a mix of two immiscible fluids in which one fluid is dispersed in the other in the presence of a surfactant. They are obtained by shearing the two immiscible fluids, which results in the fragmentation of one phase in the other.

One interesting feature of oil-in-water emulsions is that one can control the size of the dispersed fluid droplets. By definition,  $Ca$  is the ratio between the shear stress  $\tau$  and half the Laplace pressure  $P_L$ :  $Ca = 2\tau/P_L$  with  $P_L = 2\sigma/R$ ,  $\sigma$  being the surface tension and  $R$  being the radius of a dispersed phase droplet. A droplet will split if  $Ca$  is greater than a critical value  $Ca_{cr}$  which is a function of the ratio  $p$  between the viscosities of the dispersed and the continuous phases (Leal-Calderón *et al.* 2007). Consequently, it is possible to calculate the minimum droplet size  $R^*$  that one can obtain by shearing at a given shear rate  $\dot{\gamma}$  from condition  $Ca \geq Ca_{cr}$ :  $R^* = (Ca_{cr} \sigma)/(\mu_{emulsion}\dot{\gamma})$  and  $\mu_{emulsion}$  being the apparent viscosity of the emulsion. By shearing with a couette machine, which imposes a constant shear rate in the emulsion, one can obtain quasi-monodisperse droplets size distributions. The size of these droplets may be as small as typically 300 nm (Mabille *et al.* 2000). Smaller droplets may be obtained with inverse emulsions.

Concentrated oil-in-water emulsions present yield stress and their rheological behaviors are well represented by the Herschel-Bulkley model (see Annex C). Their Herschel-Bulkley parameters as well as their viscoelasticity are highly variable depending on the phases and surfactant used. By varying the concentrations of the two phases, the used fluids and the surfactant, the rheological properties of the resulting emulsion can be adapted to our needs. In general, oil-in-water emulsions present viscoelastic behavior due to the elastic deformation of the oil droplets.

Degradation of emulsions over time is the result of two different mechanisms: Ostwald ripening and coalescence. Ostwald ripening is caused by the difference in Laplace pressure between droplets having different sizes: the dispersed phase is transferred from small droplets to large droplets. The rate at which the size of the drops increases is determined by the molecular diffusion of the continuous phase and the penetration ability through the layers of surfactant. Coalescence is caused by the rupture of the thin layers between droplets, which causes them to merge.

Further information on emulsions may be obtained in the book presented by Leal-Calderón *et al.* (2007).

### **Carbopol suspensions**

Carbopol is a polymer provided in a powder form. It is widely used in the development of cosmetics, hair gels, etc. It forms dispersions instead of aqueous solutions. When fairly concentrated suspensions are prepared, it forms highly viscous gels, whose rheology is extensively investigated (Kim *et al.* 2003; Islam *et al.* 2004; Coussot *et al.* 2009) and well

represented by the Herschel-Bulkley model. Solid-fluid transition of Carbopol suspensions was studied by Putz and Burghelea (2009) and Tiu et al. (2006). It has been considered as a model non-thixotropic yield stress fluid by some authors (Cousset *et al.* 2009). However, hysteresis phenomena were observed by Putz and Burghelea (2009) and thixotropy by Miller (2010). On the other hand, Kim *et al.* (2003) presented images of the microstructure of Carbopol suspensions, evidencing that the polymer molecules form highly structured hydrogel networks. The large dimensions of their microstructure may lead to retention in porous media. Also, that microstructure implies that Carbopol suspensions are viscoelastic. Their viscoelastic behavior was studied by Kim *et al.* (2003) and Benmouffok-Benbelkacem *et al.* (2010). Finally, it should be noted that some Carbopols are toxic due to significant amounts of residual benzene from their manufacturing process (Kim *et al.* 2003).

### **Alumina and bentonite suspensions**

Another type of yield stress fluids is made up of suspensions of metallic powders. Bentonite and alumina suspensions are some of the most studied metallic suspensions. Carrier *et al.* (2007) explained that in the case of alumina ( $\text{Al}_2\text{O}_3$ ) aqueous suspension, alumina firstly hydrates superficially and then it forms supersaturated solutions leading to precipitation of large hydroxide particles. Therefore, the composition of the final material is heterogeneous and consequently, the experiments with this fluid are not easily reproducible. Alumina suspensions have been reported to be both thixotropic and viscoelastic (Zhu and Smay 2011; Hirata *et al.* 2010). It has to be noted that elastic deformation is explained by the metallic nature of the suspended particles. Therefore, the more their concentration is elevated, the more the suspension is viscoelastic. That is also applicable to bentonite suspensions, which have also been reported to be thixotropic (Ambrose and Loomis 1933).

As can be concluded from this subsection, concentrated xanthan gum solutions are in principle the “apparent” yield stress fluids that present the simplest behavior in porous media and are therefore the most suitable for the application presented in this work. The reason is that they do not manifest noticeable thixotropy, viscoelasticity or other parasite effects which are reported in the case of the other candidates.

### **2.3. Flow of yield stress fluids through porous media**

This section is devoted to the flow of yield stress fluids through porous media. We will address the flow of a Herschel-Bulkley fluid through a single capillary and a bundle of capillaries, presenting some relationships and concepts that will be used in the following chapters. Then, we will continue with the state of the art for predicting the flow of yield stress fluids through porous media, i.e. macroscopic models and network modelling. At the end of the section, the particular case of the flow of polymer solutions in porous media will be treated.

### 2.3.1. Laminar flow of Herschel-Bulkley fluids through a straight cylindrical capillary and through a bundle of capillaries

The steady, laminar and fully developed simple shear flow of an incompressible fluid through a horizontal straight cylindrical capillary of radius  $r$  will be considered here (Figure 16). The force balance in the axial direction ( $z$  coordinate) on a differential volume element of fluid situated at a distance  $x$  from the axis of the capillary can be written as follows:

$$P(\pi x^2) - (P - \Delta P)(\pi x^2) = \tau(2\pi x L)$$

where  $L$  is the length of the capillary and  $\Delta P$  is the pressure drop. The expression of the shear stress as a function of the pressure drop and the radial coordinate ( $x$  coordinate) can be obtained from the previous equation:

$$\tau = \frac{\Delta P}{L} \frac{x}{2} \quad (2.31)$$

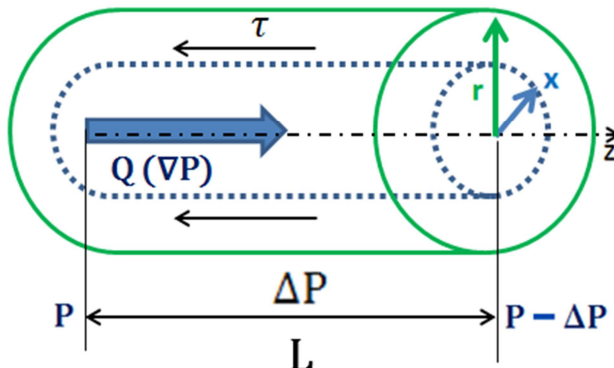


Figure 16: Flow of an incompressible fluid through a straight horizontal capillary.

It has to be noted that no assumption has been made so far concerning the rheology of the fluid. As can be seen in the last equation, there is a linear dependence of the shear stress on the radial coordinate for a given pressure gradient. Indeed, the stress is zero on the axis of the capillary and it attains its maximum value on the wall  $\tau_w$  (Figure 17):

$$\tau_w = \frac{\nabla P r}{2} \quad (2.32)$$

Now focusing on the flow of a yield stress fluid, the critical radius  $r_c$  is defined as the value of the  $x$  coordinate at which the stress equals the yield stress:

$$r_c = \frac{2\tau_0}{\nabla P} \quad (2.33)$$

In the previous expression and henceforth  $\nabla P$  will be taken as the magnitude of the pressure gradient. Consequently, if a yield stress fluid is subjected to a pressure gradient  $\nabla P$ , and no-

slip condition on the wall is assumed, **no flow will occur in the capillaries whose radius is smaller than  $r_c$** . Indeed, if  $r < r_c$ , then  $\tau < \tau_0$  for all values of  $x$ , so  $\dot{\gamma} = 0$  for all values of  $x$  and, given that there is no slip, the axial velocity  $V(x)$  is 0 for all values of  $x$ .

Now, the case of a Herschel-Bulkley fluid (including Bingham for  $n=1$ ) will be considered. It is noted that  $\dot{\gamma} = \frac{dV}{dx} = 0$  for  $x < r_c$ , so  $V(x)$  is constant. On the other hand, for  $r_c < x < r$ , the velocity will progressively decrease from the constant velocity to zero at the wall. From Eq. (2.19) and Eq. (2.31.), we can write:  $\frac{\Delta P}{L} \frac{x}{2} = \tau_0 + k \left( \frac{dV}{dx} \right)^n$ . The integration of that expression with respect to  $x$  provides the velocity profile (Figure 17) and the flow rate through the capillary (Skelland 1967):

$$V(\nabla P, r, x) = \begin{cases} \frac{nr}{(n+1)} \left( \frac{\nabla P r}{2k} \right)^{\frac{1}{n}} \left[ \left( 1 - \frac{2\tau_0}{\nabla P r} \right)^{\frac{(n+1)}{n}} - \left( \frac{x}{r} - \frac{2\tau_0}{\nabla P r} \right)^{\frac{n+1}{n}} \right] & \text{for } x \geq r_c \\ \frac{nr}{(n+1)} \left( \frac{\nabla P r}{2k} \right)^{\frac{1}{n}} \left( 1 - \frac{2\tau_0}{\nabla P r} \right)^{\frac{(n+1)}{n}} & \text{for } x \leq r_c \\ V = 0 & \text{if } r \leq r_c \end{cases} \quad (2.34)$$

$$q(\nabla P, r) = \begin{cases} \left\{ 1 - 2 \left[ \frac{\left( 1 - \frac{2\tau_0}{r\nabla P} \right)^2}{\frac{1}{n} + 3} + \frac{\frac{2\tau_0}{r\nabla P} \left( 1 - \frac{2\tau_0}{r\nabla P} \right)}{\frac{1}{n} + 2} \right] \right\} \left[ \frac{r}{n+1} \left( \frac{r\nabla P}{2k} \right)^{\frac{1}{n}} \left( 1 - \frac{2\tau_0}{r\nabla P} \right)^{\frac{1}{n}+1} \right] \pi r^2 & \text{for } \nabla P \geq \frac{2\tau_0}{r} \\ 0 & \text{for } \nabla P \leq \frac{2\tau_0}{r} \end{cases} \quad (2.35)$$

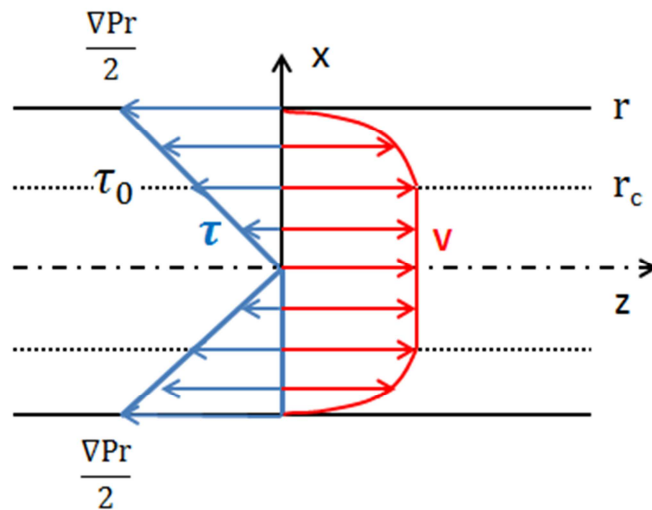


**Figure 17: Shear stress profile and velocity profile corresponding to the flow of a Herschel-Bulkley fluid through a capillary of radius  $r$ .**

Now, if the porous medium is assumed to be well represented by a bundle of parallel capillaries of various radii distributed following a probability density function  $p(r)$  (Figure 18), the average flow rate in a pore for a given pressure gradient  $\nabla P_j$  is given by:

$$\bar{q}(\nabla P_j) = \int_0^\infty q(\nabla P_j, r) p(r) dr \quad (2.36)$$

Therefore, the total flow rate  $Q$  for a given  $\nabla P$  is related to  $q(\nabla P, r)$  through the following relationship:

$$Q(\nabla P_j) = NP \times \int_0^\infty q(\nabla P_j, r) p(r) dr \quad (2.37)$$

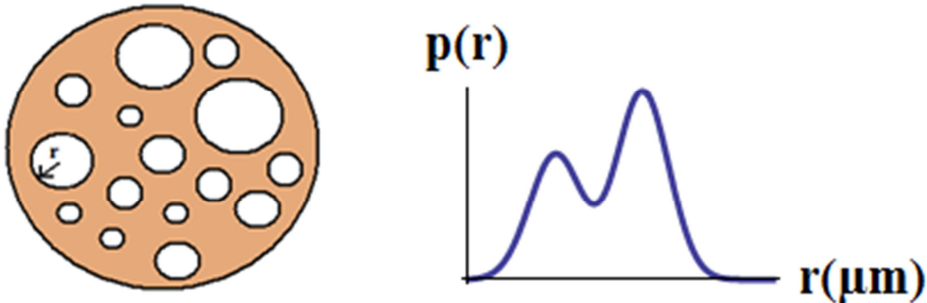


Figure 18: Schematic representation of the bundle-of-capillaries model and its PSD.

$NP$  being the number of pores. In the case of a porous sample composed of a bundle of capillaries, the number of pores  $n_i$  of a given radius  $r_i$  is calculated as follows ( $R$  is the radius of the porous sample and  $L$  its length):

$$\begin{aligned} n_i &= \text{volume probability of } r_i \times \frac{\text{Pore volume of the sample}}{\text{Individual pore volume of } r_i} \\ &= \text{volume probability of } r_i \times \frac{\varepsilon \pi R^2 L}{\pi r_i^2 L} = \frac{p(r_i) \pi r_i^2 L}{\sum_j \pi p(r_j) r_j^2 L} \frac{\varepsilon \pi R^2 L}{\pi r_i^2 L} \\ &= \frac{\varepsilon R^2 p(r_i)}{\sum_j p(r_j) r_j^2} \end{aligned} \quad (2.38)$$

Consequently,  $NP$  is calculated with  $NP = \frac{\varepsilon R^2}{\sum_j p(r_j) r_j^2}$  with  $p(r_i)$  being the frequency of  $r_i$ .

Besides, if  $p(r)$  is a continuous function (probability density function),  $NP$  is given by:

$$NP = \frac{\varepsilon R^2}{\int_0^\infty p(r) r^2 dr} \quad (2.39)$$

In practice, the upper limits of the integrals in (2.36) and (2.37) is finite and is equal to the radius of the largest pores  $r_{\max}$ , and the lower limit corresponds to the smallest pore radius that participates in the flow  $r_{\min}(\nabla P_j) = \frac{2\tau_0}{\nabla P_j}$  at the involved pressure gradient  $\nabla P_j$ . Moreover, from Eq. (2.35) and Eq. (2.37), it can be seen that when all pores are conducting the overall flow rate at high pressure gradients ( $\nabla P \gg \frac{2\tau_0}{\text{radius of the smallest pores in the porous medium}}$ ) is a power law of  $\nabla P_j$  with an exponent of  $1/n$ .

### **2.3.2. Predicting the flow rate as a function of the pressure gradient for the flow of yield stress fluids through porous media**

The main approaches to predict the flow of yield stress fluids through porous media are presented here below.

#### **Macroscopic models**

The objective of macroscopic models is to provide expressions of the flow rate  $Q$  through a porous medium as a function of the pressure gradient  $\nabla P$ . These expressions should include only macroscopic properties of the fluid and the porous medium. Although Darcy's law Eq. (2.1) correctly predicts and represents  $Q(\nabla P)$  for laminar and steady flow of Newtonian fluids, this model does not apply for non-Newtonian fluids. A number of macroscopic models have been proposed for shear-thinning fluids, but only a few are applicable for yield stress fluids.

In the case of Herschel-Bulkley fluids, the most common approach consists in modifying Darcy's law by introducing three parameters associated with the three parameters of Herschel-Bulkley fluid model. Some authors obtained Darcy's modified laws based on the capillaries bundle model or on the flow around isolated particles (e.g. Pascal 1983). Nevertheless, these models lead to different results and are not backed on experimental measures due to scarce experimental work available. In particular, they may not be universal expressions but expressions that have to be adapted case-by-case (Balhoff and Thompson 2004). A first parameter should take into account the threshold pressure below which there is no flow (associated with  $\tau_0$ ). A second parameter should reflect the viscosity reduction with increasing flow rates in the case of a shear-thinning fluid (associated with  $n$ ). Finally, the last parameter is linked to the fluid consistency  $k$ . Recently, Chevalier *et al.* (2013) presented a macroscopic model for the flow of yield stress fluids through porous media, based on the correlation of experimental measures of  $Q(\nabla P)$  through packings of glass beads:

$$d_m \nabla P = 5.5\tau_0 + 85k \left( \frac{V_D}{d_m} \right)^n \quad (2.40)$$

where  $d_m$  is the mean diameter of the beads and  $V_D$  is Darcy's velocity. However, that expression is "*a priori*" only valid for bead packings and the yielding term ( $5.5\tau_0$ ) and the second coefficient ( $85k$ ) may differ for different yield stress fluids. In effect, the yielding

term was only validated for water-in-oil emulsions and proved to be different for Carbopol solutions in water by these authors. Whereas the yielding term was said to be related to the mobilization of the fluid in the widest path, the second coefficient would find its origin in the complex multiscale flow of the porous medium. Balhoff and Thompson (2006) proposed a macroscopic model for shear-thinning flow in packed beds obtained from results of network modelling. Their model works well when its parameters are adjusted, but this implies a non-predictive case-by-case treatment. Furthermore, the model is not valid for more complicated porous media or highly shear-thinning fluids.

In all cases, extended Darcy's laws are unable to correctly describe the transition region in which more and more pores join the flow, because according to these models the network is either fully blocked or fully flowing. However, in reality the pore network progressively yields. For instance, these models predict for Bingham fluids a linear relationship between Darcy velocity and pressure gradient whereas experimental evidence, predict a nonlinear behavior at transition (Sochi *et al.* 2008). Recently, Talon and Bauer (2013) used a Lattice-Boltzmann scheme to predict the flow of Bingham fluids in porous media. They distinguished three scaling regimes. Regime I corresponds to the flow of the first channel (threshold path) which starts to flow at a threshold pressure.  $Q(\nabla P)$  is linear when only one channel is flowing. Regime II corresponds to the incorporation of more and more pores when the pressure is increased. In that regime, the relation between the flow rate of a Bingham fluid and the threshold pressure was found to follow a quadratic law. Finally, when all channels are flowing at sufficiently high pressures  $Q(\nabla P)$  is linear (Regime III). It has to be pointed out that given that yield stress is an idealization, yield stress fluids do actually flow in all pores, though with a very high viscosity, below Regime I.

### **Network modelling**

Another approach to obtain  $Q(\nabla P)$  is the use of physically representative networks to model the flow of non-Newtonian fluids through porous media (Lopez *et al.* 2003; Balhoff and Thompson 2004). Firstly, a network is generated as briefly explained in Section 2.1.3. Then, the mass conservation equation is applied to each node so as to obtain the flow rate and pressure distribution as well as the total flow rate and pressure drop through the network. This process is iterative and time-consuming (non-Newtonian laws are not linear). Another problem is that for non-Newtonian fluids there are no analytical solutions for the flow through irregularly shaped pores, so adapted expressions based on the flow through a cylindrical capillary have to be used. Lopez *et al.* (2003) used model networks based on Berea sandstone and sand-pack to compute apparent viscosity as a function of Darcy's velocity for the flow of shear-thinning fluids without yield stress. It is equivalent to obtaining  $Q(\nabla P)$  because apparent viscosity is linked to  $\nabla P$  through Darcy's law as will be seen later. That approach succeeded in predicting four experiments without any adjustable parameter. However, scaling of the results with respect to the permeability is needed.

More complications arise from the fact that yield stress fluids require a minimum stress to initiate flow. Sochi *et al.* (2008) extended the works of Lopez *et al.* (2003) to the flow of yield

stress fluids through porous media. The predictions of their network modelling were compared to the predictions of the bundle-of-capillaries model, which permitted to draw enlightening conclusions such as lower pressure gradients in the network than in the bundle for shear-thinning flow with yield stress. Also, these predictions were compared to experimental data, finding good agreement only in some cases. Furthermore, these authors represented the average throat radius participating in the flow through the network as a function of the pressure gradient, which is valuable information as it is closely related to the critical throat radius that joins the flow at each pressure gradient Eq. (2.33).

It has to be borne in mind that a detailed description of the pore space is required in order to perform network modelling. Besides, an important flaw of network modelling is that a general analytical expression of  $Q(\nabla P)$ , which is clearly more practical, cannot be obtained.

In conclusion, there is currently no universal approach to predict  $Q(\nabla P)$  in the case of yield stress fluids.

### **The threshold path**

A particularity of the flow of yield stress fluids through porous media is the existence of a threshold pressure below which no flow occurs, which is related to the yield stress of the fluid and the local dimensions of the pore space. Actually, strictly speaking, there is no such pressure threshold for the same reasons that yield stress cannot be proved to exist. It is expected that some flow will occur if enough time is allowed. Anyway, if we accept the existence of a threshold pressure below which there is no flow during the duration of our application, it is clear that its determination involves the determination of the threshold path which first flows. Several authors have developed different algorithms to predict that threshold path, obtaining quite different results (Balhoff *et al.* 2012; Chen *et al.* 2005; Sochi and Blunt 2008). In fact, the determination of this threshold path is currently the subject of debate between authors (Sochi 2013).

#### **2.3.3. Flow of polymer solutions in porous media**

The main concerns related to the flow of yield stress fluids through porous media that have been presented so far can be summarized as follows:

- Most of the present knowledge of flow in porous media concerns only Newtonian fluids.
- There are no macroscopic models nor network simulations able to predict  $Q(\nabla P)$ .
- Prediction of the threshold pressure needed to initiate flow in a porous medium is not well mastered.

- Only a few experimental works have been published, which impede comparison with models. Besides, the experimental protocols used in each case are different, which complicates comparison between results.

Concentrated polymer solutions are often represented as having an apparent yield stress (Song *et al.* 2006; Sochi 2010). For the sake of comprehension, and given their implication in the experimental part of this work that will be presented later, polymeric solutions will be considered in order to emphasize how the behavior of complex fluids in porous media differ from their bulk behavior.

As stated by several authors (Chauveteau 1982; Omari *et al.* 1989; Sorbie 1991) rotation of polymer macromolecules is hindered in the vicinity pore walls. That entails the formation of a depleted layer in which the polymer concentration is lower than in the center of the pores. Consequently, the local polymer concentration increases from zero on the pore wall to its bulk concentration at a distance of typically the macromolecular radius of gyration (in dilute regime) or the mesh size (semi-dilute regime). This effect has a greater impact in small pores whose size is the same order of magnitude as that of the depleted layer. The average apparent viscosity in the porous medium is then lower than bulk viscosity and an apparent slip effect is observed at low shear rates. However, at high flow rates this effect is less important, given that the macromolecules are oriented in the direction of flow.

Another complication occurring when the pore dimensions are the same order of magnitude as macromolecular size is the existence of an inaccessible pore volume. In that case, the macromolecules are too large to enter the parts of the pore space which are connected by the narrowest constrictions. Macromolecules cannot flow through these constrictions unless they are oriented due to strong shear rates or elongation, resulting in a strong decrease in apparent viscosity when a critical shear rate is attained.

In the case of highly flexible polymers and viscoelastic polymers, the converging-diverging nature of the pore space entails additional pressure losses due to stretching at high flow rates (Chauveteau 1982; Sorbie 1991). Besides, shear-thickening behavior brings about an increase in apparent viscosity in the presence of regions where the elongation velocity becomes greater than a critical value. In other words, shear-thickening behavior is observed when the ratio of the relaxation time of a polymer to the duration of a given state of deformation state (Deborah number) exceeds a critical value (Omari 1987). Also, as already explained, pore space is tortuous, which implies that the fluid path is longer than the macroscopic length of the porous medium and the effective pressure gradient is consequently reduced.

Polymer retention is another consequence of the interaction between porous medium and polymer. Three mechanisms can be distinguished: polymer adsorption, mechanical entrapment and hydrodynamic retention (see Figure 19, and Sorbie 1991 for more details concerning these phenomena).

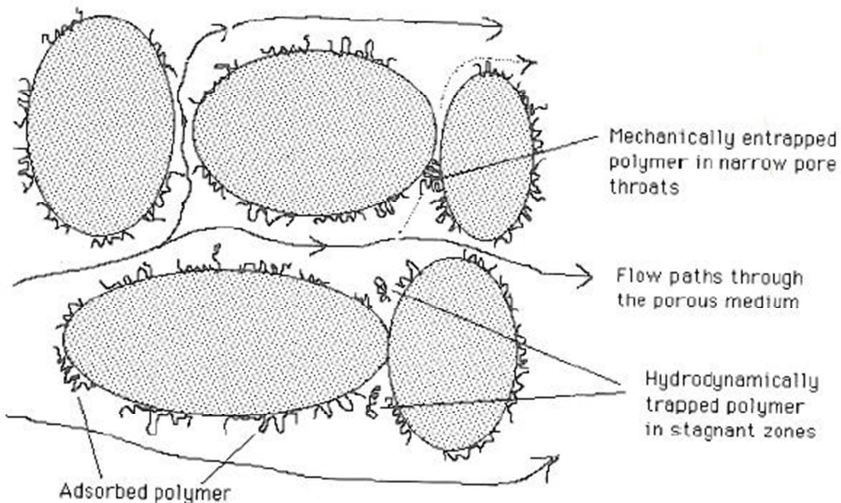


**Figure 19: Schematic diagram of polymer retention mechanisms in porous media (Sorbie 1991).**

The effective rheology of a fluid is characterized by means of a rheometer, outside the porous medium and is expected to reproduce the rheological behavior of the fluid in a given application. However, the apparent rheology of a yield stress fluid injected through a porous medium differs from the effective one due to the mentioned interactions between fluid and porous material. Based on Darcy's law, apparent viscosity  $\mu_{app}$  may be defined as:

$$\mu_{app} = \frac{KA\nabla P}{Q} \quad (2.41)$$

It is noted that in the preceding subsections, "apparent viscosity" referred to the ratio between shear stress and shear rate  $\mu = \frac{\tau}{\dot{\gamma}}$ . However, hereafter "apparent viscosity" will refer to the viscosity defined by Eq. (2.41).

Polymer retention in porous media may lead to a reduced value of permeability K. Therefore, the observed pressure drop may be due not only to viscosity of the fluid but also to retention. This aspect has to be borne in mind when using Eq. (2.41) to represent the apparent viscosity of the fluid. Indeed,  $\mu_{app}$  can be increased in the presence of polymer retention, so Eq. (2.41) does not strictly represent the viscosity of the solution in that case.

Moreover, it is interesting to compare  $\mu_{app}$  to effective viscosity  $\mu$  ( $\mu = \tau/\dot{\gamma}$  measured using a rheometer). That demands definition of an apparent shear rate  $\dot{\gamma}_{app}$  in the porous medium, which is of the form (Lopez *et al.* 2003; Chauveteau 1982; Sorbie 1991):

$$\dot{\gamma}_{app} = \beta \frac{Q/A}{\sqrt{K\varepsilon}} \quad (2.42)$$

where  $\beta$  is an empirical shift parameter which depends on the effective rheology and the pore structure. It has been reported that in spite the diverse nature of the phenomena modifying rheology in porous media, the form of  $\mu(\dot{\gamma})$  is quite similar to that of  $\mu_{app} (\beta \frac{Q/A}{\sqrt{K\varepsilon}})$

apart from the shift parameter  $\beta$  in the case of some polymer solutions as xanthan gum aqueous solutions. Unfortunately, the value of  $\beta$  cannot be reliably predicted so far.

Polymers are usually added to water prior to injection in oil reservoir in order to increase its viscosity and consequently reduce its mobility  $(\frac{K}{\mu})_{\text{water}}$ . This effect is commonly represented in terms of mobility reduction or resistance factor ( $R_M$ ):

$$R_M = \frac{(\frac{K}{\mu})_{\text{water}}}{(\frac{K}{\mu})_{\text{polymer solution}}} \quad (2.43)$$

When inertial effects are negligible,  $R_M$  is calculated by measuring the pressure drop during flow of water (solvent) through a native porous medium  $\Delta P_w$  and subsequently measuring the pressure drop during flow of polymer  $\Delta P_p$  at the same flow rate, so that  $R_M = \Delta P_w / \Delta P_p$  (Omari 1982).

Also, the porous medium is commonly flushed with water after injection of the polymer solution so as to evaluate the permeability reduction  $R_k$  caused by the adsorbed layer. To do so, the permeability to water is measured once the solution has been removed from the pores and only the adsorbed polymer layer remains.  $R_k$  is defined as the ratio between this reduced value of  $K$  and the original  $K$  before injection of polymer solution. However, it should be noted that measurement of  $R_k$  is not easy in the case of highly concentrated polymer solutions because water forms viscous fingers when performing the postflush (Sorbie 1991, Seright 2010).

Moreover, in a homogeneous porous medium with high permeability, the equivalent hydrodynamic thickness of the adsorbed polymer layer  $e$  can be estimated as (Chauveteau 1982; Omari 1982):

$$e = \bar{r} - \bar{r}_a = \sqrt{\frac{8K}{\varepsilon}} - \sqrt{\frac{8R_k K}{\varepsilon}} \quad (2.44)$$

where  $\bar{r}$  is the original average pore radius and  $\bar{r}_a$  is the average pore radius after polymer adsorption. Both radii are calculated with Eq. (2.2). The thickness of the adsorbed layer of flexible polymers such as HPAM is much larger than that of rigid polymers such as xanthan gum. In fact, xanthan gum macromolecules are flattened onto the surface so that the hydrodynamic thickness of the adsorbed layer is entirely negligible in numerous cases (Chauveteau 1982). This is schematically shown in Figure 20. Therefore, permeability reduction is usually negligible ( $R_k \sim 1$ ) for xanthan gum solutions and the permeability to water previous to polymer injection is used in Eq. (2.41). Also,  $R_k$  and  $R_M$  have been shown to decrease with flow rate and pore size (Kohler and Chauveteau 1978; Chauveteau and Kohler 1980).

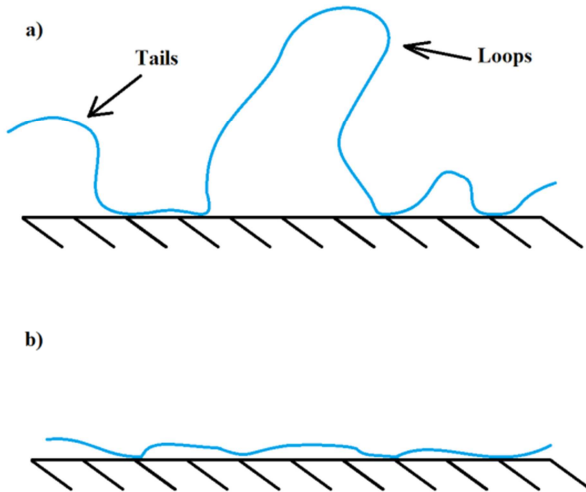


**Figure 20: Schematic representation of adsorbed layers. a) Flexible polymer (e.g. HPAM). b) Rigid polymer (e.g. xanthan gum).**

## **2.4. Obtaining the PSD of a porous medium from the injection of a yield stress fluid**

Now, we will present the theoretical basis and the currently available methods to obtain the PSD of a porous medium from the injection of a yield stress fluid.

### **2.4.1. Theoretical principles**

Let us recall the expression for the average flow rate of a yield stress fluid through a bundle of capillaries (Eq. 2.36):

$$\bar{q}(\nabla P_j) = \int_0^\infty q(\nabla P_j, r) p(r) dr$$

That expression is a Volterra equation of the first kind. In effect, as  $q(\nabla P_j, r)$  encompasses the rheological characteristics of the fluid, an inversion procedure of the integral equation above leads to the determination of the pore size distribution  $p(r)$ .

In their original work, Ambari *et al.* (1990) studied the simple case of a Bingham fluid ( $n = 1$ ). Chaplain *et al.* (1992) extended the previous work to a bundle of randomly oriented capillaries and more recently, Oukhlef *et al.* (2011) considered the case of Herschel–Bulkley fluids. They showed that the analytical inversion of Eq. (2.36) leads to the following expression of  $p(r)$ :

$$p(r) = \frac{2^{(w+3)} k^w (\nabla P)^2}{16(w!) \pi \tau_0 r^{(w+3)}} \left[ (w+4) \frac{\partial^{(w+1)}}{\partial \nabla P^{(w+1)}} + \nabla P \frac{\partial^{(w+2)}}{\partial \nabla P^{(w+2)}} \right] \bar{q}(\nabla P) \quad \text{with } \nabla P = \frac{2\tau_0}{r} \quad (2.45)$$

with  $w = 1/n$  being a real number. If  $1/n$  is not an integer, the last equation involves the calculation of fractional derivatives, which may be complex in some cases (Weilbeer 2005).

It has to be noticed that in a real experiment, it is  $Q(\nabla P)$  which is calculated instead of  $\bar{q}(\nabla P_j)$ . Nevertheless, given that they are proportional,  $p(r)$  can be obtained by using  $Q(\nabla P)$  in Eq. (2.45) instead of  $\bar{q}(\nabla P_j)$  with a subsequent normalization of the obtained PSD.

### **2.4.2. Available methods**

In order to test this method, Oukhlef (2011) performed “*in silico*” experiments of a Herschel–Bulkley fluid flowing through a bundle of capillaries with a pre-defined PSD. A polynomial function was then used to fit at best the raw numerical data ( $Q$ ,  $\nabla P$ ) and  $p(r)$  was calculated using Eq. (2.45). The obtained results were then compared to the original pore size distribution. He showed the method to work very well in the case of Bingham fluids ( $n = 1$ ). However when  $n \neq 1$  the procedure is less convincing since high fluctuations are noticed at low pore radii and the quality of the obtained results is reported to depend on the degree of the polynomial function chosen for the fitting step in the procedure (see Oukhlef *et al.* 2011 for details). Indeed, the choice of this degree is not clear and the assessment of its effect on the results implies comparison with the real distribution in each case, which is unknown in a practical situation. Besides, due to the calculation of higher order derivatives and fractional derivatives, numerous ( $Q$ ,  $\nabla P$ ) data are required and numerical noise is observed. Furthermore, the inversion of the experimental function should be only done in the range of pressure gradients corresponding to the particular PSD which is unknown “*a priori*”.

In parallel to our method, Malvaut (2013) studied the experimental feasibility of the method presented by Oukhlef *et al.* (2011, 2014). He characterized model porous media: bundles of glass capillaries (diameter greater than 1 mm) and bundles of capillaries drilled in short plastic cylinders of PVC and PMMA (diameters ranging from 400 to 1600  $\mu\text{m}$ ). He also characterized a sintered polyethylene (mean pore diameter of 200  $\mu\text{m}$  approximately). The experimental procedure consisted in injecting a commercial mayonnaise (yield stress fluid) through the porous medium with a pressure-controlled system. The pressure was imposed by a gas reservoir pushing a piston which in turn pushed the yield stress fluid through the porous medium. The resulting flow rate was measured by means of a precision balance and the pressure drop was obtained from a pressure sensor connected to the ends of the porous medium. In his work, Malvaut used the analytical inversion (Eq. 2.45) as well as a numerical inversion of Eq. (2.37) to characterize model porous media. Unfortunately, the procedure is not sufficiently detailed to be reproduced here for comparison with our results. Malvaut’s results confirmed that the analytical inversion led to PSDs strongly dependent on the degree of the fitting polynomial. Nevertheless, he established an objective criterion for the choice of that degree, even if it does not lead to satisfactory PSDs in all cases. On the other hand, the PSD obtained through numerical inversion agreed in some cases with optical measures and mercury porosimetry. Similar procedures performed by the author of the present work suggest that such numerical inversion may lead to negative probabilities for some pore size classes

when applied to laboratory experimental measures, which is not physically possible. A better understanding of the inversion procedures of Malvaut (2013) would be required in order to draw unequivocal conclusions.

In conclusion, even there has recently been a significant progress concerning the numerical and experimental implementation of yield-stress-based porosimetry, no available method has been proved to be applicable to characterize PSDs of natural porous media.

### 3. The Yield Stress fluids Method (YSM)

The development of a new and intuitive method to obtain the PSD of a porous medium from raw data obtained from laboratory measurements will be presented in this chapter. First of all, the basis of the method will be presented together with the procedure to obtain the PSD. Then, the method will be numerically validated through “*in silico*” experiments. At the end of the chapter, the design of experiments will be presented with the purpose of determine the properties of the fluid and the equipment (pump, pressure sensor) needed to characterize porous media within a given range of PSD.

#### 3.1. The basis of the YSM: Physical principle

Like in standard mercury porosimetry, and as in the analytical method presented in the previous section, the porous medium is modeled as a bundle of capillaries whose radii are distributed according to a probability density function  $p(r)$  and hence, the flow rate through a class of pores of representative radius  $r_i$  under a pressure gradient  $\nabla P$ ,  $q(\nabla P, r_i)$ , is given by Eq. (2.35) for  $r = r_i$ . During a typical experiment, a yield stress fluid whose rheology is described by the Herschel–Bulkley model (Eq. 2.19) is injected through the porous medium to be investigated and a set of  $N + 1$  raw data  $(Q_i, \nabla P_i)$  with  $i = (1, \dots, N + 1)$  are collected and then arranged in an ascending manner. The range of the data should be so that the lowest flow rate is as close to zero as possible and the upper flow rate lies in the interval where  $Q(\nabla P)$  scales as  $\nabla P^y$  with  $y$  close to  $1/n$  (see subsection 2.3.1). Therefore, it is assumed that  $Q_1$  is sufficiently low so that no pore class contributes significantly to flow below  $\nabla P_1$ . On the other hand, each  $\nabla P_i$  defines a class of pores of representative radius  $r_i$  taken here as being  $r_i = \alpha \frac{2\tau_0}{\nabla P_i}$  ( $r_1 > r_2 > \dots > r_N$ ) where  $\alpha$  is a factor greater than unity whose precise value will be discussed later. Besides, rather than using Eq. (2.45) to determine the PSD, we simply express that the measured flow rate at a given  $\nabla P_j$  is greater than or equal to the sum of the contributions of all the pores whose radii are larger than  $r_j$ . So we write  $Q_j \geq \sum_{i=1}^{j-1} n_i q(\nabla P_j, r_i)$  where  $n_i$  represents the number of pores of each  $i$ -th class. In order to obtain the PSD, the  $N$  unknowns  $n_i$  must be determined by solving the following system of inequalities:

$$\left\{ \begin{array}{l} Q_2 \geq n_1 q(\nabla P_2, r_1) \\ Q_3 \geq n_1 q(\nabla P_3, r_1) + n_2 q(\nabla P_3, r_2) \\ \vdots \\ Q_j \geq n_1 q(\nabla P_j, r_1) + n_2 q(\nabla P_j, r_2) + \dots + n_{j-1} q(\nabla P_j, r_{j-1}) \\ \vdots \\ Q_{N+1} \geq n_1 q(\nabla P_{N+1}, r_1) + n_2 q(\nabla P_{N+1}, r_2) + \dots + n_N q(\nabla P_{N+1}, r_N) \end{array} \right. \quad (3.1)$$

The previous inequalities express the fact that the measured flow rate at a given  $\nabla P_j$  should be greater than or equal to the one calculated if only pores of radii larger than  $r_j$  are involved (Figure 21).

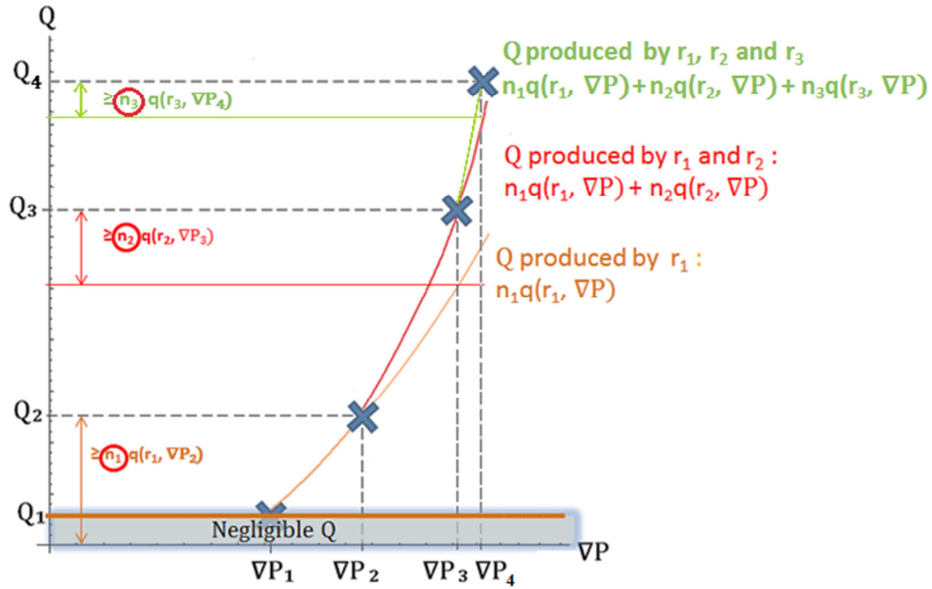


Figure 21: Scheme of the principle of the method.

### 3.2. PSD determination

One may consider solving the previous system of inequalities using a standard optimization method. In each iteration, a set of  $n_i$  with  $i = (1, \dots, N + 1)$  would be tested and the respect of the  $N$  constraints would be evaluated. Then another set would be tested and so on until a set corresponding to an optimal fit to the measures is found. Nevertheless, this approach does not take into account the fact that when adjusting a set of  $(Q_i, \nabla P_i)$  data, the value of  $n_j$  has an influence on the value of  $n_k$  with  $k > j$ . Indeed, generating combinations of  $n_i$  that do not consider such an aspect would lead to PSDs with a highly overestimated number of small pores, because they would not be restricted by the number of larger pores.

In the routine used to calculate a targeted  $n_i$ , and starting with  $n_1$ , successive and increasing positive values are scanned until one of the inequalities is violated and the maximum value is assigned to  $n_i$ . In this procedure, and as large pores contribute significantly to the total flow rate, the scanning should be more refined when the considered pore radius is large. The step with which the scanning of  $n_i$  is carried out is defined by the next formula:

$$\text{Step}_i = \frac{\zeta q(\nabla P_{N+1}, r_N)}{q(\nabla P_{N+1}, r_i)} \quad (3.2)$$

where  $\zeta$  is an index that determines the refinement of the scanning and whose value is not important provided that it is low enough ( $\zeta \leq 0.05 \frac{\varepsilon^2 R^2}{8K}$ ). Eq. (3.2) expresses that the minimum contribution to flow that will be considered for a given pore size  $r_i$  at the highest pressure gradient  $\nabla P_{N+1}$  is the same for all  $r_i$ .

Once  $n_i$  ( $i = 1, \dots, N$ ) have been calculated, the probability in terms of relative frequency  $p(r_i)$  is obtained through:

$$p(r_i) = \frac{n_i}{\sum_{j=1}^N n_j} \quad \text{for } i = 1 \dots N \quad (3.3)$$

Besides, the probability in terms of relative volume  $p_v(r_i)$  is determined with:

$$p_v(r_i) = \frac{n_i \pi r_i^2}{\sum_{j=1}^N n_j \pi r_j^2} \quad \text{for } i = 1 \dots N \quad (3.4)$$

The total flow rate  $Q$  as a function of the pressure gradient  $\nabla P$  corresponding to the obtained PSD may be then calculated as follows:

$$Q(\nabla P) = \sum_{i=1}^N n_i q(\nabla P, r_i) \quad (3.5)$$

However, a filtering step is necessary. Indeed, all the pore classes  $r_j$  for which the number of pores  $n_j$  is only bounded by the highest couple of experimental data  $(Q_{N+1}, \nabla P_{N+1})$  are excluded. The reason is that these pore classes are bounded by  $(Q_{N+1}, \nabla P_{N+1})$  just because no further flow rates or pressure gradients have been imposed during the experiments, so no meaningful information on the number of these pores can be obtained. Consequently:

$$\begin{aligned} \text{If } Q_{N+1} &> \sum_{g=1}^{s-1} n_g q(\nabla P_{N+1}, r_g) \\ \text{and } Q_{N+1} &= \sum_{g=1}^s n_g q(\nabla P_{N+1}, r_g) \end{aligned} \quad (3.6)$$

then  $n_s$  is unknown

Here, it has been set that the representative radius  $r_i$  of a class of pores is linked to  $\nabla P_i$  through  $r_i = \alpha \frac{2\tau_0}{\nabla P_i}$  where  $\alpha$  is a factor greater or equal to unity. The fundamental reason of this is that for a given  $\nabla P_i$  the resulting  $Q_i$  is due to the pores whose radii are strictly larger than  $\frac{2\tau_0}{\nabla P_i}$ . In other words,  $\nabla P_i$  represents only the onset of contribution to the flow of pores of radius  $\frac{2\tau_0}{\nabla P_i}$ . To determine the suitable value of  $\alpha$ , which will be named  $\alpha^*$ , successive increasing values will be used to solve the system (3.1), starting with  $\alpha = 1$ . For each value of  $\alpha$ , the quality of the fit of the resulting PSD to the experimental data is assessed through:

$$E = \sum_{i=1}^{N+1} \left[ \frac{(Q(\nabla P_i) - Q_i)}{Q_i} \right]^2 \quad (3.7)$$

where  $Q_i$  and  $\nabla P_i$  with  $i = (1, \dots, N + 1)$  are the experimental data of pressure gradient and flow rate, and  $Q(\nabla P_i)$  is calculated with Eq. (3.5).  $\alpha^*$  is then **the value of  $\alpha$  that minimizes E**. This criterion for the selection of  $\alpha^*$  will be called **E-criterion** from now on. In the next section, the influence of the value of  $\alpha$  on the representativeness of the obtained PSD will be studied.

### **3.3. Numerical validation of YSM**

We will begin by validating YSM in the case of numerically generated experiments. An ideal Herschel-Bulkley fluid with known properties will be numerically injected through a set of different PSDs so as to generate  $(Q, \nabla P)$  data. Then, the YSM will be used to exploit these  $(Q, \nabla P)$  data in order to verify whether the original PSD is recovered in each case. Also, a sensitivity analysis of the obtained PSD to errors in the rheological parameters and to noise and spacing of the  $(Q, \nabla P)$  data will be presented.

#### **3.3.1. Numerical experiments**

A yield stress fluid, whose yield stress, consistency and flow index are respectively  $\tau_0 = 10$  Pa,  $k = 1$  Pa s<sup>n</sup> and  $n = 0.60$  was injected numerically through a bundle of 1,000,000 capillaries whose radii are distributed according to the following bimodal probability density function:

$$p(r) = \frac{\omega_1}{\sqrt{2\pi\sigma_1^2}} e^{-\frac{(r-m_1)^2}{2\sigma_1^2}} + \frac{\omega_2}{\sqrt{2\pi\sigma_2^2}} e^{-\frac{(r-m_2)^2}{2\sigma_2^2}} \quad (3.8)$$

which is a weighted sum of two normal laws with means  $m_1 = 12$   $\mu\text{m}$  and  $m_2 = 24$   $\mu\text{m}$ , standard deviations,  $\sigma_1 = 3$   $\mu\text{m}$  and  $\sigma_2 = 6$   $\mu\text{m}$ , and weights  $\omega_1 = 2/3$  and  $\omega_2 = 1/3$ . The preceding PSD will be named “original PSD” from now on. 50 different pressure gradients ( $N + 1 = 50$ ) given by  $\nabla P_i = \frac{2\tau_0}{z_i}$  with  $i = (0, \dots, N)$ ,  $z_i = z_{\max} - \frac{(z_{\max} - z_{\min})}{N} i$ ,  $z_{\min} = m_1 - 3\sigma_1$ ,  $z_{\max} = m_2 + 3\sigma_2$  were considered and the resulting flow rates were calculated using Eq. (2.37). The obtained data are displayed in Figure 22.

#### **3.3.2. PSD determination**

YSM was applied to the  $(Q_i, \nabla P_i)$  data and the  $\alpha^*$  satisfying E-criterion was found to be 1.07. The calculated PSD in terms of  $n_i$  (number of pores of radius  $r_i$ ) is in very good agreement with the original PSD (Figure 23). Furthermore, in order to study the influence of  $\alpha$ , the PSDs corresponding to several values of  $\alpha$  were calculated and compared to the original PSD (see Figure 24 for some  $\alpha$  values). From this figure it can be observed that the obtained PSDs globally capture the right form of the original PSD. Within the values of  $\alpha$  considered here, the agreement is qualitatively worse with  $\alpha = 1$ . Moreover, when  $\alpha > 1.07$  the calculated PSDs deviate more or less from the original PSD and  $\alpha = \alpha^* = 1.07$  is shown to be the best value in the present case.

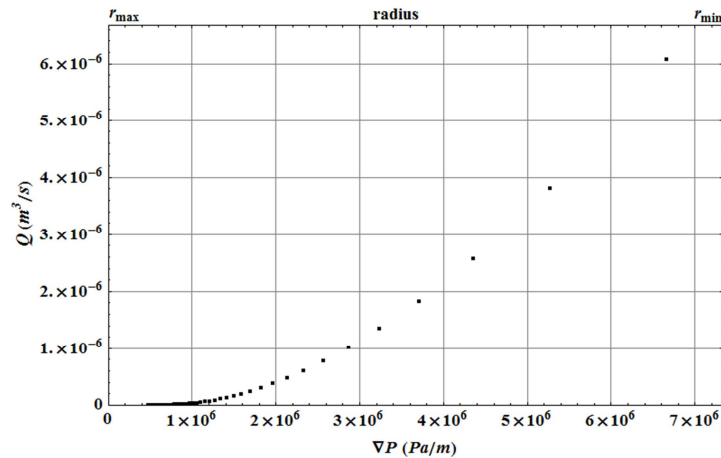


Figure 22: ( $Q_i$ ,  $\nabla P_i$ ) data corresponding to the numerical injection of a yield stress fluid with  $\tau_0 = 10$  Pa,  $k = 1$  Pa s<sup>n</sup> and  $n = 0.60$  through a bundle of 1,000,000 capillaries whose radii are distributed according to the original  $p(r)$ . The upper axis represents the radii of the pores joining the flow at each  $\nabla P$  (smaller pores at high  $\nabla P$ ).

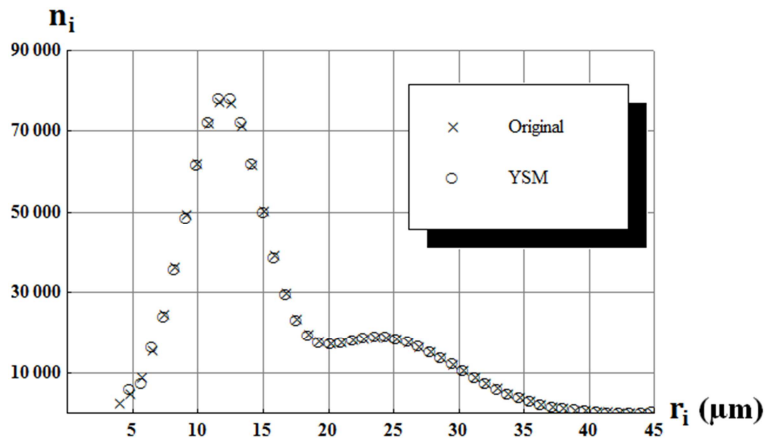


Figure 23: Calculated PSD (circles) versus original PSD (crosses) corresponding to the numerical experiment.  $\alpha^* = 1.07$ .

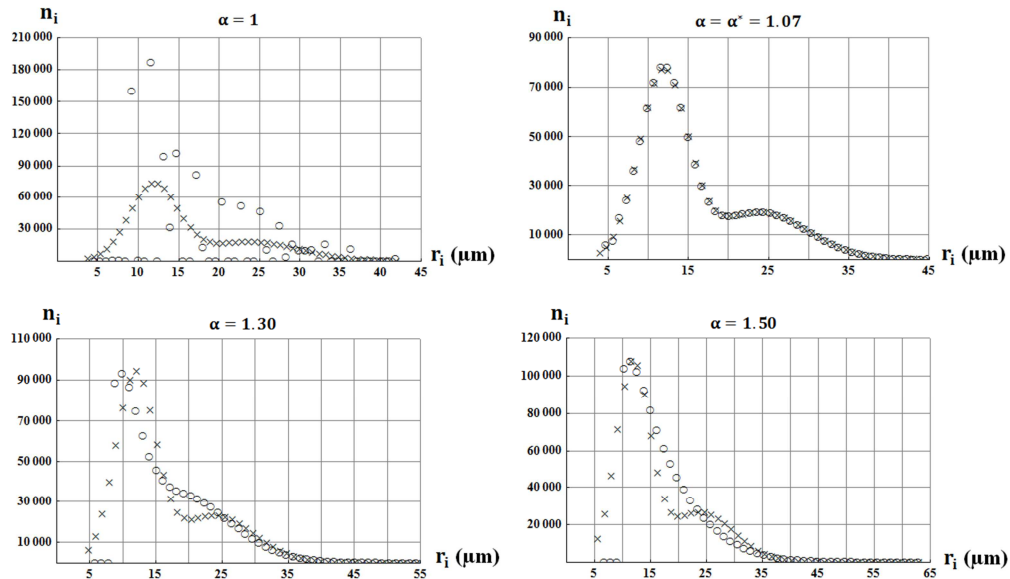


Figure 24: Calculated PSD (circles) versus original PSD (crosses) corresponding to the numerical experiment for different values of  $\alpha$ .

To go further, these values of  $\alpha$  were tested in the case of different sets of distribution parameters  $m_1$ ,  $m_2$ ,  $\sigma_1$ ,  $\sigma_2$ ,  $\omega_1$  and  $\omega_2$ , and the deviation from the original PSD was evaluated by calculating the quantity  $d(\alpha)$ :

$$d(\alpha) = \sum_{i=1}^N \left| \frac{n_{i0}}{\sum_{i=1}^N n_{i0}} - \frac{n_i(\alpha)}{\sum_{i=1}^N n_i(\alpha)} \right| \quad (3.9)$$

where  $N + 1$  is the number of data ( $N = 49$ ),  $n_{i0}$  is the number of pores of radius  $r_i$  corresponding to the original PSD (after discretization),  $n_i(\alpha)$  is the number of pores of radius  $r_i$  for the considered  $\alpha$ , and  $\sum_{i=1}^N n_{i0}$  is the total number of pores (1,000,000 in this case). The value of  $d(\alpha)$  is bounded below by zero (no difference) and above by two. The obtained deviations as a function of  $\alpha$  are presented in Table 1, where it is observed that whatever the considered distribution, the value of  $\alpha^*$  obtained by applying the method is approximately the same (1.01-1.08). Moreover, better PSDs are obtained for  $\alpha > 1$  and they are less satisfactory as  $\alpha$  diverges from the  $\alpha^*$  given by the method (1.01-1.08).

<b><math>m_1</math> (μm)</b>	12	12	6	18	12	12	12
<b><math>m_2</math> (μm)</b>	24	24	48	21	24	24	24
<b><math>\sigma_1</math> (μm)</b>	3	3	3	3	1.5	3.5	3
<b><math>\sigma_2</math> (μm)</b>	6	6	6	6	3	8	6
<b><math>\omega_1</math></b>	2/3	1/3	2/3	2/3	2/3	2/3	1
<b><math>\omega_2</math></b>	1/3	2/3	1/3	1/3	1/3	1/3	0
<b><math>d(\alpha = 1)</math></b>	1.11	0.98	1.35	1.29	1.23	1.49	1.13
<b><math>d(\alpha = 1.05)</math></b>	0.01	0.01	0.07	0.02	0.03	0.09	0.01
<b><math>d(\alpha = 1.10)</math></b>	0.03	0.03	0.16	0.06	0.12	0.03	0.04
<b><math>d(\alpha = 1.30)</math></b>	0.29	0.51	1.33	0.27	0.49	0.26	0.30
<b><math>d(\alpha = 1.50)</math></b>	0.27	0.60	1.33	0.30	0.60	0.30	0.61
<b><math>\alpha^*</math> from E-criterion</b>	1.07	1.07	1.04	1.07	1.04	1.08	1.01
<b><math>d(\alpha = \alpha^*)</math></b>	0.02	0.01	0.04	0.03	0.02	0.02	0.02

**Table 1:** Deviation from the original PSD obtained for a set of numerical experiments for different values of  $\alpha$  and given fluid properties ( $\tau_0 = 10$  Pa,  $k = 1$  Pasn, and  $n = 0.60$ ). The original PSDs are defined using Eq. (3.8).

### **3.3.3. Sensitivity analysis: fluid properties, measurement parameters and errors**

#### **a) Fluid parameters**

The  $(Q_i, \nabla P_i)$  data presented in Figure 22 have been exploited with YSM introducing erroneous values of  $\tau_0$ ,  $k$  and  $n$  in order to assess the effect their overestimation and underestimation on the obtained PSD.

### 1) $\tau_0$ value

Erroneous yield stresses  $\tilde{\tau}_0$  with values  $0.7\tau_0$ ,  $0.9\tau_0$ ,  $1.1\tau_0$  and  $1.3\tau_0$  have been used ( $\tau_0 = 10$  Pa) to exploit the  $(Q_i, \nabla P_i)$  data presented in Figure 22, and the resulting PSDs are presented in Figure 25. As can be seen in that figure, the errors in yield stress value entail horizontal shifting of the obtained PSDs with respect to the original one. That shift is directed toward large pores in the case of overestimated  $\tau_0$  and toward small pores in the case of underestimated  $\tau_0$ . However, the form of the PSD is conserved in all cases. An error in the value of  $\tau_0$  introduced in the direct simulation of the flow in the bundle of capillaries will lead to the  $Q(\nabla P)$  curves presented in Figure 26. As for the PSDs mentioned above, a modification in  $\tau_0$  will lead to a shift in the  $Q(\nabla P)$  curves.

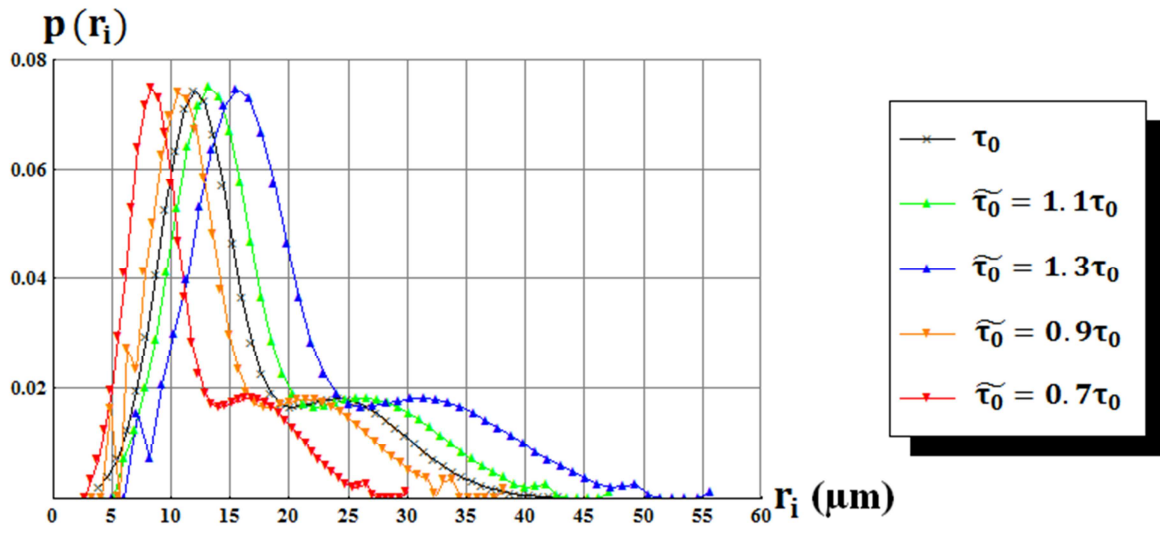


Figure 25: Effect of the error in the value of  $\tau_0$  on the obtained PSDs.

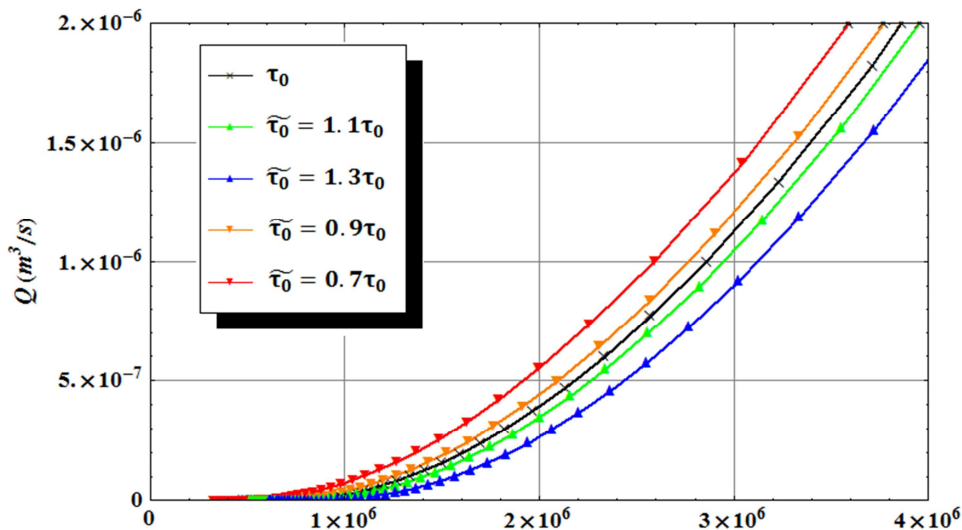


Figure 26:  $Q(\nabla P)$  data obtained for the same PSD presented in Figure 22 with the different values of  $\tilde{\tau}_0$ .

## 2) k value

Likewise, erroneous consistencies  $\tilde{k}$  with values 1.1k, 0.9k, 1.3k and 0.7k have been used ( $k = 1\text{Pas}^n$  is the correct value) to exploit the  $(Q_i, \nabla P_i)$  data presented in Figure 22, and the resulting PSDs are presented in Figure 27. From this figure, it is remarked that errors in the consistency value do not entail significant changes in the obtained PSDs. Nonetheless, it should be noted that even if no significant change in the probabilities of each pore size class is observed, the calculated number of pores  $n_i$  with each radius does change. It is because the probabilities are normalized with the total number of pores ( $p(r_i) = n_i / \sum_j n_j$ ) that no change is detected.

Figure 28 shows the  $Q(\nabla P)$  curves that would be obtained for the same PSD with the different values of  $k$ . It can be seen that differences in  $k$  produce deviations of the  $Q(\nabla P)$  curves that are proportional to flow rate. That means that a greater number of pores compensates an underestimation of  $k$  and a lesser number of pores compensates an overestimation of  $k$ .

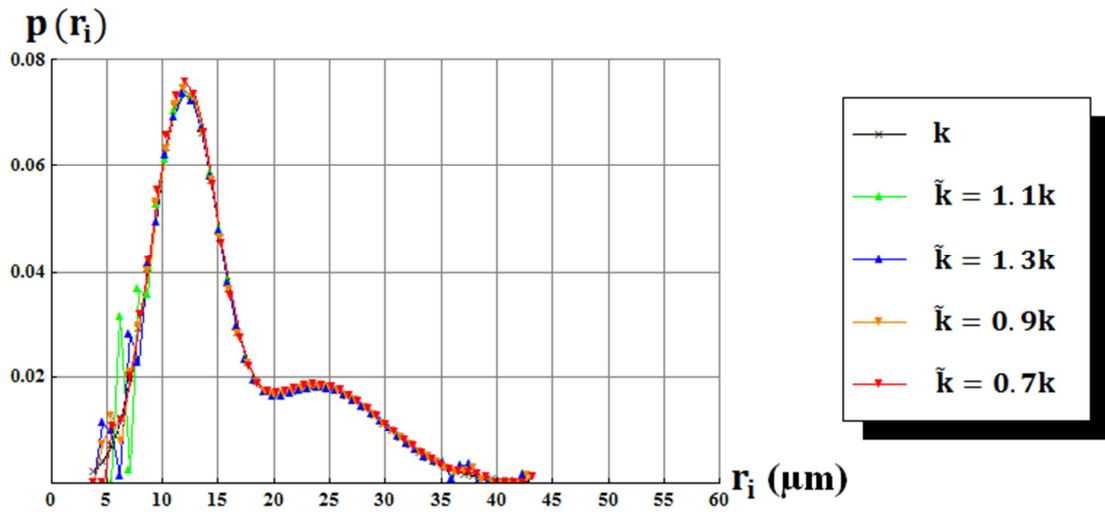


Figure 27: Effect of the error in the value of  $k$  on the obtained PSDs.

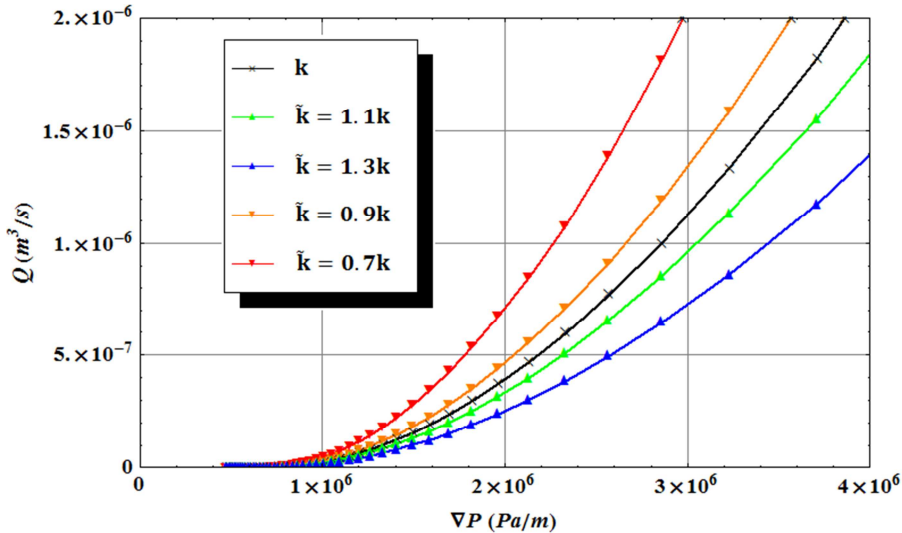


Figure 28:  $Q(\nabla P)$  data obtained for the same PSD presented in Figure 22 with the different values of  $\tilde{k}$ .

### 3) $n$ value

Similarly to the preceding cases, erroneous flow indexes  $\tilde{n}$  with values  $0.95n$ ,  $0.983n$ ,  $1.017n$  and  $1.05n$  have been used ( $n = 0.60 \text{ Pa s}^n$ ) to exploit the  $(Q_i, \nabla P_i)$  data presented in Figure 22, and the obtained PSDs (in terms of number of pores of each pore radius class) are displayed in Figure 29. Unlike the previous cases, it is observed that errors in  $n$  have a strong effect on the obtained PSDs, deforming it especially in the small pores region. In Figure 30, it can be noted that different  $n$  produce deviations of the  $Q(\nabla P)$  curves which increase with pressure gradient. Nonetheless, now these deviations are not proportional to  $Q$  but they follow a power-law.

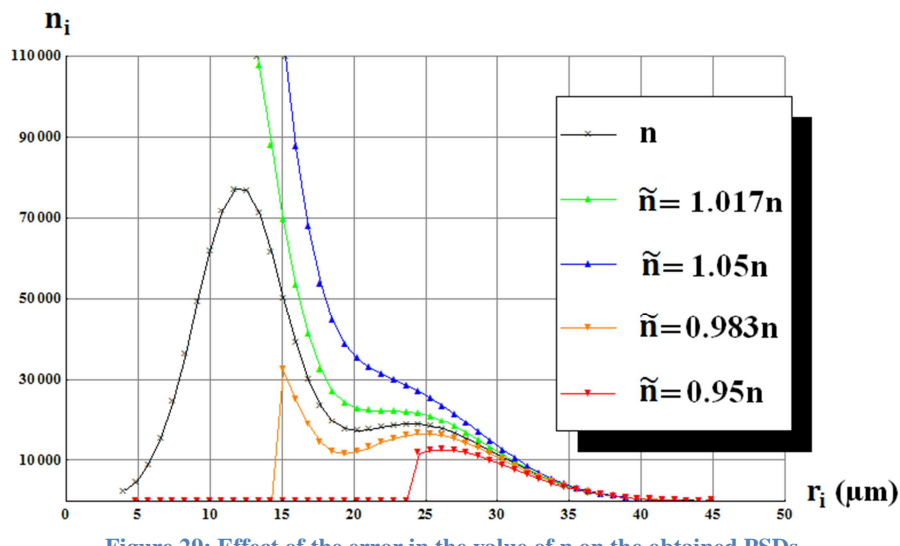


Figure 29: Effect of the error in the value of  $n$  on the obtained PSDs.

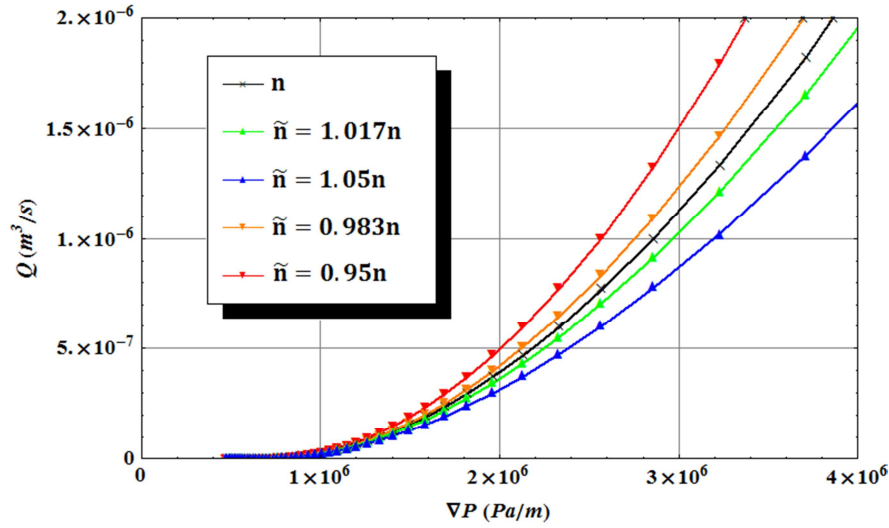


Figure 30:  $Q(\nabla P)$  data obtained for the same PSD presented in Figure 23 with the different values of  $\tilde{n}$ .

It is emphasized that even if the errors in the rheological parameters  $\tau_0$ ,  $k$  and  $n$  may shift or deform the PSD, that does not generate significant deviations of  $\alpha^*$  with respect to the case in which there is no error ( $\alpha^*$  very close to 1.07 in all cases).

### b) Pressure gradient sampling

Our objective now is to study the influence of the sampling of pressure gradients on the quality of the obtained PSD. Four runs of a Herschel-Bulkley fluid with  $\tau_0 = 10 \text{ Pa}$ ,  $k = 1 \text{ Pa s}^n$  and  $n = 0.6$  were performed through a porous medium whose PSD is the one presented in Figure 23. In each experiment, the imposed pressure gradients  $\nabla P_i$  were selected as presented in Table 2, with  $i = (0, \dots, 49)$ . The PSDs obtained in the four experiments are represented together in Figure 31.

Sampling method	$z_i$	$\nabla P_i$
1	$z_{\max} - \frac{(z_{\max} - z_{\min})}{N} i$	$\frac{2\tau_0}{z_i}$
2		$\frac{2\tau_0}{z_{\max}} + \frac{i}{N} \left( \frac{2\tau_0}{z_{\min}} - \frac{2\tau_0}{z_{\max}} \right)$
3		$\nabla P_i$ such that $Q_i$ are equidistant
4	$z_{\max} - \frac{(z_{\max} - z_{\min})}{N} (i \pm \text{random}_i)$	$\frac{2\tau_0}{z_i}$

Table 2: Sampling methods used in the experiments.  $z_{\max} = m_2 + 3\sigma_2$ ;  $z_{\min} = m_1 - 3\sigma_1$ ;  $\text{random}_i$  was a random real number between -0.5 and 0.5

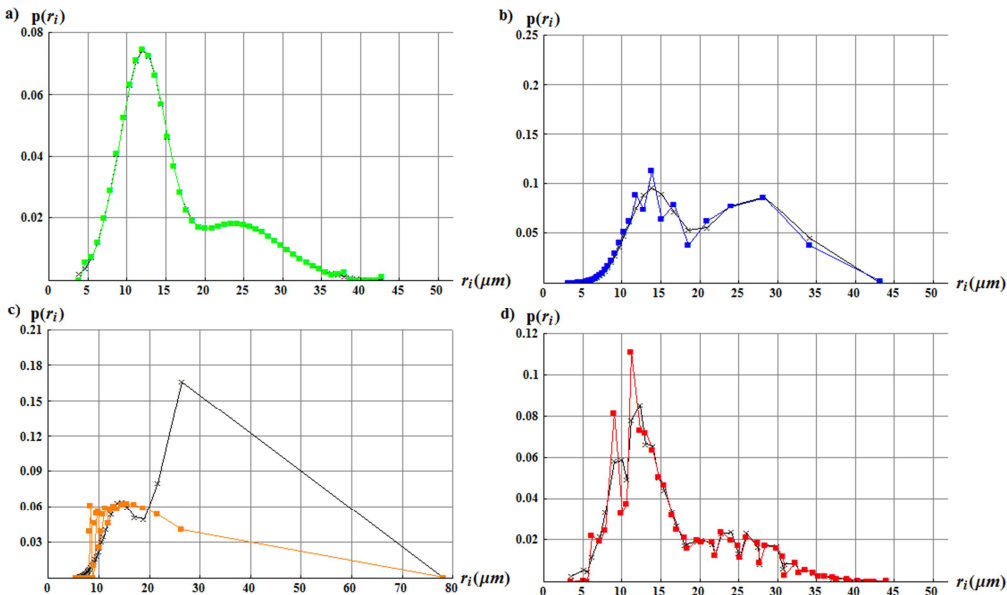


Figure 31: Original PSD (black) compared with the obtained PSDs as a function of  $\nabla P_i$  sampling. a) Sampling method 1. b) Sampling method 2. c) Sampling method 3. d) Sampling method 4.

We can see that the best results are obtained (for the same number of data) in the first experiment. In that case, the pore radii classes given by Equation (2.33) are equidistant. However, results are acceptable in all cases excepting the third experiment. It should be noted that the original PSD is the same in all cases but the form seems different due to the pore sizes classes represented in each case.

An important remark to be made is that similar values of  $\alpha^*$  ( $\alpha^*$  very close to 1.02) were calculated whatever sampling method, except for the case in which flow rates are equidistant ( $\alpha^*=1.50$ ).

### **c) Sensitivity to noisy ( $Q_i, \nabla P_i$ ) data**

The  $(Q_i, \nabla P_i)$  data presented in Figure 22 have been altered by introducing random noise in every data couple. Then, these altered data have been exploited with YSM using the correct values of  $\tau_0$ ,  $k$  and  $n$ . The effects of several error sources on the agreement between the original PSD and the PSD obtained from the so altered  $(Q_i, \nabla P_i)$  data have been evaluated. The main error sources are the following:

- 1. Systematic errors in  $Q_i$ .
- 2. Systematic errors in  $\nabla P_i$ .
- 3. Random errors in  $\nabla P_i$ .

Concerning the tested magnitude of the error, constant errors of the type 1 and 2 result in shifting of the obtained PSD of the same order as that produced by errors in  $\tau_0$ . However, errors of type 1 and 2 whose magnitudes are proportional to  $Q_i$  and  $\nabla P_i$  respectively do not have any significant influence on the obtained PSD, as occurred with errors in  $k$ . Therefore, we will focus on errors of type 3, which correspond to the less favorable case.

#### **1) Effect of the number of noisy ( $Q_i, \nabla P_i$ ) data couples**

Once again, the original PSD presented in Figure 23 was considered together with a fluid whose Herschel-Bulkley parameters are respectively  $\tau_0 = 10$  Pa,  $k = 1$  Pas<sup>n</sup> and  $n = 0.60$ . Six numerical experiments were performed with 10, 20, 30, 40, 50 and 60  $(Q_i, \nabla P_i)$  data respectively.  $\nabla P_i = \frac{2\tau_0}{z_i}$  with  $i = (0, \dots, N)$ ,  $z_i = z_{\max} - \frac{(z_{\max} - z_{\min})}{N} i$ ,  $z_{\min} = m_1 - 3\sigma_1$ ,  $z_{\max} = m_2 + 3\sigma_2$ . Then, the resulting  $(Q_i, \nabla P_i)$  data have been altered by introducing a random noise of  $\pm 1\%$  in every  $\nabla P_i$ . Finally, the altered sets have been exploited in each case, and the obtained PSDs are displayed in Figure 32. From that figure, it is deduced that the obtained PSDs do not agree as well with the original PSD as in the absence of noise. However, the shape of the PSD is coarsely preserved. The influence of the number of data is not easy to determine and no clear trend can be deduced, except that a smaller number of data leads to less oscillating probabilities but also less detailed PSDs. Indeed, the obtained PSD is affected by noisy  $(Q_i, \nabla P_i)$  data whatever the number of data.

## 2) Effect of the range of noisy ( $Q_i, \nabla P_i$ ) data couples

The same PSD and fluid as in the preceding experiments has been used to generate 50 ( $Q_i, \nabla P_i$ ) data with  $\pm 1\%$  random noise in  $\nabla P_i$ , but in this occasion the range of  $\nabla P_i$  has been extended in order to evaluate whether the obtained PSD was still close to the original one or conversely they were displaced toward the larger or smaller pore radii. The new range of  $\nabla P_i$  was from  $\frac{2\tau_0}{m_2 + 9.33\sigma_2}$  to  $\frac{2\tau_0}{m_1 - 3.67\sigma_1}$ . The resulting PSD is displayed in Figure 33 and it is noticed that its position on the axis of abscissa is unaffected. As a consequence, it can be concluded that YSM provides PSDs whose position on the axis of abscissa (pore radii) is the same as that of the original PSD even in the presence of noise.

## 3) Effect of the magnitude of the noise in the ( $Q_i, \nabla P_i$ ) data couples

The objective now is to assess how the magnitude of the random errors in ( $Q_i, \nabla P_i$ ) data affect the obtained PSD. Two experiments with  $N+1=50$  were performed in which 1% and 5% random errors were respectively included. The obtained PSD in each case was compared to the original one, as shown in Figure 34. As expected, the deviation from the original PSD was more important in the case in which the error was greater. The values of  $\alpha^*$  were 1.71 for 1% error and 2.45 for 5% error, which suggests that less precise data lead to higher values of  $\alpha^*$ .

Moreover, one may wonder whether the position of the principal probability peaks on the axis of abscissa is preserved whatever the range of  $\nabla P_i$ . To answer that question, a third experiment was performed maintaining a random error of 5% but enlarging the  $\nabla P$  interval limits between  $\frac{2\tau_0}{m_2 + 9.33\sigma_2}$  and  $\frac{2\tau_0}{m_1 - 3.67\sigma_1}$ . As shown in Figure 35, the position of the obtained PSD was still close to that of the original PSD when using a wider range of  $\nabla P_i$  and a slightly better agreement between both PSDs is observed.

## 4) Fit with a polynomial

$N+1=50$  ( $Q_i, \nabla P_i$ ) data with 1% random error were obtained by numerically injecting the same fluid as in the preceding experiments in the original PSD. With the aim of reducing the influence of noisy data on the obtained PSD, the ( $Q_i, \nabla P_i$ ) points were fitted to a polynomial.

The order of the polynomial was chosen in such a manner that further increase of that order did not significantly reduce deviations from the ( $Q_i, \nabla P_i$ ) data. For such optimum polynomial order,  $Q$  was evaluated at each  $\nabla P_i$  and these new data couples were exploited. As observed in Figure 36, the use of such fitting procedure produces deviation of the obtained PSD with respect to the original one.

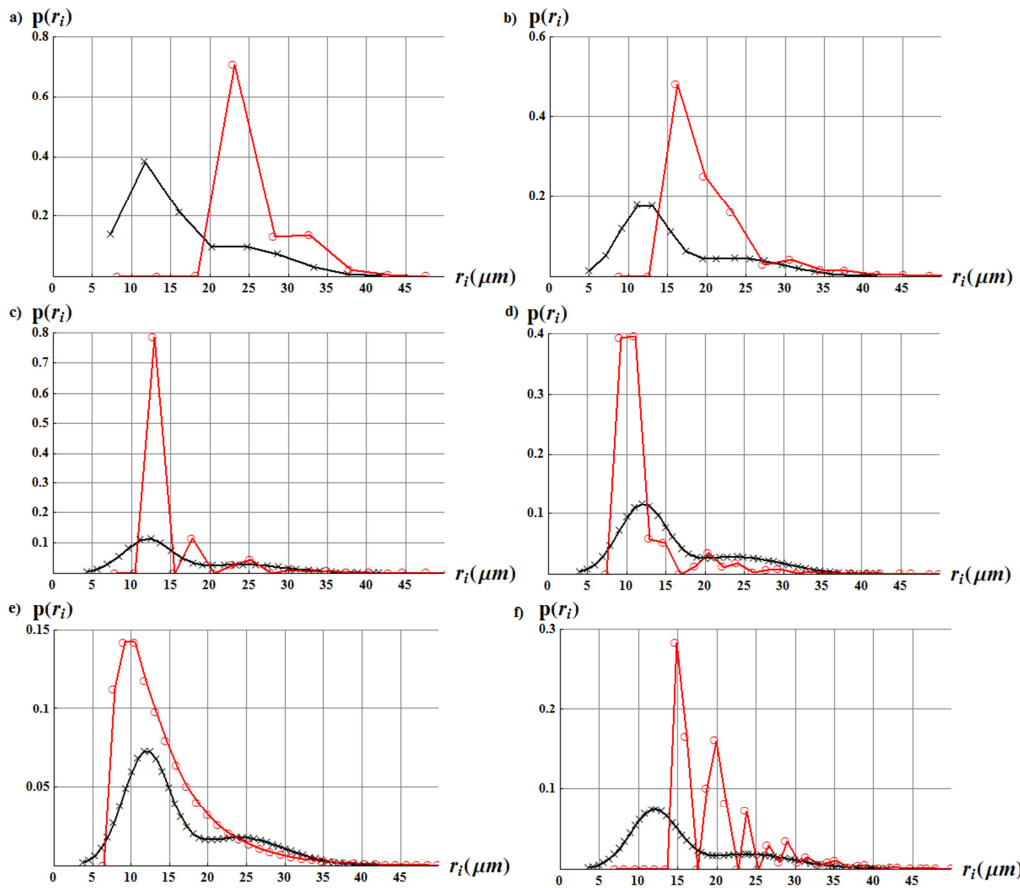


**Figure 32:** Obtained PSDs (red) from noisy ( $Q_i, \nabla P_i$ ) data compared to the original PSD (black) as a function of the number of data. a) 10 data, b) 20 data, c) 30 data, d) 40 data, e) 50 data, f) 60 data.

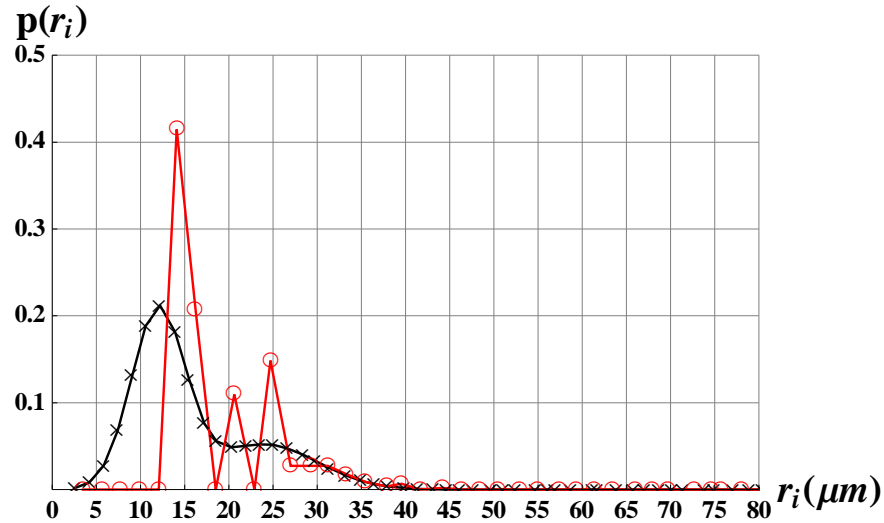


**Figure 33:** Original PSD (black PSD) compared to the PSD obtained from noisy ( $Q_i, \nabla P_i$ ) data spread over a wide range of  $\nabla P$  (red PSD).

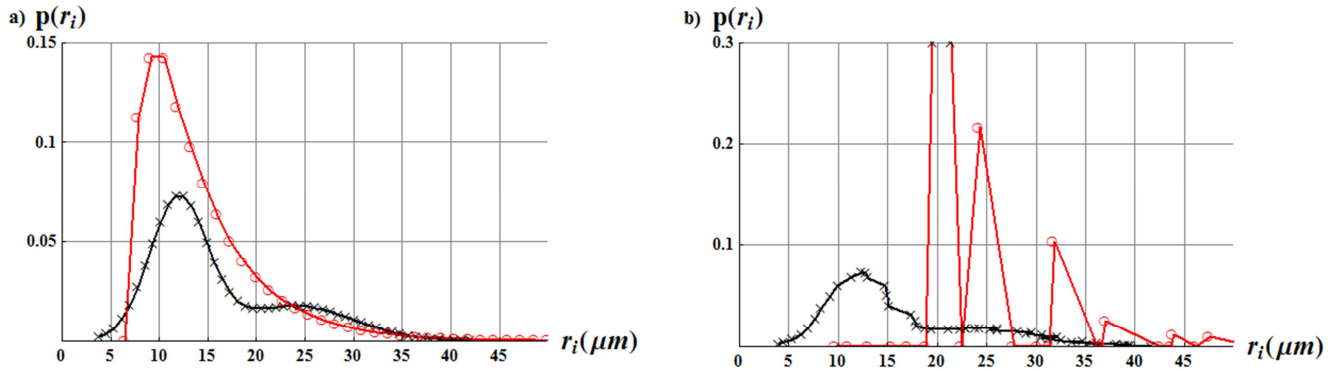


**Figure 34:** Original PSD (black PSD) compared to the PSDs obtained from  $(Q_i, \nabla P_i)$  data with a) 1% random error in  $\nabla P_i$  and b) 5% random error in  $\nabla P_i$ .

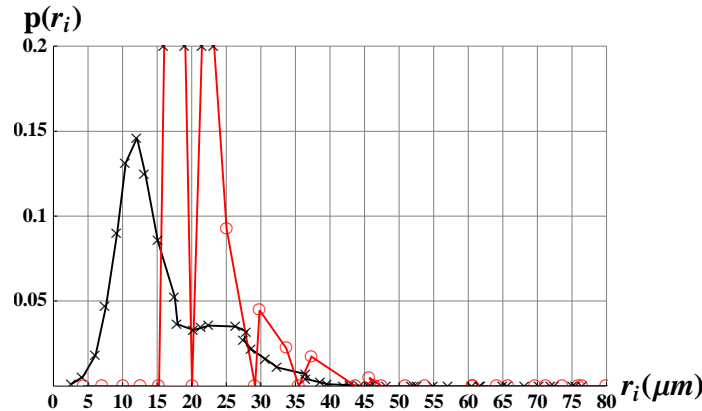


**Figure 35:** Original PSD (black PSD) compared to the PSDs obtained from  $(Q_i, \nabla P_i)$  data with 5% random error in  $\nabla P_i$ . In this case, the range of  $\nabla P_i$  was wider than before.

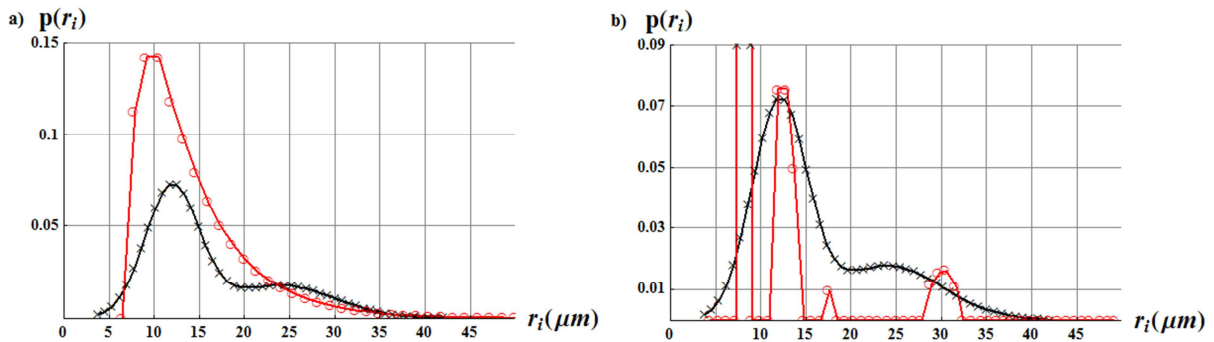


**Figure 36:** Obtained PSDs (red) compared to the original PSD (black) a) without fit, b) with polynomial fit.

## Conclusions

In this section, YSM has been numerically validated with success. The method has been proved to provide correct results for all the set of tested PSDs. Besides, the effect of errors in rheological parameters on the quality of the obtained PSD has been studied. It can be concluded that whereas the method is robust vis-à-vis the errors in  $k$  and  $n$ , it seems to be sensitive to imprecisions in  $n$ , so special attention has to be paid to the accurate characterization of  $n$ . Extremely high precision in the value of these rheological parameters is hard to achieve, so this problem may at first seem unavoidable. However, it has to be borne in mind that in this study  $\tau_0$ ,  $k$  and  $n$  have been independently altered. In fact, in real situations,

a set of  $(\tau, \dot{\gamma})$  measures are fitted to the Herschel-Bulkley model in order to obtain the value of these three parameters. That means that each parameter will not vary independently, but increasing or decreasing one of them will also affect the other two. That interdependency will soften the severe effects seen above. In any case, a possible solution is to perform an iterative process in which several values of  $n$  in the interval of uncertainty are tested and the best result in terms of fit to experimental data would be kept. That fit to experimental data can be assessed through Eq. (3.7).

In other respects, the effect of errors in the  $(Q_i, \nabla P_i)$  data has been quantified by considering the worst situation where a random noise in a zigzag fashion is introduced. Even if it has been proved that noisy data significantly affect the quality of the obtained PSD, it has to be observed that the position of the resulting PSDs on the horizontal axis is still correct. Besides, it has been noticed that the value of  $\alpha^*$  is higher in the presence of errors. Moreover, data have also been smoothed by using a polynomial fitting procedure. Unfortunately, exploitation of such smoothed data was unsatisfactory and the agreement between original and calculated PSDs was worse.

### **3.3.4. Comparison of YSM with available methods based on yield stress fluids injection**

A set of numerical experiments were carried out in order to assess the performance of the methods presented by Oukhlef (2011, 2014) and Malvaul (2013). However, only results obtained with Oukhlef's method will be presented here given that the numerical inversion proposed by Malvaul was not fully described.

#### **Analytical inversion**

The analytical method presented by Oukhlef was proved to work well in the case of a Bingham fluid, i.e. for  $n = 1$ , with a loss of performance in the case of Herschel-Bulkley fluids for which  $n \neq 1$ . To illustrate this, Oukhlef's method was applied to the  $(Q_i, \nabla P_i)$  data shown in Figure 22, which correspond to the numerical injection of a yield stress fluid with  $\tau_0 = 10$  Pa,  $k = 1$  Pa s<sup>n</sup> and  $n = 0.60$  through a bundle of 1,000,000 capillaries whose radii are distributed according to the PSD shown in Figure 23. As can be observed in Figure 37, the obtained PSD is highly oscillating in the small pores region, presents negative probabilities and its agreement with the original PSD is worse than that of the PSD provided by YSM (Figure 23). Therefore, it can be stated that YSM provides better results than those of the available method in the considered case. In order to assess such conclusion; a set of experiments were carried out involving different types of PSDs and different rheological parameters, which leaded to the same conclusions.

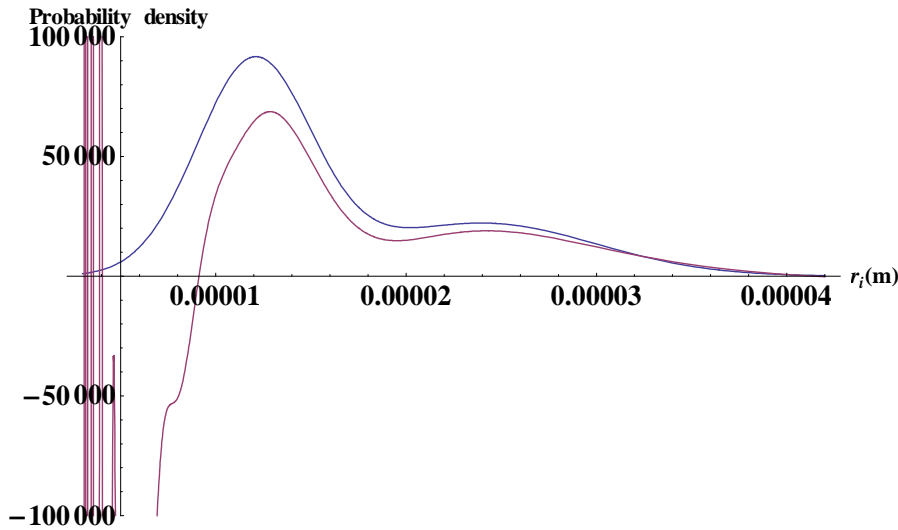


Figure 37: PSD obtained with the analytical inversion presented by Oukhlef (2011) (purple) compared to the original PSD (blue).

### 3.4. Design of experiments

In this section, the technical characteristics of the elements that constitute the experimental device will be related to the type of PSD to be determined. The experimental setup is a conventional one: the fluid is injected through the porous sample by means of a volumetric pump and the pressure drop across the core is measured for a range of imposed flow rates.

Let us begin by defining the standard type of PSD that we wish to characterize with our system: e.g. Gaussian, bimodal or other form, its standard deviation, its average, its mean, etc. The total flow rate as a function of the pressure gradient is given by Eq. (2.37):

$$Q(\nabla P_j) = \frac{\varepsilon R^2}{\int_0^\infty p(r)r^2 dr} \int_0^\infty q(\nabla P_j, r) p(r) dr = NP \times \int_0^\infty q(\nabla P_j, r) p(r) dr$$

In order to design the experiment, it was considered sufficient to analyze pore sizes whose cumulative probability lies between 5% and 99%. Therefore, the pore radii whose cumulative probabilities are 5% and 99% according to  $p(r)$  are named  $r_{min}$  and  $r_{max}$  respectively. Also, it is considered that the largest pore in the sample has a radius of  $2r_{max}$ , but its frequency is low enough so that its effect on the total flow rate is negligible above the pressure at which the pores with radius  $r_{max}$  begin to participate in flow.

As explained before, the range of the data should be so that the upper flow rate lies in the interval where  $Q(\nabla P)$  follows the power law  $\nabla P^y$  with  $y$  close to  $1/n$ . It is considered that the pressure loss at which a pore with radius  $r_{min}/2$  would start to flow is high enough to satisfy the previous condition. This pressure loss is  $\Delta P_{max} = 4\tau_0 L/r_{min}$  with  $L$  being the length of the core. If the pump to be used is able to impose a range of flow rates from  $Q_{min}$  to  $Q_{max}$ , the following constraints have to be satisfied:

$$Q_{\max} \geq NP \int_{r_{min}}^{2r_{\max}} f_1(r, r_{\min}, r) \left( \frac{2r\tau_0}{kr_{\min}} \right)^{\frac{1}{n}} \pi r^2 p(r) dr \quad (3.10)$$

$$Q_{\min} \leq NP \int_{r_{\max}}^{2r_{\max}} f_2(r, r_{\max}, n) \left( \frac{r\tau_0}{kr_{\max}} \right)^{\frac{1}{n}} \pi r^2 p(r) dr \quad (3.11)$$

with

$$f_1(r, r_{\min}, n) = \left\{ 1 - 2 \left[ \frac{\left(1 - \frac{r_{\min}}{2r}\right)^2}{\frac{1}{n} + 3} + \frac{\frac{r_{\min}}{2r} \left(1 - \frac{r_{\min}}{2r}\right)}{\frac{1}{n} + 2} \right] \right\} \left[ \frac{r}{\frac{1}{n} + 1} \left(1 - \frac{r_{\min}}{2r}\right)^{\frac{1}{n}+1} \right]$$

$$f_2(r, r_{\max}, n) = \left\{ 1 - 2 \left[ \frac{\left(1 - \frac{r_{\max}}{r}\right)^2}{\frac{1}{n} + 3} + \frac{\frac{r_{\max}}{r} \left(1 - \frac{r_{\max}}{r}\right)}{\frac{1}{n} + 2} \right] \right\} \left[ \frac{r}{\frac{1}{n} + 1} \left(1 - \frac{r_{\max}}{r}\right)^{\frac{1}{n}+1} \right]$$

$$NP = \frac{\varepsilon R^2}{\int_0^\infty p(r)r^2 dr}$$

where  $R$  is the radius of the porous sample.

It is assumed that the pump can work at relative pressures ranging from  $P_{\min}$  to  $P_{\max}$  with:

$$P_{\min} \leq 2\tau_0 L / r_{\max} \quad (3.12)$$

$$P_{\max} \geq 4\tau_0 L / r_{\min} \quad (3.13)$$

Conditions (3.10) and (3.11) can be rewritten as follows:

$$k \geq \frac{\tau_0}{Q_{\max}^n} \left[ NP \times \left( \frac{2}{r_{\min}} \right)^{\frac{1}{n}} \times \int_{r_{\min}}^{2r_{\max}} f_1(r, r_{\min}, r) \pi r^{2+\frac{1}{n}} p(r) dr \right]^n \quad (3.14)$$

$$k \leq \frac{\tau_0}{Q_{\min}^n} \left[ NP \times \left( \frac{1}{r_{\max}} \right)^{\frac{1}{n}} \times \int_{r_{\max}}^{2r_{\max}} f_2(r, r_{\max}, r) \pi r^{2+\frac{1}{n}} p(r) dr \right]^n \quad (3.15)$$

Conditions (3.12) and (3.13) can also be rewritten, obtaining:

$$\frac{r_{\max} P_{\min}}{2L} \leq \tau_0 \leq \frac{r_{\min} P_{\max}}{4L} \quad (3.16)$$

Inequalities (3.14), (3.15) and (3.16) can be used to estimate the upper and lower bounds of the properties of the fluid needed to characterize a standard PSD with a given pump. Analogously, the same inequalities can be used to estimate the properties of the pump needed to characterize a standard PSD with a given fluid. However, it has to be kept in mind that these formulas only give very rough estimates of these properties because they are based on a bundle-of-capillaries of the porous medium.

## 4. Laboratory experiments

---

In this chapter, we test the method presented in Chapter 3 in the case of xanthan gum solutions injected through a sintered silicate with unknown PSD. Firstly, preliminary experiments are presented with the objective of establishing the grounds of the experimental procedure adopted later. Then, we will study the effect of polymer concentration of the solutions on the characteristics of the PSDs obtained with YSM. Afterwards, YSM will be applied to different types of porous media so as to study the quality of the obtained PSDs. Also, viscosity and density measurements of the effluent during saturation with brine and xanthan solution will be presented in order to assess the effects of pore blocking, polymer adsorption and polymer degradation. Moreover, a modified YSM will be proposed as a consequence of the conclusions drawn from these experiments

---

### **4.1. Preliminary laboratory experiments**

In this section, two preliminary laboratory experiments will be presented. They are called *preliminary* because they are the basis upon which further studies will be designed. Indeed, these experiments constitute the basis of the experimental protocol and the sensitivity studies that will be presented in the next chapters. The main steps of a typical experiment are:

- Yield stress fluid preparation.
- Rheological measurements with a stress-controlled rheometer.
- Evacuation of the air in the sample.
- Saturation of the porous sample with water and porosity measurement.
- Permeability measurement.
- Saturation of the porous sample with the yield stress fluid.
- $Q(\nabla P)$  measurements during the yield stress fluid injection.

The experimental procedure will be detailed in the next sections as well as the exploitation of the experimental data used to obtain the PSD of the analyzed porous core.

#### **4.1.1. Materials**

The fluid to be injected is a xanthan gum solution obtained by dissolving an amount of xanthan gum powder (Rhodigel, Prolabo, VWR International) in de-ionized and filtered water containing 400 ppm of  $\text{NaN}_3$  (Sodium Azide, Sigma-Aldrich, Riedel-de Haën Trademark) used as a bactericide. The concentration of xanthan gum solution  $C_p$  was alternatively fixed at 6000 or 7000 ppm depending on the experiment. Its measured pH was very close to 7. In solution state, an isolated xanthan macromolecule is more or less rigid and has a contour length of typically 1  $\mu\text{m}$  (Mongruel and Cloitre 2003) and a transverse size of approximately 2 nm. In the case of porous media whose large pores have a radius greater than 1  $\mu\text{m}$ , no plugging effect is expected at low  $\nabla P$  (only largest pores are involved in the flow). Under high  $\nabla P$  the shear rate  $\dot{\gamma}$  may be so high that the xanthan molecules are oriented in the direction of

flow with a limiting angle close to  $45^\circ$ , so the limiting pore radius that can be investigated should be comparable to 350 nm ( $\approx \text{Sin}(45^\circ) \times 1/2 \mu\text{m}$ ). The porous medium sample used in this study is a synthetic sintered silicate (Aerolith®10 purchased from PALL Corporation, USA) with porosity and permeability provided by the manufacturer of respectively  $\varepsilon = 0.40$  and  $K = 5 \text{ D}$ .

#### **4.1.2. Rheograms of the injected fluids**

The polymer solutions were characterized by means of a stress-controlled rheometer (ARG2, TA Instruments, France) equipped with a cone-plate geometry. After loading the sample, a delay of 5 minutes was observed before starting the rheological measurements. Then, the shear rate corresponding to a given shear stress was recorded *versus* time and its value was collected when its variation was less than a prescribed tolerance (typically 5 %) during three consecutive sample periods of 10 seconds. The maximum time allowed for each measure of shear rate was 1 minute. The imposed shear stresses ranged linearly from 0 to the one producing a shear rate of approximately  $1000 \text{ s}^{-1}$ . All the measures were taken at  $20^\circ\text{C}$ , which is the temperature maintained during the flow experiments. The rheograms obtained by plotting  $\tau$  versus  $\dot{\gamma}$  are displayed in Figure 38. As can be observed, the rheology is well approximated by a Herschel–Bulkley model for each xanthan concentration even if, as explained before, the yield stress is only apparent. This conclusion is in agreement with the observations made by others researchers (Song *et al.* 2006), as already presented in subsection 2.2.5. The fitting procedure used here consists in minimizing the sum

$$\sum_i (\tau(\dot{\gamma}_i) - \tau_i)^2 \dot{\gamma}_i \quad (4.1)$$

where  $\tau(\dot{\gamma})$  is given by Eq. (2.19) and  $(\dot{\gamma}_i, \tau_i)$  are experimental data. That allows us to determine the values of the yield stress  $\tau_0$ , the flow index  $n$ , and the consistency  $k$  for each  $C_p$  as specified in the figure caption. The square of the difference between  $\tau(\dot{\gamma}_i)$  and  $\tau_i$  is weighted by  $\dot{\gamma}_i$  in order to ensure a good fit for high shear rates while obtaining an apparent yield stress. Figure 39 shows the viscosity *versus* shear rate measures corresponding to both concentrations. It is observed that the viscosity at lowest shear rates (plateau viscosity) is greater in the case  $C_p = 7000 \text{ ppm}$ . Therefore, and as it is expected, the higher the polymer concentration, the closer the behavior to that of a yield stress fluid.

Again, it has to be noted that xanthan gum solutions are not actually yield stress fluids (if yield stress fluids do really exist). However, they present a very high Newtonian plateau of viscosity at low shear rates and a drastic shear-thinning behavior (the plateau viscosity of the 7000 ppm solution is approximately  $10^4$  times its viscosity at  $100 \text{ s}^{-1}$ ). For that reason, and as a first approximation, their rheology is well fitted by a Herschel–Bulkley model (Sochi 2010). Some authors claim that this procedure leads to arbitrary values of the yield stress and that other methods might be used to obtain the correct value of the yield stress (Nguyen and Boger 1983; Balhoff *et al.* 2011). Moreover, the rheology of these solutions may also be well fitted

using the popular Carreau model, but unfortunately no rigorous analytical relation expressing  $Q$  versus  $\nabla P$  in a capillary tube exists for this model (Balhoff *et al.* 2011, 2012). Therefore, the use of an asymptotic rheological law (truncated power law) should result in errors of the same order as those introduced by the Herschel–Bulkley model. Nevertheless, from a practical point of view, the most important issue in this method is to obtain a pseudo-yield stress below which the contribution of a pore size to the total flow rate is negligible.

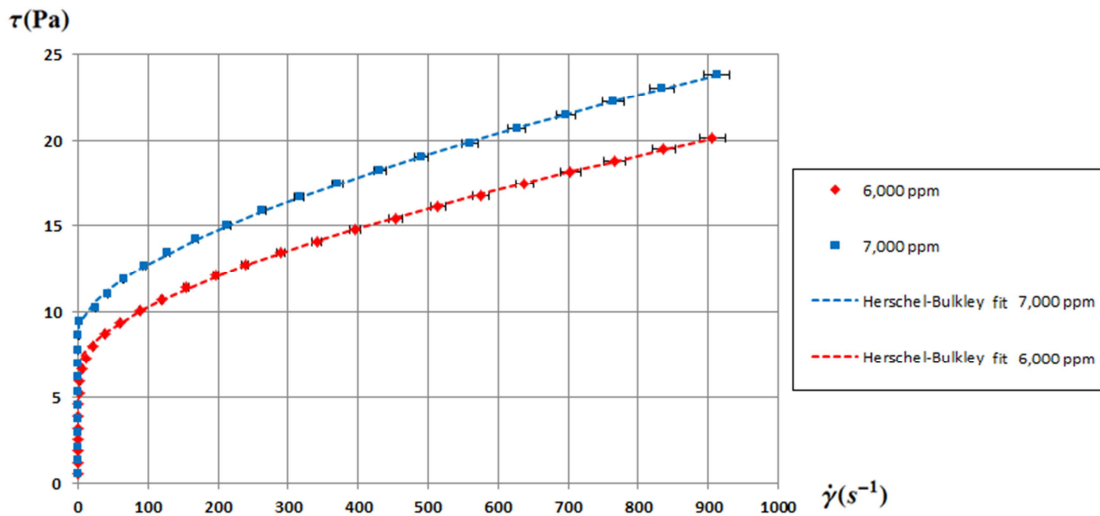


Figure 38: Rheograms of the xanthan gum solutions used in laboratory experiments and their fits by a Herschel–Bulkley law.  $C_p = 7000 \text{ ppm}$ :  $\tau_0 = 9.04 \text{ Pa}$ ,  $k = 0.21 \text{ Pas}^n$ ,  $n = 0.63$ .  $C_p = 6000 \text{ ppm}$ :  $\tau_0 = 6.86 \text{ Pa}$ ,  $k = 0.20 \text{ Pas}^n$ ,  $n = 0.62$ .

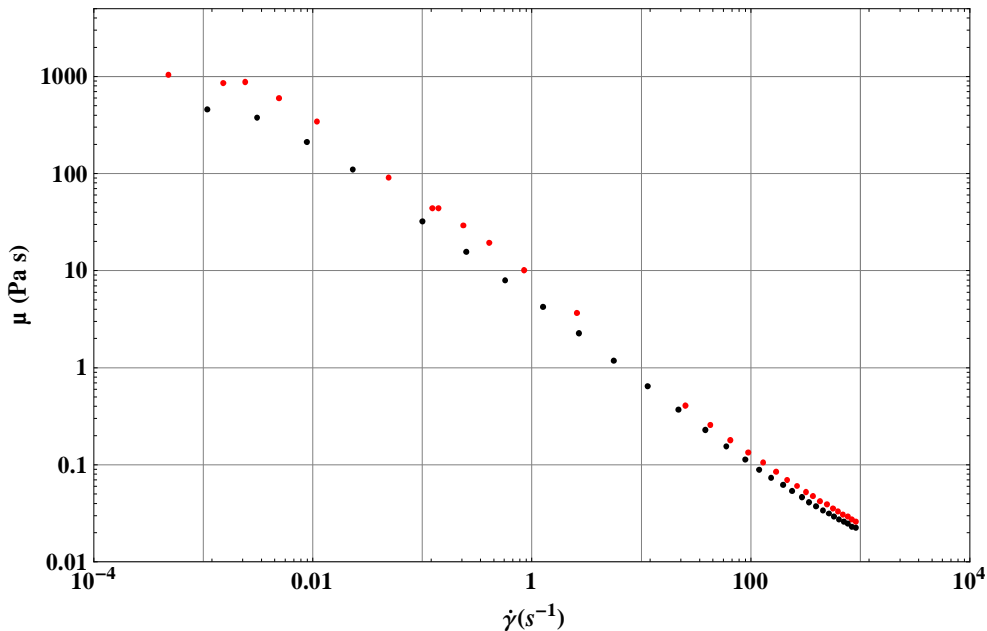


Figure 39: Viscosity as a function of shear rate for the xanthan gum solutions used in the preliminary laboratory experiments.  $C_p = 7000 \text{ ppm}$  (red),  $C_p = 6000 \text{ ppm}$  (black).

In order respects, the PSD obtained with YSM was proved to be sensitive to errors in  $n$ . In order to assess whether these errors affect the fit to the experimental data, an error of  $+1.7\%$  was introduced in the value of  $n$  obtained by our fitting procedure (minimization of Eq. (4.1)). Then, the resulting fit was compared to the original one as displayed in Figure 40. It is

observed that the introduction of such an error clearly affects the quality of the fit to the experimental data, so such an error seems unlikely to happen.

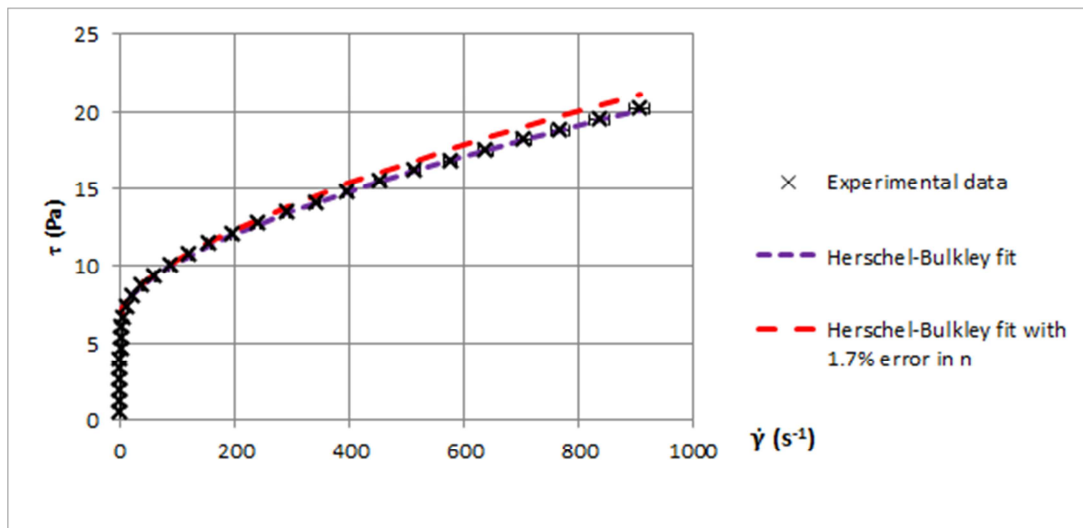


Figure 40: Herschel-Bulkley fit to the experimental measures with and without a 1.7% error in  $n$ .

#### 4.1.3. Experimental setup and procedures

A schematic representation of the experimental setup is displayed in Figure 41 and the corresponding experimental realization is shown in Figure 42. From left to right in Figure 41 there are (1) a syringe pump (PHD Ultra, Harvard Apparatus) filled alternatively with the polymer solution or the de-ionized water which ensures fluids injection at controlled flow rates, (2) the porous medium to be investigated (cylindrical cores of 5 cm diameter and 10 cm length), and (3) a vessel to collect the outgoing fluid. A pressure sensor (Rosemount 3051 Pressure Transmitter) is also connected to the inlet and the outlet of the porous medium. The following procedure was adopted to prepare the porous media. The two ends of the core were in contact with aluminum injector plates. Surfaces in contact with the porous medium were coated with Teflon (Du Pont, Washington, D.C., USA) to prevent any ion exchange between the metal and the core. The lateral surface of the porous medium was coated with a non-wetting epoxy resin then wrapped with epoxy-coated fiberglass to insure liquid imperviousness and mechanical strength.

First of all, the porous sample was saturated with  $\text{CO}_2$ , whose solubility in water is very high, in order to avoid the presence of gas bubbles during the experiments. Next, the porous medium was saturated with degassed de-ionized and filtered water and kept at rest for approximately 12 hours. Then, prior to the injection of xanthan gum solutions, the permeability to water and porosity of the sample were measured. Moreover, and to avoid any further formation of gas bubbles inside the porous medium, the polymer solution was degassed too under moderate vacuum. After that, 2 pore volumes of xanthan gum solution were injected at a flow rate corresponding to  $\text{Pe} = 400$ , which was an intermediate flow rate among those to be imposed during the experiments.  $\text{Pe}$  is the Péclet number as defined by Sheng (2011):

$$Pe = \frac{\vartheta d_p}{D_c} \quad (4.2)$$

where  $\vartheta$  is the average interstitial velocity  $\vartheta = Q/(A\varepsilon)$ ,  $d_p$  is the equivalent cylindrical pore diameter (Eq. 2.7) and  $D_c$  is the molecular diffusion coefficient, taken as  $2.5 \cdot 10^{-8} \text{ cm}^2/\text{s}$  (Sorbie 1991). Once the 2 pore volumes were injected at  $Pe = 400$ , an additional pore volume was injected at the highest flow rate to be imposed during the experiments so as to ensure that the yield stress fluid filled all the pore size classes. Once saturated with xanthan solution, the porous medium was kept at rest for approximately 12 hours (overnight). In these preliminary experiments, the imposed flow rate was steeply increased and the corresponding pressure drops were recorded as a function of time. For each flow rate, the corresponding pressure drop was collected when the steady state was reached. This procedure was repeated for all flow rates. The choice of imposing the flow rate instead of the pressure as done by Clain (2010) and Malvaut (2013) was motivated by the difficulties to measure very small flow rates with a precision balance within a reasonable time lapse: drop by drop, evaporation, etc. Besides, given that  $Q$  follows a power law with respect to  $\nabla P$  with a power index greater than unity, small inaccuracies in  $\nabla P$  should result in wide variation of the measured  $Q$ . It should be finally noted that the temperature of the lab was kept constant at  $20^\circ\text{C} \pm 0.1$  during all the experiments.

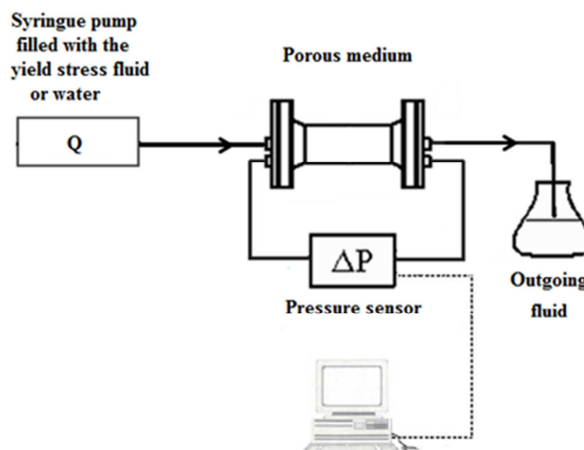


Figure 41: Schematic representation of the experimental setup.

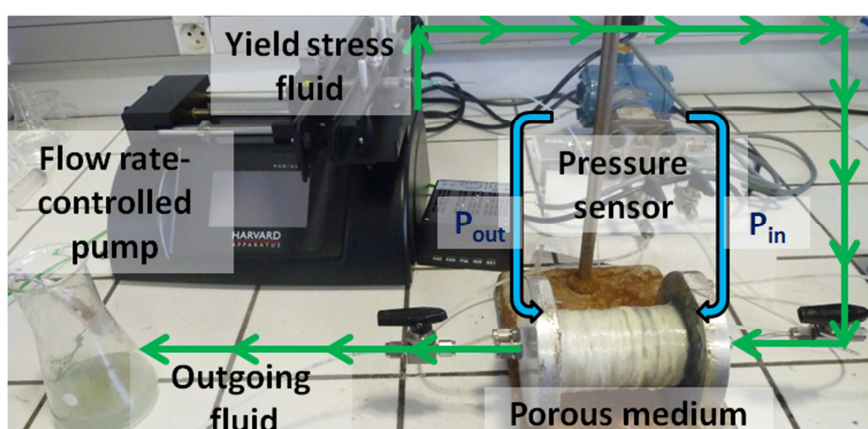


Figure 42: Experimental realization of the setup.

#### **4.1.4. Measurements of pressure gradient as a function of flow rate**

At the end of the experiment a set of  $(Q_i, \nabla P_i)$  raw data was obtained (Annex A). Figure 43 shows such data for  $C_p = 7000$  ppm with 39 data points ( $N + 1 = 39$ ). We note that the plot of  $Q$  versus  $\nabla P$  is of power law form as expected. Moreover, from this data set, it is possible to determine the range of pore radii that may be explored by using Equation (2.33). The precision of the pressure drops measurements given by the manufacturer was  $\pm 260$  Pa in the whole range of this experiment. Nevertheless, the uncertainty in the pressure loss measurements for our particular application was estimated as being 25% for  $Q \in (0.05, 0.62$  ml/h), 2.5% for  $Q \in (0.62, 150$  ml/h) and 0.5% for  $Q > 150$  ml/h (error bars hardly visible in the figure because of their small size).

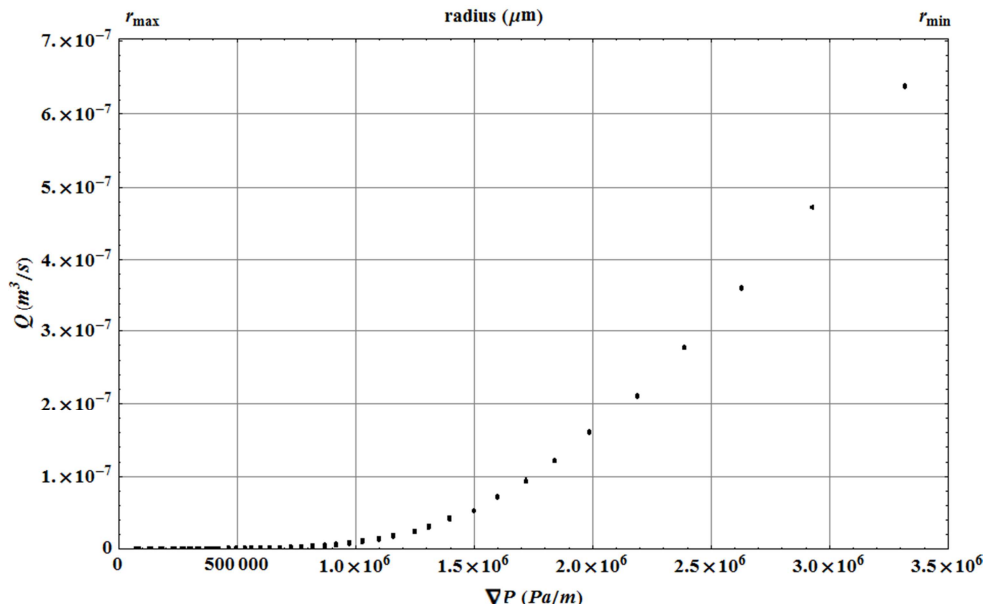


Figure 43: Experimental  $(Q_i, \nabla P_i)$  data obtained from the injection of a xanthan gum solution with  $C_p = 7000$  ppm through a sintered A10 silicate. The upper axis represents the radii of the pores joining the flow at each  $\nabla P$  (smaller pores at high  $\nabla P$ ).  $Q$  error:  $\pm 0.25\%$ .

#### **4.1.5. Results and comparison with MIP**

The method presented in Section 3.2 was applied to the  $(Q_i, \nabla P_i)$  raw data collected in the case of the investigated porous medium for  $C_p = 7000$  ppm. The obtained PSD expressed in terms of relative volume of pore classes of representative radii  $r_i$ ,  $p_v(r_i)$ , is displayed in Figure 44 together with the one deduced from MIP. It should be emphasized here that even if for the sake of simplicity we usually refer to the PSD deduced from MIP as “PSD from MIP” or “PSD obtained by MIP”, MIP does not actually provide any PSD. Obtaining PSDs from MIP experiments implies previous interpretation as explained in Section 2.1.4.

The value of  $\alpha^*$  obtained using the E-criterion was 1.3. The investigated porous medium was also characterized by means of the classic mercury porosimetry and the obtained results are presented together in the same figure. Examination of this figure shows that both PSDs are

approximately of Gaussian form. It appears therefore that there is a very good agreement between the PSD determined using the present method and the one delivered by MIP.

It has been shown numerically that the value of  $\alpha^*$  depends on the precision of the  $(Q_i, \nabla P_i)$  data. Hence, the observed difference between values of the current  $\alpha^* = 1.3$  and the one previously obtained for numerical experiments  $\alpha^* = 1.01 - 1.08$  may be attributed to the lower precision of the laboratory raw data. The fact that the fluid used is a pseudoplastic fluid without a true yield stress may also be considered as a source of such shift in  $\alpha^*$ . Furthermore, and as in numerical experiments, a sensitivity analysis has been carried out in order to study the effect of the value of  $\alpha$  on the obtained PSD. This is illustrated in Figure 45. Once again, it is observed that  $\alpha$  should be greater than unity and that the MIP is very well reproduced by choosing  $\alpha = \alpha^*$ . Besides, the PSDs obtained for  $\alpha$  close to  $\alpha^*$  are also in good agreement with MIP. However, and as already explained, MIP should not be taken as providing the absolute truth concerning PSDs. MIP is used here only to compare both methods and because it is the current reference for PSDs.

Complementary experiments were carried out under the same conditions and by changing only xanthan concentration to  $C_p = 6000$  ppm. In that case the obtained  $\alpha^*$  was 1.2 and the determined PSD was found to be slightly shifted to small pore radii when compared to the PSD corresponding to  $C_p = 7000$  ppm (Figure 46). This should be expected as when xanthan concentration is lowered the fluid rheology deviate more appreciably from the Herschel–Bulkley fluid type. This implies that the higher the polymer concentration, the better is the reliability of the obtained PSDs. A sensitivity analysis concerning the effect of  $\alpha$  was also carried out in this case ( $C_p = 6000$  ppm), leading once more to the conclusion that  $\alpha$  values close to  $\alpha^*$  provide similar PSDs (data not shown).

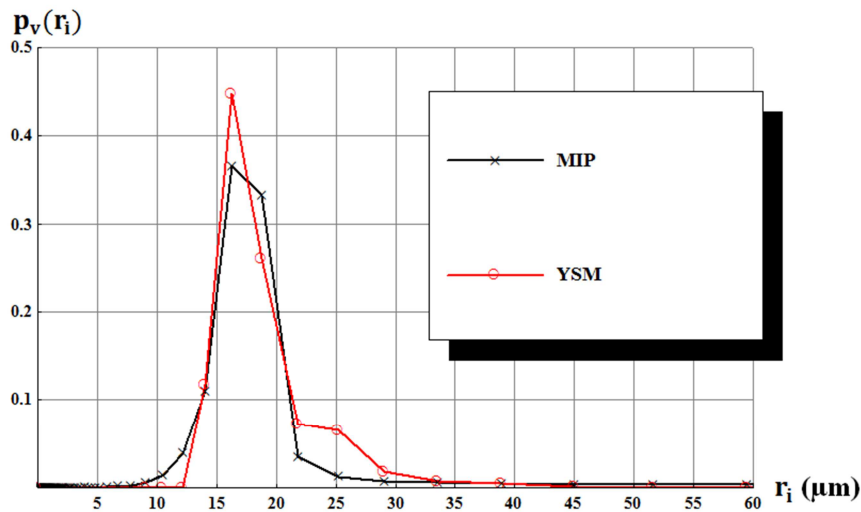


Figure 44: PSD obtained with YSM compared to PSD deduced from MIP for the preliminary experiment with  $C_p = 7000$  ppm.

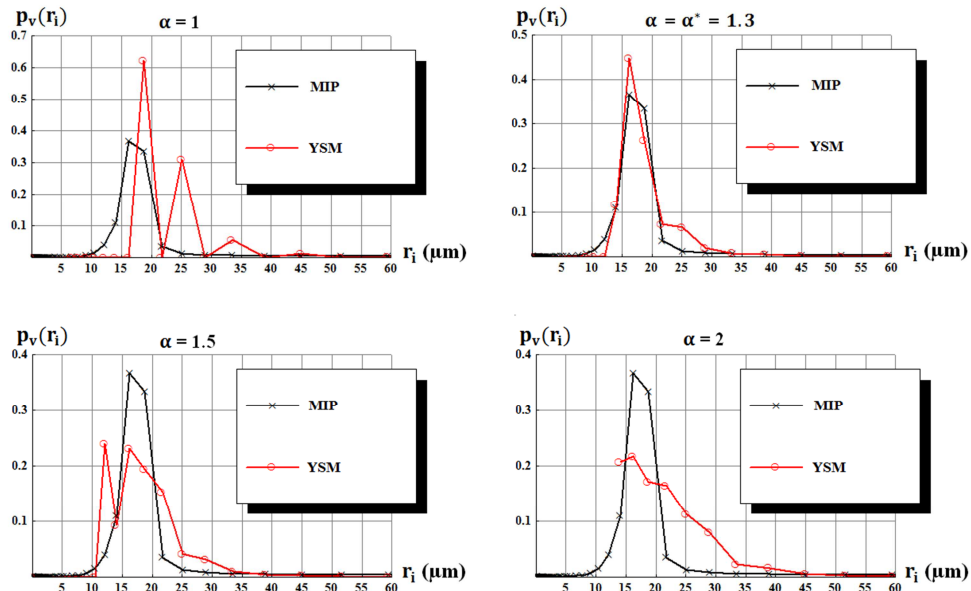


Figure 45: PSD obtained with the present method corresponding to  $C_p = 7000$  and different  $\alpha$  and comparison with PSD from MIP.

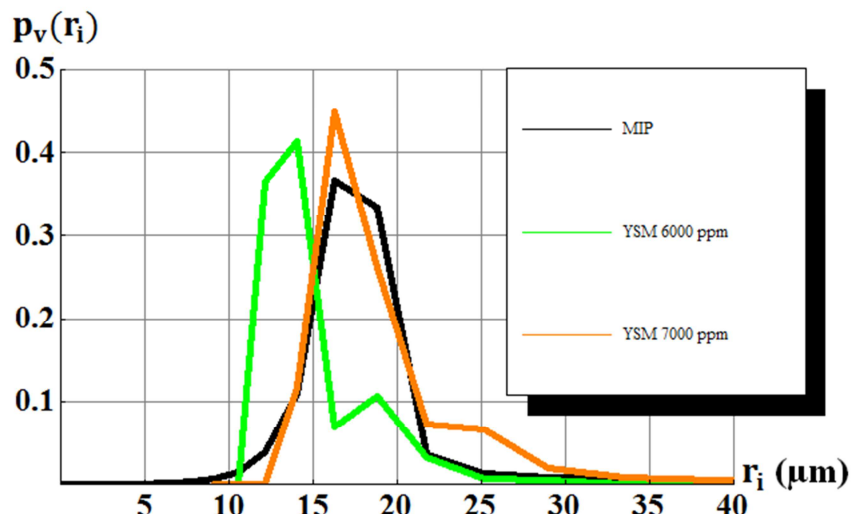


Figure 46: PSDs obtained with MFS at 6000 ppm and 7000 ppm compared with that provided by MIP.

#### 4.1.6. Conclusions

Preliminary flow experiments of yield stress fluids through porous media have been performed and YSM has been applied to the obtained data. As explained before, the experimental measurements that have been exploited in this section are only preliminary experiments whose objective was to draw some conclusions concerning the experimental feasibility of the method. From that, the following remarks may be made:

- Measurements, if carefully performed, provide  $(Q_i, \nabla P_i)$  raw data that can be exploited using YSM. Therefore, it is possible to apply YSM in the case of laboratory experiments in order to obtain PSD of real porous media.

- PSDs obtained with YSM are expected to present smaller radii than those obtained by MIP because, as already seen, the “dimension of the pore” characterized with mercury porosimetry is the diameter of the largest entrance or opening towards a pore volume. Nevertheless in the case of the tested porous material, the agreement between MIP and YSM was very good.
- The effect of  $\alpha$  has been studied as in the numerical case. Higher values of  $\alpha$  have been obtained and PSDs are not very sensitive to moderated variations of  $\alpha$  in the range close to  $\alpha^*$ .
- The xanthan gum used during these experiments produced turbid solutions. Given that turbidity is linked to the presence of impurities and aggregates in the fluid, it was consequently decided to explore other commercial products in order to select a pure xanthan gum which produced transparent solutions.
- During these preliminary experiments the flow rates have been imposed in ascending order. However, problems linked to polymer retention and depletion layer are expected to mostly appear at low flow rates. Therefore, it should be more judicious to carry out tests in descending order.
- The xanthan gum was dissolved in water using a magnetic stirrer. However, it was decided that the use of overhead stirrers would be preferred in order to avoid formation of aggregates within an acceptable lapse of time.
- The degassing process of xanthan gum solutions is more complex than it may seem. Indeed, given that these fluids are highly viscous, the migration of the air bubbles from the bulk volume to the free surface is slow. Besides, if a strong vacuum is imposed, the degassing of xanthan gum solutions is accompanied by water evaporation, which changes the xanthan concentration of the solution. Therefore, it was decided to use a pump able to impose a stronger vacuum, control the evolution of the fluid mass while degassing and break the vacuum regularly when evaporation is detected. Also, the used vacuum pump should not be sensitive to water vapors.
- The time required to attain a steady state depends on the considered flow rate. Based on these preliminary experiments, the corresponding minimum time needed to attain steady state was determined. Therefore, it was possible to carry out all further experiments with an optimized volume of injected fluid. By doing so, the eventual polymer retention at the core inlet would be minimized too.

## **4.2. Sensitivity of the obtained PSD to polymer concentration**

As seen in the previous section, the polymer concentration of the solution was shown to have an influence on the quality of the PSDs obtained through the use of YSM. Now, that influence will be analyzed by injecting solutions with different concentrations in the same type of porous medium.

### **4.2.1. Materials**

Like in the preliminary experiments presented in the preceding section, the fluid to be injected is a xanthan gum solution obtained by dissolving an amount of xanthan gum powder in de-ionized and filtered water containing 400 ppm of  $\text{NaN}_3$  (Sodium Azide, Sigma-Aldrich, Riedel-de Haën Trademark) as a bactericide. Nevertheless, after comparing several xanthan gums, Satiaxane CX 930 (Arlès agroalimentaire, France) was selected because it contained less impurities than the others and the obtained solutions were visually transparent. Five xanthan gum solutions with polymer concentrations ( $C_p$ ) of 4000, 5000, 6000, 7000 and 8000 ppm were prepared using an overhead stirrer with blade impeller (Heidolph, RZR 2041). During their preparation, the xanthan powders were progressively added to the water while stirring and once all the powder was added, the solution was kept under moderate stirring (500 rpm) for a time period of 12 to 24 hours depending on the concentration. Its measured pH was very close to 7 in all cases. After that, the fluid was stocked at low temperature for 12 hours and then degassed using a vacuum pump (Vacuum Pumps MPC Ultimate Pressure < 2 mbar, ILMVAK GmbH). In these experiments, the porous media were 5 samples obtained from a same original core of sintered silicate (Aerolith®10 purchased from PALL Corporation, USA). The samples were cylindrical with a length of 10 cm and a diameter of 5 cm. It has to be highlighted that in spite of the fact that the samples were of the same material, slight differences in the measured permeability were observed (6.5 – 9.5 D), always with a porosity close to 45%.

### **4.2.2. Rheograms of the fluids**

The rheograms of these five solutions were determined and the  $\tau(\dot{\gamma})$  data were fitted to a Herschel-Bulkley law following the same procedure presented in subsection 4.1.2. The obtained rheograms and corresponding fits are displayed together in Figure 47. These data were also plotted in terms of viscosity *versus* shear rate as shown in Figure 48. From this figure it is obvious that when polymer concentration is high, the viscosity at the lowest shear rates seems to diverge (within the considered shear rates interval) attaining very high values before drastically decreasing, thus approaching Herschel-Bulkley model. Besides, the Herschel-Bulkley parameters corresponding to the best fit of the rheograms in Figure 47 were represented as a function of  $C_p$  in Figure 49. It is observed that whereas  $\tau_0$  and  $k$  are strongly dependent on  $C_p$ ,  $n$  is almost constant.

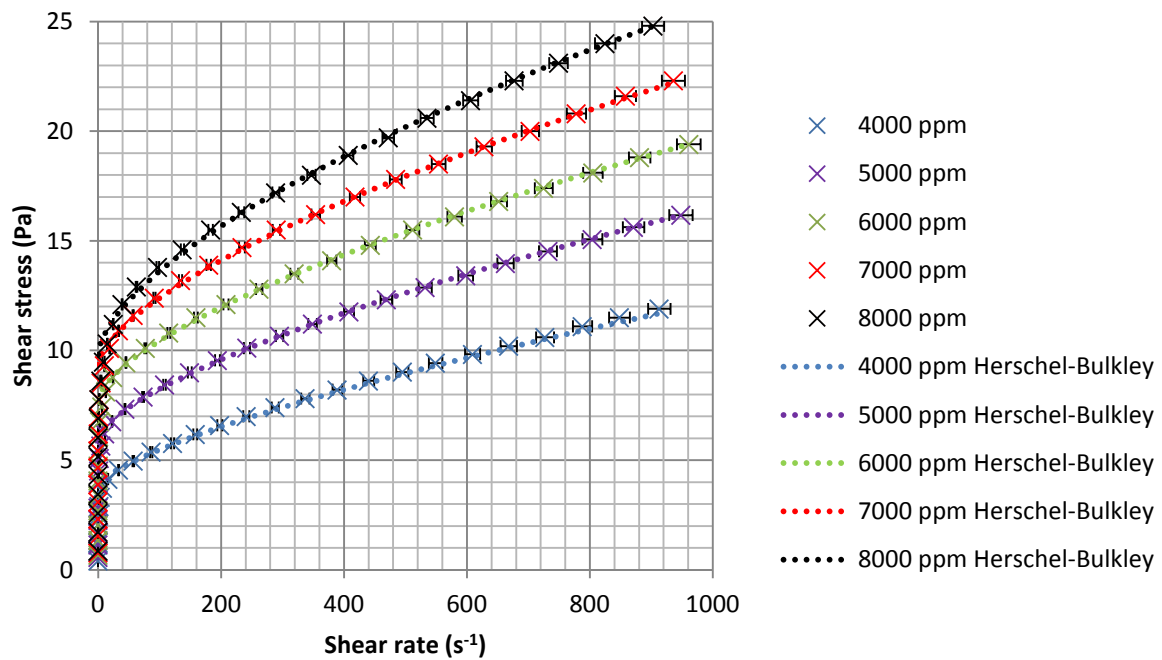


**Figure 47:** Measured shear stress as a function of shear rate for xanthan gum solution with different concentrations and their corresponding Herschel-Bulkley fits.

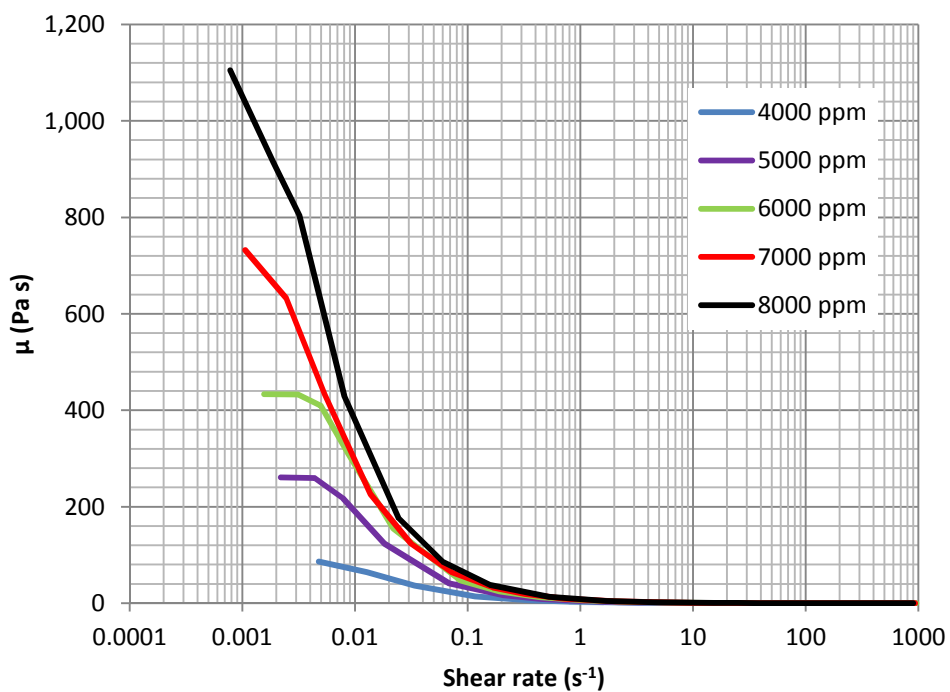


**Figure 48:** Viscosity as a function of shear rate corresponding to xanthan gum solution with different concentrations.

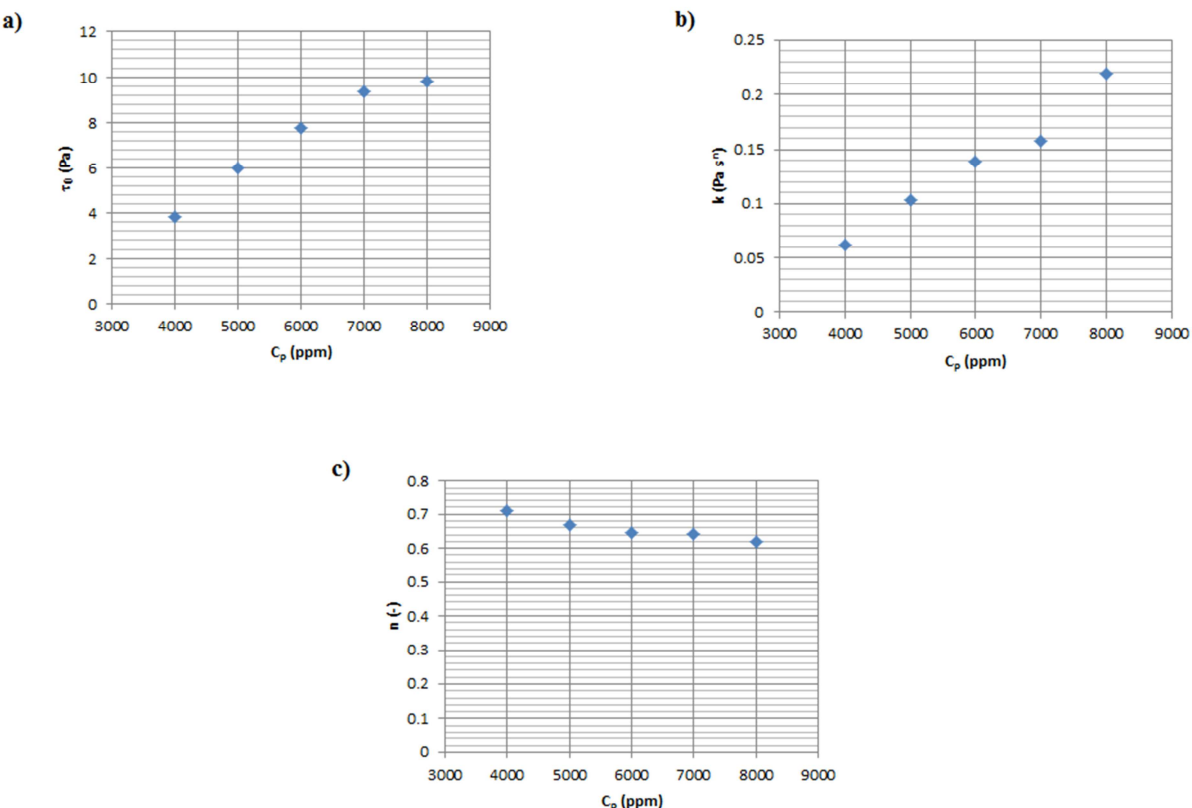


Figure 49: a) Yield stress ( $\tau_0$ ), b) consistency ( $k$ ) and c) flow index ( $n$ ) as a function of the concentration of xanthan gum in the aqueous solutions.

#### 4.2.3. Experimental setup and procedure

The experimental setup is the same as for preliminary experiments (see Figure 41 and Figure 42). Also, the experimental procedure previous to  $Q(\nabla P)$  measurements was similar to that of the preliminary experiments except the modification of fluid degassing and fluid preparation steps as explained before. In the present experiments, the imposed flow rate during the injection of the solutions was steeply **decreased**, and the corresponding pressure drops were measured at steady state using a pressure sensor (Rosemount 3051 Pressure Transmitter). The time allowed for each measure was optimized in order to minimize the possible polymer retention in the porous medium. The range of imposed flow rates was the same for all investigated polymer concentrations (2000 ml/h to 0.05 ml/h) except for 4000 ppm. In that case the flow rates were slightly greater because the lower viscosity implied lower magnitude of the pressure gradients which in turn generated higher uncertainty in the measurements. The temperature of the lab was kept constant at  $20^\circ\text{C} \pm 0.1$  during all the experiments.

#### 4.2.4. Measurements of pressure gradient as a function of flow rate

A set of  $N+1$  ( $Q_i, \nabla P_i$ ) raw data were collected during each experiment (Annex A), with  $N+1$  ranging from 39 to 53. Figure 50 summarizes the results obtained for all polymer concentrations  $C_p$ . From these data it is possible, by using Equation (2.33), to determine the range of pore radii that can be explored. Then the procedure described in Section 3.2 is used to obtain the PSD. As expected, the more the solution is concentrated, the more the pressure

loss is important for a given flow rate. It is reminded here that  $\nabla P$  is linked to  $\tau$  in the same manner that  $Q$  is linked to  $\dot{\gamma}$ . Therefore, the  $\tau(\dot{\gamma})$  plot is similar to the  $\nabla P(Q)$  plot. Also, it is remarked that for yield stress fluid, a threshold pressure exists below which there is no flow. But in the case of real fluids with apparent yield stress, there is not such a threshold pressure. Instead, there is a pressure gradient below which the flow rate is negligible (as can be observed in Figure 50).

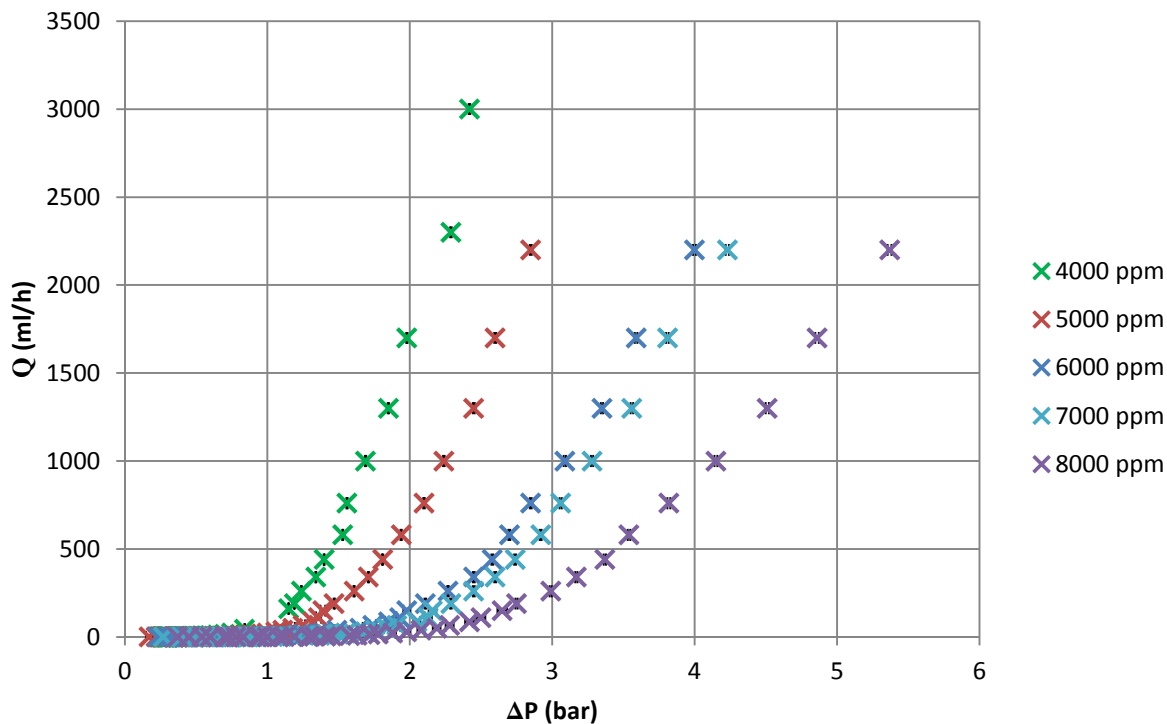


Figure 50: Experimental ( $Q_i, \nabla P_i$ ) data obtained from the injection of xanthan gum solutions with  $C_p$  ranging from 4000 to 8000 ppm through a sintered A10 silicate.  $\Delta P$  error: see subsection 4.1.4.  $Q$  error:  $\pm 0.25\%$ .

#### 4.2.5. Apparent viscosity compared to effective viscosity

As explained in subsection 2.3.3, it is possible to represent the apparent viscosity of the fluid in the porous medium by using Eqs. (2.41) and (2.42). Besides, permeability reduction  $R_k$  is usually close to 1 for xanthan gum solutions, so  $K$  is assumed to be unchanged during the polymer flow experiments. Therefore, the  $K$  used in Eqs. (2.41) and (2.42) will be taken as being the permeability to water previous to polymer from now on. Figure 51 presents the apparent and the effective viscosity for each polymer concentration as a function of shear rate, where the empirical shift parameter  $\beta$  has been taken here equal to 1.

However, the empirical value of  $\beta$  was also calculated as follows. Firstly, effective rheologies were fitted to a Carreau model by obtaining the value of  $\delta$  and the Carreau parameters  $\mu_0$ ,  $\mu_\infty$ ,  $n$  and  $\lambda$  minimizing the next sum in each case:

$$\sum_i [\tau_i - \mu(\dot{\gamma}_i)\dot{\gamma}_i]^\delta \dot{\gamma}_i^\delta \quad (4.3)$$

where  $\mu(\dot{\gamma})$  is the Carreau viscosity defined by Equation (2.15) and  $\dot{\gamma}$  and  $\tau_i$  are the steady state experimental shear stresses and the corresponding shear rates given by the rheometer. The resulting values for Carreau parameters and  $\delta$  are presented in Table 3. The use of a Carreau model instead of a Herschel-Bulkley model was motivated by the fact that, as explained in subsection 2.2.2, yield stress value cannot be measured within a finite time period. Therefore, in the scale of time used in our experiments, rheology of xanthan solutions is better represented by a strong viscosity decrease from a very high Newtonian-viscosity plateau as shear rate is increased (Carreau model), which approaches the behavior of a yield stress fluid.

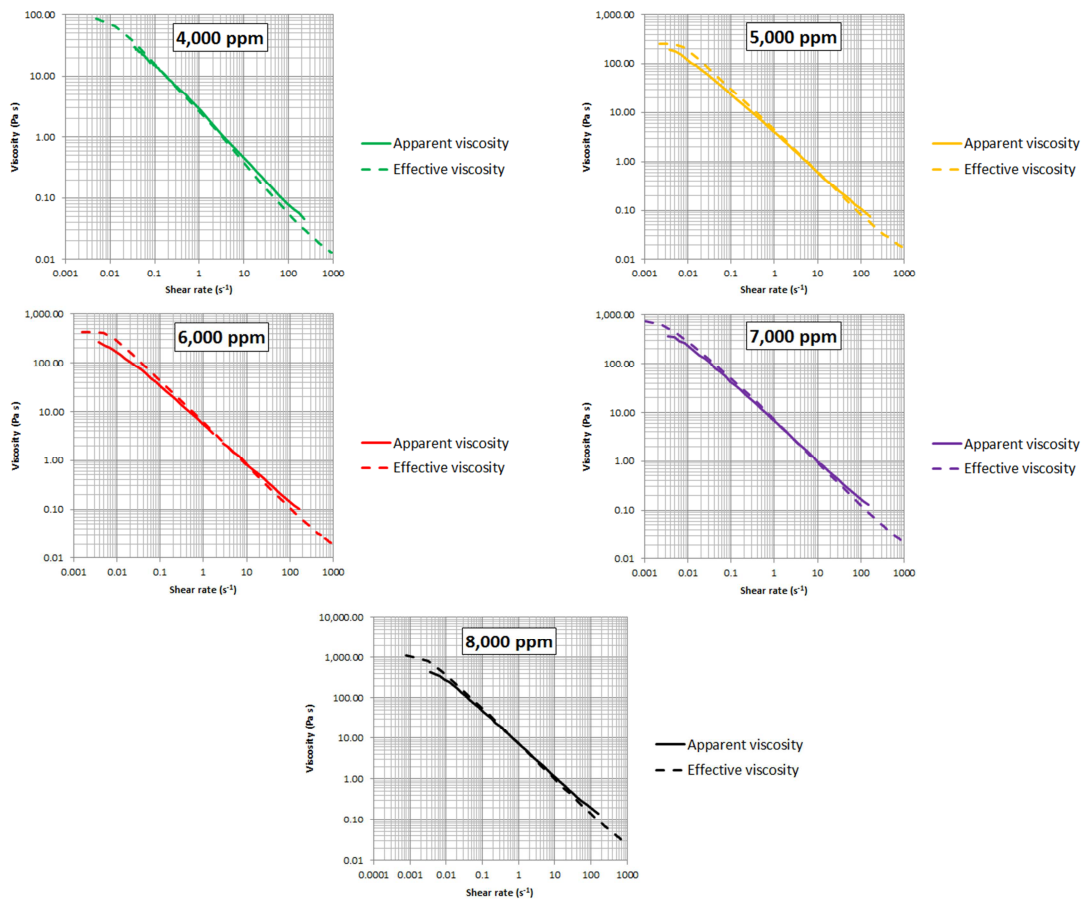


Figure 51: Apparent (in porous media) viscosity compared to effective (rheometer) viscosity for each  $C_p$ .

$C_p$ (ppm)	$\mu_0$ (Pa s)	$\mu_\infty$ (Pa s)	$\lambda$ (s)	$n$	$\delta$
4000	86.4	0.0054	60.3	0.145	0
5000	268	0.0062	109	0.124	0
6000	467	0.0067	141	0.115	0
7000	732	0.0078	181	0.109	0.43
8000	1110	0.0085	313	0.126	0

Table 3: Carreau parameters obtained for xanthan gum solutions at  $C_p$  ranging from 4000 ppm to 8000 ppm.

Secondly, the apparent rheology of the fluid in the porous medium was also fitted to a Carreau model by minimizing Eq. (4.3) with  $\dot{\gamma}_i = \frac{Q/A}{\sqrt{K\varepsilon}}$  and  $\tau_i = \frac{KVP}{\sqrt{K\varepsilon}}$ , thus obtaining the apparent Carreau parameters  $\mu_{0app}$ ,  $\mu_{\infty app}$ ,  $\lambda_{app}$ ,  $n_{app}$  (Table 4).

Finally, the value of  $\beta$  was calculated as being the one which gives the same onset of shear thinning behavior ( $1/\lambda$ ) in the rheometer and in the porous medium (Sorbie 1991). The previous condition is satisfied when  $\beta$  respects the next relationship:

$$\beta = \frac{\lambda_{app}}{\lambda} \quad (4.4)$$

$C_p$ (ppm)	$\mu_{0app}$ (Pa s)	$\mu_{\infty app}$ (Pa s)	$\lambda_{app}$ (s)	$n_{app}$
4000	33.1	0.0077	23.4	0.210
5000	198	0.012	136	0.197
6000	264	0.015	128	0.195
7000	361	0.020	130	0.177
8000	433	0.032	140	0.173

Table 4: Apparent Carreau parameters obtained for the injection of xanthan gum solutions at  $C_p$  ranging from 4,000 ppm to 8,000 ppm through A10 sintered silicates.

Consequently, the apparent rheology in the porous medium can be expresses through the modified Carreau relationship:

$$\frac{\mu_{app} - \mu_{\infty app}}{\mu_{0app} - \mu_{\infty app}} = [1 + (\lambda_{app}\dot{\gamma})^2]^{\frac{n_{app}-1}{2}} = [1 + (\lambda\beta\dot{\gamma})^2]^{\frac{n_{app}-1}{2}} \quad (4.5)$$

with  $\mu_{app} = \frac{KA\nabla P}{Q}$  and  $\dot{\gamma} = \frac{Q/A}{\sqrt{K\varepsilon}}$ . The obtained values for  $\beta$  are listed in Table 5. A comparison of the effective and apparent viscosities is displayed in Figure 52. The difference between Figure 51 and Figure 52 is that Figure 52 shows the apparent rheology using the obtained  $\beta$  whereas in Figure 51 it is assumed that  $\beta = 1$ . The main advantage of Figure 52 is that one can compare the viscosity in the porous medium to the effective viscosity for a given shear rate. Moreover, it is possible to determine “*a posteriori*” the range of shear rates experienced by the fluid in the porous medium (Table 6). Knowing this, it is henceforth possible to ensure that the scanned shear rates interval in the porous medium is similar to that in the rheometer.

$C_p$ (ppm)	$\beta$
4000	0.39
5000	1.26
6000	0.91
7000	0.72
8000	0.45

Table 5: Values of  $\beta$  corresponding to the injection of xanthan gum solutions with different  $C_p$  through A10 silicate samples.

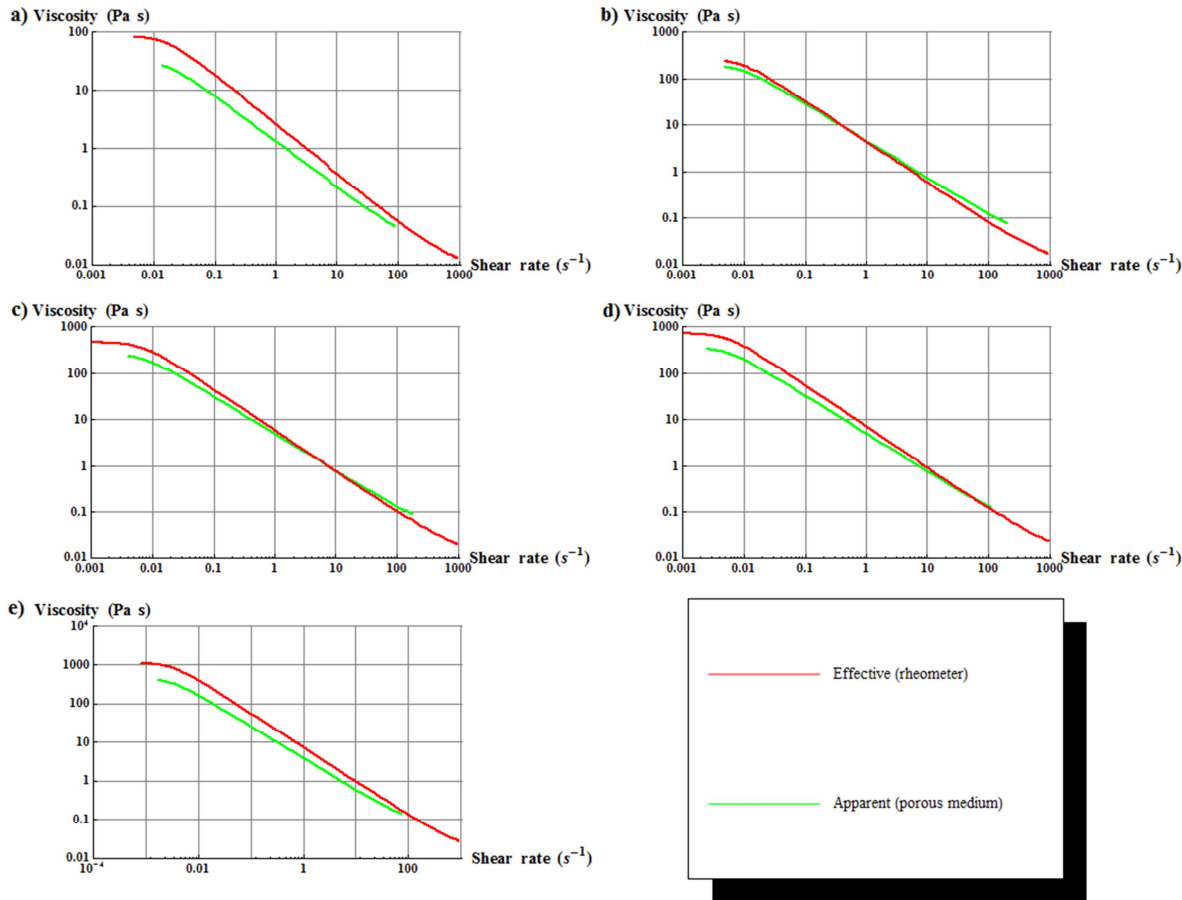


**Figure 52: Apparent (in porous media) rheology compared to effective (rheometer) rheology for each C<sub>p</sub>. The value of  $\beta$  has been taken into account to represent the apparent rheology. a) C<sub>p</sub> = 4000 ppm; b) C<sub>p</sub> = 5000 ppm; c) C<sub>p</sub> = 6000 ppm; d) C<sub>p</sub> = 7000 ppm; e) C<sub>p</sub> = 8000 ppm.**

C <sub>p</sub> (ppm)	1/λ (s)	̇γ <sub>min</sub> (s <sup>-1</sup> )	̇γ <sub>max</sub> (s <sup>-1</sup> )
4000	0.0170	0.0138	87
5000	0.0092	0.0047	206
6000	0.0071	0.0034	149
7000	0.0055	0.0025	109
8000	0.0032	0.0017	73

**Table 6: Onset of shear-thinning (1/λ), minimum (̇γ<sub>min</sub>) and maximum (̇γ<sub>max</sub>) shear rate in the porous medium for each concentration.**

In Table 3, one can observe that the Newtonian viscosities of xanthan gum solutions increase with C<sub>p</sub>, while the onset of shear-thinning behavior (1/λ) decreases. Besides, except for 8000 ppm, n decreases with C<sub>p</sub> meaning that the shear-thinning behavior is more pronounced at higher C<sub>p</sub> as expected. Similar comments may also be made with respect to apparent Newtonian viscosities and n listed in Table 4.

Nevertheless, it is also remarked that n<sub>app</sub> > n, which means that the apparent shear-thinning behavior in porous media is less pronounced than the effective one as can be seen in Figure 52. These differences may be explained by the presence of a depleted layer which causes a reduction of apparent viscosity whose effect is more important at low flow rates, as presented in subsection 2.3.3.

It is noted as well (Table 6) that the single case with  $\beta > 1$  corresponds to the highest  $\dot{\gamma}_{\max}$ . Also,  $\beta$  is proved to be proportional to  $\dot{\gamma}_{\max}$  in the case of this porous medium, as shown in Figure 53. That suggests that the value of  $\beta$  is strongly dependent on the range of flow rates imposed during the experiments. The only experiment that does not respect that proportionality is the one with  $C_p = 4000$  ppm, for which  $\dot{\gamma}_{\min}$  is much higher because the lowest Q were not imposed as explained before.

In Chapter 2, we saw that  $\beta$  is generally linked to pore geometry in the literature. However, it has to be pointed out that the range of Q imposed during the experiments is considerably larger in the present work than in other works related to the injection of polymer solutions through porous media. As a consequence, the influence of the range of Q on  $\beta$  is best evaluated here.

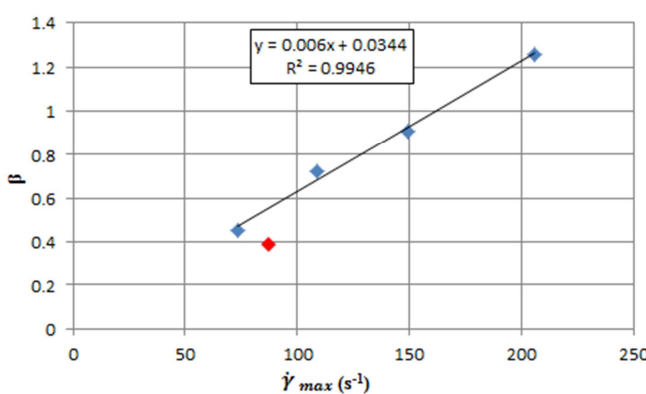


Figure 53: Value of  $\beta$  compared to the maximum apparent shear rate in each case, showing proportionality.

#### 4.2.6. PSDs obtained with YSM

The method presented in Section 3.2 was applied to the  $(Q_i, \nabla P_i)$  raw data resulting from the injection of the xanthan gum solutions through the A10 sintered silicate porous medium following the same procedure as in preliminary experiments. It is remarked that similar values of  $\alpha^*$  were obtained with E-criterion for all polymer concentrations as shown in Table 7 ( $\alpha^*$  is comprised between 1.2 and 1.4 for  $4000 \text{ ppm} \leq C_p \leq 8000 \text{ ppm}$ ). The resulting PSDs expressed in terms of relative volume  $p_v(r_i)$  of pore classes of representative radii  $r_i$  are displayed in Figure 54 and they are compared with the PSD deduced from MIP in Figure 55. For comparison, the represented pore size classes of YSM have been regrouped in Figure 55 in order to match those of MIP.

Even if the PSDs are quite similar in all cases, one can realize that the more the polymer concentration is high (except for 8000 ppm), the larger is the pore size corresponding to the peak of the PSD and the lesser is the deviation of the obtained PSD from that of MIP. As explained before, more reliable PSDs are expected for higher concentrations due to the better approximation to a yield stress behavior. Some of the reasons why 8000 ppm doesn't respect this general tendency may be: 1) pore plugging which is more likely to happen at high  $C_p$  and will introduce additional pressure drops which would be interpreted as smaller pore radii 2) the difficulty in preparing homogeneous concentrated solutions, 3) weak gel transition

(Carnali 1991). Consequently,  $C_p = 7000$  ppm was selected for the experiments presented in the next section, as this concentration it is high enough to approach the yield stress behavior without presenting the concerns observed for  $C_p = 8000$  ppm. It is also noted that the PSDs obtained for  $C_p = 7000$  ppm and  $C_p = 6000$  ppm are different from those obtained in the preliminary experiments. However, it has to be taken into account that the experimental procedure was different concerning the fluid preparation and the imposition of flow rates. In effect, even if the PSD obtained for  $C_p = 7000$  ppm and  $C_p = 6000$  in the preliminary experiments were closer to the one deduced from MIP, the results presented in this section are expected to be more reliable because of the improved procedure used here. In any way, it is remarked that PSDs obtained by YSM are quite close to those obtained by MIP for this material, even if strictly speaking, the quality of the PSD should not be assessed through its agreement with that deduced from MIP.

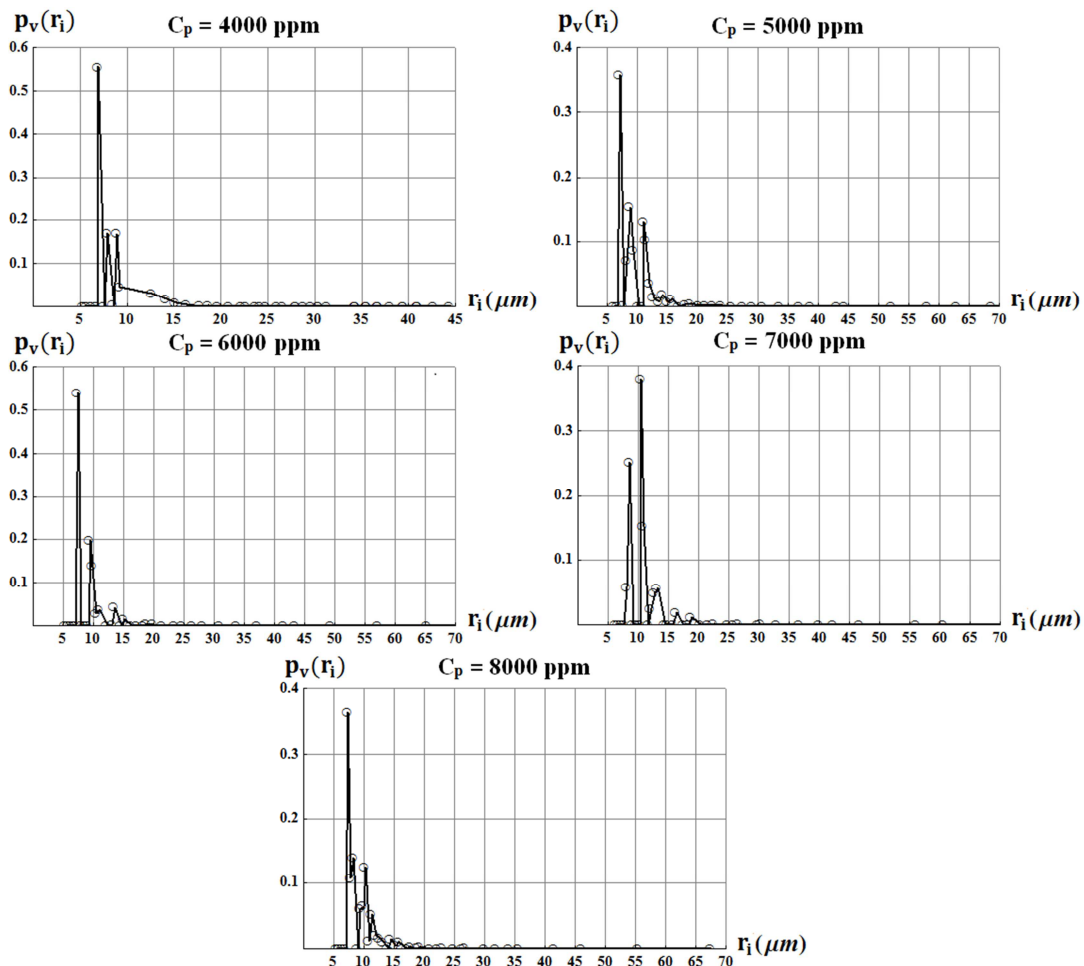


Figure 54: PSDs obtained by applying YSM to  $Q(\nabla P)$  measures resulting from the injection of 5 xanthan gum solutions with different  $C_p$  through analogous samples of A10 sintered silicate.

$C_p$ (ppm)	$\alpha^*$
4000	1.4
5000	1.3
6000	1.2
7000	1.2
8000	1.3

Table 7:  $\alpha^*$  obtained for each  $C_p$ .

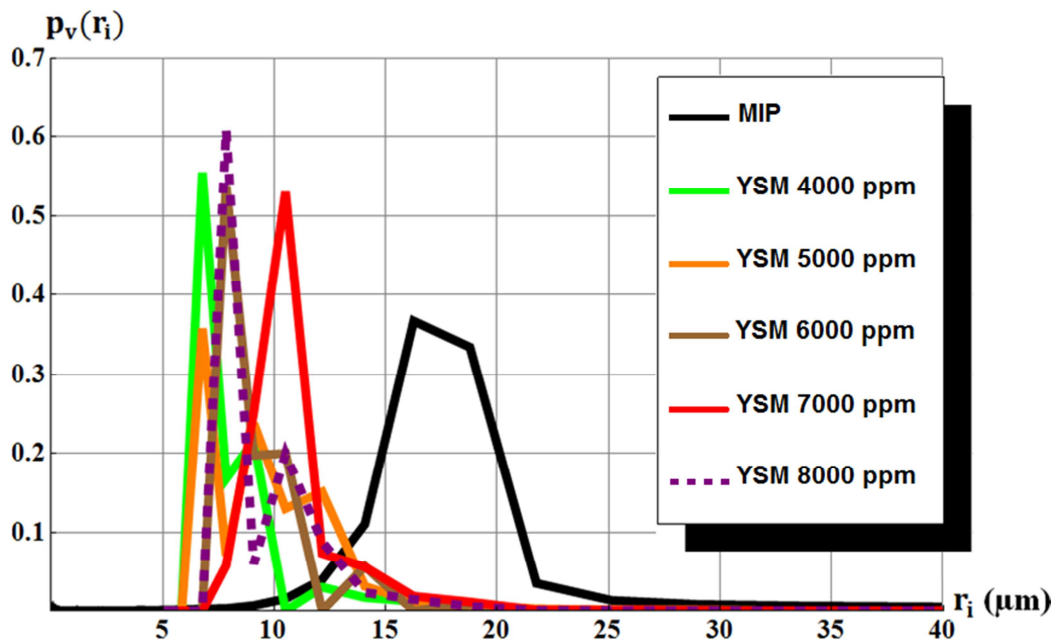


Figure 55: PSDs obtained with YSM compared with the PSD obtained with MIP for the analyzed A10 sintered silicate.

### **4.3. Sensitivity of the obtained PSD to the type of porous medium**

Up to now, only results for a single material (sintered silicate porous medium) have been presented while the concentration of the xanthan solutions has been changed. In this section the effect of the type of porous medium and its permeability on the quality of the PSDs obtained through YSM will be assessed. To do that, xanthan gum solutions with the same polymer concentration were injected through different types of porous media.

#### **4.3.1. Materials**

In these experiments, the injected fluids were xanthan gum solutions prepared by dissolving an amount of xanthan gum powder (Satiaxane CX 930, Arlès agroalimentaire, France) in de-ionized and filtered water containing 400 ppm of  $\text{NaN}_3$  (Sodium Azide, Sigma-Aldrich, Riedel-de Haën Trademark) as a bactericide. Two xanthan gum solutions with polymer concentration ( $C_p$ ) of 7000 ppm were prepared using an overhead stirrer with blade impeller:

- Solution 1:  $C_p = 7000 \text{ ppm}$ ,  $\text{NaCl}$  concentration ( $C_s$ ) = 0 ppm.
- Solution 2:  $C_p = 7000 \text{ ppm}$ ,  $\text{NaCl}$  concentration ( $C_s$ ) = 5000 ppm.

It is noted that Solution 2 contained salt because it was to be injected in natural clayey porous media, and that should avoid swelling of clays and reinforce the granular cohesion of the sample. See Baudracco and Aoubouazza (1995) for a study on the effect of clay swelling on the permeability of Berea and Vosges sandstones. The pH of these solutions was very close to 7 in all cases. During their preparation, the xanthan powders were progressively added to the water or brine while stirring. Once the powder was completely added, the solution was kept under moderate stirring (500 rpm) for at least 12 hours. After that, the fluid was stocked at

low temperature (approximately 5°C) for 12 hours and then degassed with a vacuum pump (Alcatel 2004A) equipped with a vapor trap.

In these experiments, 5 cylindrical samples of different porous media were analysed (see Figure 56):

- Sample 1: Aerolith®10 (PALL Corporation, USA).
- Sample 2: Aerolith®10 (PALL Corporation, USA).
- Sample 3: Bentheimer Sandstone (Kocurek Industries, Inc., USA).
- Sample 4: Castlegate Sandstone (Kocurek Industries, Inc., USA).
- Sample 5: Berea Sandstone (Cleveland Quarries, USA).

The measured porosities and permeabilities as well as the lengths (L) and diameters (D) of these 5 cylindrical cores are given in Table 8.

Sample	K (mD)	$\epsilon$	L (cm)	D (cm)
1	9000	0.45	10	5
2	2400	0.40	5	3.8
3	2200	0.25	5	3.8
4	750	0.25	5	3.8
5	38	0.22	5	3.8

Table 8: measured porosities, permeabilities and dimensions of the cores.

Solution 1 was injected in Sample 1 while Solution 2 was injected in Samples 2 to 5. It has to be noted here that while the experiment with Sample 1 was carried out at the Institute of Mechanics and Engineering of Bordeaux (TREFLE Department), the experiments with the others samples (natural porous media) were performed at the CSTJF (*Centre Scientifique et Technique Jean-Féger*) of TOTAL S.A. (Pau, France) due to the specific equipment needed, so the devices and instruments used in these experiments were not the same in all cases as will be specified later.

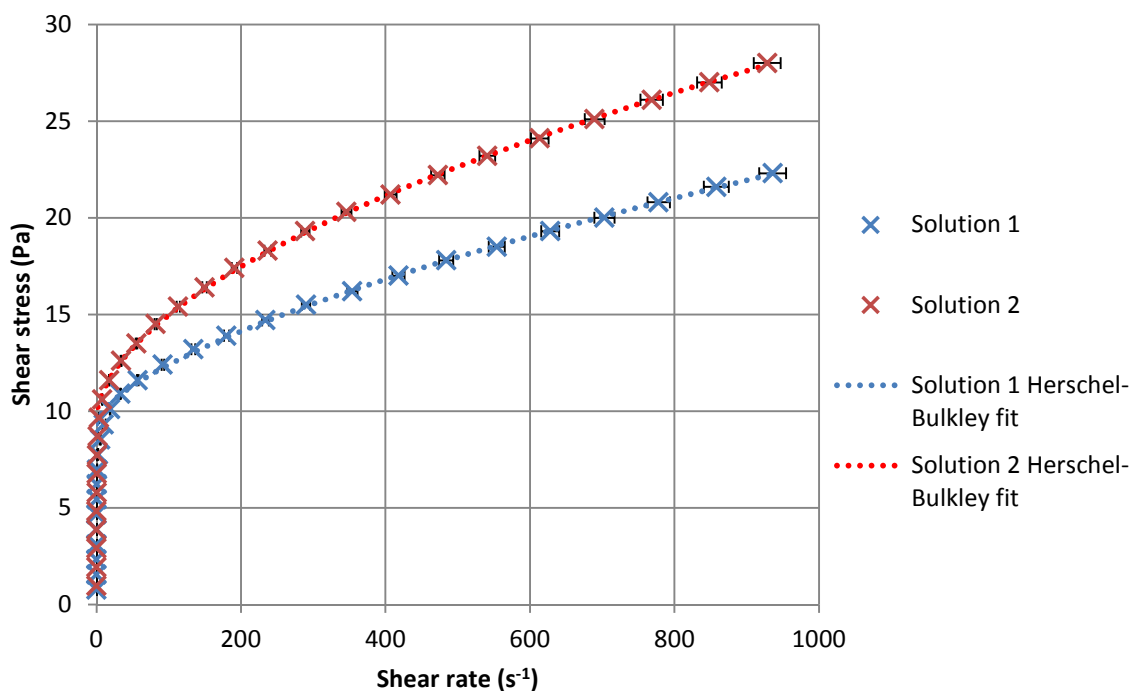


Figure 56: Cores corresponding to the 5 porous media analyzed in this study. From left to right in the first row: a) A10 sintered silicate; b) less permeable and porous A10 sintered silicate; c) Bentheimer sandstone; d) Castlegate sandstone; e) Berea sandstone.

### **4.3.2. Rheograms of the injected fluids**

The effective rheology of Solution 1 was characterized by means of a stress-controlled rheometer (ARG2 from TA Instruments, France) equipped with cone-plate geometry and following the procedure described in 4.2.2. However, in the case of Solution 2 a different stress-controlled rheometer (MCR 302 from Anton Paar) equipped with double-gap geometry was used. Given that the injection of Solution 2 in the porous media were to be made at  $18^{\circ}\text{C} \pm 1$ , the rheological measurements were taken at  $18^{\circ}\text{C}$ . The imposed shear stresses ranged linearly from 0 to the one producing a shear rate of approximately  $1000 \text{ s}^{-1}$ . Once again, a delay of 5 minutes was observed after loading the sample in the rheometer (before starting the measurements). The time allowed for each measure decreased linearly with stress from 100 seconds to 10 seconds. An important remark concerning the use of double-gap geometry with very viscous fluids is that the fluid should be loaded by using an appropriate needle in order to ensure that the liquid fills the whole gap. It should be done carefully and slowly so as to avoid polymer degradation. Even if this remark might seem trivial, we may put forward that incorrectly loading of the fluid may result in completely erroneous measures of viscosity.

The obtained rheograms and the corresponding Herschel-Bulkley fits are presented in Figure 57. Also, the obtained Herschel-Bulkley parameters for each solution are listed in Table 9. It can be remarked that Solution 2, which contains NaCl, is more viscous at high shear rates (Figure 58). Even if salted solutions are expected to be less viscous, that difference is not important for us, forasmuch as both solutions have an apparent yield stress. This difference in viscosity may be due in part to the different preparation of both solutions (e.g. different vacuum pumps) and the slightly different temperature during the measurements.



**Figure 57: Rheograms of the 2 solutions used in these experiments and their Herschel-Bulkley fits.**

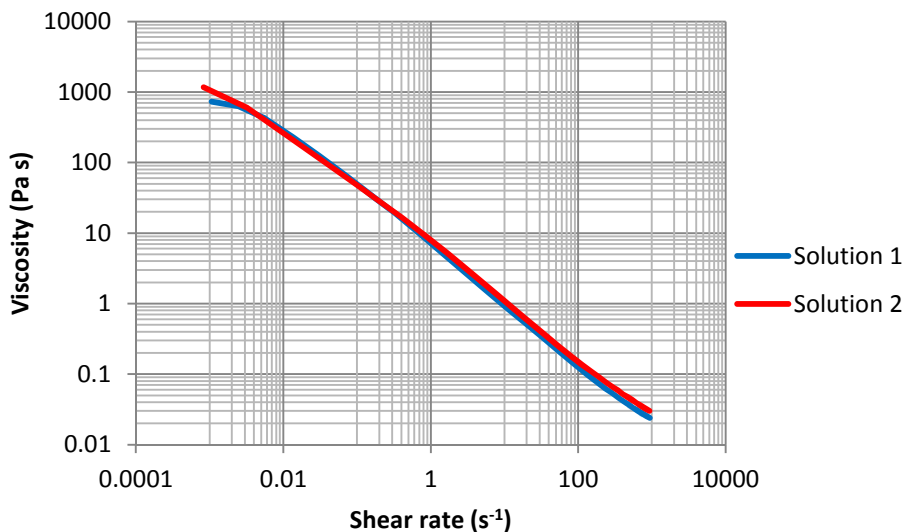


Figure 58: Viscosity as a function of shear rate for Solutions 1 ( $C_s = 0$  ppm) and 2 ( $C_s = 5000$  ppm).

Solution	$\tau_0$ (Pa)	k (Pa s <sup>n</sup> )	n
1	9.35	0.158	0.643
2	9.61	0.430	0.549

Table 9: Herschel-Bulkley parameters corresponding to Solutions 1 and 2.

On the other hand, one may wonder about the homogeneity of these solutions. Three samples of Solution 2 were extracted from its container at different depths. These three samples were rheologically characterized with the rheometer and the obtained results are compared in Figure 59. In this figure, all data collapse on the same master curve, indicating that the solution was homogeneous.

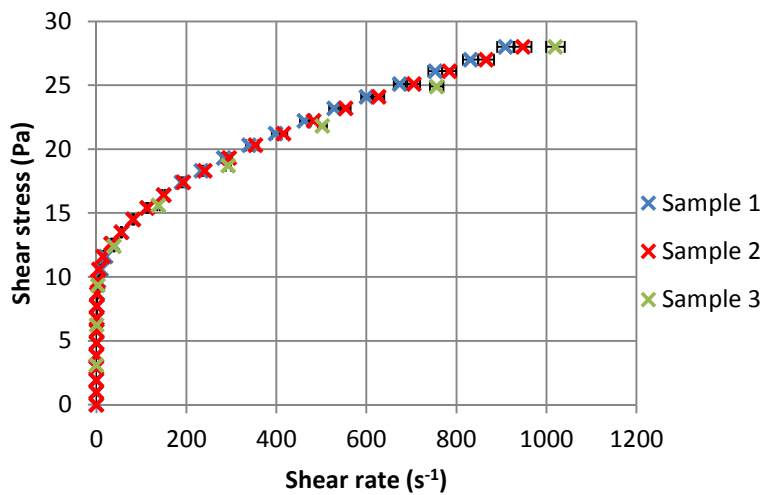


Figure 59: Rheograms corresponding to three samples of Solution 2. The samples have been extracted at different depths in the container so as to evaluate the homogeneity of the fluid.

Finally, thixotropic effects were evaluated by measuring  $\tau(\dot{\gamma})$  firstly through imposition of ascending shear stresses and then through imposition of descending shear stresses. As can be observed in Figure 60, no noticeable thixotropy is observed for this fluid.

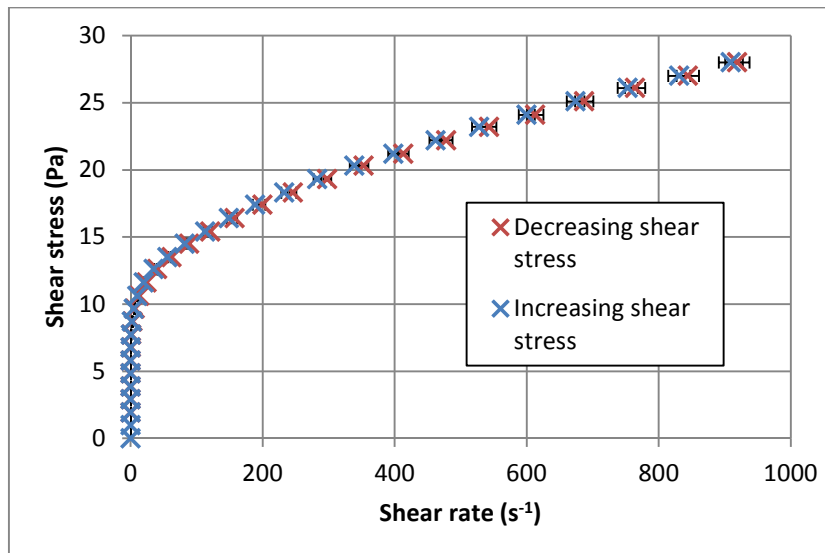


Figure 60: Rheograms of Solution 2 corresponding to ascending and descending imposition of shear stresses. They are used to verify that the fluid does not present significant thixotropy.

#### **4.3.3. Experimental setup and procedure**

In the case of Sample 1, the experimental setup is the same as the one presented in Section 4.2.

For Samples 2 to 5, some modifications were included in the experimental setup. These modifications were mostly motivated by the higher pressures induced by the low permeabilities of these samples. In fact, the classic resin-fiberglass setup would leak and the syringe pump would not be able to work at high pressures. For that reasons, the sample was mounted in a Hassler core holder (Vinci Technologies, France) instead of the resin-fiberglass setup. Besides, a robust piston pump was used in these experiments (Composites & Technologies, T-Pump v 1.9.). The main advantages of this pump are the fact that it can work at the high pressures required for injection in less permeable media and the greater volume of fluid that can be continuously injected without stopping to reload with respect to the syringe pump. Also, metallic tubing was used in the high pressure zones for safety reasons. Furthermore, a density meter (Anton Paar, DMA 512) was connected to the outlet of the porous medium to measure the density of the outgoing fluid during saturation of the sample with xanthan solution. A fraction collector (Gilson, FC 203B fraction collector) was also installed downstream of the density meter in order to collect samples for subsequent measurements with a rheometer (Figure 61). These density and viscosity measurements of the effluent will be presented in the next section. The preparation of the fluids was the same as in the previous experiments (subsection 4.2.3), apart for the use of a different vacuum pump (Alcatel 2004A) for the degassing step.

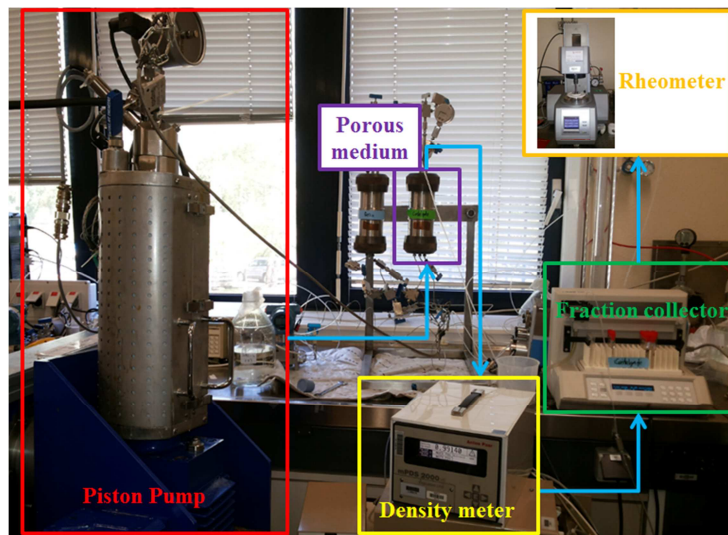


Figure 61: Experimental setup used during saturation with xanthan gum solutions.

Concerning the experimental procedure for Samples 2 to 5, the first step consisted in mounting the sample in the Hassler core holder. The sample was inserted into a Viton sleeve and two metallic grids were put at both ends of the core so as to prevent detachment of grains. After that, the Viton sleeve containing the core and the grids was mounted in the core holder and confined with pressurized brine (5000 ppm NaCl) surrounding the sleeve in order to avoid lateral leaks. In our experiments, the confinement pressure was 20 bars, that was superior to the maximum pressure loss along the porous sample during the experiment and the continuity of that confinement was ensured by a Gilson 307 piston pump.

Once the sample was mounted and confined, it was outgassed using a vacuum pump (Alcatel 2004A) instead of saturating the sample with CO<sub>2</sub>. Then, when a strong vacuum was reached, the core holder was connected to a graduated burette containing degassed brine (5000 ppm NaCl) prepared with filtered water so as to saturate the sample and then determine its porosity. The brine-saturated porous medium was then kept at rest during approximately 12 hours. After that, the permeability to brine was measured.

The next step consisted in injecting 3 pore volumes of xanthan gum solution with a flow rate corresponding to Pe = 2000 (intermediate flow rate) followed by a pore volume at the highest flow rate to be imposed during the experiments (1000 ml/h). It is reminded here that D<sub>c</sub> is approximately  $2.5 \cdot 10^{-8}$  cm<sup>2</sup>/s for calculation of the flow rate corresponding to Pe = 2000 (see subsection 4.1.3). The density and viscosity of the outgoing fluid during the saturation of the porous medium with xanthan solution were continuously measured (Figure 61), as will be presented in the next section. The core holder was placed vertically during the saturation and the xanthan solution (more dense than the brine) was injected from the bottom. Once saturated with xanthan solution, the porous medium was kept at rest during at least 12 hours.

Then, the Q(ΔP) measurements were carried out with the core holder in horizontal position (Figure 62). The imposed flow rate was steeply **decreased** and the corresponding pressure drops were measured at the steady state with a pressure sensor (Rosemount 3051 Pressure

Transmitter). The time allowed for each measurement was optimized in order to minimize the duration of the experiment, hence reducing polymer retention in porous media while attaining equilibrium pressures. The range of imposed flow rates was the same for all samples (1000 ml/h to 0.01 ml/h) and the temperature of the lab was kept constant at  $T = 18^\circ\text{C} \pm 1$  during all the experiments.

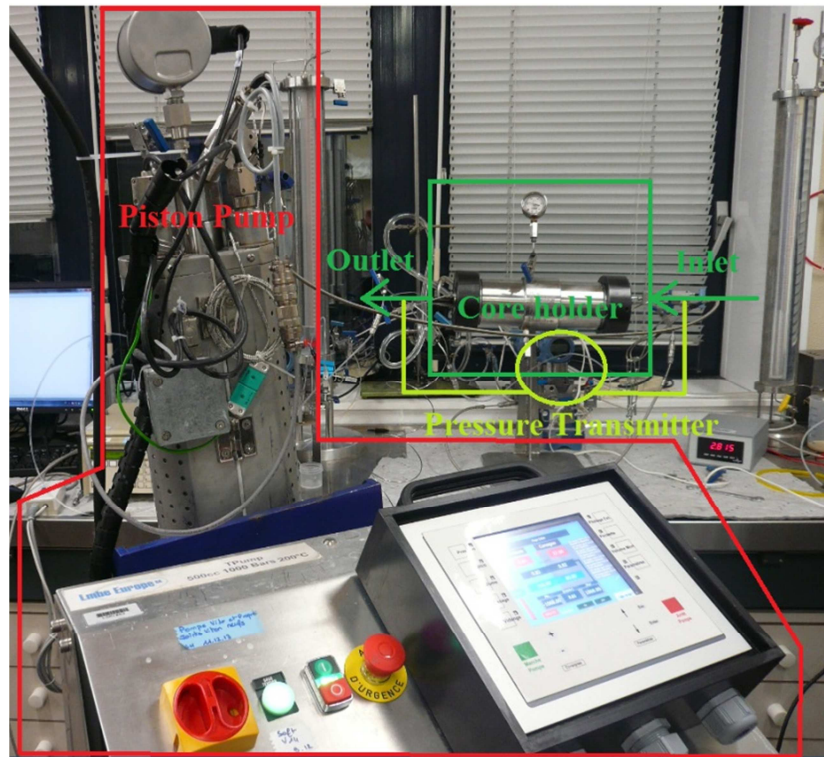


Figure 62: Experimental setup used for the  $Q(\nabla P)$  measurements.

#### 4.3.4. Measurements of pressure gradient as a function of flow rate

A set of  $N+1$  ( $Q_i, \nabla P_i$ ) raw data were collected in each experiment (Annex A) with  $N+1$  ranging from 37 to 40. It was decided to impose the same range of flow rates in all experiments (except for Sample 1 whose diameter was 1.3 times greater). This range of flow rates was from 1000 ml/h to 0.01 ml/h, i.e. the largest technically allowed range. Figure 63 shows the results obtained for each rock sample. It is noted that, apart from Sample 2, the less the material is permeable, the more the pressure loss is important for a given flow rate. Figure 64 shows the same data in a log-log scale in order to allow a better visualization of the low-flow-rates region. Some deviations with respect to the general tendency are observed for the measures at low flow rates. Such deviations are explained in part by the fact that while for Herschel-Bulkley fluids  $Q$  is zero below a minimum pressure gradient due to infinity viscosity below the yield stress, for real fluids with apparent yield stress the behavior is not so abrupt as viscosity tends to a Newtonian plateau at low flow rates. Moreover, other phenomena have been reported at these low flow rates, as will be presented in the next section.

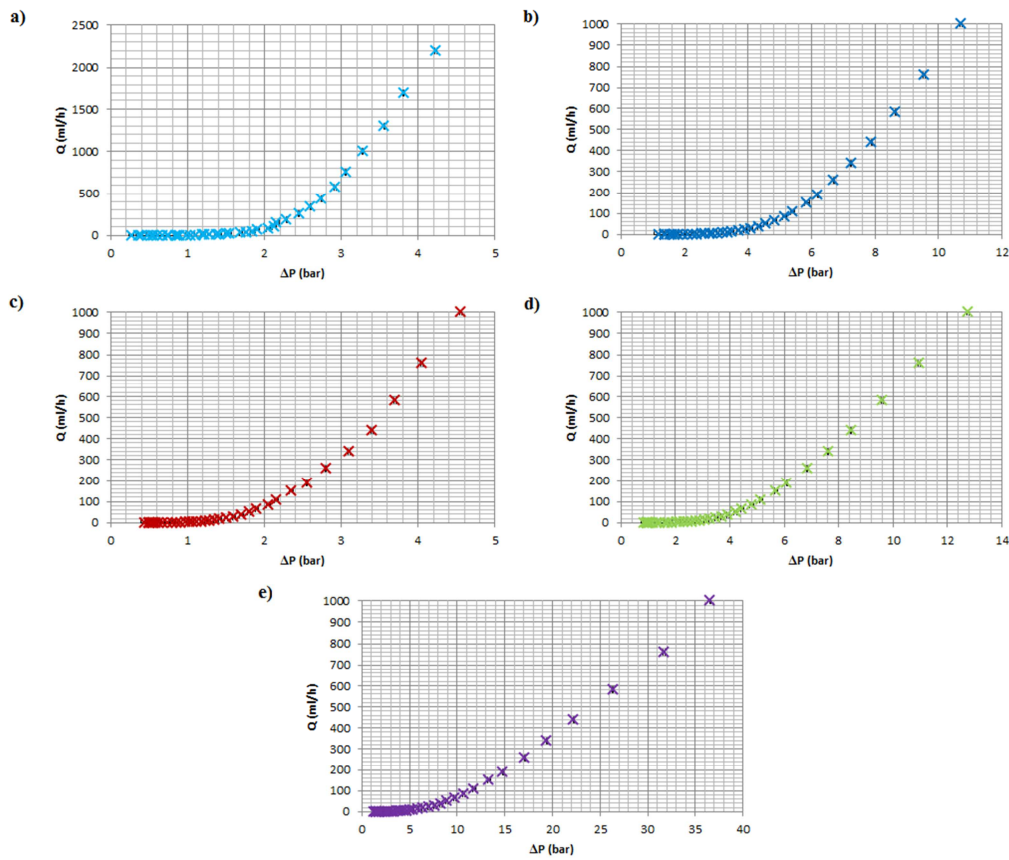


Figure 63: Experimental ( $Q_i$ ,  $\Delta P_i$ ) data obtained from the injection of a) Solution 1 through Sample 1; Solution 2 through b) Sample 2; c) Sample 3; d) Sample 4; e) Sample 5.  $\nabla P$  error:  $\pm 0.25\%$  for  $Q > 150$  ml/h,  $\pm 1.25\%$  for  $150 \geq Q > 0.62$  ml/h,  $\pm 12\%$  for  $Q \leq 0.62$  ml/h. Q error :  $\pm 0.25\%$ .

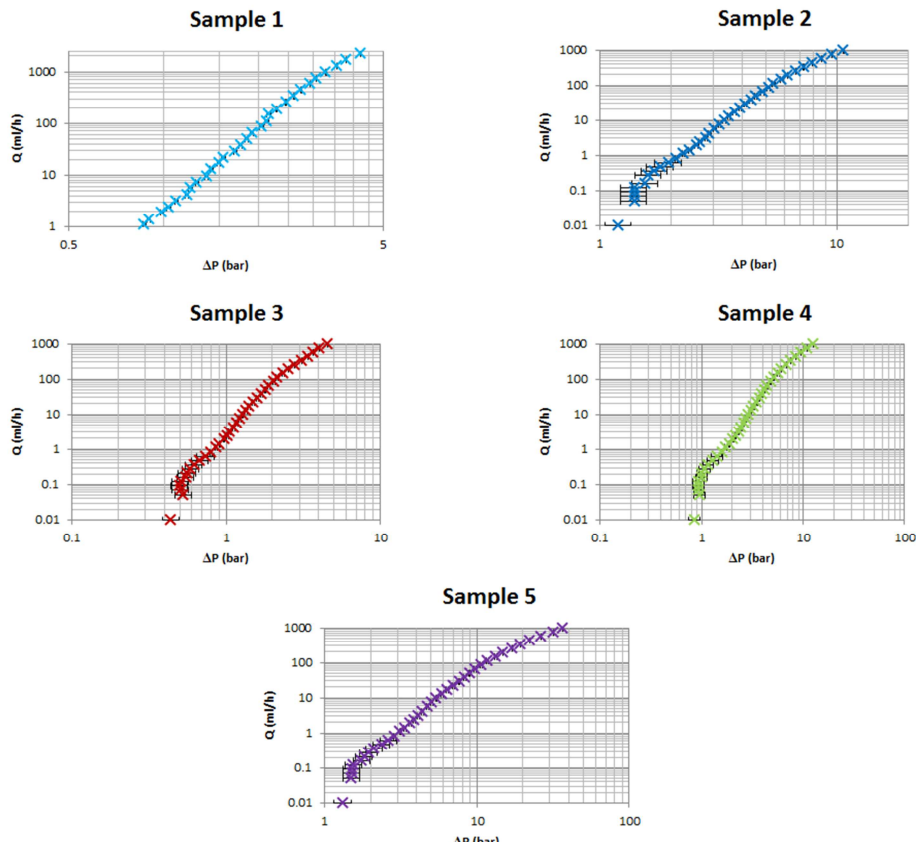


Figure 64: Experimental ( $Q_i$ ,  $\nabla P_i$ ) data.  $\nabla P$  error:  $\pm 0.25\%$  for  $Q > 150$  ml/h,  $\pm 1.25\%$  for  $150 \geq Q > 0.62$  ml/h,  $\pm 12\%$  for  $Q \leq 0.62$  ml/h. Log-log scale.

### **4.3.5. Apparent viscosity compared to effective viscosity**

Following the same procedure as in subsection 4.2.5, the apparent and effective viscosities of the yield stress fluids injected in each porous medium are represented in Figure 65 taking  $\beta = 1$ . The Carreau parameters corresponding to the effective and apparent viscosities of both solutions are listed in Table 10 and Table 11. Moreover, the calculated values of  $\beta$  giving the same critical shear rate for the shear thinning onset are presented in Table 12. From Table 10 one can observe that Solution 2 has greater Newtonian plateau viscosities and  $n$  index. This means that it is more viscous, as already pointed out, and slightly less shear-thinning than Solution 1.

In all cases,  $n_{app}$  is greater than  $n$  so the apparent shear-thinning behavior is less pronounced in the porous media than in the rheometer. These differences are due to apparent wall slip generated by the presence of a depleted layer close to pore walls, as explained in subsection 4.2.5. Besides, the two samples with  $\beta < 1$  (Samples 2 and 3) are also the only ones for which  $\mu_0 < \mu_{0app}$ . Moreover,  $\mu_\infty < \mu_{\infty app}$  in all cases except for Sample 5. In fact, Sample 5 is the less permeable medium and the only one for whom the Newtonian plateau is almost attained at the highest flow rates imposed during the experiments. It is highlighted that previous works in the literature stated that  $\beta > 1$  in sandstone cores (Sorbie 1991). However, the range of shear rates imposed in the present experiments is unusually large, and that seems to have an impact on the value of  $\beta$ . Also, the polymer solutions have an unusually high concentration and viscosity as mentioned above.

Solution	$\mu_0$ (Pa s)	$\mu_\infty$ (Pa s)	$\lambda$ (s)	$n$	$\delta$
1	732	0.0078	181	0.109	0.43
2	1170	0.0092	347	0.138	0.26

Table 10: Carreau parameters of the solutions injected through the analyzed porous media.

Sample	$\mu_{0app}$ (Pa s)	$\mu_{\infty app}$ (Pa s)	$\lambda_{app}$ (s)	$n_{app}$
1	361	0.020	130	0.177
2	2350	0.064	510	0.175
3	2030	0.024	1450	0.193
4	568	0.038	240	0.200
5	142	0.0063	286	0.249

Table 11: Apparent Carreau parameters obtained for the injection of xanthan gum solutions through the different porous media used in the present study.

Sample	$\beta$
1	0.72
2	1.47
3	4.18
4	0.69
5	0.83

Table 12: Values of  $\beta$  corresponding to the injection of xanthan gum solutions at  $C_p = 7000$  ppm through the analyzed porous media.

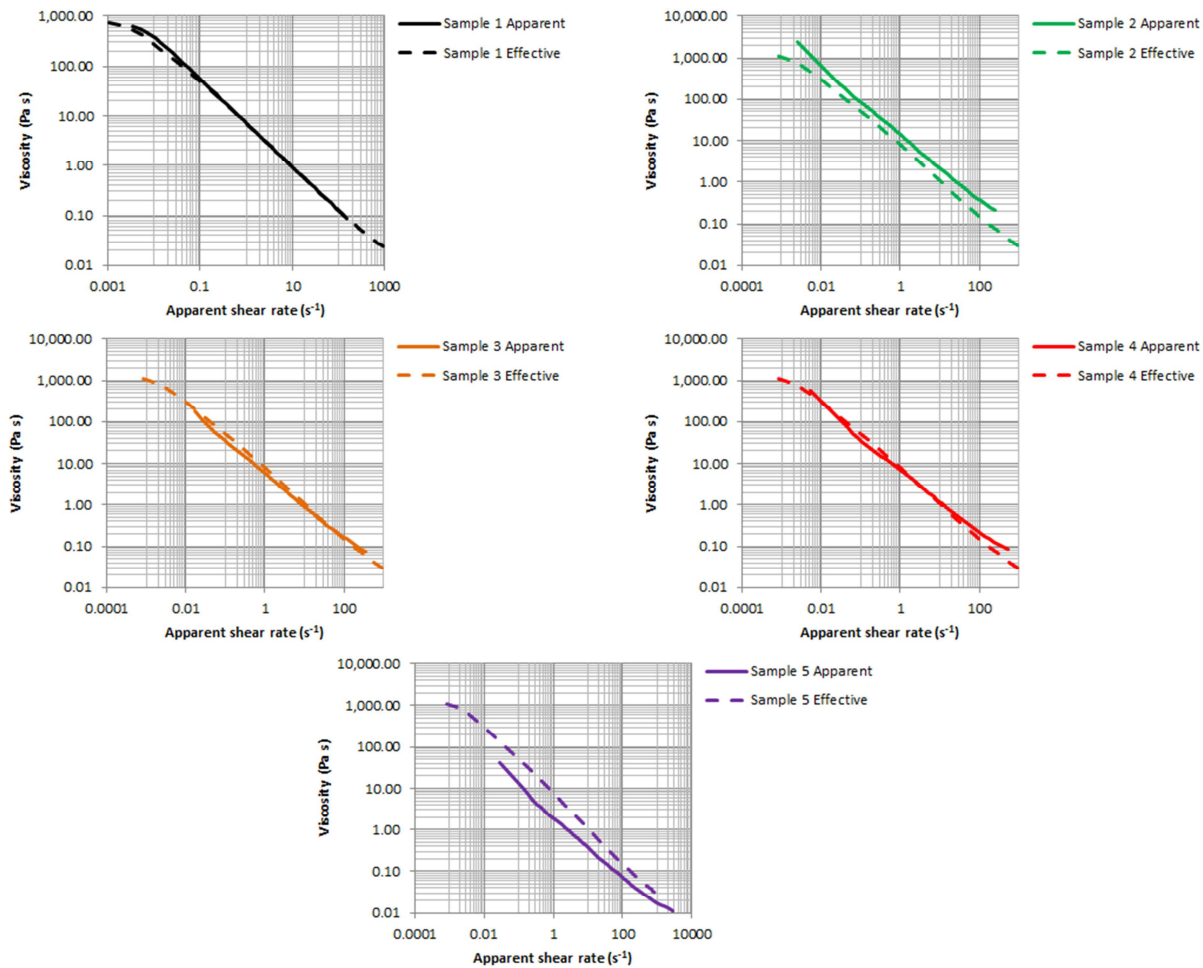


**Figure 65:** Apparent (in porous media) viscosity compared to effective (rheometer) viscosity for each core.

The apparent viscosities using the calculated  $\beta$  are compared to the effective viscosities in Figure 66. Also, the range of apparent shear rates in each case is listed together with the onset of shear-thinning in Table 13. As in the preceding experiments, it is henceforth possible to ensure that the scanned shear rates interval in the porous medium is similar to that in the rheometer.

#### **4.3.6. PSDs obtained with YSM**

The method presented in Section 3.2 was applied to the  $(Q_i, \nabla P_i)$  raw data presented in Figure 63 resulting from the injection of Solution 1 through Sample 1 and from the injection of Solution 2 through samples 2 to 5. The procedure was the same as in the preliminary experiments. The corresponding PSDs expressed in terms of relative volume of pore classes of representative radii  $r_i$ ,  $p_v(r_i)$ , are displayed in Figure 67. Besides, the PSDs obtained in the 5 cases are regrouped in Figure 68 for comparison. Also, the corresponding  $\alpha^*$  and the average pore radius predicted by Eq. (2.2) are listed in Table 14. It is remarked that, apart from Sample 2, these PSDs are coherently arranged with respect to such average pore radius (Figure 68). Moreover,  $\alpha^*$  is not permeability-dependent as can be seen in Table 14.

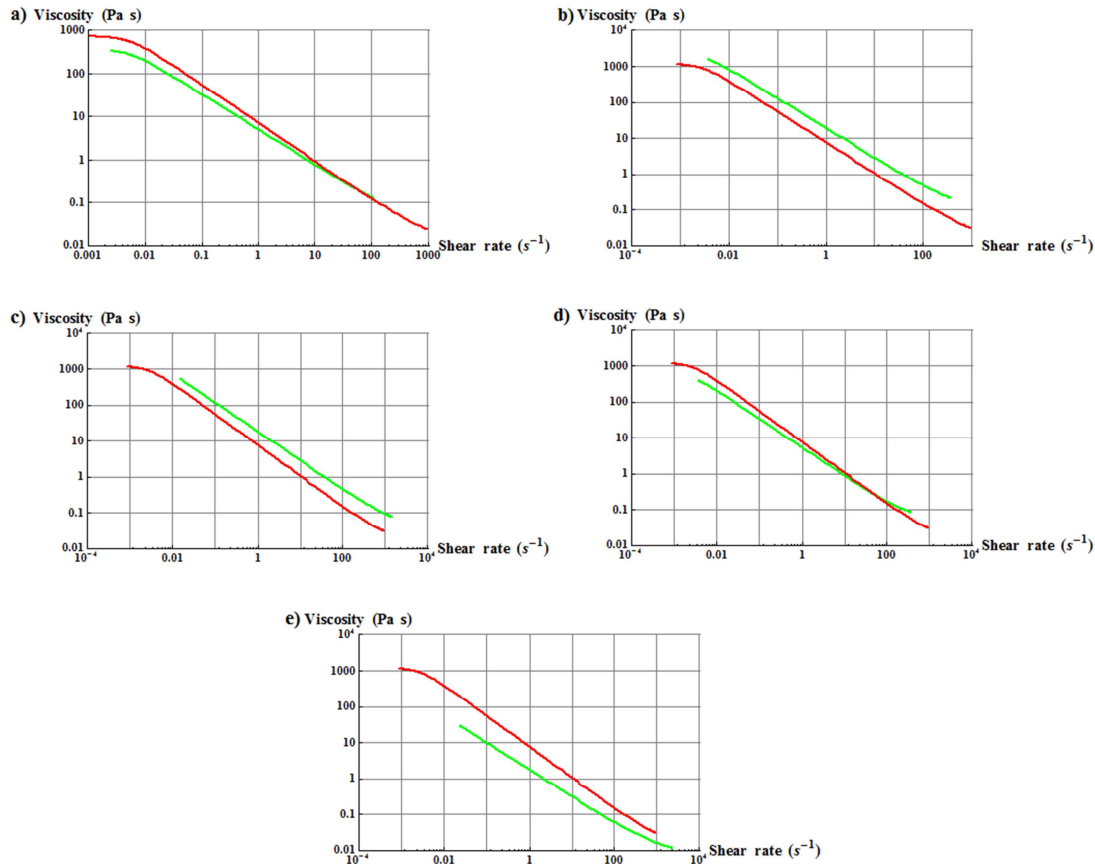


**Figure 66:** Effective (red) rheology and apparent (green) corresponding to the injection experiments for a) Sample 1; b) Sample 2; c) Sample 3; d) Sample 4; e) Sample 5.

Sample	$1/\lambda$ (s)	$\dot{\gamma}_{\min}$ ( $s^{-1}$ )	$\dot{\gamma}_{\max}$ ( $s^{-1}$ )
1	0.00553	0.00247	109
2	0.00289	0.00363	363
3	0.00289	0.0143	1430
4	0.00289	0.00365	365
5	0.00289	0.0232	2320

**Table 13:** Onset of shear-thinning ( $1/\lambda$ ), minimum ( $\dot{\gamma}_{\min}$ ) and maximum ( $\dot{\gamma}_{\max}$ ) apparent shear rate for each porous medium.

Sample	$\alpha^*$	$\bar{r}$ (Eq. 2.2) ( $\mu m$ )
1	1.2	12.6
2	1.2	6.9
3	1.3	8.4
4	1.2	4.9
5	1.3	1.2

**Table 14:** Obtained  $\alpha^*$  and  $\bar{r}$  from Eq. (2.2).

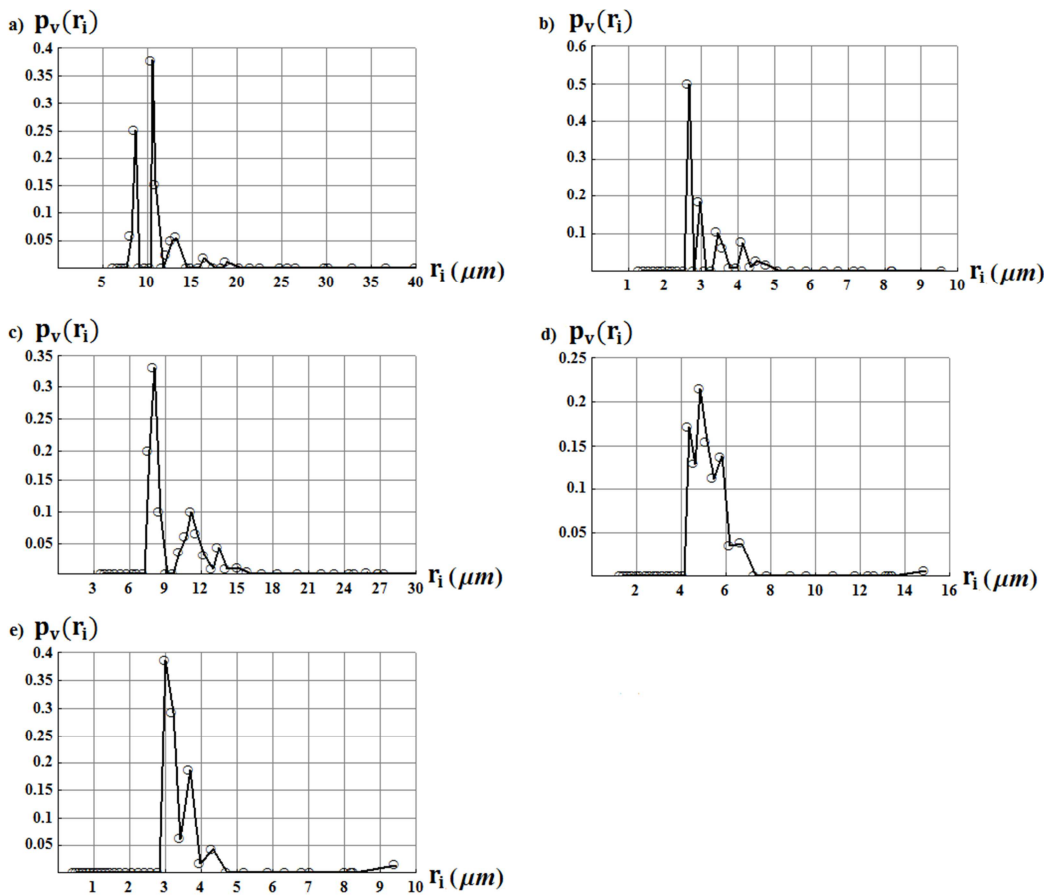


Figure 67: PSDs obtained with YSM. a)Sample 1; b)Sample 2; c)Sample 3; d)Sample4; e)Sample 5.

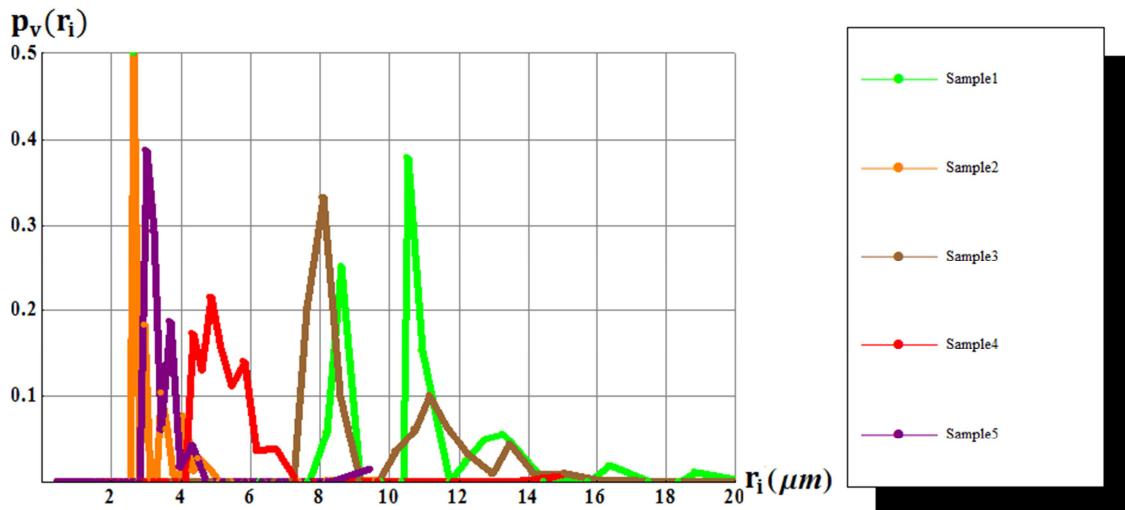


Figure 68: Comparison of the PSDs obtained with YSM.

#### 4.4. Complementary laboratory measurements

Several additional measurements were conducted in parallel to those presented in the preceding section. The goal of these complementary tests is to provide evidence about the importance of polymer retention, mechanical degradation and adsorption of the molecules in the porous media. Firstly, the BTC (breakthrough curve) resulting from the injection of brines

with different concentrations through the porous medium is compared to that coming from injection of xanthan solutions. By this way, and ignoring the possible plugging in the very small pores, comparison of such BTC may give information about polymer adsorption and other possible phenomena. Moreover, the viscosity of the effluent during saturation and at the end of experiments is presented so as to draw additional conclusions on the polymer retention and polymer mechanical degradation.

#### **4.4.1. Dispersion tests in porous media**

After saturation of Samples 2 to 5 with brine and before their saturation with xanthan gum solution, a dispersion test was performed in order to characterize the dispersion of the injection front through these porous media. This test consisted in injecting a tracer (brine with different NaCl concentration) through each porous medium and in measuring the evolution of the fluid density at the outlet. To do so, two NaCl brines at concentrations of 5000 and 20000 ppm respectively were prepared. At the initial time, the media were fully saturated with 5000 ppm brine. Then, the 20000 ppm brine was injected by means of a piston pump with a flow rate corresponding to a  $Pe = 1$  (Eq. 4.2) so as to guarantee homogeneous fluid penetration, taking  $D_c = 5 \cdot 10^{-9} m^2/s$ . During this injection, the density of the outgoing fluid was continuously measured with a density meter (Anton Paar, DMA 512) until the density reached a plateau value corresponding to the density of the injected brine (typically after injection of 3 pore volumes). At that time, 5000 ppm brine was injected through the 20000-ppm-brine-saturated porous medium and the density of the effluent was measured. These BTC are presented in Figure 69, where  $D$  is the density of the effluent,  $D_f$  is the density of the influent brine and  $D_0$  is the density of the fluid saturating the porous medium. The pore volume in this figure represents the total pore volume as determined through the saturation procedure described in subsection 4.3.3 instead of the effective pore volume visited by the tracer.

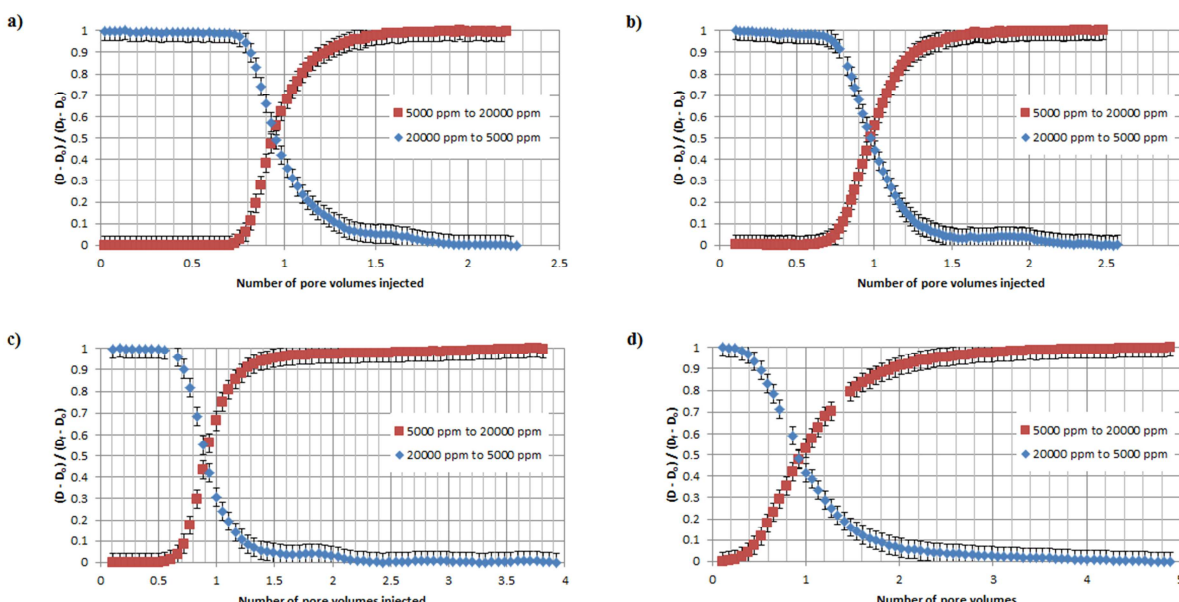


**Figure 69: Density evolution of the effluent as a function of the number of pore volumes of tracer injected through the core. The flow rate corresponds to  $Pe = 1$ .** a) Sample 2; b) Sample 3; c) Sample 4; d) Sample 5.

The simplified equation for dispersion of a moving fluid in porous media, assuming a semi-infinite homogeneous isotropic medium with a plane source at  $z = 0$ , unidirectional flow, constant average velocity throughout the length of the flow path and without any mass transfer between solid and liquid phases is (Ogata and Banks 1961):

$$\frac{\partial C}{\partial t} + \vartheta \frac{\partial C}{\partial z} = \psi \frac{\partial^2 C}{\partial z^2} \quad (4.6)$$

where  $C$  is the concentration of the tracer,  $z$  is the longitudinal coordinate,  $\vartheta$  is the average interstitial velocity,  $\vartheta = Q/(\varepsilon A)$ , and  $\psi$  is the longitudinal dispersion coefficient. The solution of Eq. (4.6) in the case of our experiment is expressed as (Ogata and Banks 1961; Sheng 2011):

$$\frac{C - C_0}{C_{\text{inj}} - C_0} \simeq \frac{1}{2} \operatorname{erfc} \left( \frac{z - \vartheta t}{2\sqrt{\psi t}} \right) \quad (4.7)$$

with  $C_0$  being the concentration at  $t = 0$  and  $C_{\text{inj}}$  being the injected concentration. Given that density  $D$  is proportional to concentration, we can write  $\frac{C - C_0}{C_{\text{inj}} - C_0} = \frac{D - D_0}{D_f - D_0}$ . The  $z$  coordinate considered is the outlet of the porous medium so  $z = L$ . Accordingly, Eq. (4.7) is rewritten as:

$$\frac{D - D_0}{D_f - D_0} \simeq \frac{1}{2} \operatorname{erfc} \left( \frac{L - \vartheta t}{2\sqrt{\psi t}} \right) \quad (4.8)$$

Therefore, the data presented in Figure 69 were fitted to the complementary error function given by Eq. (4.8) with  $t = (\text{Number of pore volumes injected} \times \text{pore volume})/Q$ , thus obtaining  $\psi$  for each experiment. The resulting fits are presented in Figure 70 (only the injection of 5000 ppm to 20000 ppm is presented because of symmetry).

The obtained  $\psi$  are listed in Table 15. As can be deduced from this Table, Sample 5 (Berea Sandstone) is the more dispersive medium, which may be the consequence of a more dispersed PSD (Perkins and Johnston 1963). Also, from Eq. (4.8), it can be seen that  $\frac{C - C_0}{C_{\text{inj}} - C_0} = 0.5$  when a pore volume of tracer has been injected in the sample (Sheng 2011). However, in Figure 69,  $\frac{C - C_0}{C_{\text{inj}} - C_0} = 0.5$  slightly occurs before a pore volume has been injected. It is explained by the fact that, as already said, the total pore volume has been considered in the axis of abscissa instead of the effective pore volume visited by the tracer.

Sample	$\psi$ ( $\text{m}^2/\text{s}$ )
2	$1.0 \cdot 10^{-7}$
3	$3.8 \cdot 10^{-8}$
4	$1.1 \cdot 10^{-7}$
5	$1.0 \cdot 10^{-6}$

Table 15: Longitudinal dispersion coefficients for each porous sample in these experiments.

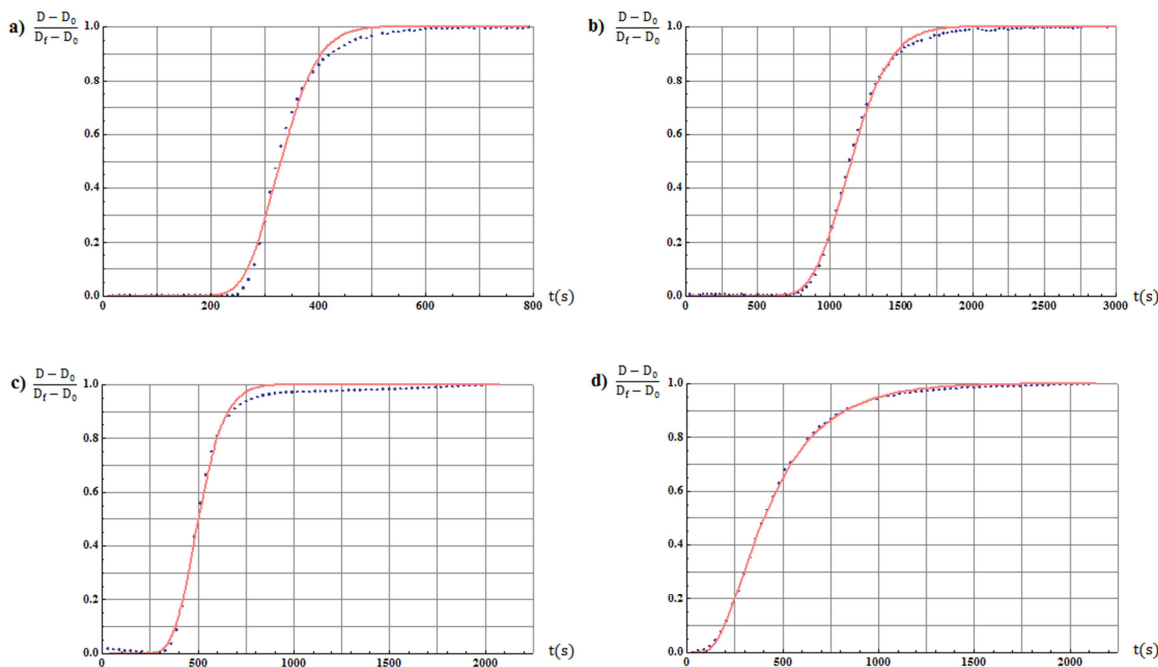


**Figure 70: Measures corresponding to the density evolution of the effluent when using a 20,000 ppm NaCl brine as a tracer (blue points) and fit by Eq. (4.8) (pink line). a) Sample 2; b) Sample 3; c) Sample 4; d) Sample 5.**

#### **4.4.2. Effluent density measurements during saturation with xanthan gum solution**

Similar experiments as those presented in the preceding subsection were performed during saturation of the porous media with xanthan gum solution (Samples 2, 3 and 5). Each medium was initially saturated with 5000 ppm brine. Then, the xanthan gum solution (Solution 2) was injected with a flow rate corresponding to  $\text{Pe} = 2000$  as explained before. The resulting measurements of relative density in the effluent (BTC) are presented in Figure 71.

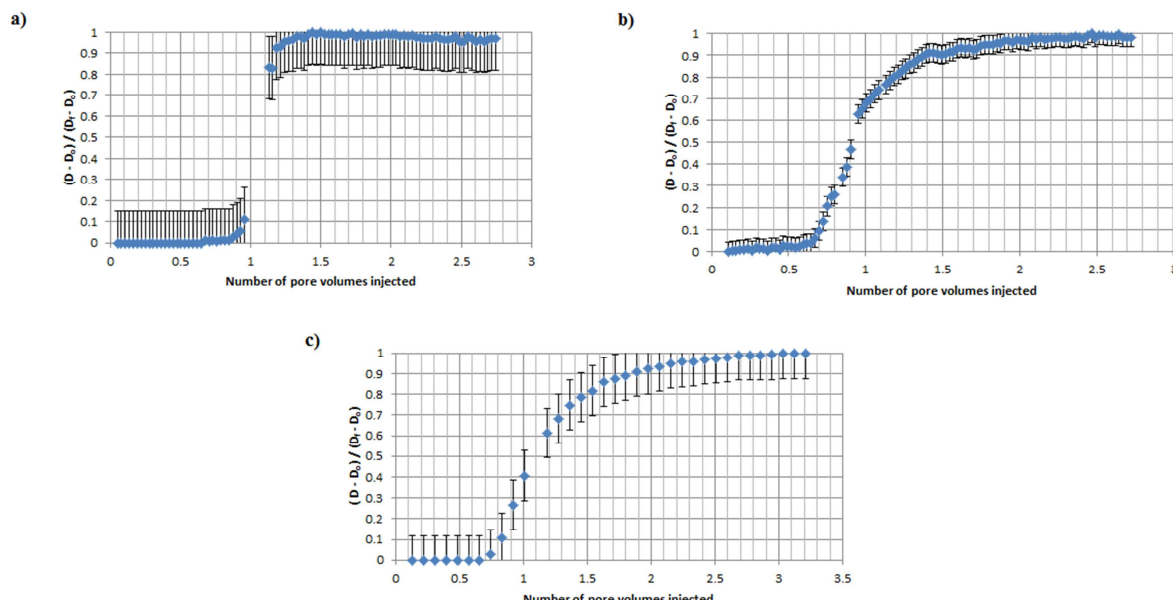


**Figure 71: Density evolution of the effluent as a function of the number of pore volumes of Solution 2 injected through the core. The injected fluid was Solution 2. a) Sample 2; b) Sample 3; c) Sample 5.**

It is noticed that the density of the effluent attains a stable plateau in all cases. Therefore, it can be deduced that polymer retention does not last significantly over time. Indeed, pore blocking or formation of a thick adsorption layer would lead to a large diminution of the section available for flow and, as a consequence, the rate of polymer retention would increase over time. That increase of retention rate would, in turn, imply a decrease in the density of the effluent, which is not observed in our experiments. Besides, it is remarked that the error bars are relatively large because the difference of density between the brine and the xanthan gum solution is only 7000 ppm.

An interesting comparison between the BTCs using brine and xanthan solution as injected fluids is presented in Figure 72. The position of each BTC with respect to the other one is determined by the cumulated effects of polymer adsorption, depleted layer and inaccessible pore volume (see Sorbie 1991; Sheng 2011 for details). In the case of Sample 3, the BTC corresponding to brine saturation is delayed with respect to that corresponding to saturation with xanthan solution, which may be explained by the existence of an inaccessible pore volume (when dimensions of polymer macromolecules are the same order as that of the pores) and a depleted layer close to pore wall. The effects of the preceding phenomena on BTC may hide those of adsorption. In contrast, for samples 2 and 5, the BTCs of xanthan solution are delayed with respect to those of brine, clearly evidencing the existence of polymer adsorption. Indeed, the amount of adsorbed polymer can be coarsely estimated (assuming linear adsorption and neglecting inaccessible pore volume effects) from the difference in pore volume between both curves when evaluated at  $\frac{D-D_0}{D_f-D_0} = 0.5$ . This polymer quantity is then divided by the solid skeleton of porous medium knowing its apparent density. Xanthan adsorption is found to be of approximately 240 µg of polymer per gram of solid for Sample 2 and 90 µg of polymer per gram of solid for Sample 5.

For comparison, it is remarked that similar flow experiments with less concentrated HPAM solutions through Bentheimer Sandstone have been conducted in our laboratory, leading to retention of approximately 50 µg of polymer per gram of solid. Other values reported in the literature are 50 µg/g for HPAM solutions containing polyacrylate through Berea sandstone (Mungan 1969), ~400 µg/g for HPAM solutions through sandpacks and ~465 µg/g for xanthan gum solutions through sandpacks (Wei *et al.* 2014). In anyway, it is noted that even if adsorption exists, xanthan gum macromolecules are flattened onto the surface so that the adsorbed layer is thin and its effects on permeability are often negligible (see subsection 2.3.3), in contrast to HPAM and other flexible polymers. This was one of the main reasons leading to the choice of xanthan solutions as injected fluid in our application.

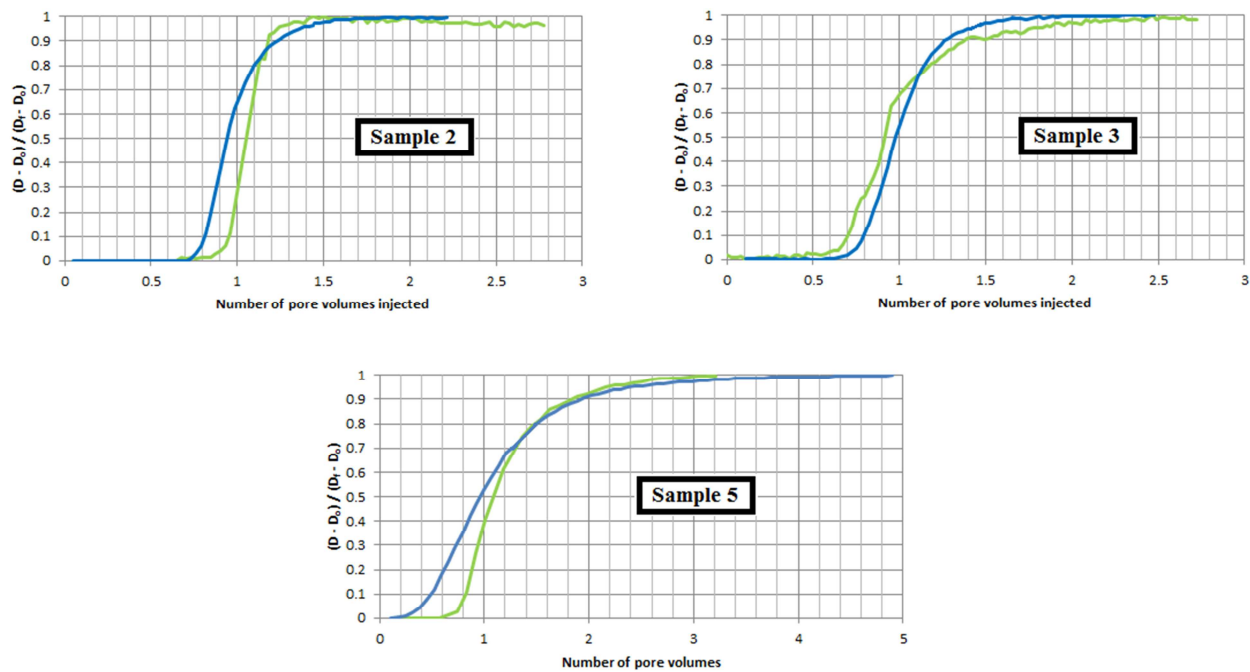


Figure 72: Measures corresponding to the density evolution of the outgoing fluid using 20000 ppm NaCl brine (blue line) and Solution 2 (green line) as injected fluids. The samples were initially saturated with 5000 ppm brine.

#### **4.4.3. Effluent viscosity measurements during saturation with xanthan gum solution**

In addition to the density measurements performed during saturation of the cores with xanthan solution, the viscosity of the effluent was also measured. For that purpose, a fraction collector (Gilson, FC 203B fraction collector) was installed downstream of the density meter so as to collect 4ml fluid samples during the saturation. Afterwards, the whole lot of fractions was characterized with a stress-controlled rheometer (MCR 302 from Anton Paar).

The viscosity of each sample was measured at two different shear rates. In fact, what was sought with this operation was to study the displacement of brine by the xanthan solution by measuring viscosity instead of density. The results for each porous medium (Samples 2 to 5) are presented in Figure 73 to Figure 76 together with the viscosity of the injected solution.

It is noticed that a significant increase of viscosity occurs only when more than a pore volume is injected, in contrast with what was observed for density measurements (Figure 73) for which half of the rise was attained when less than a pore volume had been injected. The reason is that whereas density is proportional to concentration, viscosity follows a power law. As a consequence, the increase in viscosity is produced only once the concentration of the injected fluid in the effluent is close to 100%.

Another aspect that has to be highlighted is that the viscosity of the effluent reaches a stable value as it happened with its density. However, this value is to some extent lower than the viscosity of the fluid at the inlet of the porous medium in almost all cases. The explanation of

this fact is the presence of moderate polymer adsorption that still continues even once a large number of pore volumes have been injected. Indeed the low final slope of viscosity as a function of pore volume may reflect the slow adsorption kinetics produced by continuous detachment of xanthan molecules in the adsorbed layer and their replacement by other xanthan molecules with higher molecular weight (Chauveteau and Lecourtier 1988).

One can also put forward that retention or mechanical degradation may be other sources of such observation. These phenomena will be further discussed in the next subsection. In any way, the final value of effluent viscosity during saturation is very close to the viscosity of the fluid before injection through the porous media, showing that polymer mechanical degradation is not significant.

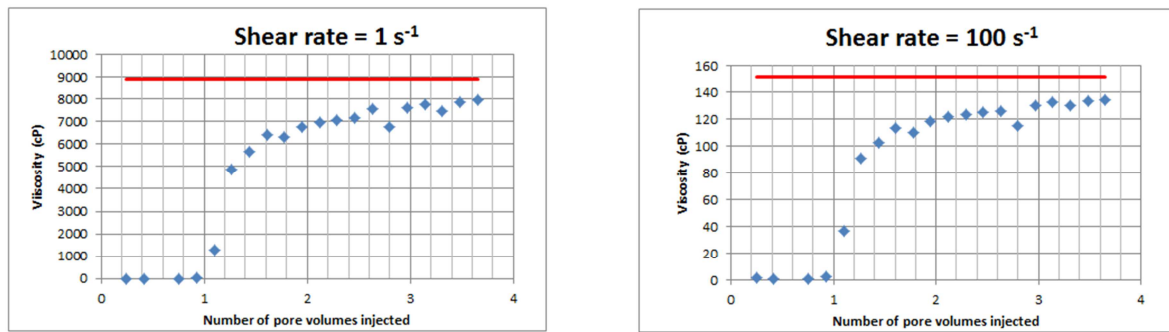


Figure 73: Sample 2: viscosity of the effluent at different shear rates as a function of the volume of Solution 2 injected (blue rhombi). The red lines represent the viscosity of Solution 2 before injection through the porous media.

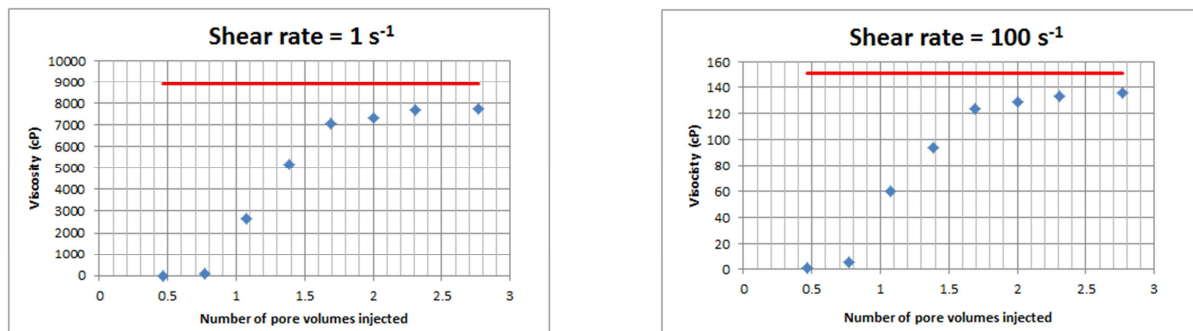


Figure 74: Sample 3: viscosity of the effluent at different shear rates as a function of the volume of Solution 2 injected (blue rhombi). The red lines represent the viscosity of Solution 2 before injection through the porous media.

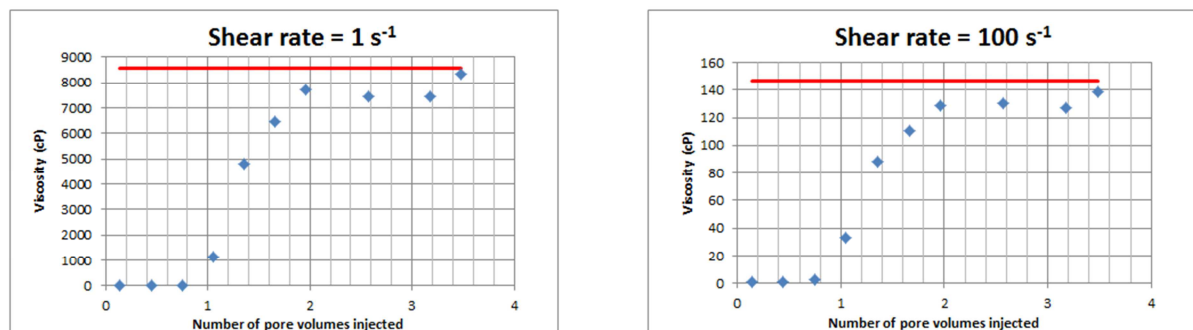


Figure 75: Sample 4: viscosity of the effluent at different shear rates as a function of the volume of Solution 2 injected (blue rhombi). The red lines represent the viscosity of Solution 2 before injection through the porous media.

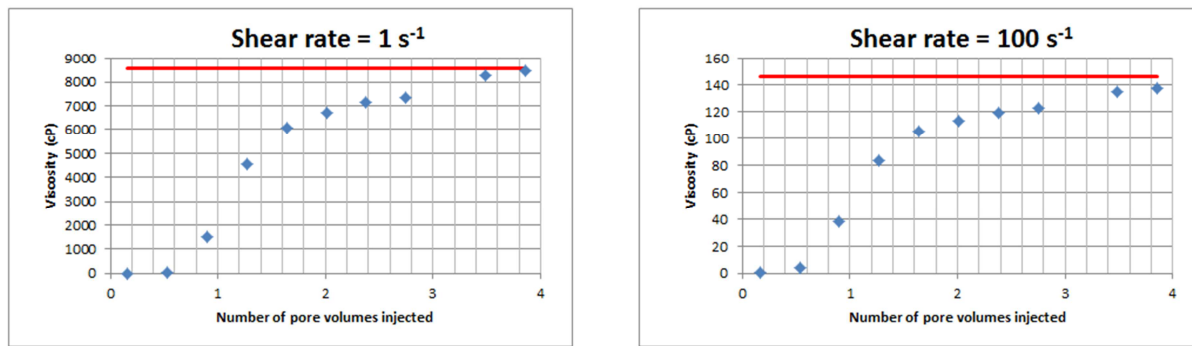


Figure 76: Sample 5: viscosity of the effluent at different shear rates as a function of the volume of Solution 2 injected (blue rhombi). The red lines represent the viscosity of Solution 2 before injection through the porous media.

#### **4.4.4. Evolution of the viscosity of the effluent during the different stages of a typical test**

As already pointed out, xanthan gum solutions flowing through porous media may experience retention, adsorption and are subjected to elongation as xanthan macromolecules pass continuously from pore bodies to pore throats. At high flow rates, such elongation may become so important that macromolecules may break resulting in polymer degradation. Also, some particles detached from the porous medium can be transported by the fluid, changing its rheology.

In the preceding subsection it has been seen that both the density and the viscosity of the effluent attained a stable value during the saturation stage, which shows that in the event of pore blocking, adsorption or degradation their effects are limited. Moreover, the viscosity of the fluid at the outlet of the porous medium was close to that at the inlet. However, a completely different situation arose after the whole Q( $\nabla P$ ) measurements sequence. Indeed, during the Q( $\nabla P$ ) measurements that are exploited with YSM, the flow rate is steeply decreased from 1000 ml/h to 0.01 ml/h. One may wonder if the rheology of the outgoing fluid is still the same after that operation.

In order to answer that question, a 4 ml fraction of outgoing fluid from Sample 2 was collected after the Q( $\nabla P$ ) measurements and its viscosity was measured at several shear rates, as presented in Figure 77. For the sake of comprehension, the rheology of the fluid entering the porous medium is also presented in that figure. As it is observed, the outgoing fluid is clearly less viscous. Such a difference cannot be explained by mechanical degradation, since a pore volume of fluid at the highest flow rate was injected during the saturation stage without producing any decrease in viscosity. In this subsection, we will present successive experiments that have been conducted so as to explain that viscosity drop.

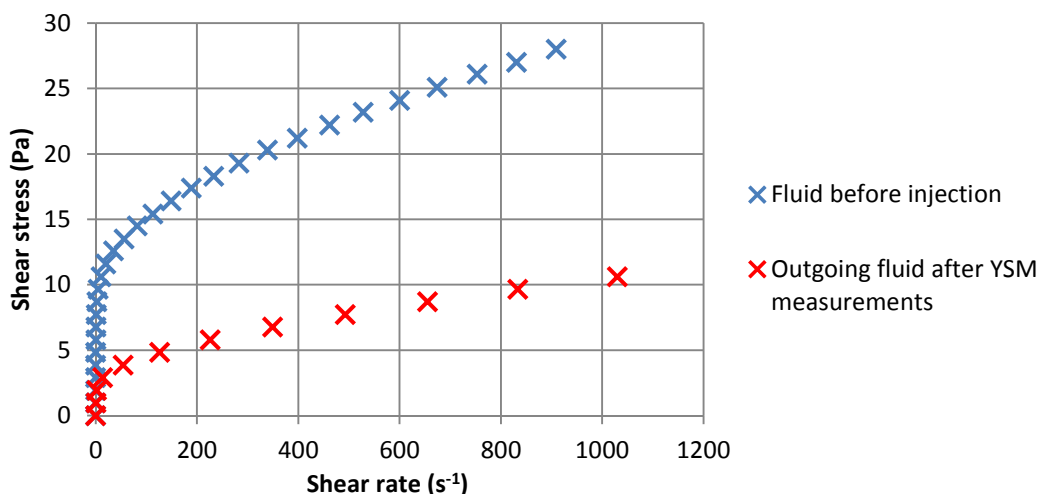


Figure 77: Rheogram of Solution 2 before injection compared to the rheogram of the outgoing fluid after the YSM measurements in Sample 2.

As a consequence of the results with Sample 2, it was decided to determine whether the viscosity drop was due to the imposition of low flow rates during Q( $\nabla P$ ) measurements. Indeed, xanthan gum molecules are not oriented in the direction of flow at low shear rates, so retention is more likely to occur under these conditions. 12 ml of fluid were injected at the highest flow rate (1000 ml/h) after the Q( $\nabla P$ ) measurements on Sample 3 and three fractions of outgoing fluid, each of 4 ml, were collected and subsequently characterized with the rheometer. The results are presented in Figure 78. The first 4 ml fraction presents a similar viscosity drop as that in Sample 2. However, it was noticed that by flooding at high flow rate, the viscosity of the effluent is increased. In effect, the second 4 ml fraction was found to be slightly more viscous than the fluid before injection suggesting that the retained molecules were swept when flooding, leading to an increase of the concentration of the effluent and therefore its viscosity. Finally, the viscosity of the third 4ml fraction was closer to the original viscosity. Therefore, it can be concluded from that experiment that the origin of the viscosity drop is the polymer retention at low flow rates.

Additional experiments were carried out so as to respond to the remaining questions. In that respect, the rheology of the outgoing fluid after the saturation of Sample 4 was measured. Besides, another fraction was collected from the outlet 12 h later, just before the Q( $\nabla P$ ) measurements, and then characterized with the rheometer without observing any significant change in viscosity as shown in Figure 79. After the Q( $\nabla P$ ) measurements, 8 ml were injected at 1000 ml/h and two 4 ml fractions were collected and characterized (see Figure 79). The same behavior than in the experiment with Sample 3 was observed, thus reinforcing the preceding conclusions.

A similar experiment was conducted with Sample 5, with a flushing step of 16 ml at 1000 ml/h after the Q( $\nabla P$ ) measurements. The corresponding results are presented in Figure 80, confirming the same behavior as in the more permeable materials. The occurrence of polymer retention may explain the deviation of the Q( $\nabla P$ ) measures at low flow rates from the general trend as viewed in Section 4.3.4.

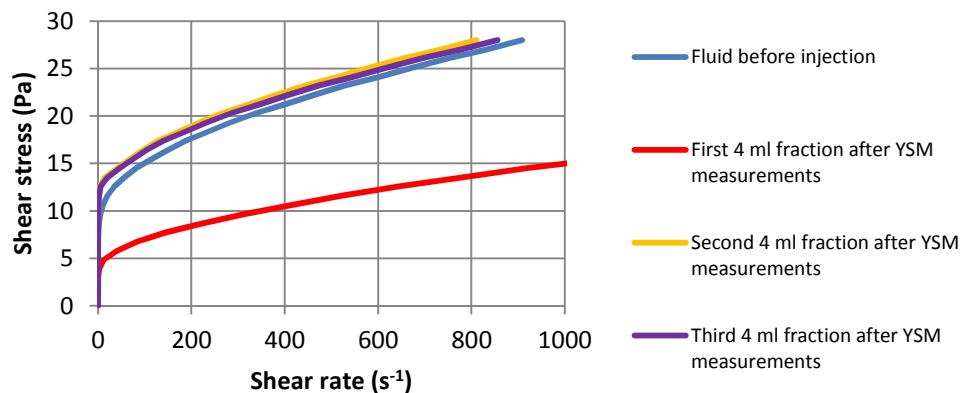


Figure 78: Rheogram of Solution 2 before injection compared to the rheograms of successive fractions of effluent after the YSM measurements in Sample 3.

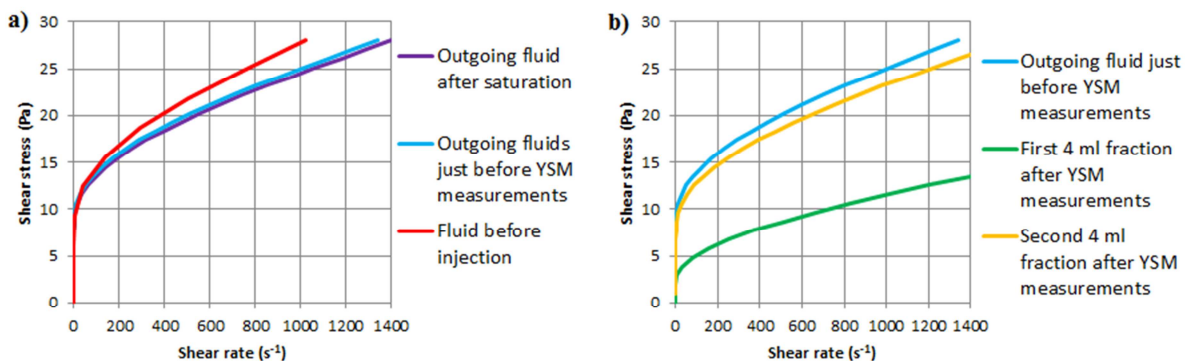


Figure 79: Sample 4: a) rheogram of Solution 2 before injection compared to the rheograms of the outgoing fluid after saturation of the sample and just before YSM measurements. b) Rheogram of the outgoing fluid just before the YSM measurements compared to the rheograms of successive fractions of outgoing fluid after the YSM measurements.

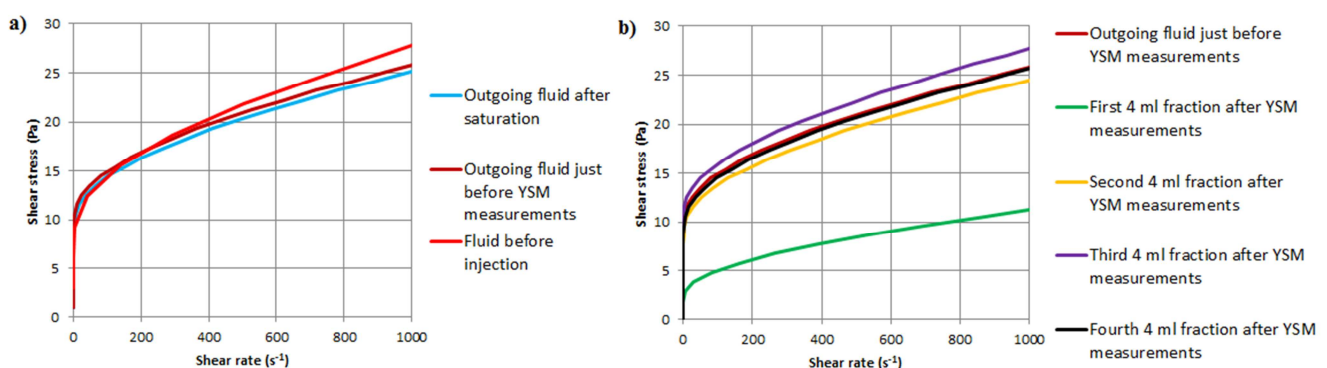
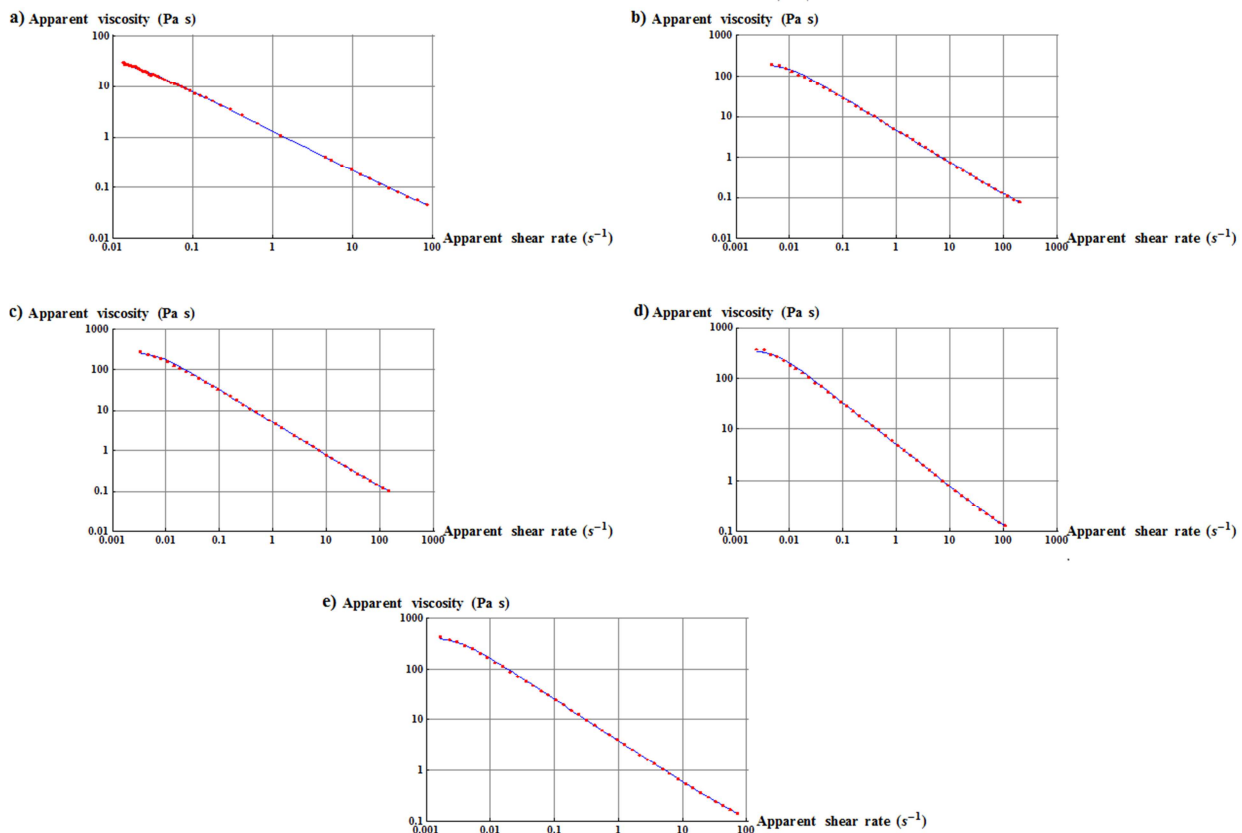


Figure 80: Sample 5: a) rheogram of Solution 2 before injection compared to the rheograms of the outgoing fluid after saturation of the sample and just before YSM measurements. b) Rheogram of the outgoing fluid just before the YSM measurements compared to the rheograms of successive fractions of outgoing fluid after the YSM measurements.

## **4.5. Modified YSM for laboratory experiments**

It was shown in Section 3.3 that the quality of the obtained PSDs was strongly affected by the presence of random noise in the  $Q(\nabla P)$  measures. On the other hand, the precision of the  $Q(\nabla P)$  measures at low flow rates was questioned in the preceding section due to the existence of polymer retention. Here, we will explore a modification of YSM aiming to limit the effect of noise and polymer retention on the quality of the obtained PSDs.

It is reminded that the apparent rheology of a Carreau fluid (or a “*pseudo*” yield stress fluid) flowing through a porous medium can be represented by defining an apparent viscosity and an apparent shear rate (Eqs. 2.41 and 2.42). Moreover, the values of  $\beta$  corresponding to each experiment were calculated in the preceding sections. Therefore, it is possible to transform the  $Q(\nabla P)$  data into  $\mu_{app}(\dot{\gamma}_{app})$  data and then fit these data to a Carreau model (Eq. 2.15). This is shown in Figure 81 and Figure 82 for the experiments presented in Sections 4.2 and 4.3 respectively.



**Figure 81:** Apparent viscosity as a function of the apparent shear rate resulting from experiments presented in Section 4.2 (red points) and fit to a Carreau model (blue lines).

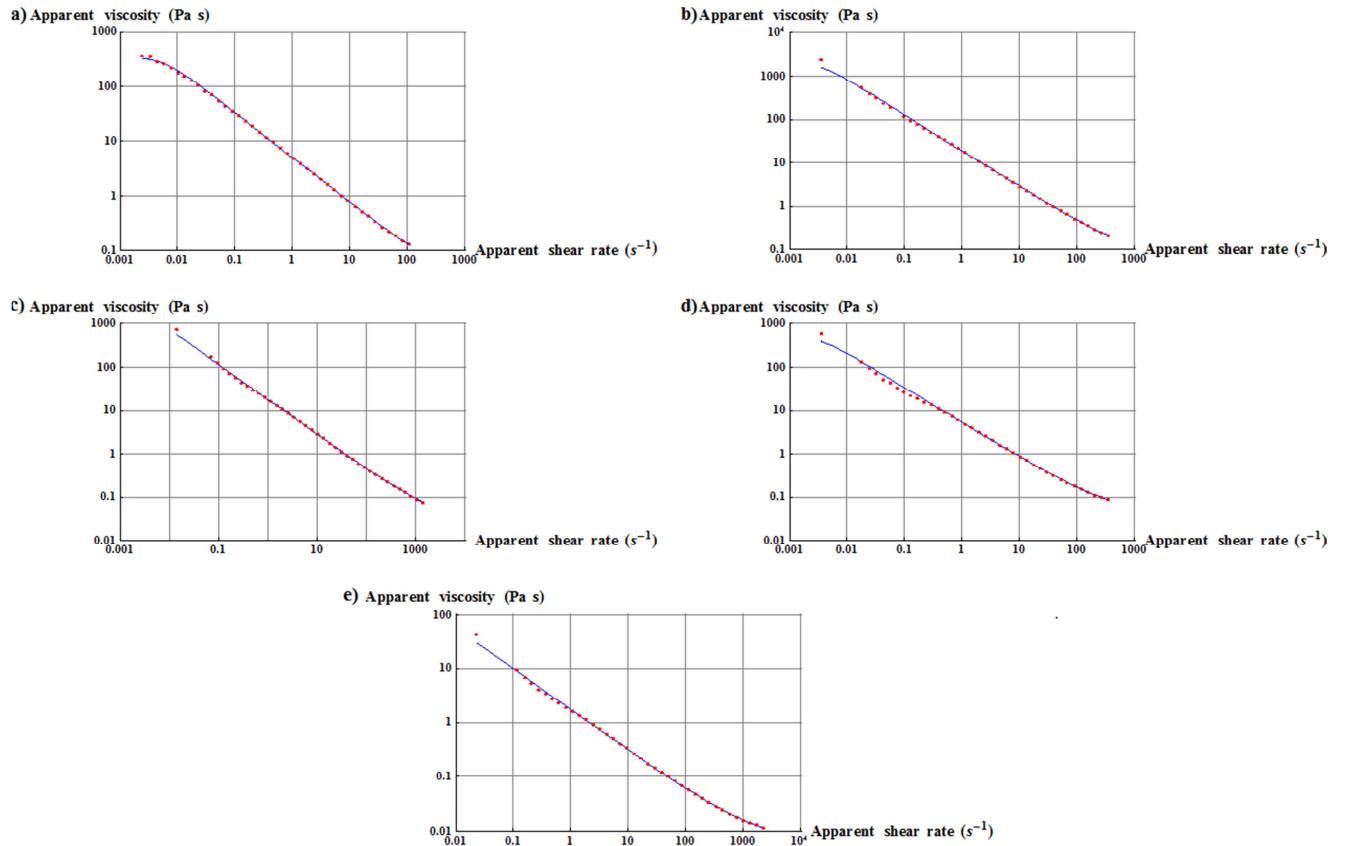


**Figure 82:** Apparent viscosity as a function of the apparent shear rate resulting from experiments presented in Section 4.3 (red points) and fit to a Carreau model (blue lines).

It is observed that the quality of these fits is good, so the apparent viscosity is well approached by a Carreau model. Besides, the next relation can be obtained from Eqs. (2.15), (2.41) and (2.42):

$$\nabla P = \frac{Q}{KA} \left[ \left[ 1 + \left( \frac{\lambda \beta}{A\sqrt{K\varepsilon}} Q \right)^2 \right]^{\frac{n-1}{2}} (\mu_{0app} - \mu_{\infty app}) + \mu_{\infty app} \right] \quad (4.9)$$

Therefore, it is possible to use the preceding relation to fit the  $Q(\nabla P)$  measures, as shown in Figure 83 for one of the experiments (see Annex B for the other experiments). One can obtain smooth  $Q(\nabla P)$  data through evaluation of this continuous function, which will reduce the effects of random noise. Moreover, this fit will correct the measures corresponding to low flow rates that are affected by polymer retention and do not follow the general tendency.

The smooth  $Q(\nabla P)$  data resulting of this fitting step as well as the PSDs calculated from them through application of YSM are presented in Annex B. Nevertheless, it has to be noted that this modified YSM has not been fully assessed concerning the exploitation of smooth data to obtain the PSD. Therefore, only the PSDs calculated in the preceding sections will be considered for further analysis in this work.

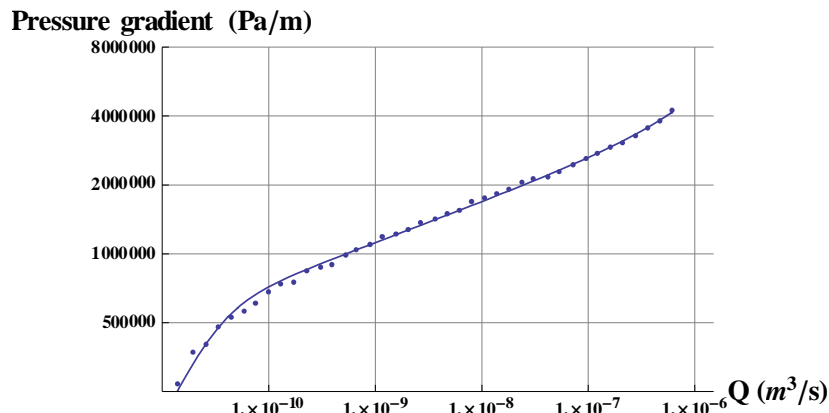


Figure 83: Measured pressure gradient as a function of flow rate (blue points) and fit (blue line) corresponding to the experiment at  $C_p = 7000$  ppm presented in Section 4.2.

## 4.6. Conclusions

On the basis of preliminary experiments, an experimental procedure to characterize the PSD of porous media with YSM has been proposed in this chapter. The fabrication and characterization of these solutions have been detailed and it has been shown that by using a simple experimental setup one can obtain the  $(Q_i, \nabla P_i)$  measures needed to characterize the PSD of a core with YSM.

A first set of experiments consisted in injecting five xanthan gum solutions with different  $C_p$  through analogous samples of A10 sintered silicate. Therefore, the rheograms of these solutions have been obtained and fitted to a Herschel-Bulkley model for each  $C_p$ . The  $Q(\nabla P)$  measurements resulting from the injection of the different solutions have been used to calculate the corresponding PSDs with the present method, showing that higher concentrations lead to PSD which are closer to those deduced from MIP. Moreover, the same  $Q(\nabla P)$  measurements have also been used to characterize the apparent viscosity in each case. This apparent viscosity represented as a function of an apparent shear rate has the same form as the effective one, but presents a less pronounced shear-thinning behavior due to the effects of apparent slip. Also the influence of the range of  $Q$  on  $\beta$  has been studied.

In Section 4.3., we have presented several flow experiments which consist in injecting xanthan gum solutions with  $C_p = 7000$  ppm through different types of porous media. The special features of these experiments, namely the range of flow rates, the high concentration of the solutions and the range of permeabilities has permitted to analyze new aspects of the apparent rheology (e.g. the connection between  $\beta$  and the range of  $Q$ ). The  $Q(\nabla P)$  measures have been exploited so as to obtain the PSDs of the samples, resulting in PSDs that are coherently arranged with regard to the average radius estimated from Eq. (2.2).

It has been remarked that the value of  $\alpha^*$  provided by the E-criterion presented in Section 3.2 is almost constant for every experiment. Its values for all concentrations and all porous media considered are comprised between 1.2 and 1.4.

Another series of experiments aiming to evaluate the importance of polymer adsorption, retention, mechanical degradation and other factors affecting the rheology of the fluid have been carried out and exploited. We can conclude that even if polymer adsorption has been observed, its effects are not expected to be important insomuch as the rigid macromolecules are flattened onto the pore surface and the density and viscosity of the effluents attain a plateau value during saturation. Mechanical degradation has been shown to be negligible given that the viscosity of the effluent is only slightly inferior to that of the fluid before injection. That small difference can be due to moderate retention. The most important issue concerns polymer retention at the lowest flow rates, when the macromolecules are not oriented in the direction of flow.

Finally, a Carreau-type fit has been presented with the objective of providing smooth ( $Q_i, \nabla P_i$ ) data and reducing the impact of random noise and polymer retention. This fitting function has been shown to correctly adjust  $Q(\nabla P)$  measures, which was not achieved through the use of polynomials. However, the potential of the modified YSM may be much more important than what has been presented here. In particular, the possibilities offered by a continuous function that can be extrapolated to flow rates that cannot be imposed with the current equipment are promising, but would demand a specific study to be fully assessed.



## 5. Comparison of YSM with other porosimetry methods

---

We have seen that PSD is an elusive characteristic of porous media whose definition depends on the method used for its determination. Nevertheless, a comparison between methods is presented here with the purpose of explaining some differences in how the results provided by each technique should be interpreted. Moreover, the information that one can obtain from each method will be illustrated through this comparison.

---

### **5.1. Results obtained by Mercury Intrusion Porosimetry (MIP) and comparison with those of YSM**

Given that MIP is the reference porosimetry method, it makes sense to begin this chapter by comparing the results of YSM with those deduced from MIP. Different materials will be analyzed with both techniques and the results in terms of PSDs and capillary pressure curves will be compared. Moreover, we will present a test to check whether the cores characterized with YSM are reusable.

#### **5.1.1. PSDs obtained by MIP**

In the preceding chapter, five different materials were analyzed with YSM. Subsequently, an analogue sample of each material was characterized by MIP with an automated mercury porosimeter (Autopore IV 9500 v1.09, Micromeritics). Photos of some of these samples are displayed in Figure 84. Besides, Figure 85 and Figure 86 show the results obtained from MIP in terms of PSD for all these materials. As can be observed in this figure, although most of the pore volume is composed of pores whose size is in the range 1 - 40  $\mu\text{m}$  for all samples, the PSDs of these porous media are sufficiently different to be distinguished.

The extrusion cycle is not considered here and all the PSDs come from the injection test. All the presented PSDs result from direct application of Eq. (2.10) with a contact angle of 140°, which is a commonly used value (Giesche 2006). It is worth noting that more elaborate exploitation methods are often used to deduce PSDs from MIP tests. Nevertheless, they require additional information supplied by other techniques. Therefore, a basic exploitation method is preferred here in order to avoid any supplementary input. In any way, it is essential to recall that the PSDs obtained by MIP are mainly sensitive to the radii of the largest entrances or openings towards the pore volumes.



Figure 84: Some of the samples characterized with MIP.

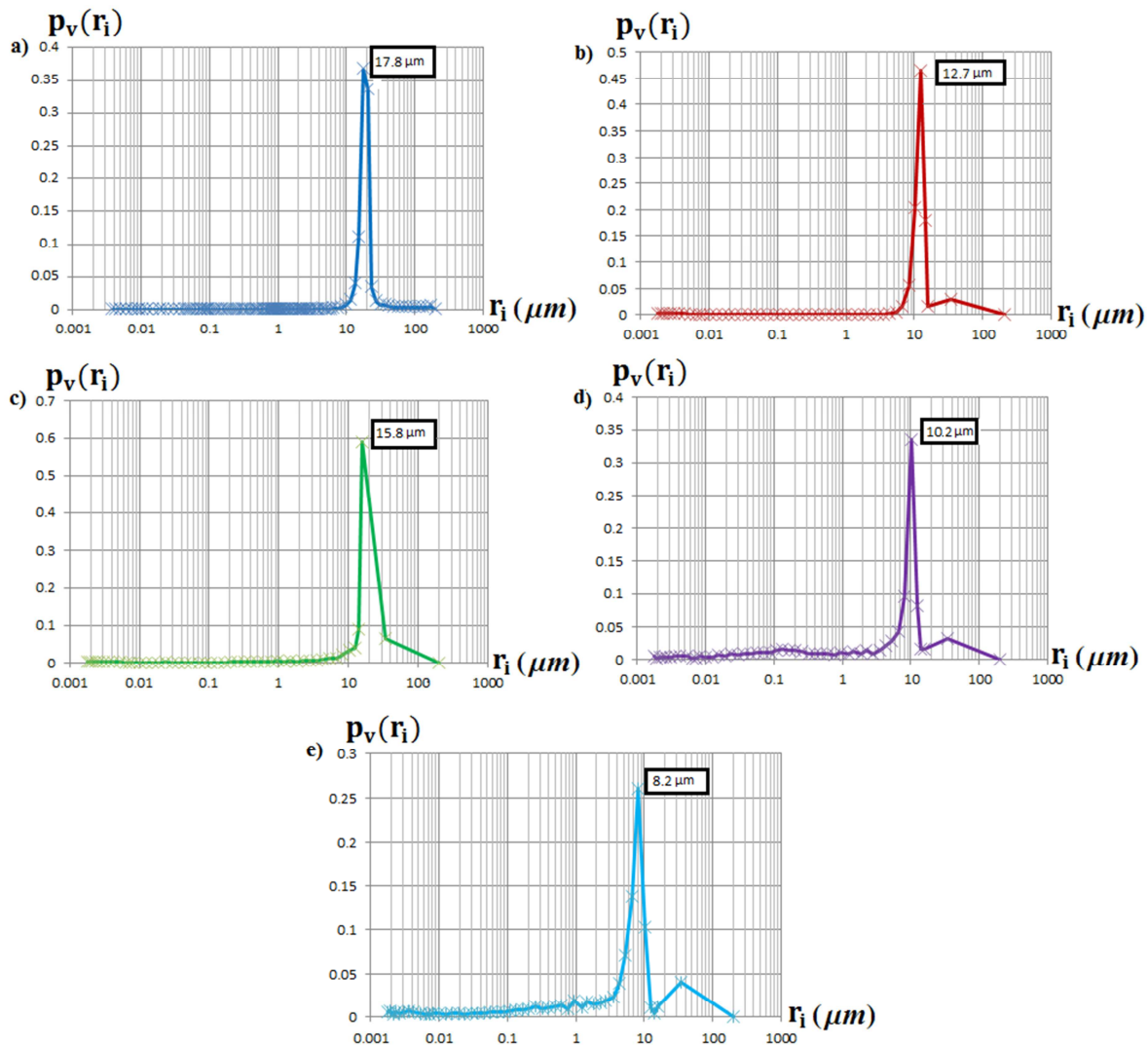


Figure 85: PSDs obtained with MIP for the 5 materials analyzed in this work. a) Sample 1; b) Sample 2; c) Sample 3; d) Sample 4; e) Sample 5.

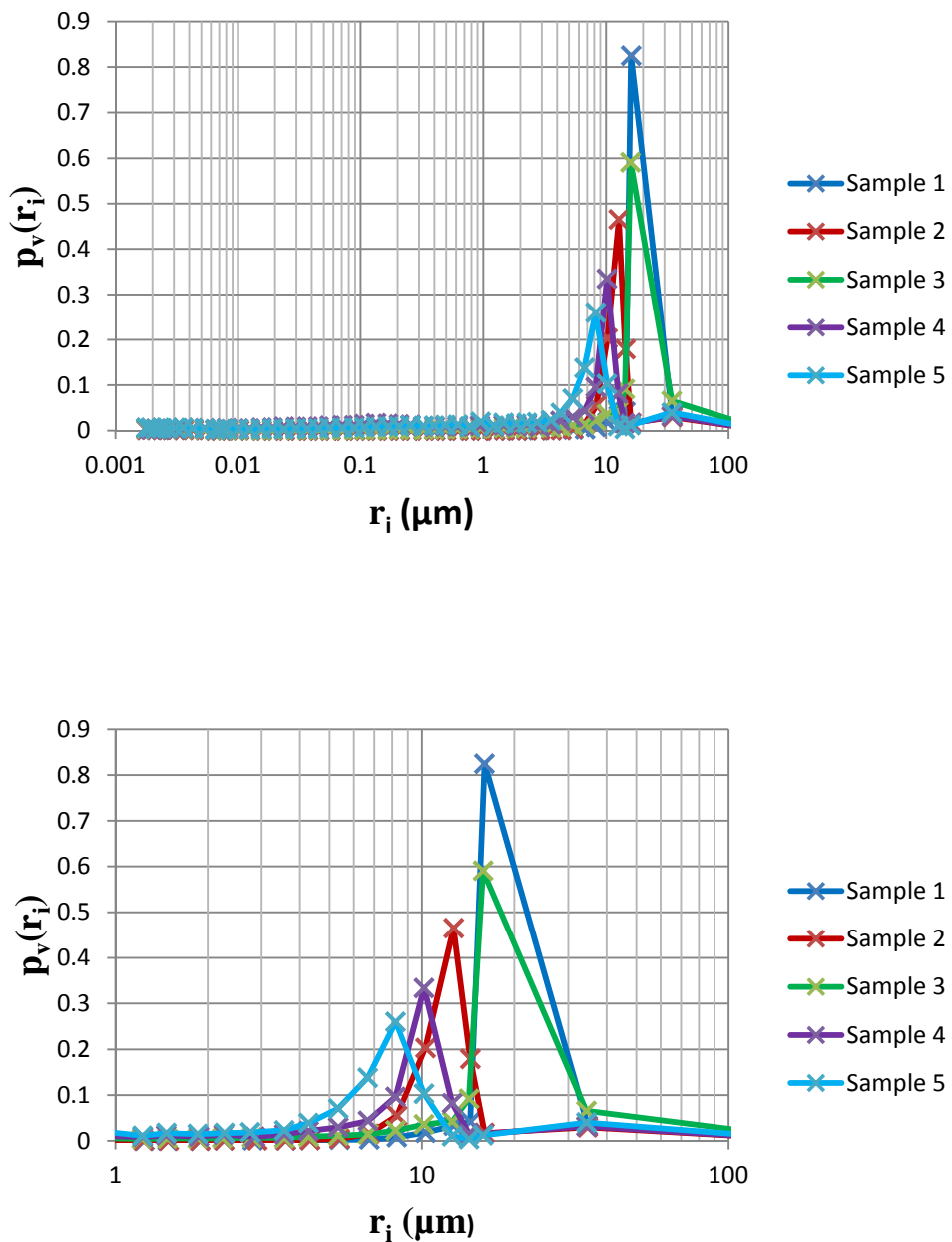


Figure 86: Comparison of the PSDs obtained with MIP for the 5 materials analyzed in this work.

### **5.1.2. Different representations of a PSD obtained with MIP**

Different ways to represent the PSD coming from a set of MIP measures may lead to contradictory conclusions. To illustrate this, we will consider the case of the MIP measures obtained with a sample analogous to Sample 4 (Castlegate Sandstone). The raw data, i.e. imposed pressure *versus* mercury saturation, are presented in Figure 87. If a contact angle of 140° is assumed, the cumulative percentage of the volume corresponding to each pore radius is shown in Figure 88 (the pressure-to-radius transformation is given by Eq. (2.10)).

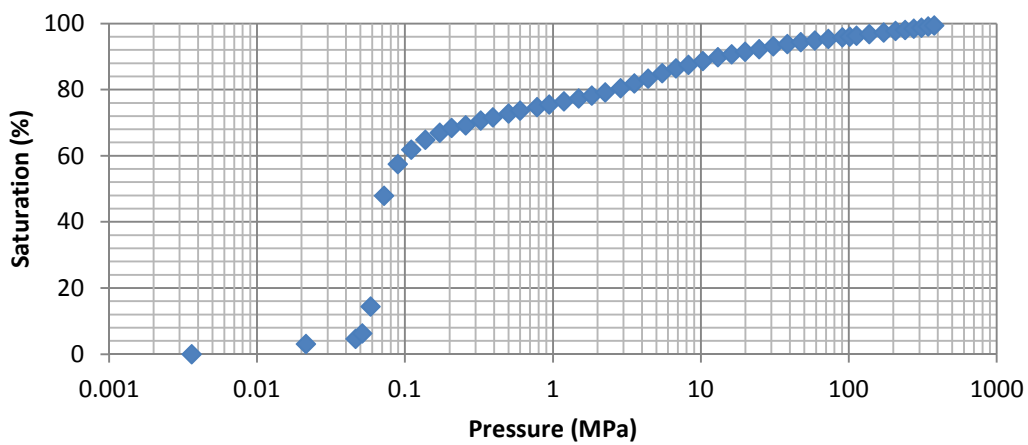


Figure 87: Mercury saturation in the porous medium as a function of the applied pressure during the MIP test with a sample analogous to Sample 4.

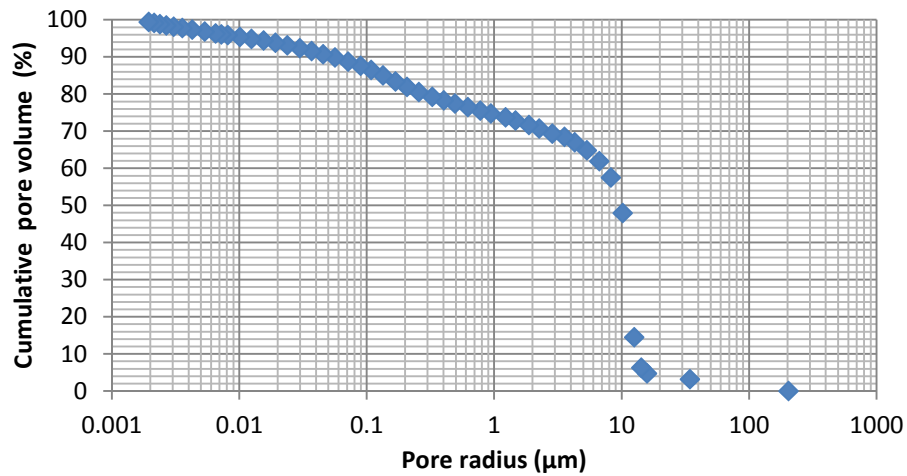


Figure 88: Cumulative percentage of the volume corresponding to each pore radius. This curve represents the percentage of the pore space (in volume) which is composed of pores whose radius is greater than the abscissa value. It corresponds to a sample analogous to Sample 4.

An important element to note is that the density of data points in the smaller pores region is much greater than that of the larger pores regions. Indeed, while the difference of radii is of almost 170  $\mu\text{m}$  between the first and the second measure, that difference is of only 0.2 nm in the end limit of the interval. Consequently, the probabilities corresponding to pore classes defined as  $r_i = -2\sigma\cos\theta/P_i$ , where  $P_i$  is the imposed pressure for each measure, will be very low for the smallest pores since the density of measurements is very high. The PSD corresponding to the classes so defined is presented in Figure 89. Analyzing that PSD, it can be incorrectly concluded that there are almost no pores with radii below 4  $\mu\text{m}$ .

However, if equidistant pore classes are defined, the PSD presented in Figure 90 is obtained. It is evident now that there is a significant proportion of pores whose radius is inferior to 4  $\mu\text{m}$ . The PSDs resulting from definition of equidistant pore classes for the other materials are presented in Figure 91. Moreover, the choice of different values of the contact angle will shift the resulting PSD, as shown in Figure 92 for Sample 4.

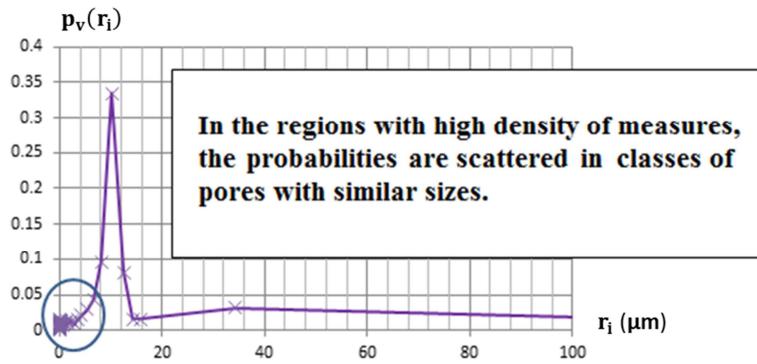


Figure 89: PSD corresponding to a sample analogous to Sample 4. The pore classes represented are defined as  $r_i = -2\sigma \cos \theta / P_i$ , where  $P_i$  is the imposed pressure for each measure.

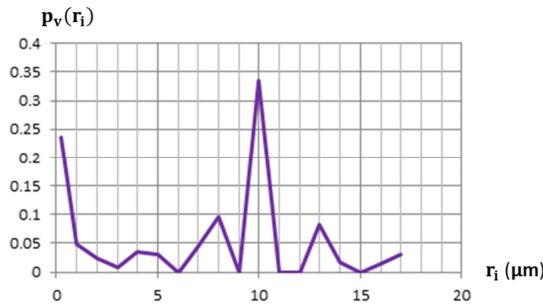


Figure 90: PSD corresponding to a sample of the same material as Sample 4. The pore classes represented are equidistant (1 μm separation between classes).

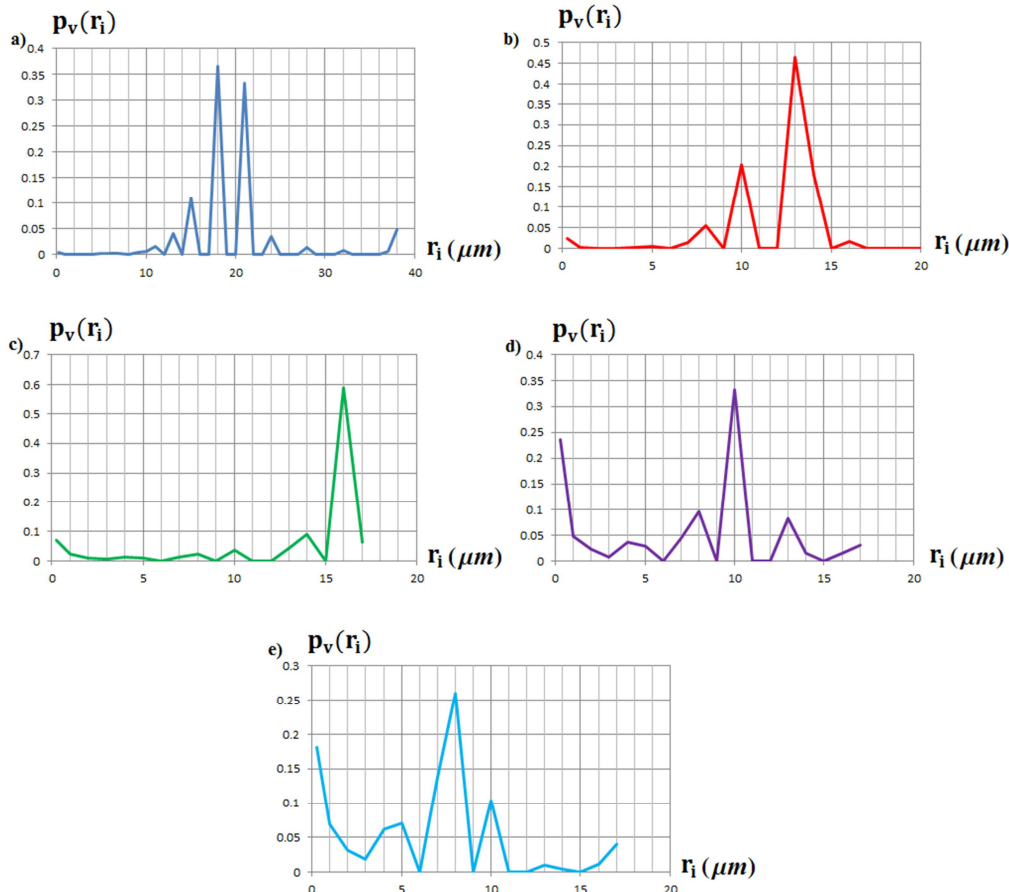


Figure 91: PSDs obtained with MIP for the 5 materials. The represented pore classes are equidistant and correspond to a sample analogous to a) Sample 1; b) Sample 2; c) Sample 3; d) Sample 4; e) Sample 5.

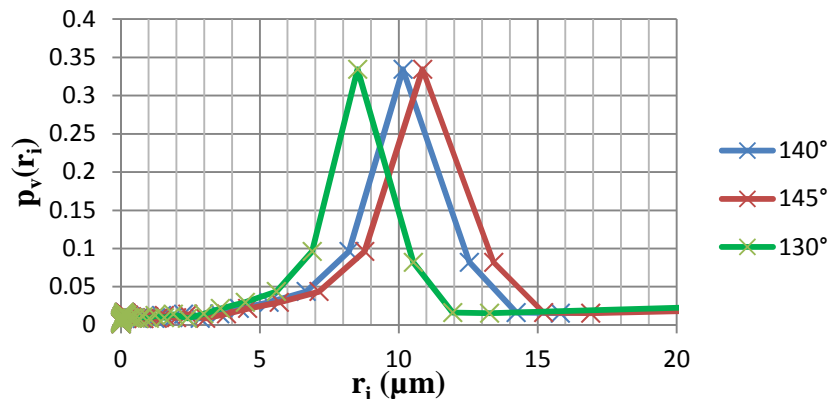


Figure 92: Effect of the choice of the contact angle on the obtained PSD for a sample analogous to Sample 4.

### **5.1.3. Comparison of the PSDs obtained by YSM and MIP.**

PSDs obtained through different techniques cannot be directly compared due to two main reasons. The first one is that, as already explained, the represented pore dimension depends on the considered technique. The second one is that the pore classes obtained in each case are not the same. In our particular comparison, the direct pore classes are  $r_i = -2\sigma\cos\theta/P_i$  for MIP whereas they are defined as  $r_i = \alpha^*2\tau_0/\nabla P_i$  for YSM. Consequently, a preliminary step when comparing PSDs of both methods consists in calculating the equivalent probabilities for the same classes. Figure 93 shows the PSDs supplied by MIP and YSM for the 5 materials analyzed here. The PSDs obtained by YSM have been adapted to correspond to the same pore classes represented by MIP.

It is noticed that the YSM yields smaller pores than MIP. However, PSDs from YSM are correctly arranged when compared with MIP results (except for Sample 2) and their shape is Gaussian in both cases. Furthermore, Eq. (2.2) is used to determine the average pore radius of a bundle of capillaries. This average pore radius was then calculated and compared with the average radius obtained by MIP and YSM for our samples, as presented in Figure 94. YSM average radius is always closer than MIP average radius to the one predicted by Eq. (2.2). The reasons will be discussed in the next chapter. In fact, there is very good accordance between YSM average radius and the average radius predicted by Eq. (2.2), apart from Sample 2 and Sample 5 (whose measure of K may be affected by swelling of clays), which is not the case for MIP.

### **5.1.4. Capillary pressure *versus* saturation for MIP and YSM**

Capillary pressure ( $P_c$ ) is one of the most commonly quantified properties when characterizing a core of porous medium in the petroleum industry. In fact,  $P_c$  controls the fluid distributions in a reservoir rock and affects oil recovery. In laboratory experiments, the capillary pressure curve is obtained by displacing a wetting fluid with a non-wetting fluid and representing the saturation of the rock with the non-wetting phase, as a function of the imposed pressure. The most used methods to measure the capillary pressure curve are MIP

and centrifugation (Tiab and Donaldson 2004; Cossé 1988). In the case of MIP the couple of fluids are mercury and air.

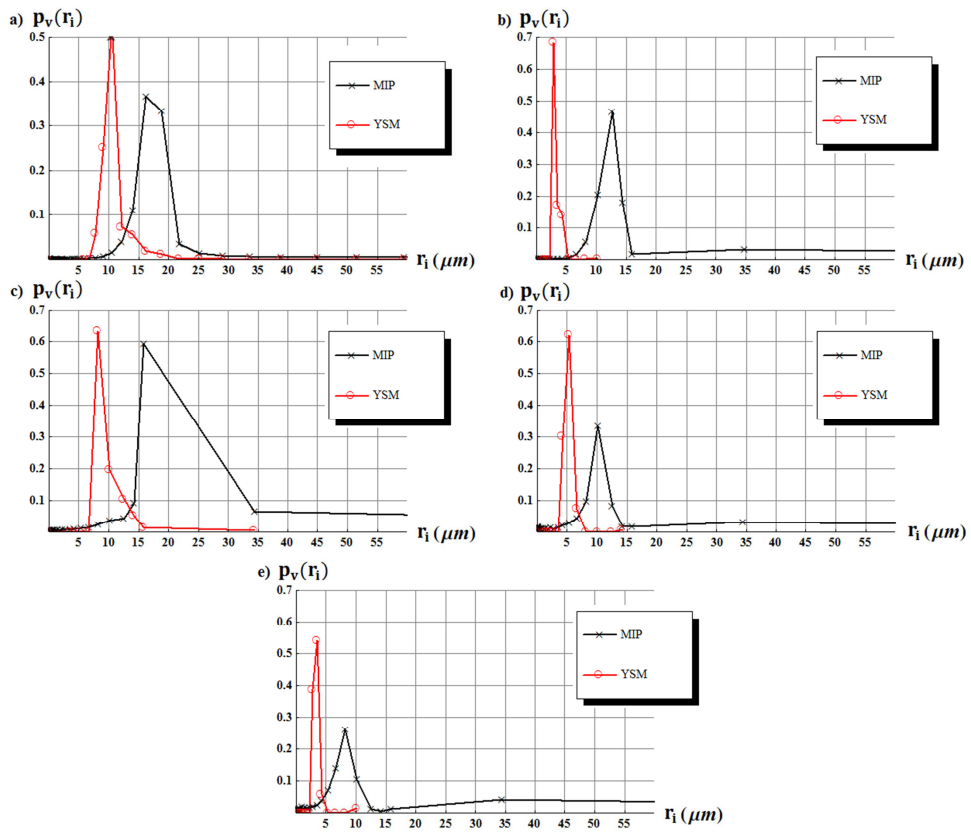


Figure 93: PSDs obtained with YSM compared with those obtained with MIP for the 5 materials. a) Sample 1; b) Sample 2; c) Sample 3; d) Sample 4; e) Sample 5.

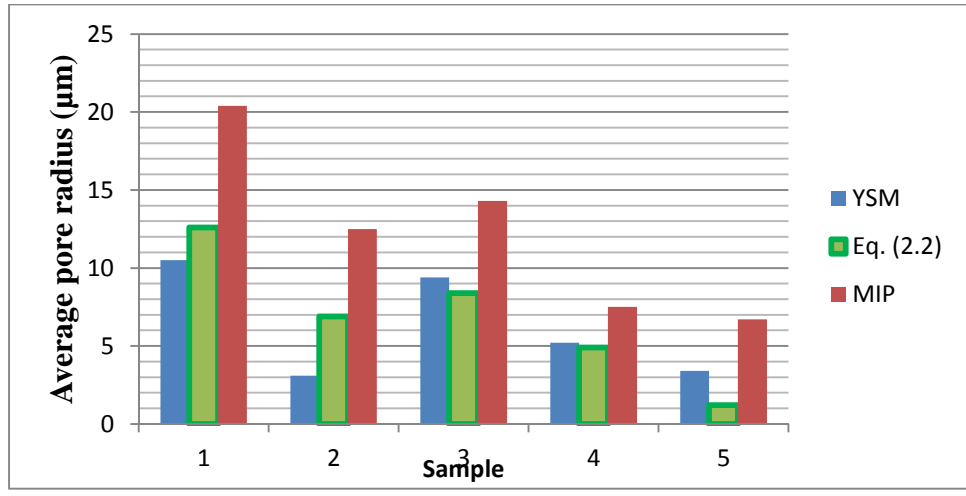


Figure 94: Comparison between the average radii obtained using YSM, MIP and Eq. (2.2).

Figure 95 presents the capillary pressure curves for both MIP and YSM, where  $S$  is the percentage of saturation in non-wetting phase (mercury). It has to be borne in mind that while this  $P_c(S)$  curve is directly measured in MIP tests, it is obtained by transforming the PSD in the case of YSM. The procedure for YSM consists in associating a  $P_c$  to each pore size class

through application of Eq. (6.1). Then, the saturation is calculated through the cumulated volume probability for each pore size class (Eq. 6.2):

$$P_{ci} = -\frac{2\sigma \cos \theta}{r_i} \quad (6.1)$$

$$S(P_{ci}) = \sum_{\forall r_i \geq -\frac{2\sigma \cos \theta}{P_{ci}}} p_v(r_i) \quad (6.2)$$

$\theta$  is assumed to be  $140^\circ$ , and  $\sigma$  is the surface tension of the mercury-air couple, i.e.  $0.485 \text{ N m}^{-1}$  at  $25^\circ\text{C}$ .

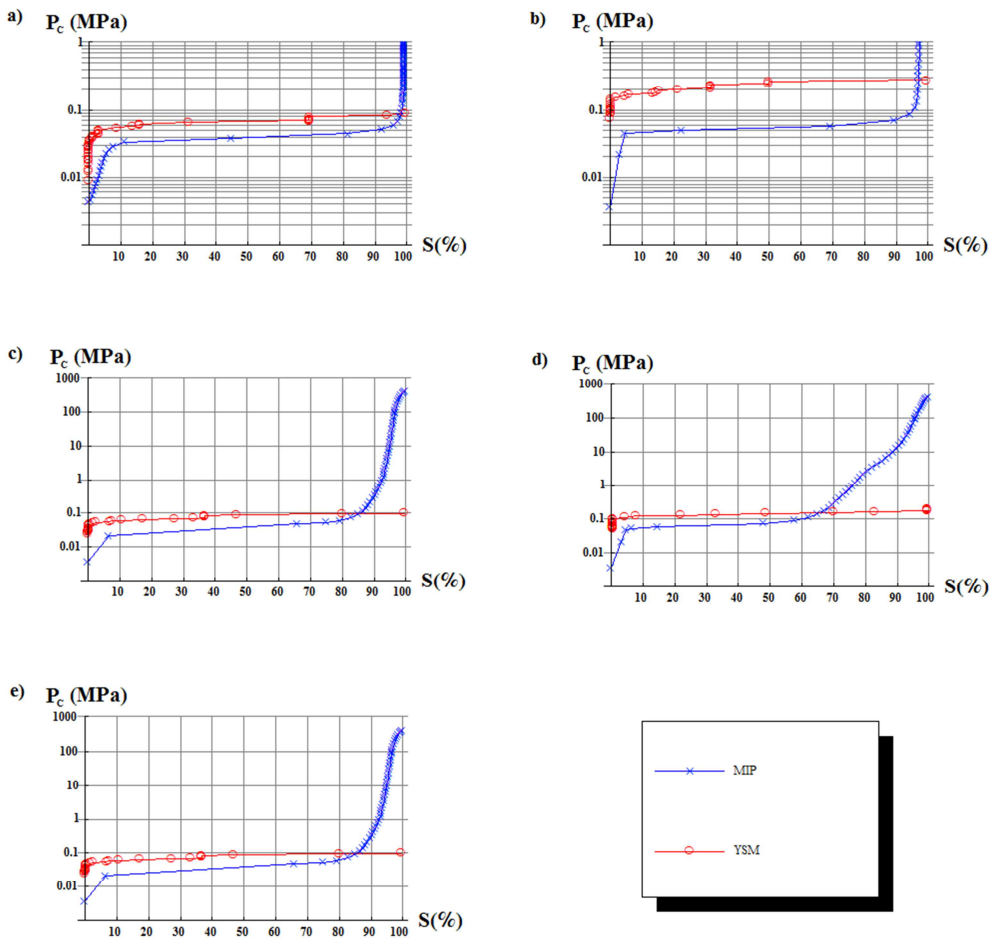


**Figure 95:** Capillary pressure as a function of the saturation of mercury measured with MIP compared with those calculated from the PSDs obtained with YSM by using  $\theta = 140^\circ$ , and  $\sigma = 0.485 \text{ N m}^{-1}$ .

By considering the consequences of directly transforming the PSDs obtained with YSM into  $P_c(S)$  by using this procedure one can draw the following conclusions:

- The pore size classes  $r_i$  calculated through YSM are intimately linked to the constrictions of porous media. In effect, the method is based on the measure of  $\Delta P$ ,

which is dominated by pore constrictions. Therefore, we consider here in first approximation that the flow of a yield stress fluid through a pore will occur only when the pressure gradient is high enough to produce flow through a cylinder having the same length as the pore and the same radius as the constriction.

- As a consequence, when using Eq. (6.1) to obtain  $P_c$ , it is implicitly assumed that the whole pore volume will be only saturated once the applied pressure is greater than the one required to penetrate its narrowest constriction.
- Hence, the capillary pressure corresponding to a given saturation must be greater in the case of YSM than in the case of MIP. It is schematically shown in Figure 96, where an idealized porous medium with only three pores is considered. For the same reasons, PSDs calculated from MIP yield larger pores than those resulting from YSM.

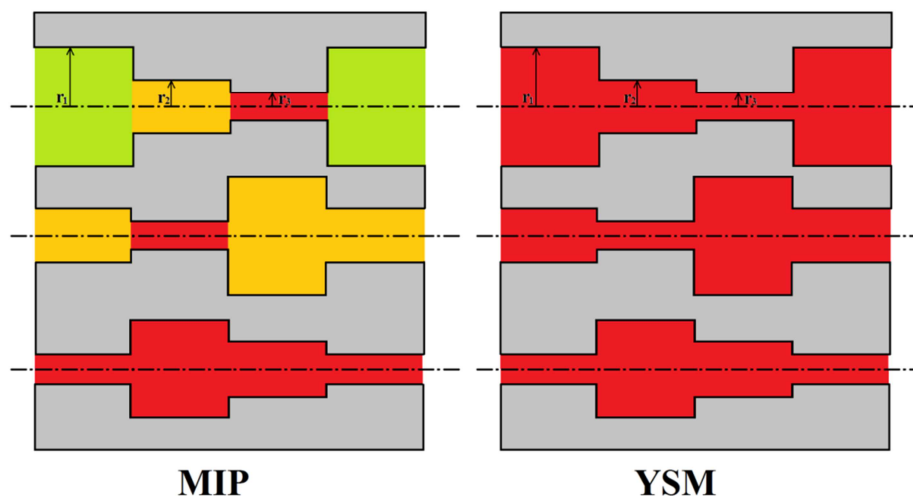


**Figure 96:** Representation of an ideal porous medium with only 3 pores showing the interpretations of saturation by both methods. Grey regions represent the solid volume. Non-grey regions represent the volume of the pores saturated with a capillary pressure of  $P_{c1} = -\frac{2\sigma\cos\theta}{r_1}$  (green),  $P_{c2} = -\frac{2\sigma\cos\theta}{r_2}$  (orange),  $P_{c3} = -\frac{2\sigma\cos\theta}{r_3}$  (red) in each case.

Returning to Figure 95, it is remarked that for all these materials there is a critical value of  $P_c$  above which  $S$  increases abruptly. This critical value measured by MIP is of the same order, although lower than the one calculated from PSDs provided by YSM. It is consistent with the arguments above. Besides, while in MIP capillary pressure curves a further increase of  $P_c$  is needed to attain the highest saturations after the plateau, this is not the case for YSM. In fact, these high capillary pressures are due to the smallest pores, which are not scanned with YSM. The reason is that their analysis with YSM would require the imposition of very high pressures and flow rates which are not possible with the current experimental setup. In fact, mercury porosimeters contain a number of pressure sensors adapted to the several orders of magnitude of pressure imposed during a test.

In view of the objective of replacing MIP for  $P_c$  determination, it is important to obtain relationships between the PSD delivered by YSM and the  $P_c$  curve. It implies finding a link between the pore radius classes obtained with YSM and the pore radius classes associated to

the pressures needed to saturate a porous medium with a non-wetting fluid. A first approach to achieve that objective is addressed here. Let us begin by assuming as before that the pressure drop along a percolating path is located exclusively in its narrower constriction. In this case, we can notice that the PSD (in number and not in volume) delivered by YSM represents the number  $n_i$  of percolating paths whose narrower constriction has a radius  $r_i$ . The total number of percolating paths is  $\sum_i n_i$ . However, the volume of the constrictions is not representative of the whole volume of the percolating paths, so  $\sum_i n_i \pi r_i^2 \ll \varepsilon \pi R^2$ . Let us assume now that all percolating paths have the same volume, which are completely contained in “pore bodies” of length  $L$  whose volume is  $\varepsilon L \pi R^2 / \sum_i n_i$ . Therefore, the radius of the “pore bodies” will be  $r_{body} = \sqrt{\varepsilon R^2 / \sum_i n_i}$ . A percolating path whose pore body radius is  $r_{body}$  and whose minimum constriction has a radius  $r_i$  will be saturated with a non-wetting fluid at pressures ranging from  $(-\frac{2\sigma \cos \theta}{r_{body}})$  to  $(-\frac{2\sigma \cos \theta}{r_i})$ . As a first approximation, we consider that a percolating path will be saturated with non-wetting fluid when pressure of  $(-\frac{2\sigma \cos \theta}{\frac{r_{body} + r_i}{2}})$  is applied. By taking into account these considerations, one may transform the PSDs obtained with YSM in its equivalent “Capillary-pressure PSDs” by using the next expressions:

$$\tilde{r}_i = \frac{r_{body} + r_i}{2} \quad (6.3)$$

$$\widetilde{p(r_i)} = \frac{n_i}{\sum_i n_i} \quad (6.4)$$

where  $\tilde{r}_i$  is the “capillary-pressure-equivalent” pore radius class and  $\widetilde{p(r_i)}$  its volume or number equivalent probability.

The “Capillary-pressure PSDs” corresponding to the experiments performed in Section 4.3 and their resulting  $P_c$  curves are presented in Figure 97 and Figure 98 together with MIP results. Good agreement is found between both methods, especially for natural media (Samples 3-5). In particular, the horizontal plateau of  $P_c$ , is well predicted. Further information can be obtained through interpretation of the PSDs obtained by YSM. Indeed,  $\sum_i n_i$  is an estimation of the total number of percolating paths and  $\bar{r} = \frac{\sum_i n_i r_i}{\sum_i n_i}$  is the average constriction radius. Therefore,  $r_{body}/\bar{r}$  can be used as an estimator of the pore to throat size ratio (listed in Table 16).

Our assumptions will be more realistic in the case where the pore to throat size ratio is high because we have supposed that all the volume is contained in the bodies and all the pressure drop is produced by the constrictions. It is effectively observed that better agreement between MIP and YSM is found when the pore to throat size ratio is high. In anyway, it is only a basic interpretation and further analysis will be required so as to provide reliable relationships by using other means.

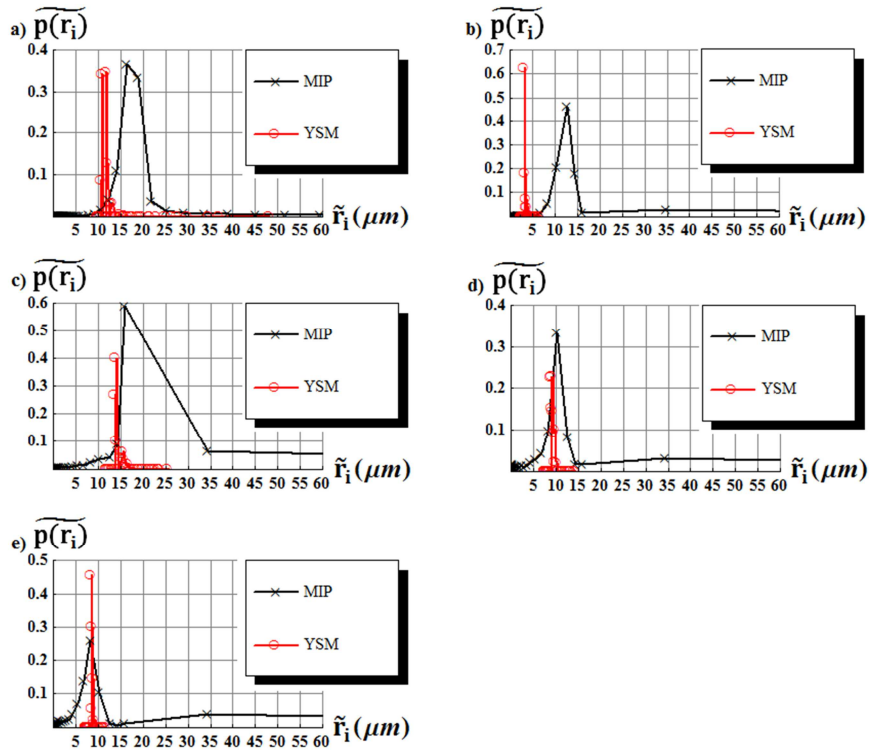


Figure 97: Capillary-pressure PSDs deduced from YSM corresponding to a) Sample 1; b) Sample 2; c) Sample 3; d) Sample 4; e) Sample 5 compared to the PSDs delivered by MIP.

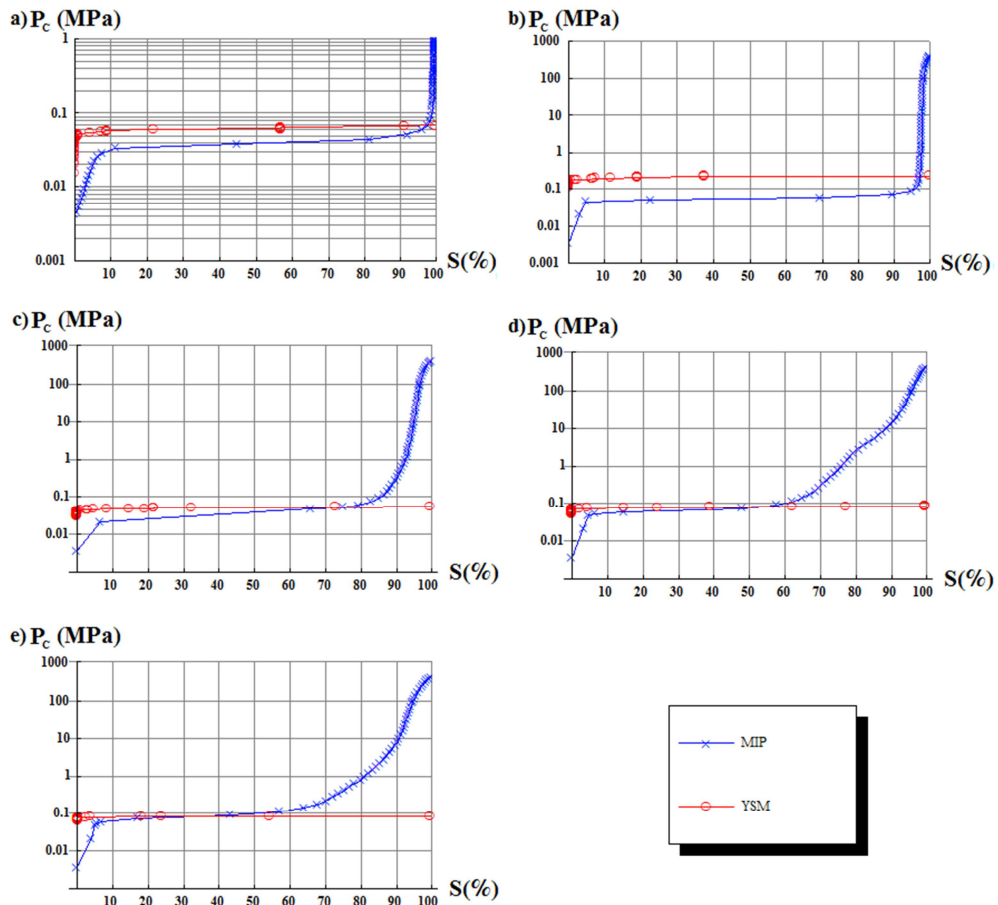


Figure 98: Capillary pressure as a function of the saturation of mercury measured with MIP compared with those calculated from the capillary-pressure PSDs deduced from YSM by using  $\theta = 140^\circ$ , and  $\sigma = 0.485 \text{ N m}^{-1}$ .

Sample	Pore to throat size ratio
1	1.26
2	1.19
3	2.10
4	2.7
5	4.20

Table 16 Pore to throat size ratio calculated using YSM.

### **5.1.5. Are the samples of porous media analyzed with YSM reusable?**

As indicated in subsection 2.1.4, one of the main flaws of MIP is that residual mercury remains trapped in the analyzed porous medium after a test. Consequently, the question is whether an YSM test alters the internal structure of the porous sample or not. In order to answer that question, the following procedure was followed: two typical YSM tests as those described in Section 4.3 were conducted on a sample of Berea Sandstone and in a sample of Aerolith A10 respectively. After the test, the Aerolith A10 was flushed with more than 20 pore volumes of demineralized water so as to remove the xanthan gum solution from pores. Then, the Hassler core holder was disassembled and the core was extracted and placed into a laboratory oven for 24 hours at 80°C. Flushing at high flow rates with water was not possible in the case of Berea sandstone because of high generated pressures (low-permeability core). Instead, the Hassler core holder was directly disassembled and the Berea sample was cleaned up by using a solvent extractor (Dionex™ ASE™ 350 Accelerated Solvent Extractor, Thermo Scientific). Once cleaned, it was also placed into a laboratory oven for 24 hours at 80°C. After the drying stage, the cores were placed into a desiccator for 6 hours. Finally, a MIP analysis was performed on each sample and the obtained PSDs were compared to the PSDs of native cores (see Figure 99).

It is noticed that no significant modification of the PSD obtained by MIP is produced after performing YSM tests on the samples. This suggests that the samples may be reusable in an experiment aiming to characterize the PSD.

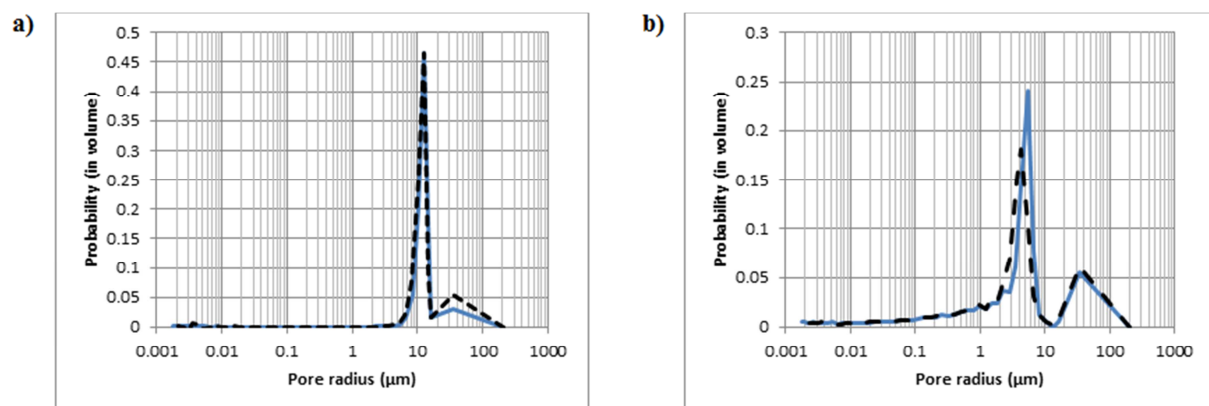


Figure 99: PSDs corresponding to the same sample of porous medium before (blue continuous line) and after (black dashed line) performing an YSM test with it. a) A10 sintered silicate; b) Berea Sandstone.

## **5.2. 3D microtomography**

Two of the materials analyzed with YSM in the preceding chapter were also studied with 3D microtomography at the CSTJF (TOTAL S.A.). Here, we will present some images of these materials as well as a first analysis aiming to deduce their PSDs. However, it should be recalled that obtaining PSDs from micro tomographies is a complex task, as explained in Chapter 2. Therefore, only a crude exploitation will be presented with the objective of drawing general conclusions about the advantages and drawbacks of this technique. Also, the obtained results will be compared to those coming from MIP in terms of PSDs and capillary pressure curves.

The porous media analyzed were an A10 sintered silicate and a Berea Sandstone. The dimensions of the samples were approximately 8 mm of diameter and 15 mm of length. During the experiments, a big set of 2D images corresponding to different slices along the axis of symmetry of the core were obtained with an X-ray microscope (520 Versa, Carl Zeiss X-ray Microscopy). It is worth recalling here that these images represent a volume (with a depth of 1 pixel) even if they are called 2D images for simplicity. Afterwards, 3D images were also constructed in both cases from combination of these 2D views.

### **5.2.1. Analysis of single 2D images obtained with microtomography**

A first image of the A10 silicate was obtained with the full section of the sample in the field of view (Figure 100). Its resolution was 4.29  $\mu\text{m}/\text{pixel}$ . No filtering was used in that image. From the observation of the image one can deduce that in spite of dealing with a synthetic rock, the pore space is far from being composed of regular forms. Also, small pores cannot be observed at that resolution. Consequently, another image (Figure 101) was taken at higher resolution ( $3.29\mu\text{m}/\text{pixel}$ ) from a  $(3 \times 3 \times 6) \text{ mm}^3$  volume. As explained before, grey pixels represent solid matter whereas black pixels correspond to void space. However, the color range is wide and it is not always evident to make that distinction in a raw image. Therefore, the image was segmented by defining a grey level threshold, giving the binary image shown in Figure 102. As already stated in Chapter 2, different criteria can be used to define the grey level threshold, so the resulting binary image is somewhat arbitrary. Then, it is possible to calculate the porosity from a 2D binary image by counting the number of void pixels over the total number of pixels. This provides a first estimation of the porosity of the sample which does not take account of heterogeneities along the axis of the sample. The porosity calculated from the A10 image was approximately 45%, which was close to the porosity as previously measured by other means.

A 2D image obtained for Berea Sandstone with a resolution of  $1.5 \mu\text{m}/\text{pixel}$  is presented in Figure 103. An important feature of this image is the presence of large white regions whose nature is not easy to determine but that probably correspond to clays. Indeed, Berea Sandstone is a natural porous medium with more constituents than the A10 sintered sandstone. Figure 104 shows the result of choosing different grey level thresholds to filter the raw image and noticeable differences are easily visible between both images. Moreover, the porosity

corresponding to each grey level threshold is significantly different, as indicated in the legend of the figure. Also, these porosities were inferior to the porosity measured in our experiments (close to 22%), indicating that a part of the porosity is not seen in the image because of its limited resolution.

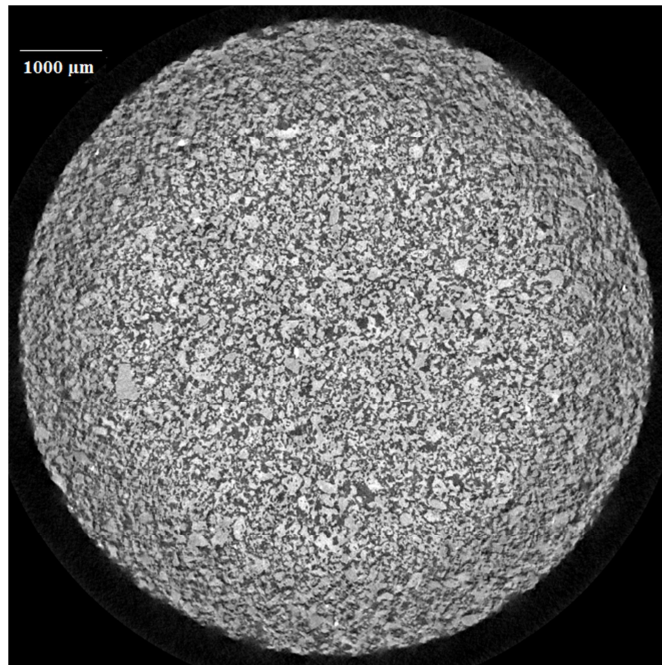


Figure 100: Microtomography of the sintered A10 silicate with the full section of the sample in the field of view. 4.29 μm/pixel resolution.

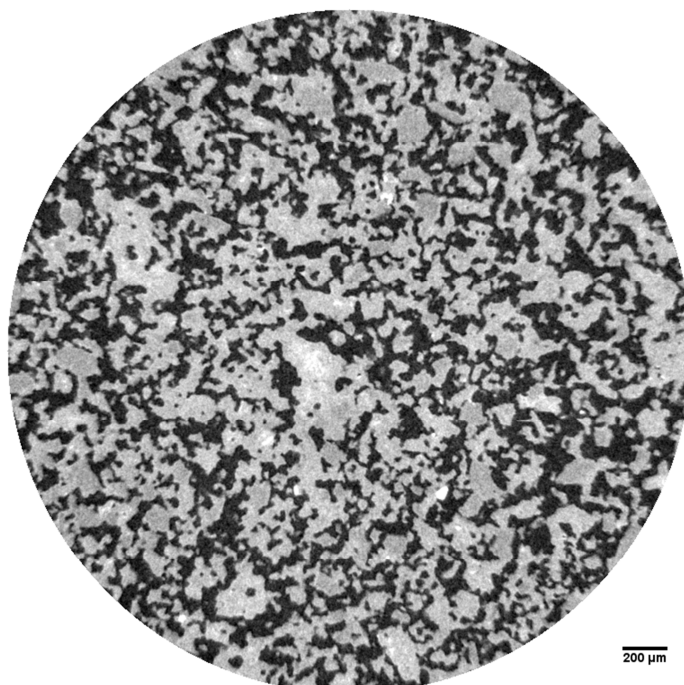
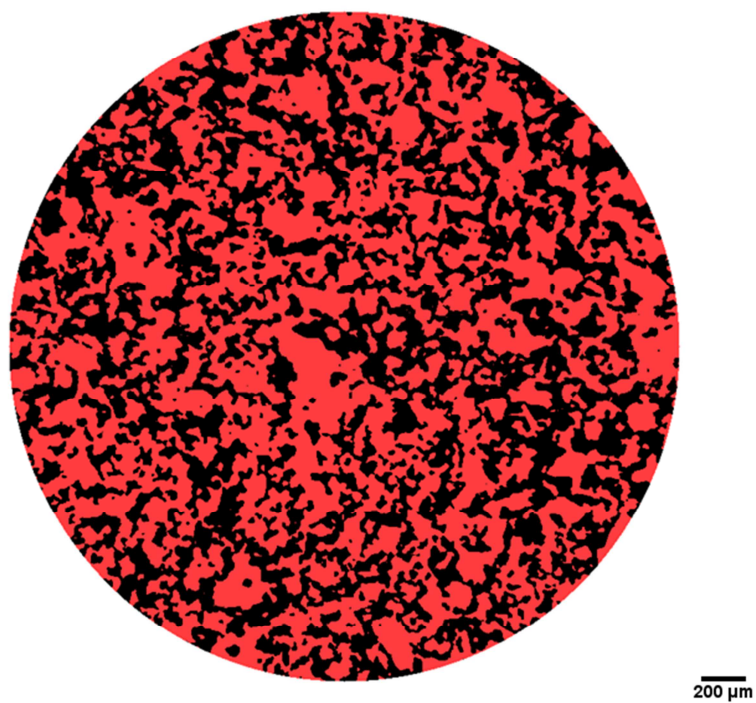
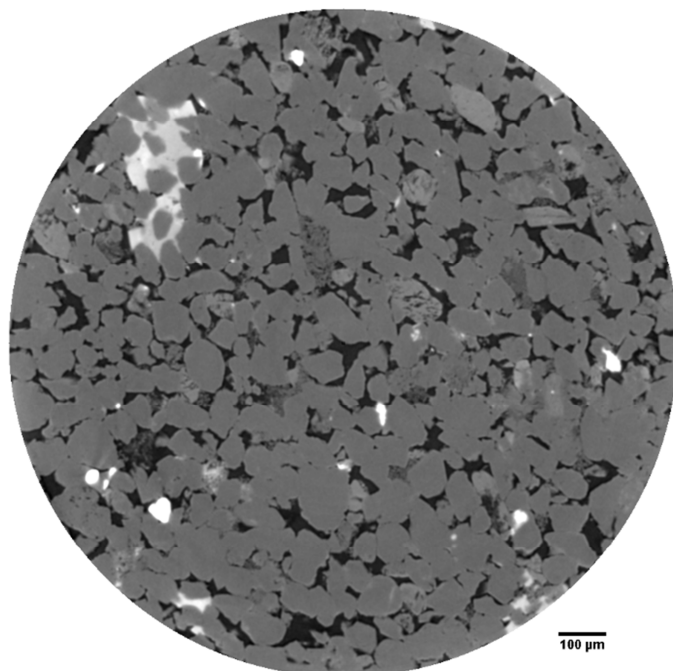


Figure 101: Microtomography of the sintered A10 silicate with higher resolution (3.29 μm/pixel) from a (3 x 3 x 6) mm<sup>3</sup> volume.



**Figure 102:** Segmented image of the sintered A10 silicate resulting from the image presented in Figure 101. Red color corresponds to solid matter whereas black color corresponds to void.



**Figure 103:** Microtomography of the Berea Sandstone with a resolution of 1.5 μm/pixel.

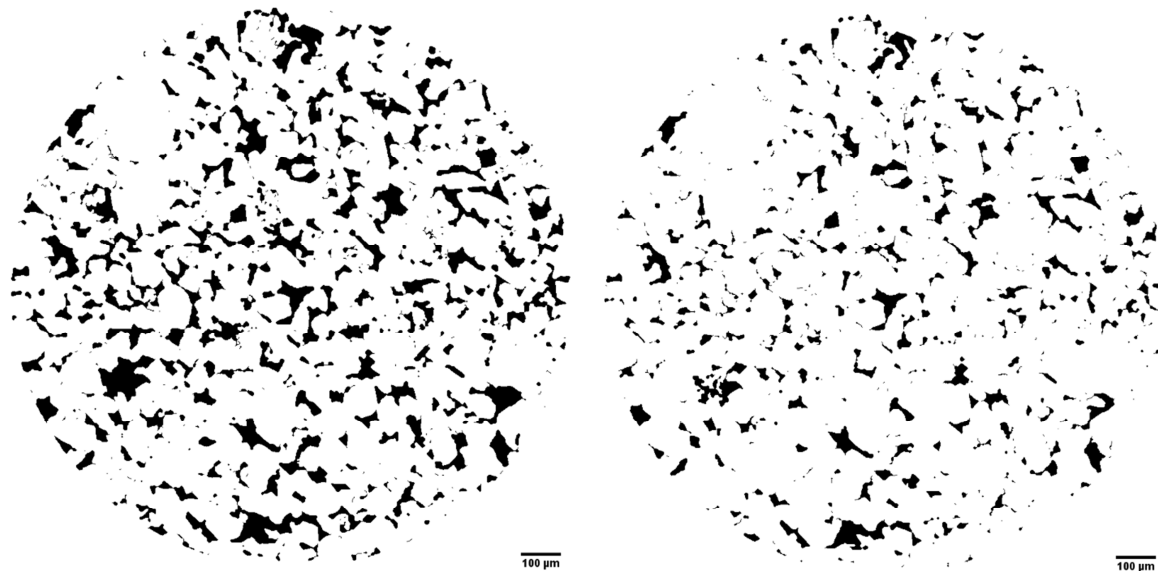


**Figure 104:** Binary images corresponding to the same original image. Different grey level thresholds were chosen in each case. The resulting porosities are 17% for the left image and 8% for the right image.

### **5.2.2. Comparison of the PSDs obtained with microtomography to those obtained with MIP.**

Calculation of the PSD from a 2D image is a complex task. The basic and simple procedure followed in this section is described here: first, the binary image was analyzed with the free software ImageJ so as to determine the isolated groups containing only black pixels in contact (void space), labeled as particles. Then, the holes within particles were filled with the protocol sketched in Figure 105. Afterwards, the area distribution of the particles was calculated. In this simple procedure, the pore size classes were calculated by assuming circular particles, so

the radius of a given particle is  $r_p = \sqrt{\frac{A_p}{\pi}}$ , with  $A_p$  being its area. The left image of Figure 104 was analyzed as explained, providing the PSD in frequency terms (number of pores with a given radius divided by the total number of pores) which is shown in Figure 106.

It has to be noted that the most frequent pore radii correspond to the minimum resolution of the image, suggesting that smallest pores are not seen in the image because of resolution limits. This PSD was expressed in terms of volume and is displayed in Figure 107 together with the PSD obtained with MIP for comparison. An important difference between the pore sizes given by each technique is thus evidenced. The PSDs coming from images of the pore space, such as those obtained by microtomography, represent the “optical” dimensions of all sections contained in the image. Therefore, both constrictions and pore bodies are considered in contrast with MIP method which is more sensitive to pore throats, demonstrating that PSD determination is method-dependent. These results agree with those previously presented in the literature for other imaging methods, e.g. those presented in Figure 108 (Dullien and Dhawan 1975). In fact, the PSD resulting from MIP are positioned in the “left tail” of the PSD derived

from microtomography just as the PSDs obtained with YSM overlap the “left tail” of the PSDs coming from MIP.

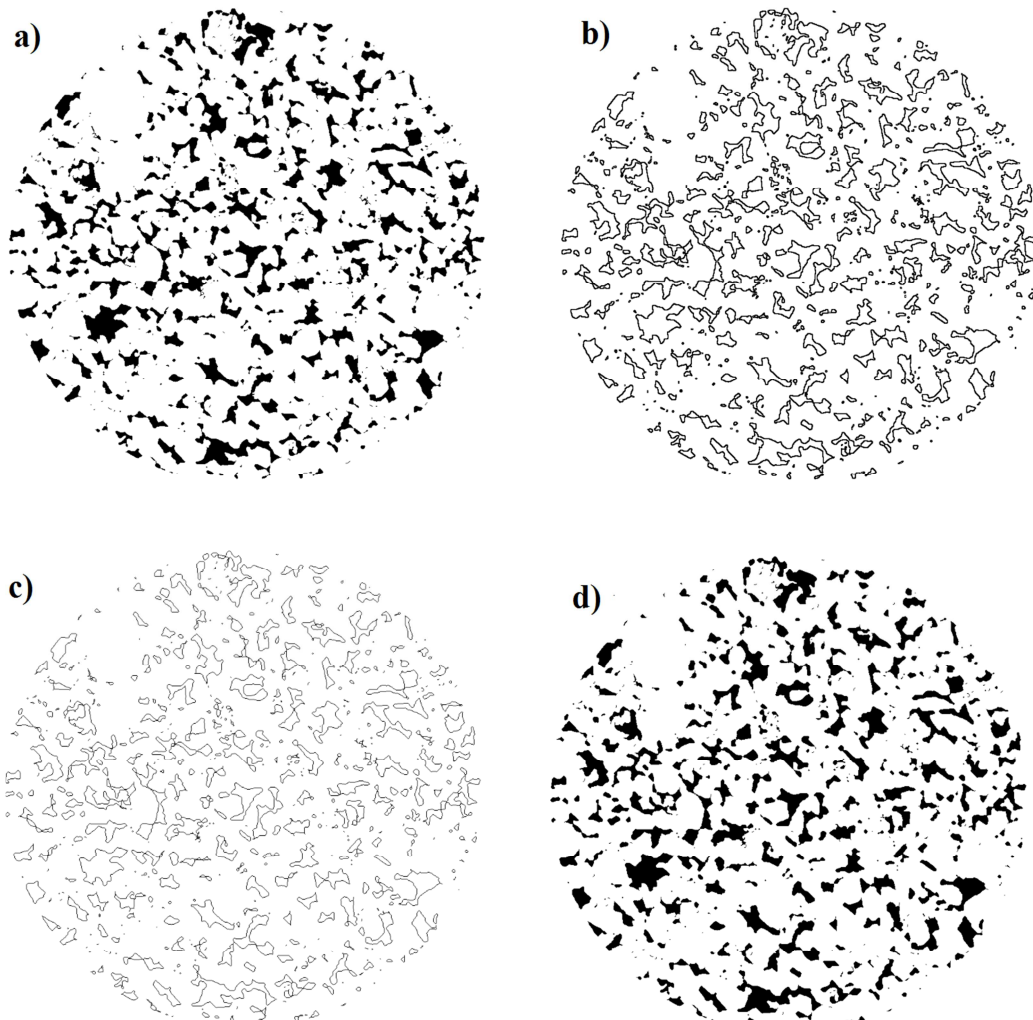


**Figure 105:** Protocol to fill the holes within the particles and to refine their edges: The original binary image a) is analyzed so as to determine the edges of the particles through the “Find edges” command of ImageJ. That step results in image b). Then the command “Skeletonize” is applied so as to reduce the edges of the elements to width of a single pixel, resulting in c). Finally, the “Fill holes” command is used, obtaining the image d).

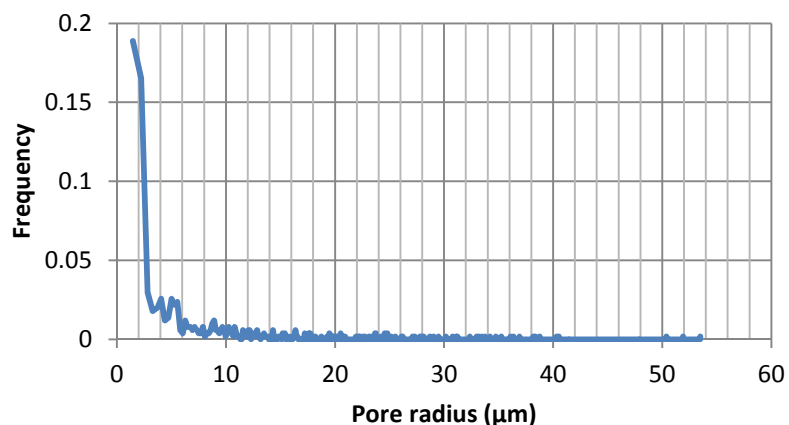


**Figure 106:** PSD in frequency (not in volume) for the 2D image of Berea Sandstone.

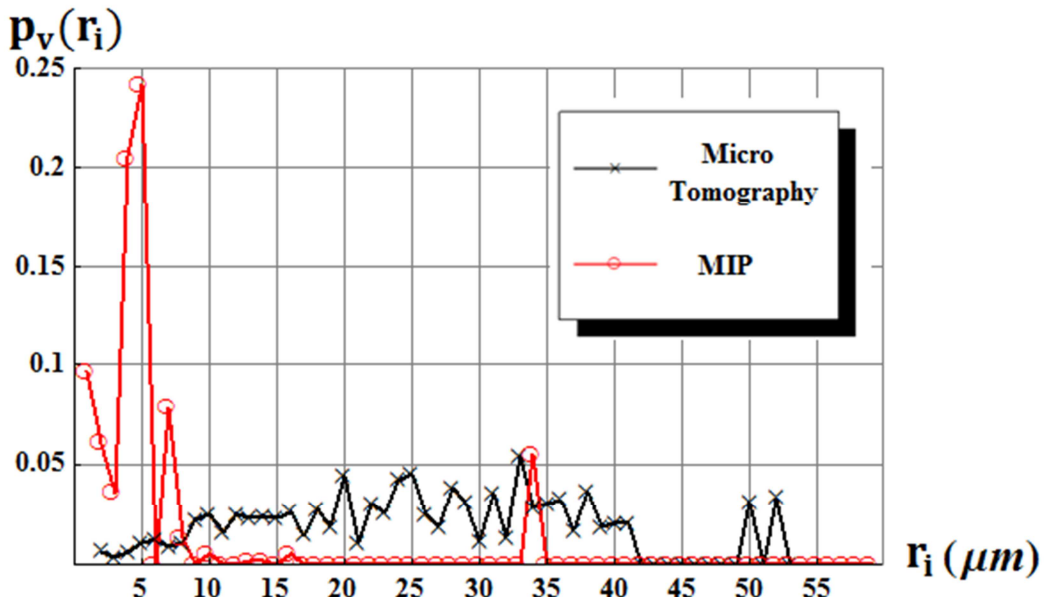


Figure 107: PSDs obtained from the 2D image (microtomography) of Berea Sandstone compared with the PSD delivered by MIP.

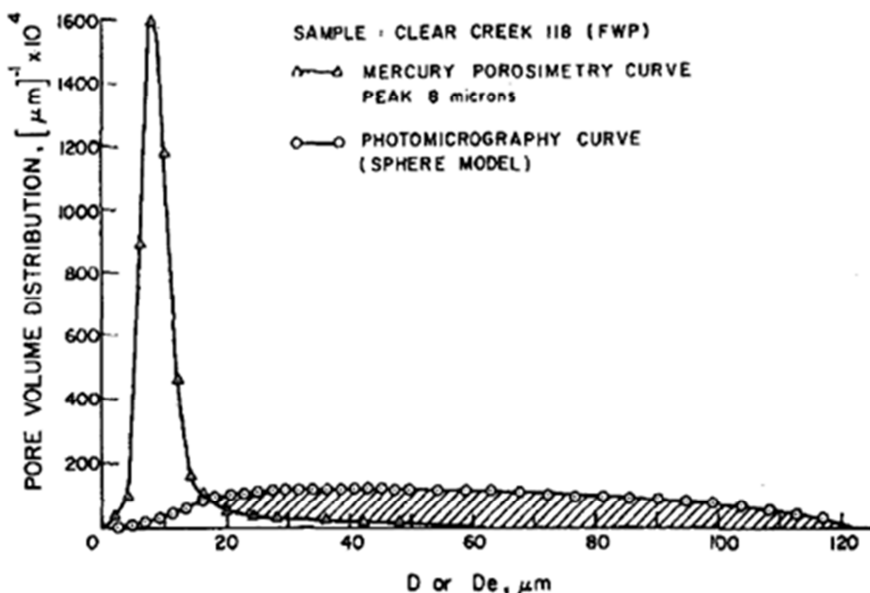


Figure 108: Comparison of the PSDs from MIP and from photomicrography for a sandstone (Dullien and Dhawan 1975). D is the pore diameter.

### 5.2.3. Analysis of 3D images obtained with microtomography

Up to now we have focused on the analysis of 2D images obtained from microtomography. Nevertheless, a 3D image can be reconstructed from combination of the acquired 2D image series. The information provided by a 3D image is more complete and representative of the sample. Figure 109 shows the PSD obtained from 3D microtomography of the A10 sintered silicate compared with that obtained by MIP. This PSD was provided by TOTAL S.A. and obtained following a procedure similar to the procedure proposed by Sheppard *et al.* (2005). Two different PSDs are presented: Pore Throat Size Distribution and Pore Body Size

Distribution. It is observed that the Throat Size Distribution is in good agreement with MIP, even if the smallest pores are not observed using microtomography. It is essential to understand that different definitions of pore lead to different PSDs for microtomography. It is clear that in the most basic version of MIP, PSDs represent the size of the constrictions (throats) that permit access to a given portion of the pore volume. That happens because MIP PSDs are obtained from  $P_c(S)$  measurements. One can notice that in the Pore Throat Size Distribution from microtomography presented in Figure 109, the pore geometries have been defined in such a way that they reproduce the results from MIP, at least for the material considered here. That implies that the resulting PSD is convenient to calculate  $P_c(S)$  curves. Other definitions of pore would indeed result in completely different PSDs.

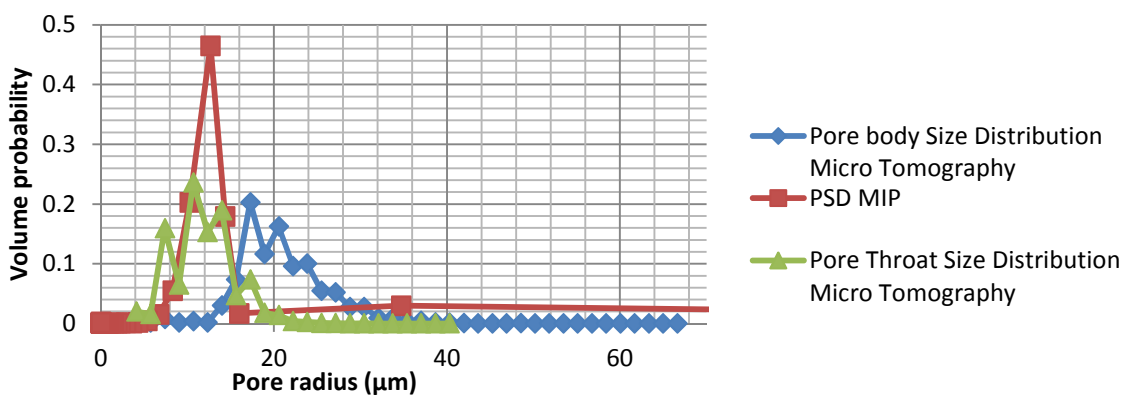


Figure 109: PSDs of the A10 sintered silicate obtained using MIP compared to those obtained using microtomography.

Further information may be obtained from 3D micro tomographies. As an example, the tortuosity distribution for the analyzed A10 silicate is presented in Figure 110. Tortuosity is defined here as the total length of the throat divided by the Euclidian distance between the centers of the pore bodies. The mean value of tortuosity in this case is 1.13. It is reminded here that tortuosity has been ignored in YSM. In fact, tortuosity would reduce the effective pressure gradient, which will entail increasing of pore sizes in the obtained PSD. In this case, the calculated pore sizes should be multiplied by 1.13, resulting in a PSD closer to that of MIP.

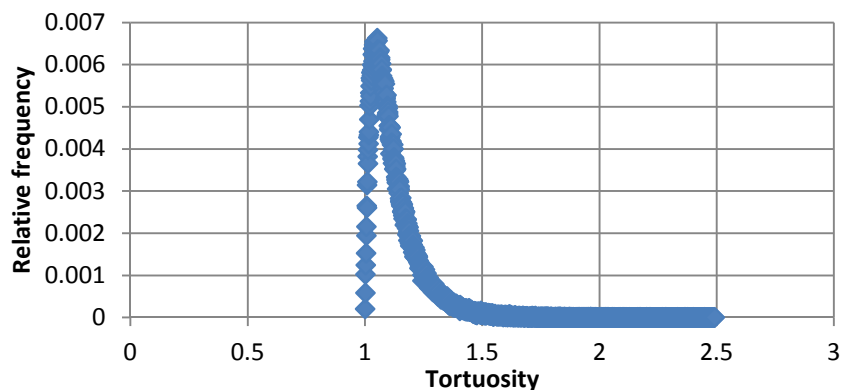
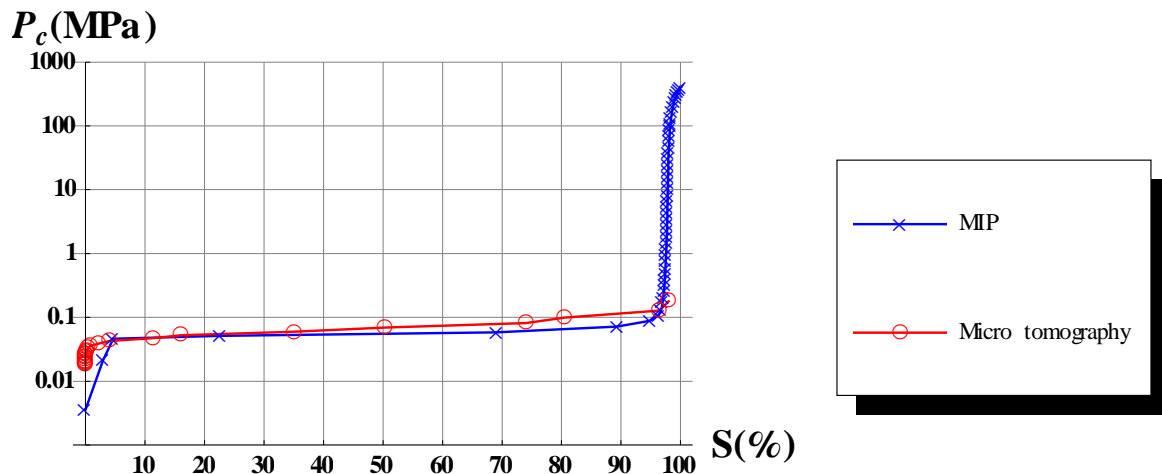


Figure 110: Tortuosity distribution of the A10 sintered silicate obtained from microtomography.

### **5.2.4. Capillary pressure versus saturation for microtomography, MIP and YSM**

As already done in subsection 4.3.4 dealing with YSM, the  $P_c(S)$  curves corresponding to the Pore Throat Distribution obtained by 3D microtomography have been calculated and are presented in Figure 111. Good agreement is found between the critical pressures in both cases. Smallest pores are not observed with this technique, so the final increase in pressure needed to attain the highest saturations is not predicted as happened with YSM. However, the reasons of that behavior are different. Indeed, small pores are not observed with tomography because of resolution limitations while higher flow rates imposed in YSM experiments should allow us to scan these pores. And even if the size of the xanthan molecules in the fluid and the slip effects are limiting factors in YSM, xanthan molecules are highly oriented with flow at the highest flow rates.

In any way, what can be concluded here is that microtomography is a useful technique to characterize  $P_c(S)$  provided that the definition of pores is appropriate. Nonetheless, this is precisely the unanswered question (in spite of recent progress): how to define pores so as to reliably calculate the petrophysical properties of interest (permeability,  $P_c(S)$ , etc.). Plougonven (2009) studied the relations between geometrical parameters of the porous microstructure extracted from micro tomographies and permeability to produce a pore network that can be used in numerical simulations.



**Figure 111: Capillary pressure as a function of the saturation of mercury measured with MIP compared with those calculated from the PSDs obtained with microtomography by using  $\theta = 140^\circ$ , and  $\sigma = 0.485 \text{ N m}^{-1}$ .**

## 6. Discussion, conclusions and prospects

Yield Stress fluids Method (YSM) includes some assumptions and modelling that have not been fully discussed so far. This final chapter provides the occasion to address in more detail some of the questions previously exposed. Moreover, final conclusions will be drawn from the results presented in this thesis and the guidelines for future work on this topic will be proposed in the last section.

### **6.1. Discussion**

Three main issues will be treated here: the pertinence of the bundle-of-capillaries model in YSM, the appropriateness of the Herschel-Bulkley model to approach the rheology of real yield stress fluids and the definition of pore size involved in each porosimetry method. This discussion takes up again some of the ideas presented in a recent paper of Rodriguez de Castro *et al.* (2014).

#### **6.1.1. Concerning the modelling of the pore space**

Let us begin by recalling that, as stated in section 2.1.2, the geometry of the pore space is so complex that any description implies the introduction of assumptions and simplifications. In effect, real porous media are of course not bundles of capillaries and it is obvious that this model is not the most realistic one and is therefore unable to take into account nonlinear opening up of pores especially in the vicinity of the yield pressure gradient (Balhoff *et al.* 2012). This is the result of a complex percolation pattern only predictable by solving the pore-level physics (Balan *et al.* 2011). The use of more complex models for porous media such as pore networks would imply the necessity of knowing more details regarding the pore geometry and connectivity (coordination number, pore body-to-pore throat aspect ratio, etc.). This information is not available unless other techniques such as microtomography and image analysis are used, as has already been emphasized by other authors (Rouquerol *et al.* 2012). Moreover, in simulations with pore networks a large but finite value of the viscosity is considered so as to emulate the yield stress (Sochi 2010; Talon and Bauer 2013). Despite recent efforts to simulate yield stress fluids flow through pore networks (Sochi and Blunt 2008; Balhoff and Thompson 2004), resolution of the pore-level physics is not possible without knowing “*a priori*” the pore topology.

The way to extend the present method to more representative models of pore space is to develop a relationship between the applied pressure gradient and the pore radius class joining the flow at this pressure gradient. In the case of a bundle of capillaries, this relationship is given by Eq. (2.33). Other relationships could be found for pore networks through simulation as suggested by the results of Sochi and Blunt (2008). The goal of the present work was to propose a simple method that allows determination of representative PSDs of real porous media without any input of topological parameters coming from other techniques. Besides,

without “*a priori*” knowledge of the structure, some geometrical parameters can be assumed fixed and an iterative process can be imagined for the determination of their value.

Finally, and as explained previously, the bundle of capillaries is also used in mercury porosimetry, so the present method will be at most “only” as bad as mercury porosimetry concerning the representativeness of pore morphology.

### **6.1.2. Concerning the rheology of the fluids used in the experiments**

Concerning yield stress fluids, they are generally complex media in which the dispersed objects are not negligibly small compared with smallest pores. So even if concentrated monosized emulsions can be considered as good candidates, the minimum pore size that can be probed is typically of a hundred nanometers (Mabille *et al.* 2000). Also, it is noticed that yield stress fluids such as Carbopol dispersions (Islam *et al.* 2004; Kim *et al.* 2003; Tiu *et al.* 2006), alumina suspensions (Zhu and Smay 2011; Hirata *et al.* 2010), or bentonite suspensions (Ambrose and Loomis 1933) are not recommended because of their inherent thixotropy and viscoelasticity. Besides, other fluids than xanthan gum solutions should be used to investigate porous media whose pore sizes are of the same order of magnitude as xanthan gum macromolecules in order to avoid pore-plugging phenomenon.

As presented in Chapter 2, some authors state that yield stress does not truly exist and is just an idealization due to limited measurement times and low experimental resolution. Long measurement times allow to observe a continuous increase in viscosity at the lowest flow rates, as argued by Møller *et al.* (2009) and verified for the fluids used here (Figure 112).

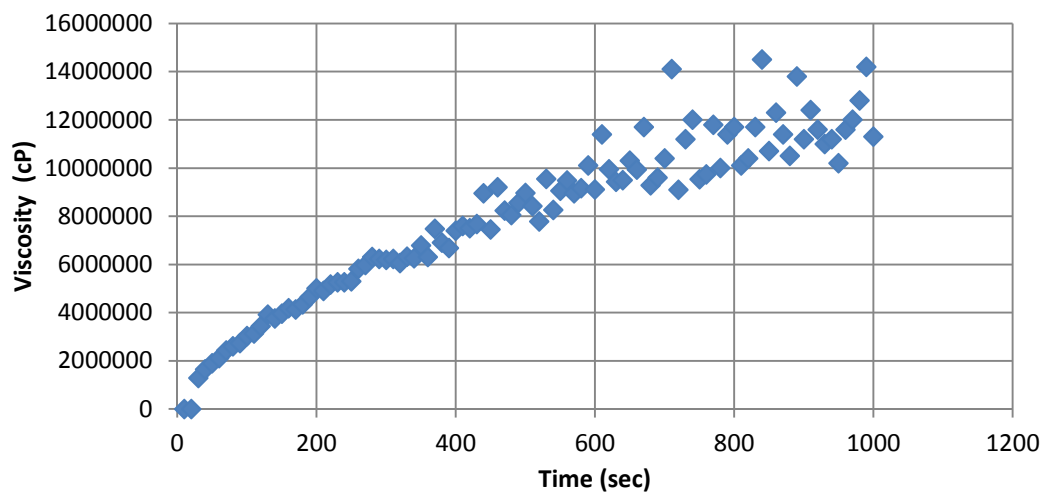


Figure 112: Evolution of the viscosity of Solution 2 over the time for a shear rate of 0.5 Pa (below the apparent yield stress). It is noted that no upper limited is attained after 1000 seconds.

Careful inspection of the rheograms of xanthan gum solutions at low shear rates shows that, strictly speaking, there is no such yield stress so at the involved time scale it is reasonable to consider that the rheology of xanthan gum solutions is better represented by a Carreau model featuring a low shear viscosity plateau. However, and as it has been put forward before, unfortunately no rigorous analytic relation expressing Q versus  $\nabla P$  in a capillary can be

obtained for this kind of fluid. Therefore, the use of an asymptotic rheological law (truncated power law) should result in errors of the same order or larger than those introduced using Herschel–Bulkley model to fit the rheological data. Moreover, to apply this model in the present method, it is necessary to define a “critical” viscosity above which a particular pore size class contributes only negligibly to the overall flow, and such “critical” viscosity would be analogous to a pseudo-yield stress. In any way, it is important that the shear-thinning character of the used fluid is sufficiently pronounced so that the fluid can be assimilated to a yield stress one (Sochi 2010). To our knowledge, this is best accomplished in the case of concentrated solutions of rigid polymers.

### **6.1.3. Concerning the apparent viscosity of the used fluids**

In this work, as in the literature (Sorbie 1991), it has been observed that the apparent viscosity of xanthan gum solutions flowing in porous media reproduced its bulk behavior when represented as a function of the shear rate, using the empirical shift factor  $\beta$ .  $\beta$  has been calculated in each case as being the value that produced the same onset of shear-thinning both in the porous medium and in the rheometer. However, two important questions remain: 1) is there actually an onset of shear-thinning for apparent viscosity in porous media? 2) And is the apparent viscosity as defined by Eq. (2.41) representative of the viscosity in the porous medium in the event of permeability reduction?

Before trying to answer these questions, let us insist on two special characteristics of the experiments presented above. The first of them is that the concentration of the fluids used here is higher than those usually used for flow experiments in porous media. In effect, most studies in the literature are limited to typically  $C_p = 1000$  ppm whereas  $C_p$  is considerably greater here. The other particularity is the wide range of flow rates imposed during the experiments.

With respect to the first question above, it is noted that even if several authors (Chauveteau and Zaitoun 1981; Sorbie 1991) have shown that apparent viscosity followed a Carreau model with a visible Newtonian plateau at low shear rates, their flow experiments were performed at low  $C_p$  ( $\sim 500$  ppm). Other authors, e.g. Cannella *et al.* (1988), whose experiments were carried out at a higher concentration ( $\sim 1000$  ppm) have shown that no Newtonian plateau actually exists for apparent viscosity at low shear rates and that shear thinning behavior is observed also at lowest shear rates. More recently, Seright *et al.* (2010), proved that the observed shear-thinning behavior at low shear rates is caused by retained high molecular weight polymer species and is an experimental artifact arising in short porous cores. In fact, this retention mostly produced in the region close to the inlet and does not penetrate deeply into the core, so the Newtonian plateau can be observed by measuring the pressure drop between intermediate regions of the sample. Returning to our experiments, Figure 66 shows that the only sample for which a Newtonian plateau is observed is Sample 1, whose length is twice that of the other samples. As a consequence, it is not totally convenient to fit apparent viscosity to a Carreau model, given that low shear rate viscosities may be affected by retention. Indeed, the “extra” apparent viscosity at low shear rates comes from the pressure

drops induced by a filtration cake instead of the viscosity of the fluid. That is proved by the fact that even if the viscosity of the outgoing fluid at the end of the experiments was lower than the one of the fluid before injection,  $\mu_{app}$  was still higher at the lowest flow rates.

With respect to the second question, it has been assumed that permeability was constant throughout the polymer flow experiments ( $R_K = 1$ ). Nevertheless, retention has been proved to exist at the lowest flow rates, so not only viscosity but also permeability depend on flow rate to some extent. Therefore, it is not strictly correct to use apparent viscosity as defined by Eq. (2.41) to represent the viscosity of the polymer in the porous medium. Alternatively, resistance factor  $R_M$  (Eq. 2.43) can be used to take into account both permeability reduction and viscosity increase (Sheng 2011, Seright et al. 2010). Permeability reduction due to polymer adsorption is also considered by using of  $R_M$ , even if  $R_K$  has been reported to be close to unity in the case of xanthan solutions as presented in subsection 2.3.3. From Eq. (2.43.) we can write:

$$R_{M_i} = \frac{K_{water}/\mu_{water}}{K_{polymer_i}/\mu_{polymer_i}} \cong \frac{K_{water}/\mu_{water}}{\frac{Q_i}{A \nabla P_i}} \quad (7.1)$$

where  $K_{polymer_i}$  is the permeability to polymer solution corresponding to the pressure gradient  $\nabla P_i$  at the flow rate  $Q_i$ , and  $A$  is the cross area of the core.

Following the same procedure as Seright (2010), the resistance factor corresponding to our experiments in different porous media has been represented as a function of the mean capillary bundle number (see Figure 113), which is defined as:

$$\text{Capillary bundle number}_i = \frac{\frac{Q_i}{A}(1 - \varepsilon)}{\sqrt{\varepsilon K_{water}}} \quad (7.2)$$

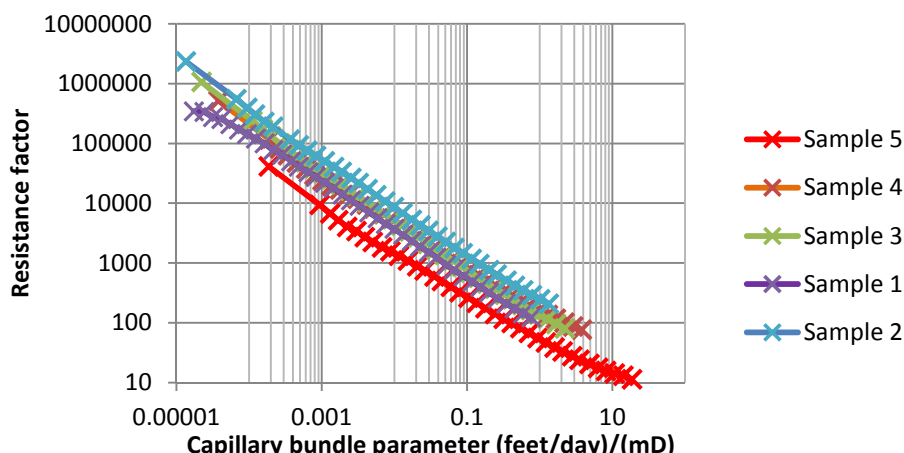


Figure 113: Resistance factor as a function of the capillary bundle parameter.

It is concluded that resistance factor correlates very well with capillary bundle parameter and the only deviation is observed for Sample 5 (Berea Sandstone). This deviation may come from the measurements of  $K_{\text{water}}$  in Berea Sandstone, which are strongly affected by clay swelling.

#### **6.1.4. Concerning the pore size determined by each method: are they directly comparable?**

From a fundamental point of view, one may wonder which characteristic size of the actual pores is determined using the present method and what the relevance of the use of the PSD deduced from MIP or microtomography is as reference PSDs. To address these questions it is firstly recalled that the experiments carried out here are essentially fluid transport experiments and, consequently, the pressure loss is mainly sensitive to hydrodynamic size of pore throats rather than size of pore bodies (Chauveteau 1996). Consequently, the present method is not appropriate when one is interested in determining characteristics such as specific surface. Besides, the PSDs obtained from mercury intrusion measurements are also dominated by pore throats, whereas pore bodies dominate in those PSDs calculated from mercury extrusion measurements. It is not then surprising that the PSD calculated with the present method are closer to those coming from mercury intrusion.

In general, PSD obtained by different methods may not be directly comparable. This aspect has to be kept in mind when comparing MIP results with other techniques such as tomography, whose results make a distinction between pore bodies size distribution and throats size distribution. Wardlaw *et al.* (1988) compared MIP distributions on carbonates with those obtained by means of an optical microscope finding poor agreement between them, especially with regard to the small pores. Vergés *et al.* (2011) applied two numerical (computed-based) methods to 3D micro-tomographies in order to obtain virtual pore representations of the pore network. They calculated the PSDs from these pore networks and compared them with the results obtained from MIP, finding significant differences between both methods in the region above the images resolution.

Chauveteau *et al.* (1996) studied the relationship between the equivalent hydrodynamic diameter of a pore  $d_h$ , the minimum pore throat diameter  $d_{\min}$  and pore throat diameters derived from MIP tests  $d_{Hg}$ .  $d_h$  is the diameter of a cylindrical capillary having the same pore length and giving the same pressure drop for the considered flow rate.  $d_{\min}$  is the minimum pore throat diameter and  $d_{Hg}$  is the pore throat diameter derived from MIP and calculated from the pressure required to invade 50% of pore volume. In porous media where pore throats are much smaller than pore bodies (pore body-to-pore throat radius  $\approx 3$  to 5 in common cases), it can be supposed that viscous dissipation is localized only in pore throats, so  $d_h$  is the throat diameter. As a consequence  $d_{Hg} > d_h > d_{\min}$ .  $d_h$  is related to permeability,  $d_{Hg}$  is related to capillary pressure and  $d_{\min}$  is important when dealing with particles retention, filtration, etc. In the same paper, the authors stated that  $d_{Hg} = d_h$  only in unrealistic porous media in which all throats had the same diameter.  $d_{Hg} \approx 1.2 d_h$  for bead packs and  $d_{Hg} \approx 1.9 d_h$  for sandstones

consolidated by deposit (Figure 114). It is remarked that if the pore size classes obtained with the present YSM method are transformed in this sense, they agree quite well with MIP. Moreover, the synthetic rock of Sample 1 possesses the narrowest PSD and is therefore the porous medium for which MIP is closely approaching YSM. Also, the authors obtained that  $d_{Hg} \approx 3$  to 4  $d_{min}$  and  $d_h \approx 2 d_{min}$ .

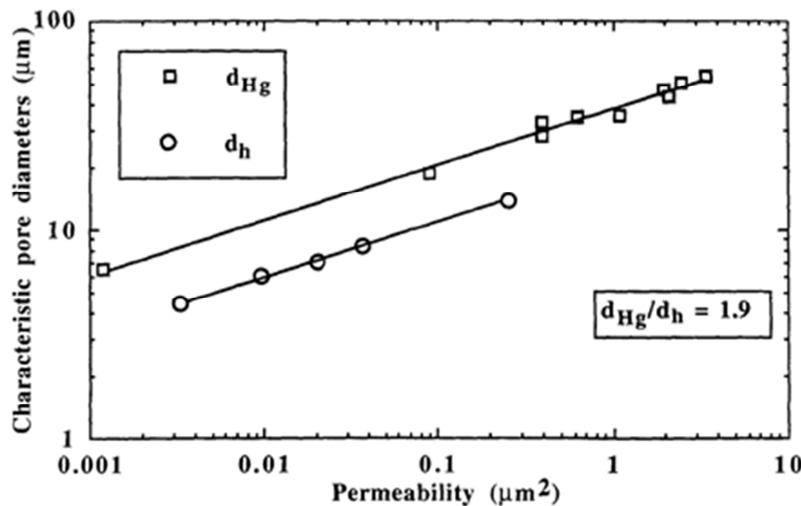


Figure 114: Characteristic pore throat diameters for Fontainebleau sandstones showing 0.25 power law dependence between  $d_h$ ,  $d_{Hg}$  and  $K$  (Chauveteau *et al.* 1996).

The use of MIP as a reference method when PSDs are devoted to calculate  $P_c(S)$  is justified, because  $P_c(S)$  is directly measured with this technique. However, MIP should not be considered as the reference method for all applications, even if it is often the case simply by tradition or because it is a routine technique. As stated by Lassen *et al.* (2008): “Unless mercury use for porosimetry is regulated, it is likely that the further development and implementation of alternatives will be slow. The measurement of pore characteristics is based on analysis standards, and establishment and a wide use and acknowledgement of new standards usually take time. Also, the alternative methods do not measure exactly the same characteristics as the mercury porosimeter, and therefore a change in methods will require the users to carry out research on comparability between the methods”. Therefore, the present work should be considered as a contribution toward this objective.

In other respects, it is important to emphasize that the range of pore sizes that can be scanned with each porosimetry technique is restricted. This is of major importance when dealing with sedimentary rocks, whose pores differ in size by several orders of magnitude. In that case, Radlinski *et al.* (2004) showed that the use of several techniques is needed to cover the whole range of pore radii from 20 Å to 500 μm in a sandstone from an oil reservoir in central Australia. The smallest pore size observable with microtomography is limited by technical resolution. However, MIP can be used to analyze a wide range of pore sizes. It is also true for YSM, provided that a yield stress fluid with appropriately small particles is used. The pressure  $P$  to be imposed for the analysis of a given pore radius  $r_i$  with MIP is given by  $P = -\frac{2\sigma\cos\theta}{r_i} \approx \frac{0.74}{r_i}$ . The pressure needed to characterize pores of radius  $r_i$  with YSM is

$P = \frac{2\tau_0 L}{r_i} \approx \frac{1}{r_i}$  (with  $\tau_0=10$  Pa and  $L = 0.05$  m). Consequently, the required pressures on laboratory scale are of the same order of magnitude in both methods.

## **6.2. Conclusions**

A new porosimetry method to characterize PSD of porous media has been presented in this thesis, in a context of international consensus on the need to develop alternatives to toxic mercury porosimetry. It is based on flow experiments of yield stress fluids through porous media. A procedure that permits to calculate the PSD from  $Q(\nabla P)$  measurements has been developed and numerically validated through “*in silico*” experiments. Moreover, the influence of several fluid and measurement parameters on the “quality” of the obtained PSD has been studied. It has been shown that errors in flow index and random noise in the  $Q(\nabla P)$  measures appear to be the most influencing sources.

An appropriate protocol for experimental implementation of YSM has been determined on the basis of conclusions drawn from preliminary experiments. Aqueous xanthan solutions have been selected as “yield stress” fluids. Then, a series of experiments have been carried out so as to analyze the effect of polymer concentration on the calculated PSD. It has been shown that the more the solutions are concentrated, the better the ideal behavior of yield stress fluids is approached and the closer the obtained PSDs are to those derived from MIP. Other series of experiments have been carried out with the same fluid and different porous media in order to study the influence of the type of porous medium on the obtained PSD. PSDs have been found to be coherently arranged with respect to the average radius from Eq. (2.2). Hence, it can be concluded that YSM is valid as a technique to measure representative PSDs.

Moreover, the apparent viscosity of the used “yield stress” fluids in the porous media has been characterized and compared to the effective viscosity measured with a rheometer. In accordance with published literature, both rheologies are similar apart from a shifting factor  $\beta$  that scales the shear rate in porous media. However, this factor  $\beta$ , which was traditionally linked to the pore geometry, has been proved to depend in the range of apparent shear rates experienced by the fluid in the porous medium. Also, the global behavior of the fluid in the porous medium has been observed to be less shear-thinning than in the rheometer. These observations have been attributed in part to the unusually wide ranges of flow rates imposed during the experiments.

The importance of polymer adsorption, polymer retention and mechanical degradation has been also assessed by means of complementary measurements of density and viscosity of the ingoing and outgoing fluids in the porous media. Whereas no sign of important adsorption and mechanical degradation has been observed, polymer retention has been shown to be important at the lowest flow rates due to the random orientation of the polymer molecules at these flow rates. That poses a concern regarding the characterization of small pores, so additional stages such as intermediate flushing should be investigated. Besides, a modified YSM aiming to obtain smooth  $Q(\nabla P)$  data, reduce the effect of random noise and increase accuracy at low

flow rates has been proposed, even if its application and potential still have to be further analyzed.

YSM has been compared to other porosimetry methods, i.e. MIP and microtomography. The PSDs obtained by these methods do not coincide in all cases as expected and the main reasons of that have been explained (represented pore dimensions are not the same). Due to its industrial interest,  $P_c(S)$  curves corresponding to each method have been obtained through a simple procedure. Evidently, MIP is the more appropriated method to obtain  $P_c(S)$  curves because they are directly measured during the tests. Nevertheless, a right definition of the correspondence between the pore dimensions characterized by each technique may lead to good estimations of  $P_c(S)$  curves using the other methods. Results from 3D microtomography have also been used to illustrate that it is highly complex to find a definition of pore geometries able to reproduce the PSDs characterized by other methods. In fact, “optically” observed pore dimensions may greatly differ from the results of other techniques if only intuitive criteria are used for such interpretation of microtomographies.

Definitely, YSM experiments are very simple. Only the measure of  $Q(\nabla P)$  is required to characterize PSD, which is a routine task in most petrophysics laboratories. As a consequence, the operators do not need any specific training and the experiments can be easily assembled. Besides, it is inexpensive because no special equipment is necessary as is the case for other porosimetry techniques (mercury porosimetry, microtomography). In fact, this advantage is not negligible if we take into account that the prices of an X-ray microscope and a mercury porosimeter are around 1,000,000 € and 50,000 € respectively. Furthermore, YSM can be applied to a wide range of porous media, is a flexible technique and is nontoxic.

Finally, a discussion on the modelling of the pore space and the fluid rheology has been presented. It has been highlighted that the complicated geometries of pore space combined with the complexity of non-Newtonian behavior, and especially of yield stress fluids, impose the use of simplifying assumptions to describe the flow of these fluids through porous media. The precise pore dimensions that are characterized by each method have also been discussed. It is worth insisting on the fact that a broader definition of PSD is essential. PSD must be conceived as a set of application-oriented probability functions, each of them being pertinent only for a particular use.

Summarizing, it can be concluded that a comprehensive exploratory work on the experimental feasibility of a new porosimetry method based on the injection of yield stress fluids has been presented. Numerous aspects of such a method have been discussed and its trickiest points have been identified, raising some yet unresolved issues. However, YSM has big potential as a porosimetry method, not only to calculate PSDs related to permeability but also to obtain  $P_c$  curves if a right relationship between the determined pore dimensions is used. Moreover, an undeniable advantage of YSM is the simplicity of experiments and the fact that they are inexpensive and easy to set up. Also, YSM is nontoxic, versatile and can be used to characterize different types of porous media. For instance, YSM would be useful to

characterize unconsolidated porous media for which MIP and other currently used methods are not efficient.

### **6.3. Prospects**

As already explained, even if the method presented in this thesis has been shown to have a big potential, it must still be consolidated, and its reliability has to be improved. Some guidelines proposed for future work are presented here.

The modified YSM for laboratory experiments presented in Section 4.5 has not yet been fully explored. The effect of increasing the number of data through evaluation of fitting functions may be assessed, as well as extrapolation of data to unattainable flow rates. That may result in an increase in the robustness of the method.

One of the main assumptions in YSM is no slip condition on solid pore walls. Consequently, it is necessary to check the validity of that hypothesis with the used fluids. One of the approaches that have already been explored but should be fully achieved is to conduct YSM tests in model porous media with known PSDs. Some possibilities that are being currently assessed are experiments in micro models and experiments in porous media produced through 3D printing. The main obstacle is the difficulty in fabricating porous media having pores smaller than typically  $10\text{ }\mu\text{m}$  with regular forms. A study in this respect was presented by Malvaut (2013). Nevertheless, the use of a different fluid and large pore dimensions of the porous media in those experiments do not permit extrapolation to our method. Other aspects that may be explored with model porous media are the effect of the irregular shape of the pores and their connectivity. Experiments in micro models will be useful to achieve that goal and to adapt the present YSM to more complex models of pore space. Also, by using model porous media with increasing complexity going from a bundle of capillaries to 2D micro models, the assumption of simple shear rate may be evaluated.

Xanthan gum aqueous solutions have been selected among several candidate “yield stress” fluids because of their more convenient behavior in porous media: reduced viscoelasticity, non-thixotropic, limited adsorption, etc. Nevertheless, other fluids are needed in the cases in which the size of the xanthan molecule is not negligible with respect to the size of the pores. A protocol to produce quasi mono disperse oil-in-water emulsions with a size of typically  $1\text{ }\mu\text{m}$  was developed and the rheology of these fluids was characterized (see Annex C). However, the lowest size of the droplets that was obtained is not as low as needed as stated before. Therefore, formulation and fabrication other types of fluids can be considered as an important research theme in relation with this method.

Given that  $P_c(S)$  curves are of great industrial interest, it is important to study their link with the pore dimension characterized by YSM. A key parameter that might help to achieve that goal is the body-to-pore throat radius. In fact, the dimensions characterized with YSM are related to pore throat radii, which are in turn related to the pressure to overcome in order to access a given pore volume. However, the magnitude of the pore volume accessed once the

throat has been penetrated (increase in saturation) is determined by the pore body radii. Knowledge of the body-to-pore throat radius may then be very useful. In fact, a procedure that has not yet been fully explored is estimation of that parameter from the ratio between measured porosity and the one provided by the PSD obtained through YSM. The ratio between measured and calculated permeabilities could also be analyzed.

Now that polymer retention has been shown to exist at low flow rates, a modified experimental protocol has to be adopted so as to reduce its impact. A possibility would be to include intermediate flooding at high flow rates. Also, the installation of pressure sensors to measure the pressure drop between intermediate sections along the sample will permit to localize the zone of polymer retention and analyze the nature of the filtration cake.

## 7. References

- Abidin, A.Z., Puspasari, T., Nugroha, W.A., Polymers for enhanced oil recovery technology. *Proc. Chem.* **4**, 11–16 (2012).
- Adamson, A. W., *Physical Chemistry of Surfaces*, John Wiley & Sons, New York, 349 (1982).
- Ahmed, U., Crary, S.F., Coates, G.R., Permeability estimation, the various sources and their interrelationships. *JPT*, 578.Trans., AIME 291 (1991).
- Al-Kharusi, A.S., Blunt M.J., *Journal of Petroleum Science and Engineering* **56**, 219–231 (2007).
- Ambari, A., Benhamou, M., Roux, S., Guyon, E., Distribution des tailles des pores d'un milieu poreux déterminée par l'écoulement d'un fluide à seuil. *C.R. Acad. Sci. Paris t.311 (II)*, 1291–1295 (1990).
- Ambrose, H. A., Loomis, Loomis, A. G., Fluidities of Thixotropic Gels, Bentonite Suspensions, *Physics* **4**, 265 (1933).
- Balan, H.O., Balhoff, M. T., Nguyen, Q.P., Rossen, W.R., Network modelling of gas trapping and mobility in foam enhanced oil recovery. *Energy Fuels* **25** (9), 3974–3987 (2011).
- Balhoff, M. T., Lake, L.W., Bommer, P.M., Lewis, R.E., Weber, M.J., Calderin, J.M., Rheological and yield stress measurements of non-Newtonian fluids using a Marsh funnel. *J. Petrol. Sci. Eng.* **77** (3–4), 393–402 (2011).
- Balhoff, M. T., Sanchez-Rivera, D., Kwok, A., Mehmani, Y., Prodanovic, M., Numerical algorithms for network modelling of yield stress and other non-Newtonian fluids in porous media. *Transp. Porous Media* **93**(3), 363–379 (2012)
- Balhoff, M. T., Thompson, K. E., A macroscopic model for shear-thinning flow in packed beds based on network modelling, *Chemical Engineering Science* **61**, 698–719 (2006).
- Balhoff, M.T., Thompson, K.E., Modelling the steady flow of yield-stress fluids in packed beds. *AIChE J.* **50** (12), 3034–3048 (2004)
- Barnes, H. A., Hutton, J. F., Walters, K., *An Introduction to Rheology*, Elsevier, Amsterdam, (1989).
- Barnes, H., Walters, K., The yield stress myth? *Rheol. Acta* **24**, 323–326 (1985).
- Baudracco, J., Aoubouazza, M., Permeability variations in Berea and Vosges sandstones submitted to cyclic temperature percolation of saline fluids, *Geothermics* **24**, 661–677 (1995).
- Benmouffok-Benbelkacem, G., Caton, F., Baravian, C., Skali-Lami, S., Non-linear viscoelasticity and temporal behavior of typical yield stress fluids, Carbopol, Xanthan and Ketchup, *RheolActa* **49**, 305–314 (2010).
- Bensoussan, A., Lion, J.L., Papanicolaou, G., Asymptote analysis for periodic structures, North-Holland Publishing Compagny, Amsterdam, The Netherlands (1978).
- Bird, R., Armstrong, R. C., Hassager, O., *Dynamics of polymeric liquids 1*, Wiley (1977).
- Blando, J. D., Singh, D., Controlling Metallic Mercury Exposure in the Workplace: A Guide for Employers, revised ed., New Jersey Department of Health and Senior Services, Trenton, NJ (2004). <<http://www.state.nj.us/health/surv/documents/mercemp.pdf>>, Accessed 14 Feb 2014.
- Boudreau, B. P., The diffusive tortuosity of fine-grained unlithified sediments, *Geochimica et Cosmochimica Acta* **60**, 3139–3142, (1996).

- Brinson, H. F., Brinson, L. C., Polymer Engineering Science and Viscoelasticity, An Introduction, Polymer Engineering Science and Viscoelasticity, 327-364, Springer (2008).
- Burlion, N., Bernard, D., Chen, D., X-ray microtomography, Application to microstructure analysis of a cementitious material during leaching process, Cement and Concrete Research 36, 346–357 (2006).
- Cannella, W. J., Huh, C., Seright, R. S., Prediction of xanthan rheology in porous media. SPE 18089, Proceedings of the SPE 63<sup>rd</sup> Annual Fall Conference, Houston, TX (1988).
- Carman, P.C., Fluid flow through granular beds. Trans. Inst. Chem. Eng. 15, 150 (1937).
- Carnali, J. O., A dispersed anisotropic phase as the origin of the weak-gel properties of aqueous xanthan gum, Journal of Applied Polymer Science 43, Issue 5, 929-941 (1991).
- Carreau, P.J., Rheological equations from molecular network theories, Trans. Soc. Rheol. 16 ( 1972 ).
- Carrier, W. D., Goodbye, Hazen; Hello, Kozeny-Carman, Journal of Geotechnical and Environmental Engineering, ASCE? (2003).
- Carrier, X., Marceau, E., Lambert, J.-F., Che, M., Transformations of alumina in aqueous suspensions, Journal of Colloid and Interface Science 308, 429-437, (2007).
- Chaplain, V., Mills, P., Guiffant, G., Cerasi, P., Model for the flow of a yield fluid through a porous medium, J. Phys. II France 2, 2145–2158 (1992).
- Chauveteau, G., Rodlike Polymer Solution Flow through Fine Pores: Influence of Pore Size on Rheological Behavior, Journal of Rheology 26 (2), 111–142 (1982).
- Chauveteau, G., Kohler, N., Influence of microgels in Xanthan polysaccharide solutions on their flow through various porous media, S. P. E. 9295. 55<sup>th</sup> An. Techn. Conf. and Exhib., Dallas (1980).
- Chauveteau, G., Lecourtier, J., Propagation of polymer slugs through adsorbent porous media. In *Water Soluble Polymers for Petroleum Recovery*, eds. Stahl, G. A. and Schulz, D. N., Plenum Publishing Corp, New York (1988).
- Chauveteau, G., Nabzar, L., El Attar , L., Jacquin, C., Pore structure and hydrodynamics in sandstones, SCA Conference Paper Number 9607 (1996).
- Chauveteau, G., Zaitoun, A., Basic rheological behavior of xanthan polysaccharide solutions in porous media: effects of pores size and polymer concentration. Proceedings of the First European Symposium on EOR, Bournemouth, England (1981).
- Chen, M., Rossen, W., Yortsos, Y. C., The flow and displacement in porous media of fluids with yield stress, Chemical Engineering Science 60, 4183-4202 (2005).
- Cheng, D. C.-H., Yield stress: A time-dependent property and how to measure it, Rheological Acta 25, 542–554 (1986).
- Chevalier, T., Chevalier, C., Clain, X., Dupla, J. C., Canou, J., Rodts, S., Coussot, P., Darcy's law for yield stress fluid flowing through a porous medium, Journal of Non-Newtonian Fluid Mechanics 195, 57–66 (2013).
- Chhabra, R. P., Richardson, J. F., Non-Newtonian Flow and Applied Rheology (Second Edition), Engineering Applications, Elsevier (2008).
- Choppe, E., Puaud, F., Nicolai, T, Benyahia, L., Rheology of xanthan solutions as a function of temperature, concentration and ionic strength, Carbohydrate Polymers 82, 1228–1235 (2010).
- Clain, X., Etude expérimentale de l'injection de fluides d'Herschel-Bulkley en milieu poreux, PhD thesis, Paris-Est, Champs-sur-Marne, (2010).

- Clarkson, C.R., Solano, N., Bustin, R.M., Bustin, A.M.M., Chalmers, G.R.L., Hec, L., Melnichenko, Y.B., Radlinski, A.P., Blach, T.P., Pore structure characterization of North American shale gas reservoirs using USANS SANS, gas adsorption, and mercury intrusion. *Fuel* 103, 606–616 (2013)
- Cossé, R., Techniques d'exploitation pétrolière: Le Gisement, Institut Français du Pétrole et Editions Technip, Paris (1988).
- Coussot, P., Tocquer, L., Lanos, C., Ovarlez, G., Macroscopic vs. local rheology of yield stress fluids, *J. Non-Newtonian Fluid Mech.* 158, 85–90 (2009).
- Cross, M. M., Rheology of non-Newtonian fluids: a new fluid equation for pseudoplastic fluids, *New journal of colloid sciences* 20, 417–437 (1965).
- Darcy, H. J., “Les Fontaines Publiques de la Vue de Dijon.” Librairie de Corps Impériaux des Ponts et Chausées et des Mines, Paris, 590-594 (1856).
- Dario, A. F., Hortencio, L. M. A., Sierakowski, M. R., Neto, J. C. Q., Petri, D. F. S., The effect of calcium salts on the viscosity and adsorption behavior of xanthan, *Carbohydrate Polymers* 84, 669–676 (2011).
- De Gennes, P.-G., *Scaling Concepts in Polymer Physics*, Cornell University Press (1979).
- Dullien, F. A. L., *Porous Media: Fluid Transport and Pore Structure* (2nd edition), Howard Brenner, Academic Press (1991).
- Dullien, F. A. L., Characterization of porous media – pore level, *Transport in Porous Media* 6; 581–606 (1991).
- Dullien, F. A. L., Dhawan, K., Bivariate Pore-Size Distributions of Some Sandstones, *Colloid Interface Sci.* 52(1), 129–135 (1975).
- Epstein, N., *Chemical Engineering Science* 44(3), 777–779 (1989).
- European Chemicals Agency, Committee for Risk Assessment (RAC) and Committee for Socio-economic Analysis (SEAC), Background document to the opinions on the Annex XV dossier proposing restrictions on Mercury in measuring devices (2011).
- Galaup, S., Liu,Y., Cerepi, A., New integrated 2D–3D physical method to evaluate the porosity and microstructure of carbonate and dolomite porous system. *Microporous Mesoporous Mater.* 154, 175–186 (2012).
- Garcia-Ochoa, F., Santosa, V.E., Casasb, J.A., Gómez, E., Xanthan gum: production, recovery, and properties. *Biotechnol. Adv.* 18, 549–579 (2000).
- Giesche, H., Mercury Porosimetry : a General (Practical) Overview, Part. Part. Syst. Charact. 23, 1–11 (2006).
- Gomez, F., Denoyel, R., Rouquerol, J., Determining the Contact Angle of a Nonwetting Liquid in Pores by Liquid Intrusion Calorimetry, *Langmuir*, 2000, 16 (9), pp 4374–4379.
- Hirata, Y., Matsushima, K., Matsunaga, N., Sameshima, S., Viscoelastic properties of flocculated alumina suspensions during pressure filtration, *Journal of the Ceramic Society of Japan* 118, 977–982 (2010).
- Hunt, A., Ewing, R., Percolation Theory for Flow in Porous Media, *Lect. Notes Phys.* 771 (Springer, Berlin Heidelberg (2009).
- Iijima, M., Shinozaki, M., Hatakeyama, T., Takahashi, M., Hatakeyama, H., AFM studies on gelation mechanism of xanthan gum hydrogels, *Carbohydrate Polymers* 68, 701–707, (2007).
- INRS, Maladies professionnelles causées par le mercure et ses composés, <http://www.inrs-mp.fr/mp/cgi-bin/mppage.pl?state=1&acc=5&gs=&rgm=2>, Accessed 14 Feb 2014 (2003).

INRS, Valeurs limites d'exposition professionnelle aux agents chimiques en France : Aide-mémoire technique, <http://www.inrs.fr/accueil/produits/mediatheque/doc/publications.html?refINRS=ED%20984>, Accessed 14 Feb 2014 (2012).

Islam, M. T., Rodríguez-Hornedo, N., Ciotti, S., Ackermann, C., Rheological Characterization of Topical Carbomer Gels Neutralized to Different pH, *Pharmaceutical Research* 21, No. 7 (2004).

Jones D. M., Walters, K., The behavior of polymer solutions in extension-dominated flows with applications to Enhanced Oil Recovery, *RheolActa* 28, 482-498 (1989).

Kate, J.M., Gokhale, C.S., A simple method to estimate complete pore size distribution of rocks. *Eng. Geol.* 84, 48–69 (2006)

Kim, J.-Y., Song, J.-Y., Lee, E.-J., Park, S.-K., Rheological properties and microstructure of Carbopol gel network systems, *Colloid PolymSci* 281, 614–623 (2003).

Khodja, M., Les fluides de forage: étude des performances et considérations environnementales. PhD thesis, Institut National Polytechnique de Toulouse (2008).

Klein, J., The Onset of Entangled Behavior in Semidilute and Concentrated Polymer Solutions, *Macromolecules* 11, (1978).

Kohler, N., Chauveteau, G., Polysaccharide plugging behavior in porous media: Preferential use of fermentation broth, S. P. E. 7425, 53th An. Techn. Conf. and Exhib., Houston (1978).

Kolodzie, S., Jr., Analysis of pore throat size and use of the Waxman-Smits equation to determine OOIP in Spindle field, Colorado, SPE-9382 in 55<sup>th</sup> SPE annual technical conference proceedings: Society of Petroleum Engineers, 4 p (1980).

Kozeny, J., Ueber kapillare Leitung des Wassers im Boden. *Sitzungsber Akad. Wiss., Wien*, 136(2a), 271–306 (1927).

Larson, R. G., *The Structure and Rheology of Complex Fluids*, Oxford University Press (1999).

Lassen, C., Andersen, B. H., Maag, J., Maxson, P., Options for reducing mercury use in products and applications, and the fate of mercury already circulating in society, European Commission, Directorate-General Environment (2008).

Leal-Calderón, F., Shmitt, V., Bibette, J., *Emulsion Science, Basic Principles*, Second Edition, Springer Science+Business Media, LLC (2007).

Lindquist, W. B., Venkatarangan, A., Pore and throat size distributions measured from synchrotron X-ray tomographic images of Fontainebleau sandstones. *J. Geophys. Res. Solid Earth* 105(B9), 21509–21527 (2000).

López, X., Valvatne, P. H., Blunt, M. J., Predictive network modelling of single-phase non-Newtonian flow in porous media, *Journal of Colloid and Interface Science* 264, 256–265 (2003).

López, X., PhD Thesis, Department of Earth Science & Engineering Petroleum Engineering & Rock Mechanics Group, Imperial College, London (2004).

Lubick, N., Malakoff, D., With Pact's Completion, The Real Work Begins, *Science* 341 (2013).

Mabille, C., Schmitt, V., Gorria, P., Calderón, F.L., Faye, V., Deminière, B., Bibette, J., Rheological and shearing conditions for the preparation of monodisperse emulsions. *Langmuir* 16, 422–429 (2000).

Malvaut, G., Détermination expérimentale de la distribution de taille de pores d'un milieu poreux par l'injection d'un fluide à seuil ou par analyse fréquentielle, PhD thesis, Arts et Métiers ParisTech–Centre Angers, Paris, (2013).

- Marrucci, G., Greco, F., Ianniruberto, G., Rheology of polymer melts and concentrated solutions, Current Opinion in Colloid & Interface Science 4, 283–287 (1999).
- Micromeritics, Methods in Fine Particle Technology 301, Norcross (1997).
- Milas, M., Rinaudo, M., Properties of the Concentrated Xanthan Gum Solutions, Polymer Bulletin 10, 271–273 (1983).
- Miller, B., Tyomkin, I., Liquid Porosimetry: New Methodology and Applications, Journal of colloid and interface science 162, 163–170 (1994).
- Miller, J., A complex fluid exhibits unexpected heterogeneous flow, Physics Today 63, Issue 7 (2010).
- Møller, P. C. F., Fall, A., Bonn, D., Origin of apparent viscosity in yield stress fluids below yielding, EPL, 87 (2009).
- Møller, P. C. F., Mewis, J., Bonn, D., Yield stress and thixotropy: on the difficulty of measuring yield stresses in practice, Soft Matter 2, 274–283 (2006).
- Mongruel, A., Cloitre, M., Axisymmetric orifice flow for measuring the elongational viscosity of semi-rigid polymer solutions. J. Non-Newton. Fluid Mech 110, 27–43 (2003).
- Morrow, N. R., Interfacial Phenomena in Petroleum Recovery, Surfactant Sciences Series 36 (1990).
- Moussatov, A., Ayral, C., Castagnède, B., Porous material characterization – ultrasonic method for estimation of tortuosity and characteristic length using a barometric chamber, Ultrasonics 39, Issue 3, 195–202 (2001).
- Mungan, N., Necmettin, Rheology and Adsorption of Aqueous Polymer Solutions, Technology (1969).
- Nelson, P.H., Permeability–porosity relationship in sedimentary rocks. Log. Anal. 35 (No. 3), 38 (1994).
- Nguyen, Q., Boger, D., Direct yield stress measurement with the vane method. J. Rheol. 29 (3), 335–347 (1983).
- Nimmo, J. R., Porosity and Pore Size Distribution, in Hillel, D., ed. Encyclopedia of Soils in the Environment: London, Elsevier, vol. 3, 295–303 (2004).
- Nooruddin, H. A., Hossain, M. E., Modified Kozeny–Carmen correlation for enhanced hydraulic flow unit characterization, Journal of Petroleum Science and Engineering 80, 107–115 (2012).
- Ogata, A., Banks, R. B., A solution of the differential equation of longitudinal dispersion in porous media, Fluid Movement in Earth Materials, Geological Survey Professional Paper 411-A, United States Government Printing Office, Washington (1961).
- Okabe, H., Blunt, M.J., Pore space reconstruction using multiple-point statistics. J. Petrol. Sci. Eng. 46, 121–137 (2005).
- Oliveira, P. D., Michel, R. C., McBride, A. J. A., Moreira, A.; S., Lomba, R. F. T., Vendruscolo, C. T., Concentration Regimes of Biopolymers Xanthan, Tara, and Clairana, Comparing Dynamic Light Scattering and Distribution of Relaxation Time, PLOS ONE 8, Issue 5 (2013).
- Omari, A., Ecoulement en milieu poreux de solutions de polyacrylamide en présence d'une couche adsorbée, PhD thesis, Université de Bordeaux 1 (1982).
- Omari, A., hydrodynamique des polymères à l'interface solide-liquide. Influence de la dépletion. Thèse pour obtenir le grade de Docteur ES Sciences Physiques (1987).
- Omari, A., Moan, M., Chauveteau, G., Wall effects in the flow of flexible polymer solutions through small pores, Rheol Acta 28:520–526 (1989).
- Øren, P.-E., Bakke S., Journal of Petroleum Science and Engineering 39, 177–199 (2003).

- Oukhlef, A., Détermination de la distribution de tailles de pores d'un milieu poreux, PhD thesis, Arts et Métiers ParisTech–Centre Angers, Paris (2011).
- Oukhlef, A., Ambari, A., Champmartin, S., Despeyroux, A., Détermination de la distribution de tailles de pores d'un milieu poreux par la méthode des fluides à seuil, 20ème Congrès Français de Mécanique, Besançon (2011).
- Oukhlef, A., Champmartin, S., Ambari, A., Yield stress fluids method to determine the pore size distribution of a porous medium, *Journal of Non-Newtonian Fluid Mechanics* 204 87–93 (2014).
- Padhy, G. S., Lemaire, C., Amirtharaj , E. S., Ioannidis ,M. A., Pore size distribution in multiscale porous media as revealed by DDIF–NMR, mercury porosimetry and statistical image analysis, *Colloids and Surfaces A: Physicochem. Eng. Aspects* 300, 222–234 (2007).
- Palaniraj, A., Jayaraman, V., Production, recovery and applications of xanthan gum by *Xanthomonas campestris*. *J. Food Eng.* 106, 1–12 (2011).
- Pascal, H., Nonsteady flow of non-Newtonian fluids through a porous medium, *Int. J. Eng. Sci.* 21 (3), 199–210 (1983).
- Paterson, M. S., The equivalent channel model for permeability and resistivity in fluid saturated rock: A re-appraisal, *Mechanics of Materials* 2, 345–352 (1983).
- Perkins, T.-K., Johnston, O.-C, A review of diffusion and dispersion in porous media, *Society of Petroleum Engineers Journal* 3, 70–83 (1963).
- Pittman, E. D., Relationship of porosity and permeability to various parameters derived from mercury injection-capillary pressure curves for sandstone: American Association of Petroleum Geologists Bulletin 76, n. 2, 191–198 (1992).
- Plougonven, E., Lien entre la microstructure des matériaux poreux et leur perméabilité. Mise en évidence des paramètres géométriques et topologiques influant sur les propriétés de transport par analyses d'images microtomographiques. PhD Thesis, Ecole Doctorale des Sciences Chimiques, Université de Bordeaux 1 (2009).
- Prodanovic, M., Lindquist, W. B., Seright, R. S., Porous structure and fluid partitioning in polyethylene cores from 3D X-ray microtomographic imaging. *J. Colloid Interface Sci.* 298, 282–297 (2006).
- Prodanovic, M., Lindquist, W. B., Seright, R. S., 3D image-based characterization of fluid displacement in a Berea core. *Adv. Water Resourc.* 30, 214–226 (2007).
- Putz, A. M. V., Burghelea, T. I., The solid-fluid transition in a yield stress shear thinning physical gel, *RheolActa* 48, 673–689 (2009).
- Quintard, M., Whitaker, S., Convection, Dispersion, and Interfacial Transport of Contaminants: Homogeneous Porous Media, *Advances in Water Resources* 17, 221–239 (1994).
- Radlinski, A.P., Ioannidis, M.A., Hinde, A.L., Hainbuchner, M., Baron, M., Rauch, H., Kline, S.R., Angstrom to millimeter characterization of sedimentary rock microstructure. *J. Colloid Interface Sci.* 274, 607–612 (2004).
- Rao, M. A., Rheology of Fluid and semisolid Foods, Principles and Applications, Food Engineering Series, Springer (2007).
- Richardson, R. K., Ross-Murphy, S. B., Non-linear viscoelasticity of polysaccharide solutions. 2: Xanthan polysaccharide solutions, *Int. J. Biol. Macromol.* 9 (1987).
- Riche, F., Schneebeli, M., Tschanz, S.A., Design-based stereology to quantify structural properties of artificial and natural snow using thin sections. *Cold Reg. Sci. Technol.* 79–80, 67–74 (2012).

- Rochefort, W. E., Middleman, S., Rheology of Xanthan Gum: Salt, Temperature, and Strain Effects in Oscillatory and Steady Shear Experiment, *J. Rheol.* 31, 337 (1987).
- Rodd, A. B., Dunstan D.E., Boger, D. V., Characterisation of xanthan gum solutions using dynamic light scattering and rheology, *Carbohydrate Polymers* 42, 159–174 (2000).
- Rodriguez de Castro, A., Omari, A., Ahmadi-Sénichault, A., Bruneau, D., Toward a New Method of Porosimetry: Principles and Experiments, *Transport in Porous Media* 101, Issue 3, 349–364 (2014).
- Rouquerol, J., Avnir, D., Fairbridge, C. W., Everett, D. H., Haynes, J. H., Pernicone, N., Ramasay, J. D. F., Sing, K. S. W., Unger, K. K., Recommendations for the characterization of porous solids, *Pure & Appl. Chem.* 66, No. 8, 1739–1758 (1994).
- Rouquerol, J., Baron, G., Denoyel, R., Giesche, H., Groen, J., Kloboes, P., Levitz, P., Neimark, A. V., Rigby, S., Skudas, R., Sing, K., Thommes, M., Unger, K., Liquid intrusion and alternative methods for the characterization of macroporous materials (IUPAC Technical Report), *Pure Appl. Chem.* 84, No. 1, 107–136 (2012).
- Schüth, F., Sing, K. S. W., Weitkamp, J., *Handbook of Porous Solids*, WILEY-VCH Verlag GmbH (2002).
- Scott Blair, G. W., *J Applied Phys* 4, 133 (1933).
- Seright, R.S., Fan, T., Wavrik, K., Balaban, R.C., New Insights into Polymer Rheology in Porous Media. Paper SPE 129200 presented at the SPE Improved Oil Recovery Symposium, Tulsa, Oklahoma, 24–28 April (2010).
- Seright, R.S., <http://baervan.nmt.edu/randy/>, Accessed 10 May 2014, (2010).
- Sheng, J. J., *Modern Chemical Enhanced Oil Recovery, Theory and Practice*, GPG, Elsevier (2011).
- Sheppard, A. P., Sok, R. M., Averdunk, H., Techniques for image enhancement and segmentation of tomography images of porous materials, *Physica A* 339, 145–151 (2004).
- Sheppard, A. P., Sok, R. M., Averdunk, H., Improved pore network extraction methods, International Symposium of the Society of Core Analysts held in Toronto, 21–25 August (2005).
- Skelland, A.H.P., *Non-Newtonian Flow and Heat Transfer*. Wiley, New York (1967).
- Sochi, T., Non-Newtonian flow in porous media, *Polymer* 51, 5007–5023 (2010).
- Sochi, T., Yield and Solidification of Yield-Stress Materials in Rigid Networks and Porous Structures, University College London, Department of Physics & Astronomy, Gower Street, London (2013).
- Sochi, T., Blunt, M.J., Pore-scale network modelling of Ellis and Herschel-Bulkley fluids, *Journal of Petroleum Science and Engineering* 60, 105–124 (2008).
- Song, Y.-Q., Novel NMR techniques for porous media research, *Cement and Concrete Research* 37, 325–328 (2007).
- Song, K.-W., Kim, Y.-S., Chang, G.S., Rheology of concentrated xanthan gum solutions: steady shear flow behavior. *Fibers Polym.* 7(2), 129–138 (2006).
- Sorbie, K. S., *Polymer-Improved Oil Recovery*, Blackie and Son Ltd (1991).
- Sorbie, K. S., Rheological and Transport Effects in the Flow of Low-Concentration Xanthan Solution through Porous Media, *Journal of Colloid and Interface Science* 145, No. I (1991).
- Southwick, J. G., Jamieson, A. M., Blackwell, J., Quasi-Elastic Light Scattering Studies of Semidilute Xanthan Solutions, *Macromolecules* 14, 1728–1732 (1981).
- Steffe, J.F., *Rheological Methods in Food Process Engineering*, Second Edition. Freeman Press, East Lansing, Michigan (1996).

- Sun, Z., Tang, X., Cheng, G., Numerical simulation for tortuosity of porous media. *Microporous Mesoporous Mater.* 173, 37–42 (2013)
- Sweerts, J.-P. R. A., Kelly, C., A., Ruud, J. W. M., Hesslein, R., Cappenberg, T. E., Similarity of whole-sediment molecular diffusion coefficients in freshwater sediments of low and high porosity, *Limnology and Oceanography* 36(2), 335–341 (1991).
- Talon, L., Bauer, D., On the determination of a generalized Darcy equation for yield-stress fluid in porous media using a Lattice-Boltzmann TRT scheme, *Eur. Phys. J. E.* 36, 139 (2013).
- Tiab, D., Donaldson, E. C., *Petrophysics. Theory and Practice of Measuring Reservoir Rock and Fluid Transport Properties*, Gulf Professional Publishing (2004).
- Tiu, C., Boger, D. V., Complete rheological characterization of time-dependent food products, *Journal of Texture Studies* 5, Issue 3, 329–338 (1974).
- Tiu, C., Guo, J., Uhlherr, P. H. T., Yielding behaviour of viscoplastic materials. *J. Ind. Eng. Chem.* 12(5), 653–662 (2006).
- Torskaya, T., Shabro, S., Torres-Verdin, C., Salazar-Tio, Revil, A., Grain Shape Effects on Permeability, Formation Factor, and Capillary Pressure from Pore-Scale Modelling, *Transp Porous Med* 102, 71–90 (2014).
- Tropea, C., Yarin, A. L., Foss, J. F., *Springer Handbook of Experimental Fluid Mechanics*, Springer (2007).
- United Nations Environment Programme (UNEP), Minamata convention on mercury. <http://www.mercuryconvention.org/Convention/tabid/3426/Default.aspx> (2013). Accessed 25 Oct 2013.
- Vergés, E., Tost, D., Ayala, D., Ramos, E., Grau, S., 3D pore analysis of sedimentary tocks, *Sedimentary Geology* 234, 109–115 (2011).
- Volkovitch, Y. M., Bagotzky, V. S., Sosenkin, V.E., Blinov, I.A., The standard contact porosimetry, *Colloids Surf.* 349, 187–188 (2001).
- Wadhai, V.S., Dixit, A.N., Production of Xanthan gum by *Xanthomonas campestris* and comparative study of *Xanthomonas campestris* isolates for the selection of potential Xanthan producer. *Indian Streams Res. J.* 1, 1–4 (2011)
- Walsh, J.B., Brace, W.F., The effect of pressure on porosity and the transport properties of rock, *Journal of Geophysical Research: Solid Earth* (1984).
- Wardlaw, N. C., McKellar, M., Mercury Porosimetry and the Interpretation of Pore Geometry in Sedimentary Rocks and Artificial Models, *Powder Technology*. 29 127–143 (1981).
- Wardlaw, N.C., McKellar, M., Yu, L.: Pore and throat size distributions determined by mercury porosimetry and by direct observation. *Carbonates Evaporites* 3, 1–16 (1988).
- Weilbeer, M., Efficient Numerical Methods for Fractional Differential Equations and Their Analytical Background. *Papierflieger* (2005).
- Wei, B., Romero-Zeron, L., Rodriguez, D., Mechanical Properties and Flow Behavior of Polymers for Enhanced Oil Recovery, *Journal of Macromolecular Science, Part B: Physics*, 53:4, 625-644 (2014).
- Wildenschild, D, Sheppard, A. P., X-ray imaging and analysis techniques for quantifying pore-scale structure and processes in subsurface porous medium systems, *Advances in Water Resources* (2012).
- Withcomb, P. J., Macosko, C. W., Rheology of Xanthan Gum, *Journal of Rheology* 22, 493, (1978).
- World Health Organization, *Environmental Health Criteria 1: Mercury*, Geneva, ISBN 92-4-154061-3 (1976).

Yanuka, M., Percolation Theory Approach to Transport Phenomena in Porous Media, *Transport in Porous Media* 7, 265-282, Kluwer Academic Publishers (1992).

Zhu, Ch., Smay, J. E., Thixotropic rheology of concentrated alumina colloidal gels for solid free form fabrication, *Journal of Rheology* 55 (2011).



## Annex A: $Q(\nabla P)$ measurements

The values of the  $Q(\nabla P)$  measures corresponding to the injection of xanthan gum solutions through porous media which have been presented and exploited in the thesis are detailed in this Annex.

### Preliminary laboratory experiments (Section 4.1)

Xanthan solution 6000 ppm Aerolith A10		Xanthan solution 7000 ppm Aerolith A10	
$Q(\text{ml/h})$	$\Delta P (\text{bar})$	$Q(\text{ml/h})$	$\Delta P (\text{bar})$
0.05	0.124	0.07	0.081
0.067	0.191	0.092	0.135
0.088	0.246	0.12	0.182
0.12	0.3	0.16	0.234
0.16	0.329	0.21	0.273
0.21	0.366	0.27	0.303
0.28	0.401	0.36	0.338
0.37	0.409	0.47	0.377
0.49	0.438	0.62	0.403
0.65	0.462	0.82	0.424
0.87	0.502	1.1	0.465
1.2	0.544	1.4	0.496
1.5	0.573	1.9	0.534
2	0.608	2.4	0.564
2.7	0.648	3.2	0.602
3.6	0.689	4.2	0.641
4.8	0.73	5.6	0.683
6.4	0.771	7.3	0.728
8.5	0.809	9.6	0.772
11	0.849	13	0.822
15	0.894	17	0.871
20	0.938	22	0.92
27	0.986	29	0.976
35	1.03	38	1.03
47	1.09	50	1.1
63	1.15	65	1.16
83	1.22	86	1.25
110	1.28	110	1.31
150	1.36	150	1.4
200	1.44	190	1.5
260	1.53	260	1.6
350	1.64	340	1.72
460	1.77	440	1.84
610	1.91	580	1.99

<b>Xanthan solution 6000 ppm Aerolith A10</b>		<b>Xanthan solution 7000 ppm Aerolith A10</b>	
<b><math>\Delta P</math> (bar)</b>	<b>Q(ml/h)</b>	<b><math>\Delta P</math> (bar)</b>	<b>Q(ml/h)</b>
820	2.09	760	2.19
		1000	2.39
		1300	2.63
		1700	2.93
		2300	3.32
		3000	3.45

### Sensitivity of the obtained PSD to the polymer concentration (Section 4.2)

<b>Xanthan solution 4000 ppm Aerolith A10</b>		<b>Xanthan solution 5000 ppm Aerolith A10</b>		<b>Xanthan solution 6000 ppm Aerolith A10</b>	
<b>Q(ml/h)</b>	<b><math>\Delta P</math> (bar)</b>	<b>Q(ml/h)</b>	<b><math>\Delta P</math> (bar)</b>	<b>Q(ml/h)</b>	<b><math>\Delta P</math> (bar)</b>
0.476	0.25	0.05	0.17	0.05	0.23
0.488	0.26	0.07	0.22	0.07	0.28
0.5	0.24	0.092	0.24	0.092	0.32
0.529	0.26	0.12	0.26	0.12	0.37
0.549	0.26	0.16	0.29	0.16	0.42
0.570	0.26	0.21	0.34	0.21	0.44
0.593	0.27	0.27	0.35	0.27	0.49
0.617	0.27	0.36	0.39	0.36	0.54
0.643	0.28	0.47	0.41	0.47	0.59
0.671	0.29	0.62	0.45	0.62	0.65
0.701	0.29	0.82	0.49	0.82	0.69
0.733	0.29	1.1	0.52	1.1	0.74
0.768	0.3	1.4	0.55	1.4	0.78
0.806	0.3	1.9	0.59	1.9	0.85
0.847	0.3	2.4	0.63	2.4	0.92
0.892	0.31	3.2	0.67	3.2	0.97
0.942	0.31	4.2	0.71	4.2	1
0.996	0.31	5.6	0.75	5.6	1.06
1.06	0.31	7.3	0.8	7.3	1.12
1.12	0.34	9.6	0.84	9.6	1.21
1.20	0.35	13	0.89	13	1.25
1.28	0.35	17	0.96	17	1.35
1.37	0.36	22	1	22	1.39
1.47	0.37	29	1.06	38	1.49
1.59	0.38	38	1.11	50	1.65
1.73	0.38	50	1.18	65	1.74
1.89	0.4	65	1.25	86	1.85
2.07	0.41	86	1.32	110	1.93
2.29	0.43	110	1.36	150	1.98
2.55	0.44	150	1.39	190	2.11
2.86	0.45	190	1.47	260	2.27
3.24	0.47	260	1.61	340	2.45

<b>Xanthan solution 4000 ppm Aerolith A10</b>		<b>Xanthan solution 5000 ppm Aerolith A10</b>		<b>Xanthan solution 6000 ppm Aerolith A10</b>	
<b>Q(ml/h)</b>	<b>ΔP (bar)</b>	<b>Q(ml/h)</b>	<b>ΔP (bar)</b>	<b>Q(ml/h)</b>	<b>ΔP (bar)</b>
3.73	0.48	340	1.71	440	2.58
4.35	0.51	440	1.81	580	2.7
5.17	0.54	580	1.94	760	2.85
6.29	0.57	760	2.1	1000	3.09
7.91	0.6	1000	2.24	1300	3.35
10.4	0.65	1300	2.45	1700	3.59
14.6	0.7	1700	2.6	2200	4
22.9	0.75	2200	2.85		
44.3	0.84				
161	1.15				
190	1.19				
260	1.24				
340	1.34				
440	1.4				
580	1.53				
760	1.56				
1000	1.69				
1300	1.85				
1700	1.98				
2300	2.29				
3000	2.42				

<b>Xanthan solution 7000 ppm Aerolith A10</b>		<b>Xanthan solution 8000 ppm Aerolith A10</b>	
<b>Q(ml/h)</b>	<b>ΔP (bar)</b>	<b>Q(ml/h)</b>	<b>ΔP (bar)</b>
0.05	0.27	0.05	0.37
0.07	0.37	0.07	0.45
0.092	0.4	0.092	0.54
0.12	0.48	0.12	0.6
0.16	0.53	0.16	0.7
0.21	0.56	0.21	0.73
0.27	0.61	0.27	0.78
0.36	0.68	0.36	0.83
0.47	0.74	0.47	0.93
0.62	0.75	0.62	0.95
0.82	0.84	0.82	1
1.1	0.87	1.1	1.08
1.4	0.9	1.4	1.12
1.9	0.99	1.9	1.19
2.4	1.04	2.4	1.29
3.2	1.1	3.2	1.33
4.2	1.19	4.2	1.41
5.6	1.22	5.6	1.45
7.3	1.28	7.3	1.58

Xanthan solution 7000 ppm Aerolith A10		Xanthan solution 8000 ppm Aerolith A10	
Q(ml/h)	$\Delta P$ (bar)	Q(ml/h)	$\Delta P$ (bar)
9.6	1.37	9.6	1.63
13	1.42	13	1.72
17	1.5	17	1.78
22	1.55	22	1.88
29	1.69	29	1.98
38	1.76	38	2.08
50	1.84	50	2.19
65	1.91	65	2.28
86	2.05	86	2.42
110	2.13	110	2.5
150	2.16	150	2.65
190	2.29	190	2.75
260	2.45	260	2.99
340	2.6	340	3.17
440	2.74	440	3.37
580	2.92	580	3.54
760	3.06	760	3.82
1000	3.28	1000	4.15
1300	3.56	1300	4.51
1700	3.81	1700	4.86
2200	4.23	2200	5.37

**Sensitivity of the obtained PSD to the type of porous medium and its permeability (Section 4.3)**

Sample 1		Sample 2		Sample 3	
Q(ml/h)	$\Delta P$ (bar)	Q(ml/h)	$\Delta P$ (bar)	Q(ml/h)	$\Delta P$ (bar)
2200	4.23	1000	10.7	1000	4.55
1700	3.81	760	9.55	760	4.05
1300	3.56	580	8.65	580	3.7
1000	3.28	440	7.9	440	3.4
760	3.06	340	7.25	340	3.1
580	2.92	260	6.7	260	2.8
440	2.74	190	6.2	190	2.55
340	2.6	150	5.85	150	2.35
260	2.45	110	5.4	110	2.15
190	2.29	86	5.15	86	2.05
150	2.16	65	4.85	65	1.9
110	2.13	50	4.55	50	1.8
86	2.05	38	4.35	38	1.7
65	1.91	29	4.1	29	1.6
50	1.84	22	3.9	22	1.5

Sample 1		Sample 2		Sample 3	
Q(ml/h)	$\Delta P$ (bar)	Q(ml/h)	$\Delta P$ (bar)	Q(ml/h)	$\Delta P$ (bar)
38	1.76	17	3.7	17	1.42
29	1.69	13	3.5	13	1.35
22	1.55	9.6	3.35	9.6	1.28
17	1.5	7.3	3.2	7.3	1.23
13	1.42	5.6	3.05	5.6	1.18
9.6	1.37	4.2	2.9	4.2	1.12
7.3	1.28	3.2	2.8	3.2	1.06
5.6	1.22	2.4	2.65	2.4	1.02
4.2	1.19	1.9	2.55	1.9	0.97
3.2	1.1	1.4	2.4	1.4	0.91
2.4	1.04	1.1	2.25	1.1	0.86
1.9	0.99	0.82	2.1	0.82	0.8
1.4	0.9	0.62	1.95	0.62	0.74
1.1	0.87	0.47	1.8	0.47	0.68
0.82	0.84	0.36	1.7	0.36	0.62
0.62	0.75	0.27	1.6	0.27	0.59
0.47	0.74	0.16	1.55	0.21	0.56
0.36	0.68	0.12	1.4	0.16	0.55
0.27	0.61	0.09	1.4	0.12	0.51
0.21	0.56	0.07	1.4	0.09	0.5
0.16	0.53	0.05	1.4	0.07	0.51
0.12	0.48			0.05	0.53
0.092	0.4			0.01	0.44
0.07	0.37				
0.05	0.27				

Sample 4		Sample 5	
Q(ml/h)	$\Delta P$ (bar)	Q(ml/h)	$\Delta P$ (bar)
1000	12.74	1000	36.59
760	10.95	760	31.74
580	9.6	580	26.34
440	8.45	440	22.24
340	7.61	340	19.39
260	6.85	260	17.09
190	6.1	190	14.79
150	5.7	150	13.34
110	5.15	110	11.75
86	4.8	86	10.7
65	4.45	65	9.75
50	4.2	50	8.95
38	3.93	38	8.3
29	3.7	29	7.65
22	3.5	22	7

<b>Sample 4</b>		<b>Sample 5</b>	
<b>Q(ml/h)</b>	<b><math>\Delta P</math> (bar)</b>	<b>Q(ml/h)</b>	<b><math>\Delta P</math> (bar)</b>
17	3.26	17	6.4
13	3.08	13	5.9
9.6	2.91	9.6	5.4
7.3	2.75	7.3	5.06
5.6	2.61	5.6	4.73
4.2	2.46	4.2	4.4
3.2	2.32	3.2	4.14
2.4	2.18	2.4	3.87
1.9	2.05	1.9	3.63
1.4	1.89	1.4	3.37
1.1	1.73	1.1	3.13
0.82	1.61	0.82	2.88
0.62	1.42	0.62	2.63
0.47	1.31	0.47	2.38
0.36	1.17	0.36	2.11
0.27	1.07	0.27	1.95
0.21	1.02	0.21	1.82
0.16	1	0.16	1.76
0.12	0.94	0.12	1.55
0.09	0.94	0.09	1.51
0.07	0.95	0.07	1.51
0.05	0.96	0.05	1.5
0.01	0.85	0.01	1.32

## Annex B: PSDs obtained with the modified YSM for laboratory experiments

The  $(Q_i, \nabla P_i)$  raw data corresponding to the experiments presented in Sections 4.2 and 4.3 were fitted following the procedure presented in Section 4.5. (see Figure B 1 and Figure B 2). After that, Eq. (4.9) was used to obtain the value of  $\nabla P$  corresponding to each  $Q_i$ , giving a new set of smooth  $(Q_i, \widetilde{\nabla P}_i)$  data where  $\widetilde{\nabla P}_i$  is the  $\nabla P$  provided by Eq.(4.9) evaluated at  $Q_i$ . Finally, the procedure presented in Section 3.2 was applied to the  $(Q_i, \widetilde{\nabla P}_i)$  data, resulting in the PSDs and  $\alpha^*$  presented in Figure B 3 and Table B 1 respectively. We can notice that the dependence of  $\alpha^*$  on  $K$  is very weak. Also, the PSDs are coherently arranged (excepting Sample 2) with respect to the average radius predicted by Eq. (2.2) as seen in Figure B 4, even if the shape is the same for almost all of them (apart from Sample 1, there are nonzero probabilities below the peak).

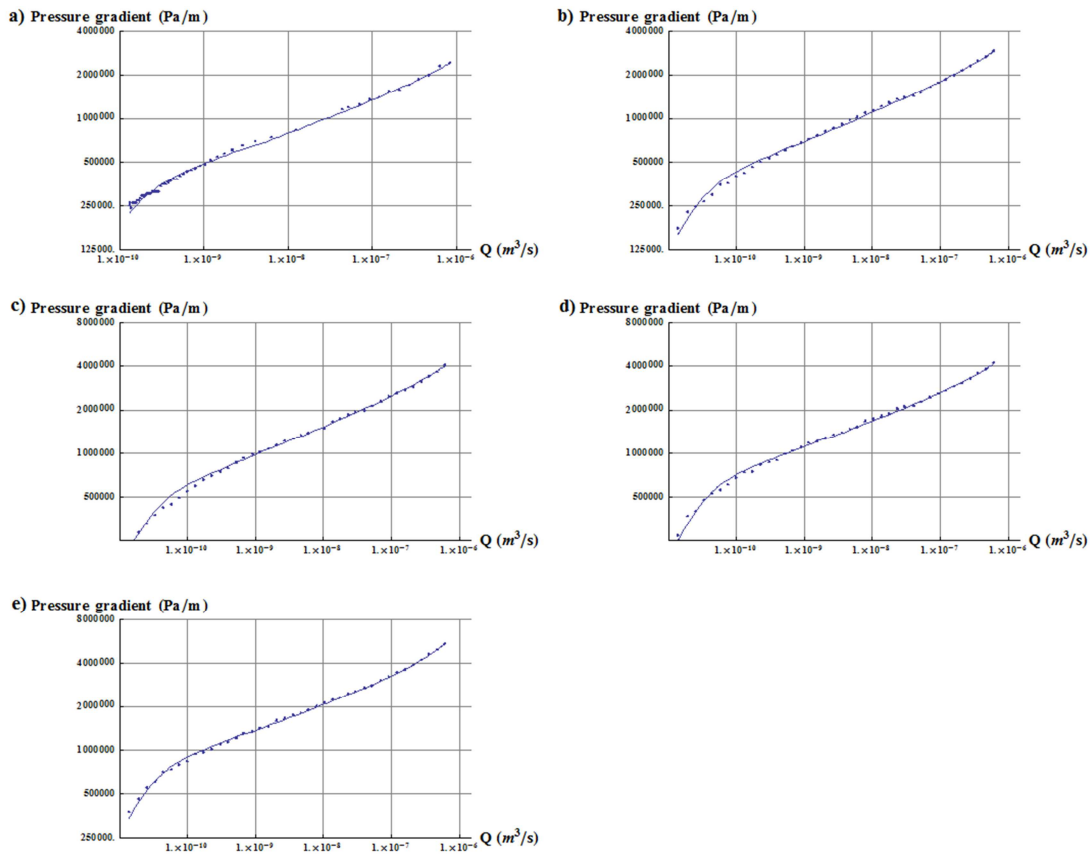
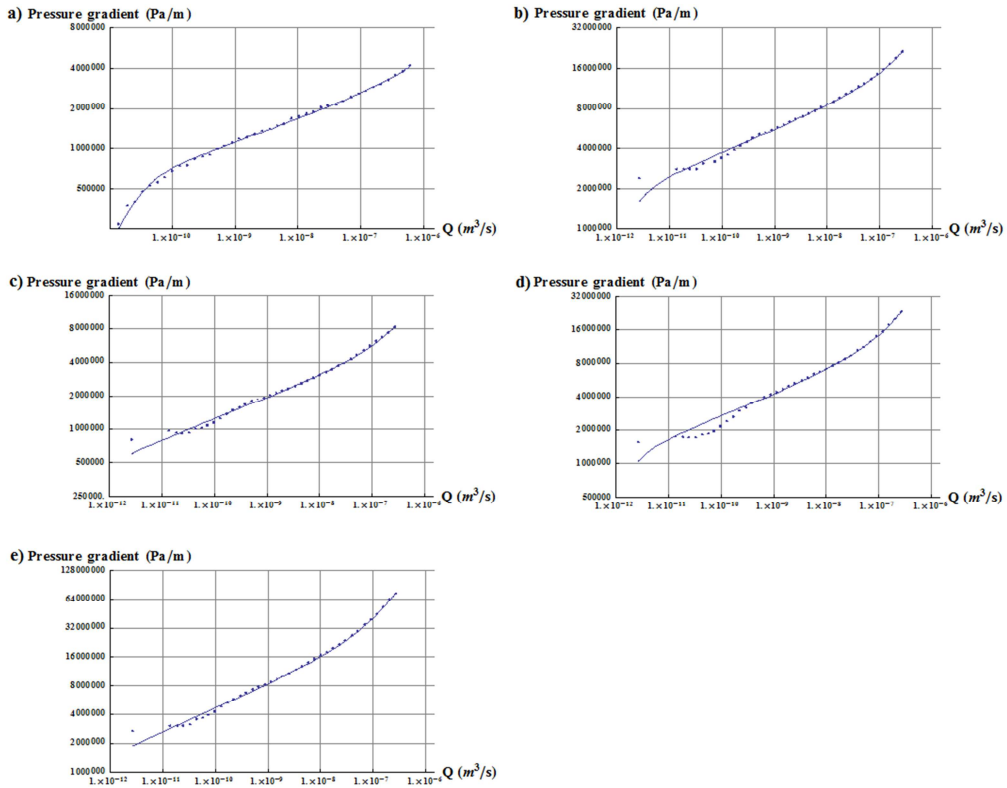
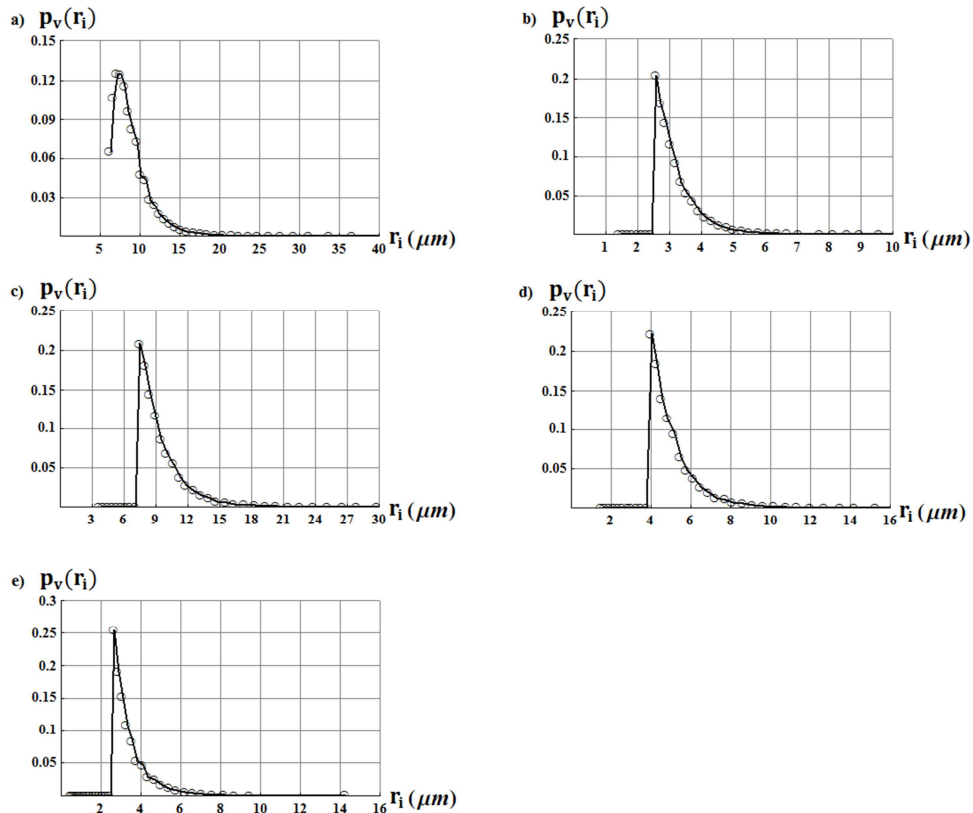


Figure B 1: Pressure gradient as a function of flow rate for the experiments presented in Section 4.2 (blue points) and fit (blue line) obtained by following the procedure explained in Section 4.5. a) Sample 1; b) Sample 2; c) Sample 3; d) Sample 4; d) Sample 5.



**Figure B 2:** Pressure gradient as a function of flow rate for the experiments presented in Section 4.3 (blue points) and fit (blue line) obtained by following the procedure explained in Section 4.5. a) Sample 1; b) Sample 2; c) Sample 3; d) Sample 4; e) Sample 5.



**Figure B 3:** PSDs of the samples analyzed in Section 4.3 obtained by exploiting the smooth ( $Q_i, \nabla P_i$ ) data obtained with the fit presented in Section 4.5. a) Sample 1; b) Sample 2; c) Sample 3; d) Sample 4; e) Sample 5.

Sample	$\alpha^*$	K (mD)
1	1.2	9000
2	1.3	2400
3	1.3	2200
4	1.4	750
5	1.4	38

Table B 1:  $\alpha^*$  corresponding to the experiments of Section 4.3. These values of  $\alpha^*$  were obtained by exploiting the smooth ( $Q_i$ ,  $\nabla P_i$ ) data obtained with the fit presented in Section 4.5.

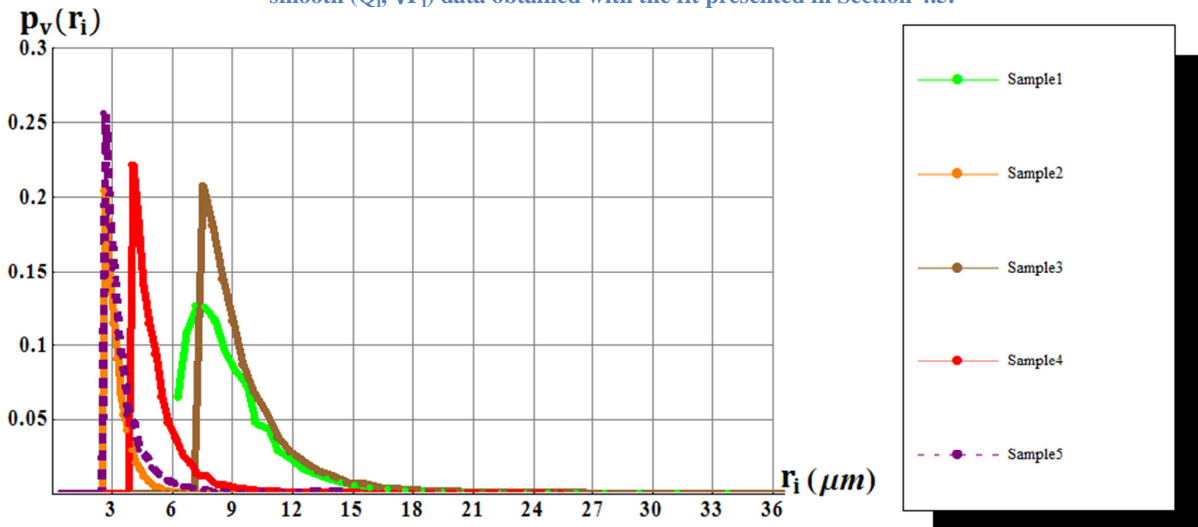


Figure B 4: Comparison of the PSDs of the samples analyzed in Section 4.3. These PSDs were obtained by exploiting the smooth ( $Q_i$ ,  $\nabla P_i$ ) data obtained with the fit presented here.



## **Annex C: Quasi mono disperse oil-in-water emulsions.**

Other fluids than xanthan gum solutions were considered as yield stress fluid candidates. The procedure to prepare and characterize concentrated quasi monodisperse oil-in-water emulsions is presented here.

### **Formulation**

A sensitivity analysis of the rheological parameters to the concentration of oil was carried out, concluding that 70% volume fraction is the most convenient for our purposes. Our emulsions were composed of 2 phases: continuous and disperse. The continuous phase itself was composed of water and nonionic surfactant (Triton X-100) at mass concentration of 30%. The disperse phase was light mineral oil (Sigma-Aldrich).

### **Preparation**

The continuous phase was first prepared by slowly adding the nonionic surfactant to the water under magnetic agitation. Then, the oil was progressively added to the continuous phase, drop by drop, while gently agitating with a spatula, until an oil concentration in volume of 85% was attained. Once all the oil had been added, a concentrated premix was obtained, which is an emulsion containing oil droplets of different sizes. The premix was then put into a Couette machine with a gap of 100  $\mu\text{m}$  between the fix and the mobile cylinders. The fluid was subjected to an almost constant shear stress corresponding to 500 rpm of the mobile cylinder. As a result, a concentrated mono disperse emulsion was produced. Then, water was added to the concentrated emulsion until 70% volume fraction of oil was obtained. Afterwards, the emulsion was degassed and the size of the drops was observed with a microscope (the emulsion is diluted before observation), as shown in Figure C 1.

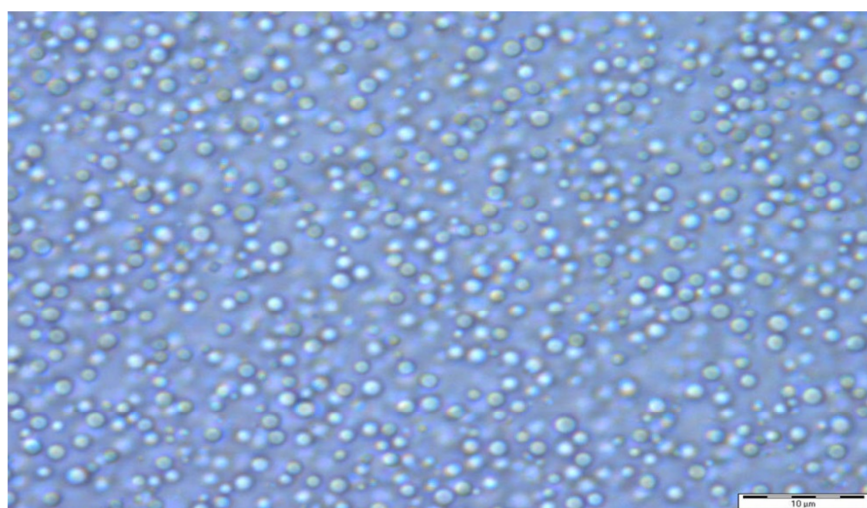


Figure C 1: Image of a quasi mono disperse oil-in-water emulsion taken by an optical microscope.

## **Characterization of the size of the oil droplets**

The size of the droplets in the emulsion was characterized by laser granulometry as seen in Figure C 2. As can be observed, a quasi mono disperse distribution centered at 1.4 µm was obtained

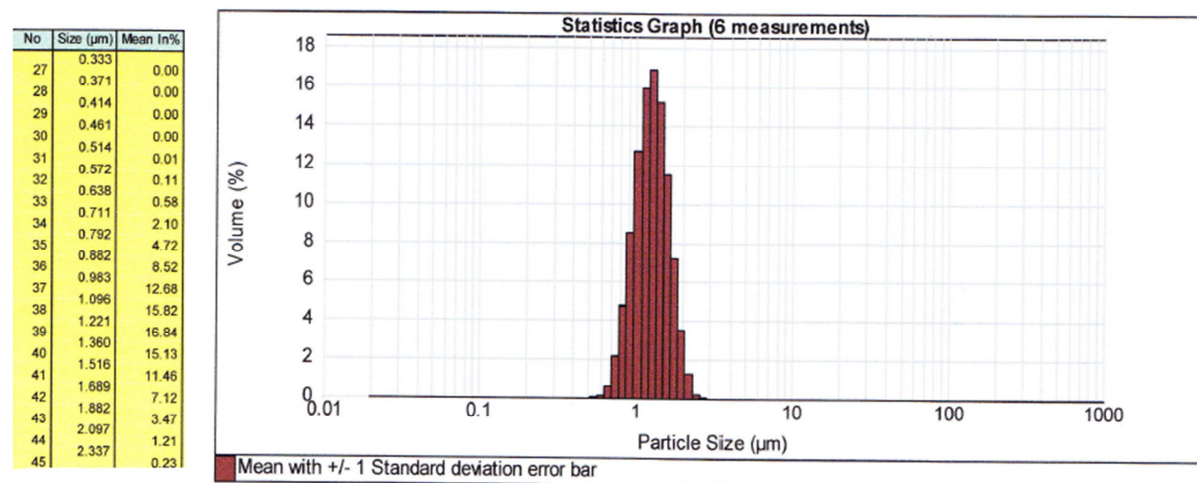


Figure C 2: Droplet size distribution of an oil-in-water emulsion obtained by laser granulometry.

## **Rheology**

The rheology of the prepared emulsion was characterized using the same protocol as for xanthan solutions, resulting in the measures listed in Table C 1 and represented in Figure C 3. The corresponding Herschel-Bulkley parameters are  $\tau_0 = 8.10 \text{ Pa}$ ,  $k = 2.24 \text{ Pa s}^n$  and  $n = 0.589$ . It is noticed that no Newtonian plateau of viscosity is attained at low shear rates and that the decrease in viscosity is more drastic than this presented by xanthan solutions. Therefore, a best approximation to an ideal yield stress fluid is obtained with this type of fluids. However, other complications arise, such as stability of the emulsions or viscoelastic behavior.

<b>Oil-in-water emulsion</b>	
$\dot{\gamma} (\text{s}^{-1})$	$\tau (\text{Pa})$
8.27E-05	1
0.08458	4.414
0.2719	7.828
1.181	11.24
4.097	14.65
10.02	18.07
17.24	21.48
25.93	24.89
36.91	28.3
49.69	31.72

**Oil-in-water emulsion**

$\dot{\gamma}$ ( $s^{-1}$ )	$\tau$ (Pa)
64.16	35.13
80.02	38.54
97.37	41.95
115.8	45.36
135.6	48.77
156.2	52.18
178.1	55.59
201.3	59
224.6	62.41
249.2	65.82
275.8	69.23
302.5	72.63
331.2	76.04
358.8	79.45
388	82.86
418.5	86.27
453.5	89.68
479.7	93.09
511.8	96.49
542.7	99.9

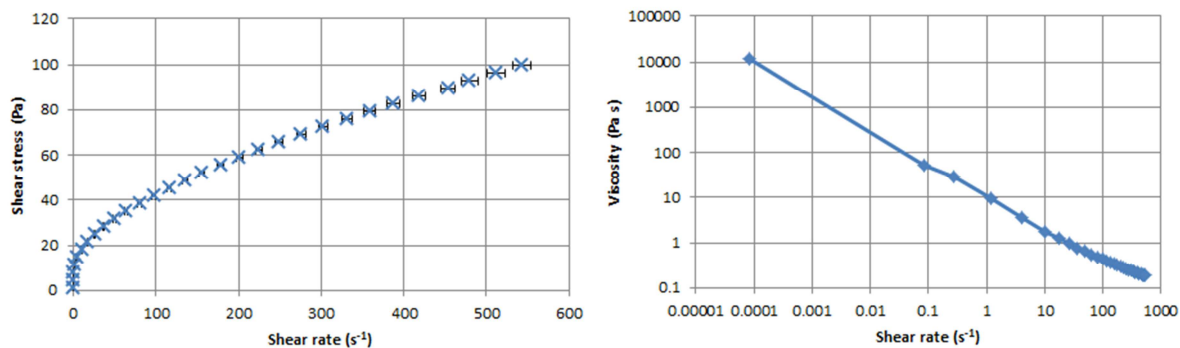
Table C 1:  $\tau(\dot{\gamma})$  measures corresponding to the oil-in-water emulsion.

Figure C 3: Shear stress and viscosity as a function of shear rate for the oil-in-water emulsion.



École doctorale n° 432 : Sciences des Métiers de l'Ingénieur

## Doctorat ParisTech

### THÈSE

pour obtenir le grade de docteur délivré par

**l'École Nationale Supérieure d'Arts et Métiers**

**Spécialité “ Mécanique-matériaux ”**

*présentée et soutenue publiquement par*

**Antonio RODRÍGUEZ DE CASTRO**

le 17 juillet 2014

**Expériences d'écoulement de fluides à seuil en milieu poreux  
comme nouvelle méthode de porosimétrie**

**(résumé en français)**

Directeur de thèse : **Azita AHMADI-SÉNICHIAULT**

Co-directeur de thèse : **Abdelaziz OMARI**

Co-encadrement de la thèse : **Denis BRUNEAU**

#### Jury

**M. Henri BERTIN**, Directeur de Recherche, CNRS, I2M – TREFLE

**M. Harold AURADOU**, Directeur de Recherche, CNRS, FAST, Orsay

**M. Seyed Majid HASSANIZADEH**, Professor, Utrecht University - The Netherlands

**Mme Azita AHMADI-SÉNICHIAULT**, Professeur, I2M – TREFLE, Arts et Métiers ParisTech

**M. Abdelhak AMBARI**, Professeur, LAMPA, Arts et Métiers ParisTech

**M. Dominique BERNARD**, Directeur de Recherche, CNRS, ICMCB

**M. Abdelaziz OMARI**, Professeur, I2M – TREFLE, INP Bordeaux

**Mme Sabine SAVIN**, Docteur-Ingénieur, TOTAL – CSTJF, Pau

**M. Denis BRUNEAU**, Maître de Conférences, I2M – TREFLE, Arts et Métiers ParisTech

Président

Rapporteur

Rapporteur

Examinateur

Examinateur

Examinateur

Examinateur

Examinateur

Invité

T  
H  
È  
S  
E



## 1. Introduction générale

---

À l'heure actuelle, la porosimétrie à mercure est la technique la plus répandue pour déterminer les distributions de taille des pores (DTP) des milieux poreux. En effet, il s'agit d'une méthode bien établie et la référence pour caractériser les DTP. Cependant, cette technique présente plusieurs inconvénients tels que la toxicité du fluide utilisé. Malgré l'existence d'autres méthodes de porosimétrie moins toxiques, aucune parmi elles n'est suffisamment performante pour remplacer la porosimétrie à mercure. De plus, la nouvelle législation qui sera mise en place à la suite de la ratification de la Convention de Minamata sur le Mercure en Octobre 2013 vise à bannir ou limiter fortement cette technique, qui est l'une des principales sources d'utilisation du mercure. D'ailleurs, il est toujours souhaitable de remplacer une méthode toxique comme celle-ci par une méthode respectueuse de l'environnement et qui en plus ne menace pas la santé de l'utilisateur. C'est pour cette raison que l'IUPAC (International Union of Pure and Applied Chemistry) a fait récemment appel à la communauté scientifique internationale (Rouquerol *et al.* 2012) en remarquant l'intérêt et le besoin de développer des méthodes de porosimétrie plus efficaces et non toxiques.

Dans ce contexte, l'objectif de la présente thèse est de proposer une nouvelle méthode expérimentale pour la caractérisation des milieux poreux en termes de leur distribution de taille des pores basée sur l'utilisation de fluides à seuil et réunissant les critères de performance et de non toxicité.

La base théorique d'une nouvelle méthode pour obtenir les DTP en mesurant le débit  $Q$  à plusieurs gradients de pression  $\nabla P$  pendant l'injection de fluides à seuil en milieu poreux a été proposée dans la littérature par Ambari *et al.* (1990). Sur la base de ces considérations théoriques, une approche intuitive pour calculer les DTP à partir de  $Q(\nabla P)$  est présentée dans ce travail. Elle consiste à considérer l'augmentation additionnelle de  $Q$  quand  $\nabla P$  est augmenté, comme conséquence des pores plus petits qui s'incorporent à l'écoulement. Le principe sous-jacent de ce comportement est la rhéologie des fluides à seuil en milieu poreux. La procédure est d'abord testée et validée numériquement. Ensuite, elle est appliquée à l'exploitation des données provenant des expériences de laboratoire et les DTP obtenues sont comparées avec celles fournies par porosimétrie à mercure, et dans certains cas avec des résultats de microtomographie 3D.

L'écoulement à travers les milieux poreux des fluides non-Newtoniens en général, et des fluides à seuil en particulier, est de spécial intérêt dans des applications comme la récupération améliorée de pétrole, la dépollution de sols, la filtration, la propagation du sang dans les reins, etc. En plus, il faut souligner que leur modélisation, simulation et implémentation expérimentale est très complexe. Par conséquent, même si l'il s'agit actuellement d'un sujet de recherché très actif et même si beaucoup de progrès a été fait, il n'existe pas encore de modèle macroscopique concluant et les simulations numériques ne sont pas capables de prédire les mesures expérimentales dans de nombreux cas. D'ailleurs, il y a

un manque de travail expérimental dans ce domaine, comme signalé par plusieurs auteurs (Chevalier *et al.* 2013), qui signalent également la difficulté pour obtenir des résultats fiables. Pour cette raison, un objectif complémentaire de cette thèse est de fournir des procédures rigoureuses ainsi que des résultats expérimentaux qui puissent être comparés avec les simulations numériques et les modèles macroscopiques.

## 2. Etat de l'art

---

Ce chapitre est divisé en quatre sections. Il commence par une étude bibliographique des milieux poreux, focalisée sur la caractérisation de la géométrie de l'espace poreux. Ensuite, quelques aspects de la rhéologie des fluides non newtoniens et leur écoulement en milieu poreux sont présentés, avec une attention spéciale au type de fluides utilisés dans les expériences qui seront présentées par la suite. Enfin, les idées théoriques qui sont à l'origine de la méthode développée dans ce travail sont expliquées.

---

### **Milieux poreux et caractérisation de la Distribution de Taille des Pore**

Les milieux poreux et l'écoulement en milieux poreux peuvent être observés ou décrits à plusieurs échelles. L'échelle macroscopique correspond aux dimensions de l'échantillon. Parmi les principales propriétés caractérisées à cette échelle se trouvent la porosité (ratio entre le volume des pores et le volume total), la perméabilité (capacité d'un milieu poreux pour conduire des fluides), la tortuosité et la surface spécifique. A l'échelle microscopique, aussi appelée échelle du pore, les dimensions caractéristiques sont du même ordre que celles des pores ou des grains. Même si l'espace poreux est continu, la structure poreuse est souvent discrétisée comme étant une succession de « volumes de pore » et de « constrictions ». Pourtant, une représentation très utilisée de l'espace poreux consiste en un faisceau de capillaires droits avec de différentes tailles suivant une fonction de densité de probabilité appelée couramment Distribution de Taille des Pores (DTP). La définition de DTP est très élusive et dépend de la méthode utilisée pour sa caractérisation.

Même si une diversité de modèles de complexité différente est disponible pour modéliser l'espace des pores, aucun parmi eux ne proportionne la « vérité absolue » et le choix dépend de l'application à étudier. Le modèle de faisceau de tubes est très populaire grâce à sa simplicité et son utilisation dans l'interprétation des résultats de techniques comme la porosimétrie à mercure. De plus, le faisceau de tubes permet d'obtenir des relations très utiles comme celle qui donne la taille moyenne des pores en fonction de la perméabilité  $K$  et de la porosité  $\varepsilon$  :

$$\bar{r} = \sqrt{\frac{8K}{\varepsilon}} \quad (1)$$

D'autres modèles plus compliqués comme les « réseaux de pores » permettent une représentation plus réaliste de l'espace poreux, mais nécessitent d'informations supplémentaires (inter connectivité des pores, ratio entre la taille des constrictions et la taille des volumes de pore, etc.) qui ne sont pas facilement accessibles.

La porosimétrie à mercure (MIP) est la technique la plus utilisée pour déduire la DTP des milieux poreux. Elle est fondée sur la mesure du volume de mercure qui pénètre un échantillon poreux en fonction de la pression appliquée. La pression appliquée doit vaincre la pression capillaire pour que le mercure pénètre dans les pores. Par conséquent, les résultats bruts de la MIP sont des courbes de pression capillaire (pression capillaire en fonction de la saturation en mercure). C'est pour cette raison que l'obtention de la DTP par la MIP nécessite d'une interprétation qui est faite en général moyennant un modèle de faisceau de tubes et l'équation de Washburn :

$$\Delta P = \frac{2\sigma \cos \theta}{r_{pore}} \quad (2)$$

où  $\Delta P$  est la différence de pression imposée au mercure,  $\sigma$  est la tension de surface mercure/air,  $\theta$  est l'angle de contact mercure/air et  $r_{pore}$  est la taille des pores pénétrés à cette différence de pression.

La MIP présente l'avantage de pouvoir caractériser une large gamme de taille de pores avec des tests courts. Pourtant, le choix de l'angle de contact est arbitraire dans la plupart des cas, les échantillons ne sont pas réutilisables et la dimension des pores caractérisée n'est pas facile à interpréter : taille des constrictions donnant accès à une proportion du volume des pores depuis la surface extérieure de l'échantillon. En plus, son inconvénient le plus important est la toxicité du mercure, qui présente un problème environnemental et un risque pour la santé. Des nombreux pays ont déjà interdit ou limité cette technique et d'autres obstacles à son utilisation seront introduits à la suite de la Convention de Minamata sur le Mercure.

Parmi les autres techniques de porosimétrie, il faut remarquer la microtomographie, qui permet une visualisation de l'espace poreux dont on peut tirer des nombreuses informations mais qui est limitée notamment par la résolution des images et par les critères de segmentation et de traitement postérieur pour la génération d'un réseau poreux.

### **Fluides complexes**

Les fluides non newtoniens sont ceux pour lesquels la viscosité n'est pas constante à une température donnée, mais elle dépend des conditions de l'écoulement. Dans ce travail, on s'intéressera aux fluides à seuils qui présentent une valeur de contrainte de cisaillement en deçà de laquelle ils ne s'écoulent pas. Le modèle le plus répandu pour les fluides à seuil est le modèle d'Herschel-Bulkley :

$$\begin{cases} \tau = \tau_0 + k\dot{\gamma}^n & \text{pour } \dot{\gamma} \geq \dot{\gamma}_0 \\ \dot{\gamma} = 0 & \text{pour } \tau \leq \tau_0 \end{cases} \quad (3)$$

où  $\tau$  est la contrainte de cisaillement,  $\dot{\gamma}$  est le taux de cisaillement,  $\tau_0$  est la contrainte de seuil du fluide,  $k$  est sa consistance et  $n$  est son indice d'écoulement.

Pourtant, la contrainte de seuil est une idéalisation puisque sa détermination requerrait des temps de mesure infinis. Pour cette raison le modèle de Carreau qui présente un plateau de viscosité très élevé mais finie à des faibles taux de cisaillement est en général plus représentatif des « *pseudo* » fluides à seuil réels. Ces « *pseudo* » fluides à seuil réels possèdent un comportement fortement rhéofluidifiant et une chute brusque de la viscosité à partir d'une valeur particulière du taux de cisaillement. Un tel comportement peut être assimilé à celui des fluides à seuil dans certaines applications en considérant une contrainte de seuil « apparente ». Parmi les « *pseudo* » fluides à seuil qui ont été comparés, les solutions aqueuses concentrées de gomme xanthane présentent le comportement le plus simple en milieu poreux tout en ayant une contrainte de seuil apparente, ce qui les rend les plus adaptés à notre application.

### **Ecoulement d'un fluide d'Herschel-Bulkley dans un faisceau de tubes**

Pour comprendre l'écoulement laminaire stationnaire des fluides à seuil à travers un milieu poreux, la notion de rayon critique est essentielle. En effet, sous un gradient de pression donné  $\nabla P$  et en supposant l'hypothèse de non-glissement sur la paroi des pores, le fluide à seuil s'écoulera seulement à travers les pores dont le rayon soit supérieur à une valeur critique  $r_c$  donnée par :

$$r_c = \frac{2\tau_0}{\nabla P} \quad (4)$$

Par conséquent, si l'on considère que le milieu poreux peut être modélisé par un faisceau de capillaires, le débit total à travers le milieu poreux est donné par :

$$Q(\nabla P_j) = NP \times \int_0^{\infty} q(\nabla P_j, r) p(r) dr \quad (5)$$

où  $Q(\nabla P_j)$  est le débit total traversant le faisceau à un gradient de pression  $\nabla P_j$ ,  $q(\nabla P_j, r)$  est le débit d'un fluide d'Herschel-Bulkley s'écoulant à travers un capillaire de taille  $r$  sous un gradient de pression  $\nabla P_j$ ,  $p(r)$  est la DTP et  $NP$  est le nombre de pores dans le faisceau.

L'inversion de la relation précédente pour obtenir  $p(r)$  est à l'origine des méthodes de porosimétrie actuelles par injection de fluides à seuil. Ces méthodes ont été testées dans des expériences numériques et de laboratoire avec des milieux poreux modèles. Les résultats numériques ont été satisfaisants dans les cas les plus simples, mais des erreurs importantes sont obtenues dans les cas plus complexes (fluide d'Herschel-Bulkley avec  $n \neq 1$ ). Quelques milieux poreux modèles ont été également caractérisés avec succès, mais la procédure d'exploitation n'est pas clairement détaillée et sa validité dans des milieux poreux naturels n'a pas été testée.



### 3. La Méthode des Fluides à Seuil (YSM)

Une nouvelle méthode intuitive pour déduire la DTP d'un milieu poreux à partir des données brutes obtenues lors des expériences de laboratoire est présentée dans ce chapitre. D'abord, la base de la méthode est détaillée ainsi que la procédure pour obtenir la DTP. Ensuite, la méthode est validée numériquement moyennant des expériences « *in silico* ». A la fin du chapitre, le dimensionnement des expériences de laboratoire est abordé.

#### La base de l'YSM: principe physique

Tout comme dans la porosimétrie à mercure, le milieu poreux es modélisé comme étant un faisceau de tubes dont les rayons sont distribués selon une fonction de densité de probabilité  $p(r)$  et par conséquent, le débit total à travers une classe de pores de rayon représentatif  $r_i$  à un gradient de pression  $\nabla P$ ,  $q(\nabla P, r_i)$ , est donné par :

$$q(\nabla P, r) = \begin{cases} \left\{ 1 - 2 \left[ \frac{\left(1 - \frac{2\tau_0}{r\nabla P}\right)^2}{\frac{1}{n} + 3} + \frac{\frac{2\tau_0}{r\nabla P} \left(1 - \frac{2\tau_0}{r\nabla P}\right)}{\frac{1}{n} + 2} \right] \right\} \left[ \frac{r}{\frac{1}{n} + 1} \left( \frac{r\nabla P}{2k} \right)^{\frac{1}{n}} \left( 1 - \frac{2\tau_0}{r\nabla P} \right)^{\frac{1}{n}+1} \right] \pi r^2 & \text{for } \nabla P \geq \frac{2\tau_0}{r} \\ 0 & \text{for } \nabla P \leq \frac{2\tau_0}{r} \end{cases} \quad (6)$$

avec  $r = r_i$ .

Lors d'une expérience type, un fluide à seuil dont la rhéologie est bien décrite par le modèle d'Herschel-Bulkley est injecté à travers le milieu poreux à analyser et  $N+1$  données  $(Q_i, \nabla P_i)$  brutes sont récupérées et ordonnées de façon ascendante. La gamme des données doit être telle que le débit le plus faible soit proche de zéro et le débit maximum soit dans l'intervalle où  $Q(\nabla P)$  suit une loi du type  $\nabla P^y$  avec  $y$  proche de  $1/n$ . En plus, il est supposé que  $Q_1$  est suffisamment faible pour qu'aucun pore ne participe dans l'écoulement en deçà de  $\nabla P_1$ . Par ailleurs, chaque  $\nabla P_i$  définit une classe de pores de rayon représentative  $r_i$ .

On peut exprimer que le débit mesuré à une pression  $\nabla P_j$  est supérieur à  $r_i = \alpha \frac{2\tau_0}{\nabla P_i}$  ( $r_1 > r_2 > \dots > r_N$ ) où  $\alpha$  est un facteur supérieur à l'unité dont la valeur précise sera discutée après. En plus, le débit à une pression  $\nabla P_j$  est supérieur ou égal à la somme des contributions de tous les pores dont le rayon est plus grand que  $r_j$ . Alors, nous pouvons écrire  $Q_j \geq \sum_{i=1}^{j-1} n_i q(\nabla P_j, r_i)$  où  $n_i$  représente le nombre de pores de la classe  $i$ . Pour obtenir la DTP, les  $N$  inconnues  $n_i$  doivent être déterminées en ressoudant le système d'inéquations ci-dessous :

$$\left\{ \begin{array}{l} Q_2 \geq n_1 q(\nabla P_2, r_1) \\ Q_3 \geq n_1 q(\nabla P_3, r_1) + n_2 q(\nabla P_3, r_2) \\ \vdots \\ Q_j \geq n_1 q(\nabla P_j, r_1) + n_2 q(\nabla P_j, r_2) + \dots + n_{j-1} q(\nabla P_j, r_{j-1}) \\ \vdots \\ Q_{N+1} \geq n_1 q(\nabla P_{N+1}, r_1) + n_2 q(\nabla P_{N+1}, r_2) + \dots + n_N q(\nabla P_{N+1}, r_N) \end{array} \right. \quad (7)$$

Le système d'inéquations précédent exprime le fait que le débit mesuré à un gradient donné  $\nabla P_j$  doit être supérieur ou égal à celui calculé si seulement les pores de rayon plus grand que  $r_j$  étaient involucrés.

### Détermination de la DTP

Dans la routine utilisée pour calculer un  $n_i$  ciblé, et en commençant par  $n_1$ , des valeurs positives successives sont scannées jusqu'à ce que l'une des inégalités est violée et alors la valeur maximum est affectée à  $n_i$ . Une fois que  $n_i$  ( $i = 1, \dots, N$ ) ont été calculés, la probabilité en termes de fréquence relative  $p(r_i)$  est obtenue avec:

$$p(r_i) = \frac{n_i}{\sum_{j=1}^N n_j} \quad \text{for } i = 1 \dots N \quad (8)$$

De plus, la probabilité en termes de volume relatif  $p_v(r_i)$  est déterminée avec :

$$p_v(r_i) = \frac{n_i \pi r_i^2}{\sum_{j=1}^N n_j \pi r_j^2} \quad \text{for } i = 1 \dots N \quad (9)$$

Tel que l'on a dit précédemment, le rayon représentatif  $r_i$  d'une classe de pores donnée est lié à  $\nabla P_i$  à travers  $r_i = \alpha \frac{2\tau_0}{\nabla P_i}$ ,  $\alpha$  étant un facteur supérieur ou égal à l'unité. La raison fondamentale est que pour un gradient de pression  $\nabla P_i$  donné,  $Q_i$  est dû aux pores dont les rayons sont strictement plus grands que  $\frac{2\tau_0}{\nabla P_i}$ . C'est-à-dire,  $\nabla P_i$  représente seulement le seuil à partir duquel les pores de rayon  $\frac{2\tau_0}{\nabla P_i}$  commencent à participer dans l'écoulement. Afin de calculer la valeur appropriée de  $\alpha$ , qui sera désormais nommée  $\alpha^*$ , des valeurs croissantes seront testées pour résoudre le système d'inéquations (7) en commençant par  $\alpha = 1$ . Pour chaque valeur de  $\alpha$ , la conformité de la DTP aux données expérimentales est évaluée moyennant :

$$E = \sum_{i=1}^{N+1} \left[ \frac{(Q(\nabla P_i) - Q_i)^2}{Q_i} \right] \quad (10)$$

où  $Q_i$  et  $\nabla P_i$  avec  $i = (1, \dots, N + 1)$  sont les données expérimentales de débit et de gradient de pression et  $Q(\nabla P_i)$  est calculé avec l'équation (5).  $\alpha^*$  est alors la valeur de  $\alpha$  minimisant  $E$ .

### Validation numérique de l'YSM

Un fluide à seuil dont la contrainte de seuil, consistance et indice de l'écoulement son respectivement  $\tau_0 = 10$  Pa,  $k = 1$  Pas<sup>n</sup> and  $n = 0.60$  a été injecté numériquement à travers un faisceau de 1.000.000 capillaires dont les rayons sont distribués selon la fonction de densité de probabilité bimodale suivante :

$$p(r) = \frac{\omega_1}{\sqrt{2\pi\sigma_1^2}} e^{-\frac{(r-m_1)^2}{2\sigma_1^2}} + \frac{\omega_2}{\sqrt{2\pi\sigma_2^2}} e^{-\frac{(r-m_2)^2}{2\sigma_2^2}} \quad (11)$$

avec  $m_1 = 12 \mu\text{m}$ ,  $m_2 = 24 \mu\text{m}$ ,  $\sigma_1 = 3 \mu\text{m}$ ,  $\sigma_2 = 6 \mu\text{m}$ ,  $\omega_1 = 2/3$  et  $\omega_2 = 1/3$ . Cette distribution est appelée distribution originelle. 50 gradients de pression différents ( $N + 1 = 50$ ) donnés par  $\nabla P_i = \frac{2\tau_0}{z_i}$  avec  $i = (0, \dots, N)$ ,  $z_i = z_{\max} - \frac{(z_{\max} - z_{\min})}{N} i$ ,  $z_{\min} = m_1 - 3\sigma_1$ ,  $z_{\max} = m_2 + 3\sigma_2$  ont été considérés et les débits  $Q_i$  résultants ont été calculés avec l'équation (5) (Figure 1)

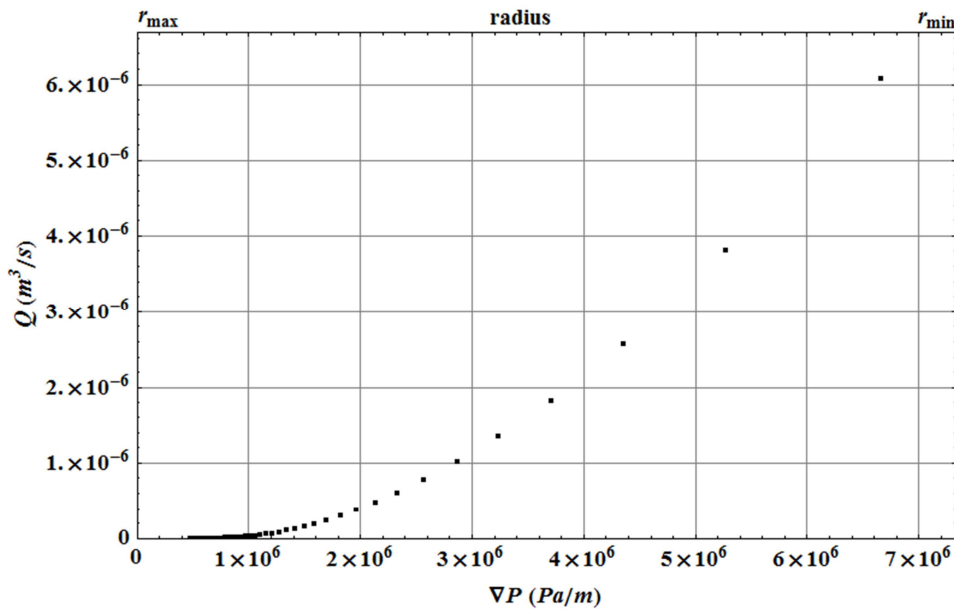


**Figure 1:** Données  $(Q_i, \nabla P_i)$  correspondant à l'injection numérique d'un fluide à seuil avec  $\tau_0 = 10 \text{ Pa}$ ,  $k = 1 \text{ Pas}^n$  et  $n = 0.60$  à travers un faisceau de 1.000.000 capillaires dont les rayons sont distribués selon  $p(r)$ .

Ensuite, l'YSM a été appliquée aux données  $(Q_i, \nabla P_i)$  et  $\alpha^*$  a été trouvé égal à 1,07. La DTP calculée en termes de  $n_i$  (nombre de pores de rayon  $r_i$ ) est en très bon accord avec la DTP originelle (Figure 2). Il a été prouvé également que parmi un ensemble de  $\alpha$  considérés,  $\alpha^*$  produit manifestement le meilleur accord entre la DTP calculée et l'originelle. Pour aller plus loin, plusieurs DTP originelles différentes ont été testées et la méthode a donné des très bons résultats dans tous les cas pour  $\alpha = \alpha^*$ . En particulier, il a été observé que  $\alpha = 1$  fourni des résultats qualitativement pires et que l'accord entre la DTP originelle et celle calculée par l'YSM est pire quand la valeur de  $\alpha$  diverge de  $\alpha^*$  (1.01 – 1.08).

Une étude de sensibilité de la DTP obtenue aux choix des paramètres de mesure, aux erreurs dans les propriétés du fluide et aux erreurs dans les mesures a été réalisée. Il a été prouvé que l'influence des valeurs de  $\tau_0$  et  $k$  sur la DTP calculée est faible ou sans importance. Cependant, les écarts dans la valeur de  $n$  ont de conséquences plus importantes car elles déforment la région des petites tailles de pore même pour des erreurs faibles. La position de la DTP sur l'axe horizontal est préservée dans tous les cas. Par ailleurs, la façon d'échantillonner les  $\nabla P_i$  lors des mesures de  $Q(\nabla P)$  ne joue pas sur la DTP calculée sauf dans le cas où les  $Q_i$  générés sont équidistants. Enfin, il a été remarqué que si bien les erreurs systématiques dans les mesures de  $(Q_i, \nabla P_i)$  n'ont pas des conséquences trop notables sur la DTP calculée, les erreurs aléatoires en « zigzag » se sont avérées très influents. Une solution visant à réduire l'importance de ces erreurs sera proposée dans le chapitre suivant.

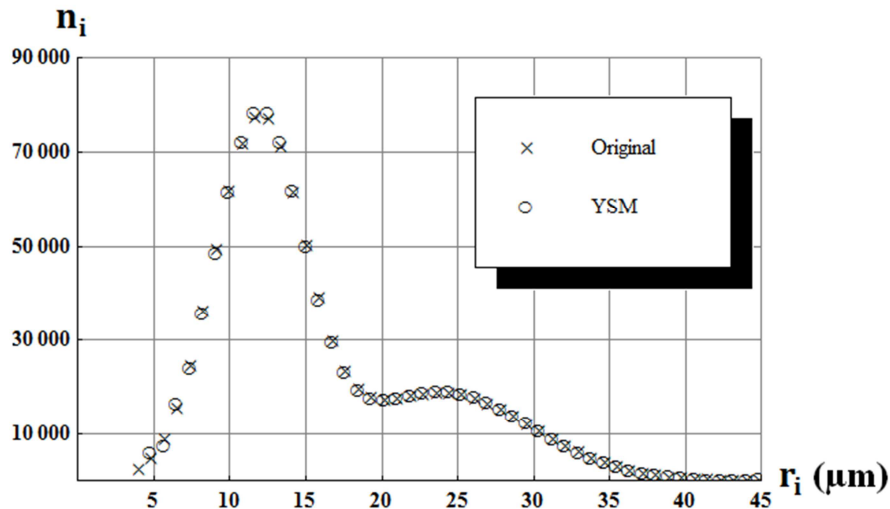


Figure 2: DTP calculée par l'YSM (cercles) comparée avec la DTP originelle (croix).

### Dimensionnement des expériences de laboratoire

Le montage expérimental est classique : le fluide est injecté à travers le milieu poreux à l'aide d'une pompe volumétrique et la chute de pression à travers l'échantillon est mesurée pour une gamme de débits imposés. Dans cette section, les caractéristiques techniques des éléments constituant l'expérience seront liées aux types de DTP ciblées.

On commence par définir le type de DTP standard  $p(r)$  que l'on souhaite caractériser avec notre système. Le débit total en fonction du gradient de pression est donné par l'équation (5) :

$$Q(\nabla P_j) = \frac{\varepsilon R^2}{\int_0^\infty p(r)r^2 dr} \int_0^\infty q(\nabla P_j, r) p(r) dr = NP \times \int_0^\infty q(\nabla P_j, r) p(r) dr$$

Afin de dimensionner l'expérience, il a été considéré suffisant d'analyser les tailles de pore dont la probabilité cumulée est comprise entre 5% et 99%. Par conséquent, les rayons des pores dont la probabilité cumulée est de 5% et 99% selon  $p(r)$  sont nommés  $r_{\min}$  et  $r_{\max}$  respectivement. Il est aussi supposé que les pores les plus grands ont un rayon de  $2r_{\max}$ , mais que leur fréquence est aussi faible pour que leur effet sur le débit total soit négligeable au-delà de la pression à laquelle les pores de rayon  $r_{\max}$  commencent à conduire.

Comme nous avons expliqué avant, la gamme des mesures doit être tel que le débit le plus fort soit dans la région où  $Q(\nabla P)$  suit la loi de puissance  $\nabla P^y$  avec  $y$  proche de  $1/n$ . Il est supposé que la différence de pression à laquelle un pore de rayon  $r_{\min}/2$  commencerait à conduire est suffisamment élevée pour satisfaire la condition précédente. Cette différence de pression est  $\Delta P_{\max} = 4\tau_0 L/r_{\min}$  où  $L$  est la longueur de l'échantillon.

Si la pompe à utiliser fournit une gamme de débits entre  $Q_{\min}$  et  $Q_{\max}$ , les conditions à respecter sont les suivantes :

$$Q_{\max} \geq NP \int_{r_{min}}^{2r_{\max}} f_1(r, r_{\min}, r) \left( \frac{2r\tau_0}{kr_{\min}} \right)^{\frac{1}{n}} \pi r^2 p(r) dr \quad (12)$$

$$Q_{\min} \leq NP \int_{r_{\max}}^{2r_{\max}} f_2(r, r_{\max}, n) \left( \frac{r\tau_0}{kr_{\max}} \right)^{\frac{1}{n}} \pi r^2 p(r) dr \quad (13)$$

avec

$$f_1(r, r_{\min}, n) = \left\{ 1 - 2 \left[ \frac{\left(1 - \frac{r_{\min}}{2r}\right)^2}{\frac{1}{n} + 3} + \frac{\frac{r_{\min}}{2r} \left(1 - \frac{r_{\min}}{2r}\right)}{\frac{1}{n} + 2} \right] \right\} \left[ \frac{r}{\frac{1}{n} + 1} \left(1 - \frac{r_{\min}}{2r}\right)^{\frac{1}{n}+1} \right]$$

$$f_2(r, r_{\max}, n) = \left\{ 1 - 2 \left[ \frac{\left(1 - \frac{r_{\max}}{r}\right)^2}{\frac{1}{n} + 3} + \frac{\frac{r_{\max}}{r} \left(1 - \frac{r_{\max}}{r}\right)}{\frac{1}{n} + 2} \right] \right\} \left[ \frac{r}{\frac{1}{n} + 1} \left(1 - \frac{r_{\max}}{r}\right)^{\frac{1}{n}+1} \right]$$

$$NP = \frac{\varepsilon R^2}{\int_0^{\infty} p(r) r^2 dr}$$

où  $R$  est le rayon de l'échantillon.

Il est supposé que la pompe peut travailler à des pressions comprises entre  $P_{\min}$  et  $P_{\max}$  avec

$$P_{\min} \leq 2\tau_0 L / r_{\max} \quad (14)$$

$$P_{\max} \geq 4\tau_0 L / r_{\min} \quad (15)$$

Les conditions (12) et (13) sont réécrites comme:

$$k \geq \frac{\tau_0}{Q_{\max}^n} \left[ NP \times \left( \frac{2}{r_{\min}} \right)^{\frac{1}{n}} \times \int_{r_{\min}}^{2r_{\max}} f_1(r, r_{\min}, r) \pi r^{2+\frac{1}{n}} p(r) dr \right]^n \quad (16)$$

$$k \leq \frac{\tau_0}{Q_{\min}^n} \left[ NP \times \left( \frac{1}{r_{\max}} \right)^{\frac{1}{n}} \times \int_{r_{\max}}^{2r_{\max}} f_2(r, r_{\max}, r) \pi r^{2+\frac{1}{n}} p(r) dr \right]^n \quad (17)$$

Les conditions (14) et (15) sont réécrites aussi, obtenant:

$$\frac{r_{\max} P_{\min}}{2L} \leq \tau_0 \leq \frac{r_{\min} P_{\max}}{4L} \quad (18)$$

Les inéquations (16), (17) et (18) peuvent être utilisées pour borner les propriétés du fluide nécessaire pour caractériser une DTP standard avec une pompe donnée. De façon analogue, les mêmes inéquations peuvent être utilisées pour estimer les propriétés de la pompe nécessaire pour caractériser une DTP standard avec un fluide donné.

## 4. Expériences de laboratoire

Dans ce chapitre, la méthode présentée dans le Chapitre 3 est testée dans le cas de solutions de gomme xanthane injectées à travers un silicate fritté dont la DTP est inconnue. D'abord, des expériences préliminaires sont présentées dans le but d'établir la base de la procédure expérimentale qui sera adoptée par la suite. Après, nous étudierons l'influence de la concentration du polymère en solution sur les caractéristiques de la DTP obtenue avec l'YSM. Ensuite, l'YSM sera appliquée à de différents types de milieux poreux afin d'étudier la qualité de la DTP obtenue dans chaque cas et évaluer les effets de la rétention, l'adsorption et la dégradation du polymère. En plus, une modification de l'YSM sera proposée sur la base des conclusions tirées des expériences.

### Expériences préliminaires de laboratoire

Deux solutions de gomme xanthane à des concentrations de polymère ( $C_p$ ) de 7000 ppm et 6000 ppm respectivement, et contenant 400 ppm de  $\text{NaN}_3$  (bactéricide) ont été préparées pour ces expériences préliminaires. Ces solutions ont été caractérisées à l'aide d'un rhéomètre à contrainte imposée équipé avec une géométrie cône-plat. Toutes les mesures rhéologiques ont été effectuées à 20°C. En effet, il a été observé que leur rhéologie était bien approximée par un modèle d'Herschel-Bulkley même si, tel que l'on a expliqué dans le Chapitre 2, la contrainte de seuil était seulement apparente. La procédure pour ajuster les mesures de  $\tau$  en fonction de  $\dot{\gamma}$  au modèle d'Herschel-Bulkley consiste à minimiser la somme

$$\sum_i (\tau(\dot{\gamma}_i) - \tau_i)^2 \dot{\gamma}_i \quad (19)$$

où  $\tau(\dot{\gamma})$  est donné par l'équation (3) et  $(\dot{\gamma}_i, \tau_i)$  sont les mesures expérimentales. Cette procédure permet d'obtenir les valeurs de  $\tau_0$ ,  $n$  et  $k$  pour chaque  $C_p$ . Il a été observé que, comme prévu, la solution la plus visqueuse reproduit le mieux le comportement décrit par le modèle d'Herschel-Bulkley.

Par ailleurs, le milieu poreux à analyser était un silicate fritte synthétique (Aerolith®10, PALL Corporation, USA) avec porosité et perméabilité de  $\varepsilon = 0.40$  et  $K = 5 \text{ D}$  respectivement. Une représentation schématique du montage expérimental est présentée dans la Figure 3. De gauche à droite il y a (1) une pompe du type pousse-seringue (PHD Ultra, Harvard Apparatus), chargée alternativement avec les solutions de polymère ou avec de l'eau distillée et déminéralisée, qui assure l'injection de fluide à débit contrôlé, (2) le milieu poreux à analyser (échantillon cylindrique  $L = 10 \text{ cm}$ ;  $R = 2,5 \text{ cm}$ ), (3) un récipient pour collecter les effluents. Un capteur de pression Rosemount 3051 Pressure Transmitter) est aussi connecté aux extrémités du milieu poreux.

La procédure suivie pour préparer le milieu poreux a été la suivante. Les deux bouts de l'échantillon ont été mis en contact avec des plaques d'injection en aluminium. Ensuite, les surfaces en contact avec le milieu poreux ont été revêtues de Téflon pour éviter l'échange ionique entre le métal et l'échantillon. Enfin, la surface latérale de l'échantillon a été revêtue avec une résine époxy non mouillante enveloppée en fibre de verre et couverte à son tour avec de la résine époxy pour assurer la étanchéité latérale et la tenure mécanique.

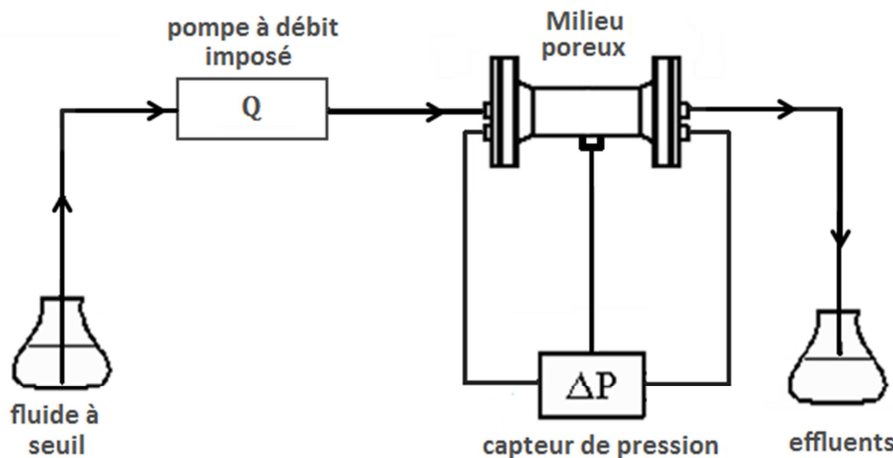


Figure 3 Représentation schématique du montage expérimental.

D'abord, le milieu poreux a été saturé avec du CO<sub>2</sub> pour éviter la présence de bulles de gaz pendant les expériences. Après, l'échantillon a été saturé avec de l'eau déminéralisée, filtrée et dégazée et laissé en repos pendant environ 12 heures. Alors, la perméabilité et porosité de l'échantillon ont été mesurées avant l'injection des solutions de xanthane dégazées. 2 volumes de pore de solution de xanthane ont été injectés à un débit intermédiaire. Un volume de pores additionnel a été envoyé au débit le plus fort qui serait imposé pendant les expériences pour assurer que la solution saturait toutes les classes de pore. Une fois saturé, l'échantillon a été laissé en repos pendant 12 heures. Dans ces expériences préliminaires, le débit a été imposé de façon croissante et la perte de charge stationnaire a été relevée. La température de la salle a été consignée à 20 °C ± 0.1 pendant toutes les expériences.

La méthode présentée dans le chapitre précédent a été appliquée aux mesures ( $Q_i$ ,  $\nabla P_i$ ) obtenues lors de ces expériences préliminaires pour obtenir les DTPs, qui sont comparées dans la Figure 4 avec la DTP déduite par la MIP. Même si la MIP ne doit pas être utilisée comme référence pour évaluer la qualité de la DTP obtenue par l'YSM, il est remarqué que l'accord est meilleur avec l'expérience à concentration plus élevée ( $C_p = 7000$  ppm). Une étude pour évaluer l'influence de  $\alpha$  a montré que la correspondance entre la MIP et l'YSM est optimum pour des valeurs de  $\alpha$  proches de  $\alpha^*$ .

Conformément à l'objectif de cette section, les observations réalisées lors ces tests préliminaires nous ont permis de décider sur les procédures à suivre dans des expériences postérieures. En effet, l'applicabilité de l'YSM aux expériences de laboratoire a été démontrée et le critère de sélection de  $\alpha^*$  s'est avéré performant. Afin de minimiser les effets

de l'éventuelle rétention de polymère aux faibles débits, il a été décidé désormais d'imposer les débits de façon décroissante lors des mesures de  $Q(\nabla P)$  et d'utiliser un xanthane plus pur. En outre, les temps de stabilisation des  $\nabla P_i$  pourront être estimés à partir des expériences préliminaires.

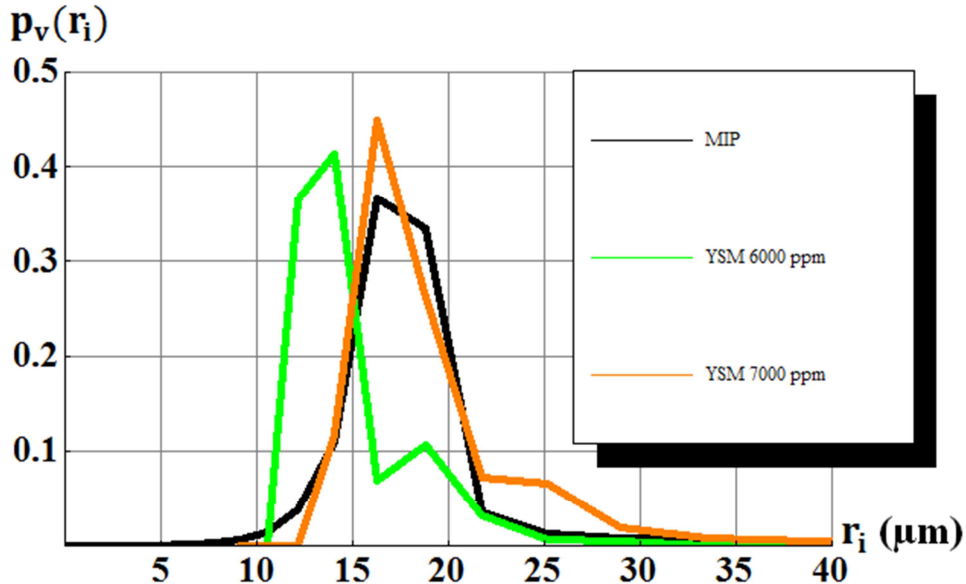


Figure 4: DTPs obtenues par l'YSM correspondant aux expériences préliminaires comparées avec la DTP déduite par la MIP.

### **Sensibilité de la DTP obtenue à la concentration de polymère**

Tel que l'on a observé dans les expériences précédentes, la concentration de polymère semble avoir un effet sur la DTP obtenue par l'YSM. Par conséquent, dans cette section on présente les expériences d'injection de 5 solutions aqueuses de xanthane ayant des  $C_p$  de 4000, 5000, 6000, 7000 et 8000 ppm à travers 5 échantillons analogues du même silicate fritté (Aerolith®10, PALL Corporation, USA).

Les rhéogrammes des 5 solutions ainsi que leurs ajustements par une loi d'Herschel-Bulkley obtenues de la même manière que dans la section précédente sont présentés dans la Figure 5. Leurs viscosités en fonction du taux de cisaillement sont présentées dans la Figure 6 dans le but d'illustrer que la chute de viscosité est plus drastique pour les solutions les plus concentrées.

Le protocole expérimental pour les mesures de  $Q(\nabla P)$  a été le même que dans les tests préliminaires, sauf pour l'imposition des débits de façon décroissante et l'optimisation des temps de chaque mesure stationnaire. A la suite de chaque expérience, un ensemble d'environ 40 données ( $Q_i, \nabla P_i$ ) a été obtenu (Figure 7).

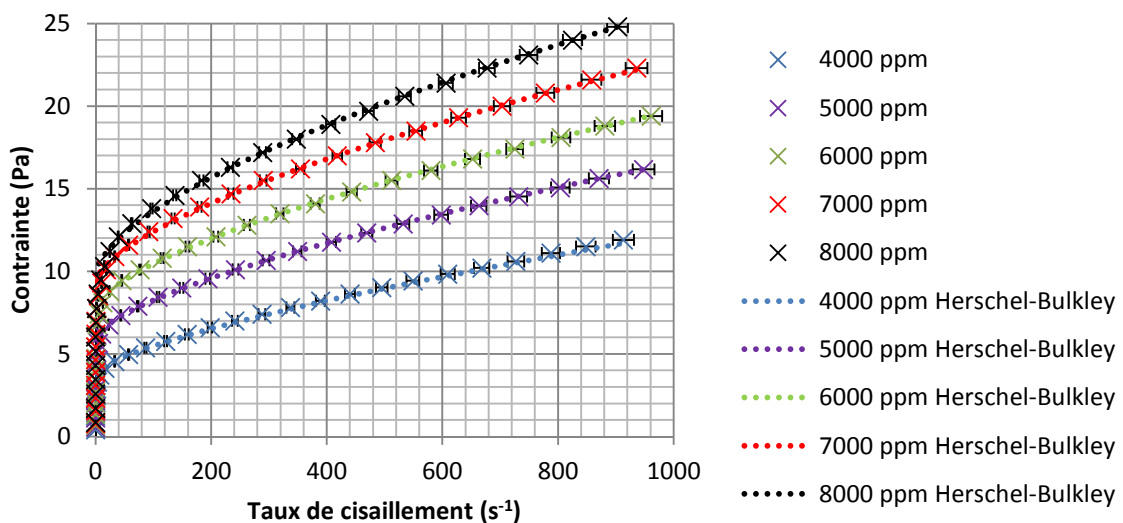


Figure 5: Rhéogrammes des solutions de xanthane utilisées dans les expériences.

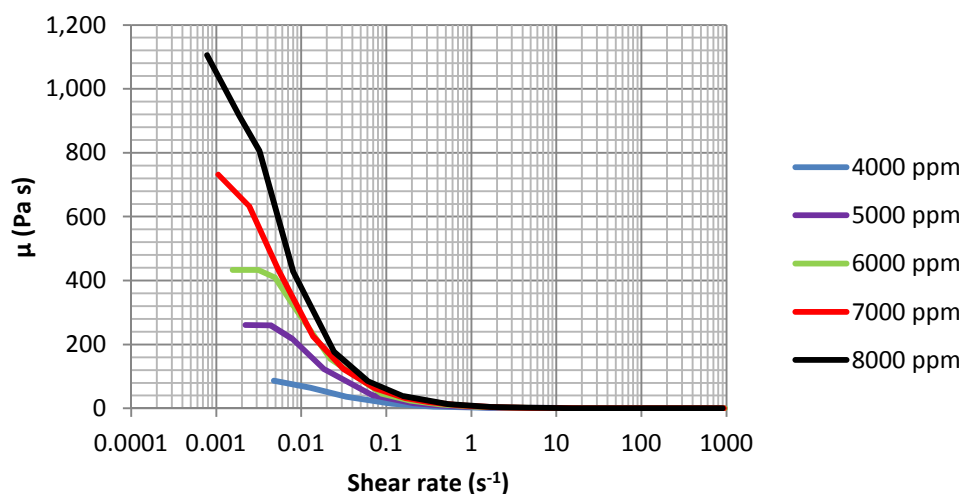


Figure 6: Viscosité en fonction du taux de cisaillement pour les solutions de xanthane utilisées dans les expériences.

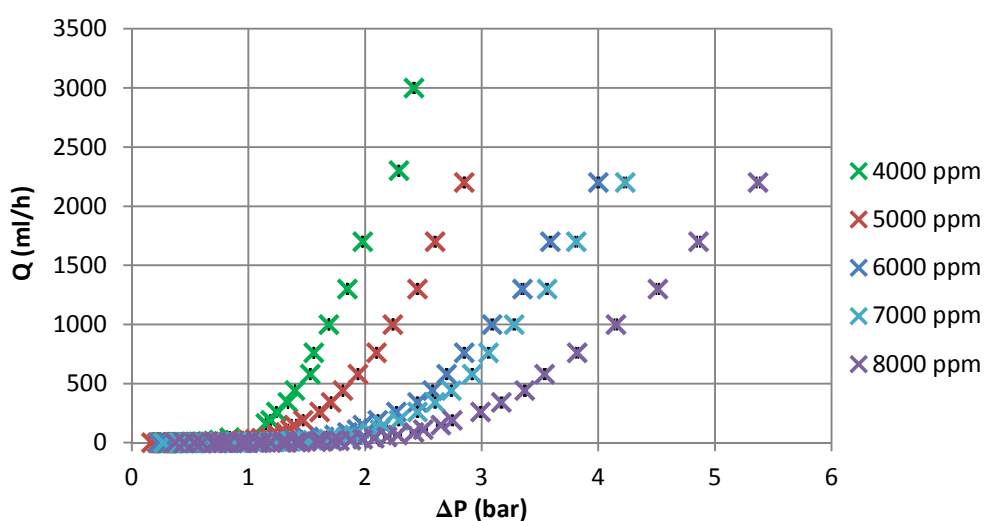


Figure 7: Données ( $Q_i, \nabla P_i$ ) expérimentales obtenues lors de l'injection de solutions de xanthane avec  $C_p$  différentes à travers un silicate fritté A10.

La viscosité effective des solutions obtenue lors des mesures avec le rhéomètre a été comparée avec la viscosité apparente dans le milieu poreux  $\mu_{app}$  défini comme suit:

$$\mu_{app} = \frac{KA\nabla P}{Q} \quad (20)$$

Le taux de cisaillement apparent considéré est de la forme :

$$\dot{\gamma}_{app} = \beta \frac{Q/A}{\sqrt{K\varepsilon}} \quad (21)$$

où  $\beta$  est un paramètre empirique de “shift” entre les rhéologies apparente et effective. A la suite de cette comparaison, il a été observé que le fluide présente un comportement apparent moins rhéofluidifiant que celui mesuré hors milieu poreux. De plus, la large gamme de débits imposée dans nos expériences a permis de constater une forte dépendance entre  $\beta$  et la gamme des taux de cisaillement apparente.

Par ailleurs, les données ( $Q_i, \nabla P_i$ ) obtenues lors des expériences ont été exploitées par l'YSM afin de calculer les DTPs correspondantes, qui sont présentées et comparées à celle déduite par la MIP dans la Figure 8. Dans cette figure, il est remarqué que les DTPS obtenues par l'YSM sont plus décalées vers les petits pores. Ceci semble cohérent dû à la nature des expériences. En effet, elles sont basées sur la mesure des pertes de charge, lesquelles sont dominées par les constrictions des pores. En plus, il est observé que plus la concentration est forte, plus les DTPs obtenues par l'YSM sont proches de celle déduites par la MIP (sauf  $C_p = 8000$  ppm). Il est rappelé ici que les DTPs correspondant aux  $C_p$  les plus élevées sont « *a priori* » les plus fiables puisque le comportement des solutions est plus proche de celui d'un fluide d'Herschel-Bulkley. Enfin, des valeurs similaires de  $\alpha^*$  sont obtenues quelle que soit la  $C_p$ .

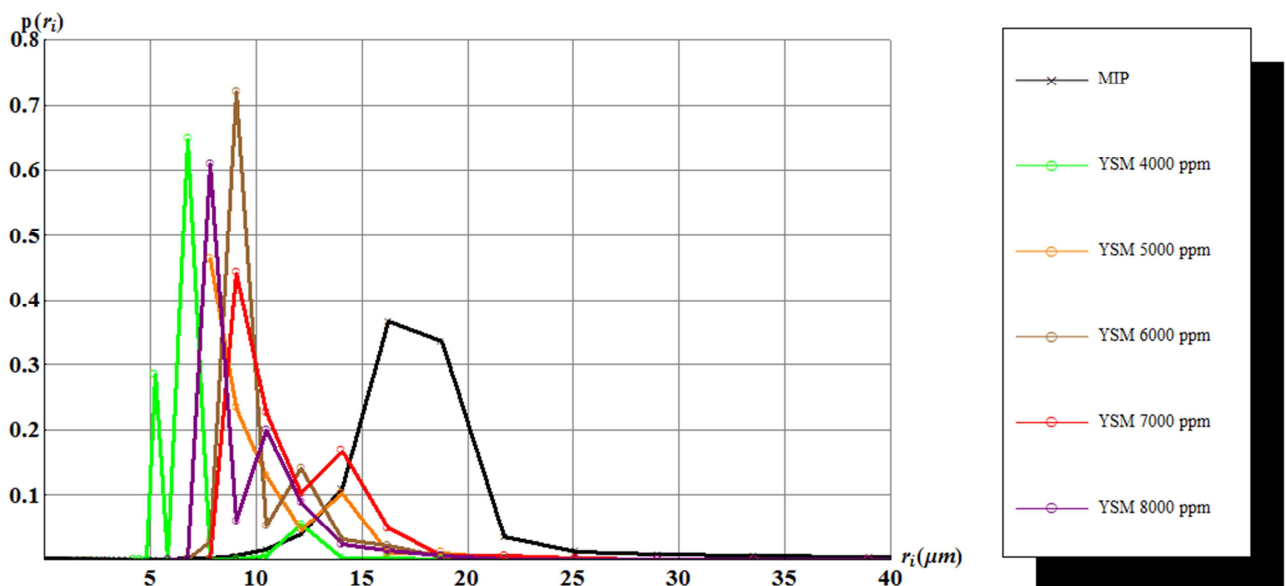


Figure 8: DTPs obtenues par l'YSM comparées avec celle déduite par la MIP pour le silicate fritté A10.

### **Sensibilité de la DTP obtenue au type de milieu poreux**

Dans cette section nous présentons les expériences d'injection de solutions aqueuses de xanthane ( $C_p = 7000$  ppm) à travers cinq milieux poreux différents. Pour ces expériences, deux solutions de xanthane ont été préparées :

- Solution 1:  $C_p = 7000$  ppm, concentration NaCl ( $C_s$ ) = 0 ppm.
- Solution 2:  $C_p = 7000$  ppm, concentration NaCl ( $C_s$ ) = 5000 ppm.

Les cinq milieux poreux analysés sont :

- Échantillon 1 : Aerolith®10 (PALL Corporation, USA).
- Échantillon 2: Aerolith®10 (PALL Corporation, USA).
- Échantillon 3: Bentheimer Sandstone (Kocurek Industries, Inc., USA).
- Échantillon 4: Castlegate Sandstone (Kocurek Industries, Inc., USA).
- Échantillon 5: Berea Sandstone (Cleveland Quarries, USA).

Les porosités et perméabilités mesurées ainsi que les longueurs (L) et diamètres (D) de ces cinq échantillons cylindriques sont donnés dans le Tableau 1 :

Sample	K (mD)	$\epsilon$	L (cm)	D (cm)
1	9000	0.45	10	5
2	2400	0.40	5	3.8
3	2200	0.25	5	3.8
4	750	0.25	5	3.8
5	38	0.22	5	3.8

Tableau 1: Porosités, perméabilités et dimensions des échantillons.

Les rhéologies effectives des deux solutions ont été caractérisées avec des rhéomètres à contrainte imposée (géométrie cône-plat pour la Solution 1 et « *double gap* » pour la solution 2) et leurs paramètres d'Herschel-Bulkley ont été déterminés comme expliqué précédemment. En plus, l'homogénéité des solutions a été vérifiée ainsi que l'inexistence d'effets thixotropiques importants.

Les expériences avec l'échantillon 1 ont été réalisées avec la Solution 1, le reste d'expériences ont été réalisées avec la Solution 2 (salée). Le montage et le protocole expérimental utilisés pour la saturation et l'acquisition des mesures de  $Q(\nabla P)$  lors de l'écoulement de la Solution 1 à travers l'échantillon 1 est le même que celui présenté dans la section précédente. Cependant, dû aux pressions plus élevées générées par les milieux moins perméables, un montage différent a été utilisé avec le reste d'échantillons : une pompe à piston très robuste (Composites & Technologies, T-Pump v 1.9.) capable de travailler à des fortes pressions a été employée et les échantillons poreux ont été montés dans une cellule Hassler (Hassler coreholder, Vinci Technologies, France) et confinés avec de l'eau pressurisée. En outre, un densimètre et un collecteur de fractions ont été installés en aval du milieu poreux pour la réalisation de mesures de densité et de viscosité qui seront présentées dans la section suivante.

Dans le cas des expériences avec les échantillons 2 à 5, la saturation du milieu poreux et les mesures de perméabilité et porosité ont été réalisées avec une saumure ( $C_s = 5000 \text{ ppm}$ ). Le protocole suivi pour les mesures de  $Q(\nabla P)$  lors de l'injection de la Solution 2 est similaires à ceux de l'échantillon 1 et la gamme de débits imposée a été de 1000 ml/h à 0.01 ml/h dans tous les cas.

De la même manière que pour les expériences présentées dans la section précédente, la viscosité effective a été comparée avec la viscosité apparente, confirmant que la viscosité apparente présente un comportement moins rhéofluidifiant. Ce comportement moins rhéofluidifiant est dû avec toute probabilité aux effets de la couche de déplétion proche des parois du pore, qui se traduit en une viscosité apparente aux faibles débits.

Par ailleurs, les données ( $Q_i, \nabla P_i$ ) obtenues dans ces expériences ont été exploitées par l'YSM, et les DTPs obtenues sont présentées dans la Figure 9. Tel que l'on voit dans cette Figure, les DTPs sont ordonnées de façon cohérente par rapport au rayon moyen prédict par l'équation (4), sauf pour l'échantillon 2. Il a été aussi démontré que la valeur de  $\alpha^*$  ne dépend pas de la perméabilité du milieu poreux.

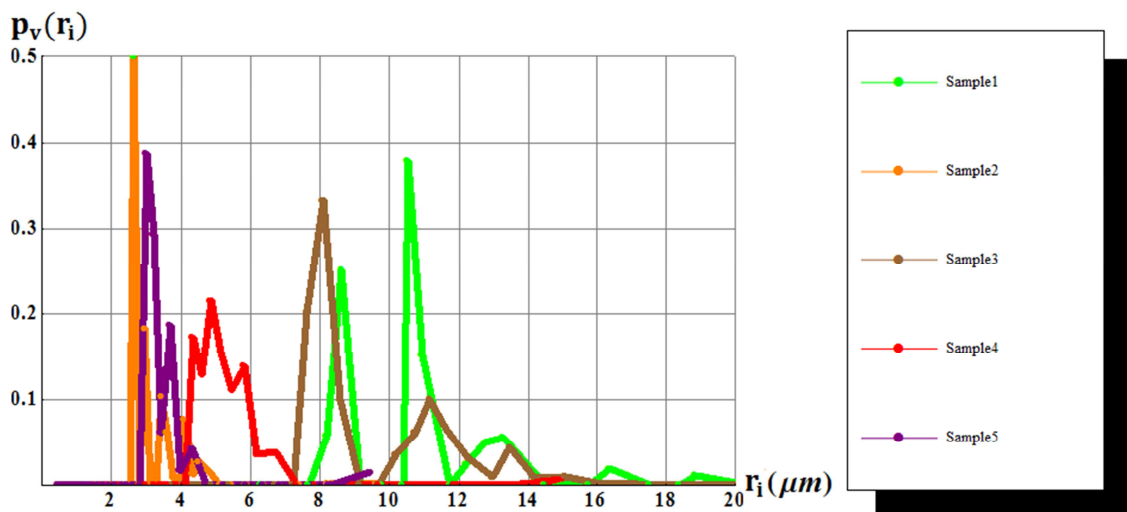


Figure 9: Comparaison des DTPs obtenues par l'YSM

### Expériences complémentaires de laboratoire

Plusieurs expériences complémentaires ont été effectuées avec les échantillons 2 à 5 afin d'évaluer les effets de l'adsorption, de la rétention et de la dégradation du polymère dans les milieux poreux.

Le premier type d'expériences consiste à tracer l'évolution de la densité des effluents en fonction du nombre de volumes de pores injectés lors de la saturation en saumure et lors de la saturation en solution de xanthane. La comparaison des deux courbes permet d'estimer la masse de polymère adsorbée à partir du décalage entre les deux courbes. A la suite de ces expériences, l'adsorption de polymère calculée est de 240 µg par gramme de solide pour

l'échantillon 2 et de 90 µg par gramme de solide pour l'échantillon 5. Même s'il existe de la rétention, on prédit que ses effets sur la perméabilité resteront peu importants du fait que la xanthane est une molécule rigide qui s'adsorbe à plat. Le retard de la courbe de traçage miscible de la saumure par rapport à celle de la solution de xanthane dans le cas de l'échantillon 3 pourrait refléter le bouchage ou l'exclusion des très petits pores, ce qui réduirait le volume balayé par la solution de polymère.

Le deuxième type d'expérience consiste à faire un traçage de la viscosité des effluents lors de la saturation en xanthane. La lente stabilisation de la viscosité du fluide sortant du milieu poreux suggère une cinétique d'adsorption très lente due au détachement et réadsorption des molécules de polymère. Cependant les effets de l'adsorption et de l'éventuelle rétention restent modérés puisqu'une valeur stable de viscosité et de densité des effluents est finalement atteinte et maintenue. Il est aussi observé que la viscosité des effluents à la fin de la saturation est légèrement inférieure à celle du fluide injecté, ce qui pourrait être la signature d'une très faible dégradation mécanique du polymère.

Les derniers tests consistent à caractériser les rhéogrammes des effluents après les mesures de  $Q(\nabla P)$  et à les comparer avec celles du fluide avant injection. Une forte réduction de la viscosité du fluide sortant du milieu poreux entre le début et la fin des mesures a été remarquée dans tous les cas. Néanmoins, un balayage à fort débit permet de récupérer la viscosité initiale. La conclusion est qu'il existe une rétention de polymère due à l'orientation aléatoire des molécules aux plus faibles débits.

### **Modification de l'YSM pour les expériences de laboratoire**

Dans le Chapitre 3 il a été montré que les erreurs aléatoires du type "zigzag" dans les mesures  $Q(\nabla P)$  exercent une influence très négative sur la DTP obtenue par l'YSM. En outre, la rétention de polymère joue sur la précision des mesures aux faibles débits. Dans cette section, on propose une modification de l'YSM qui consiste à introduire un ajustement des données  $Q(\nabla P)$  brutes afin de réduire l'effet des erreurs de mesure et de la rétention.

La viscosité apparente des solutions de xanthane en fonction du taux de cisaillement apparent est fréquemment représentée par un modèle de Carreau. En plus, la combinaison des définitions de viscosité apparente et du taux de cisaillement apparent avec le modèle de Carreau donnent la relation suivante entre  $\nabla P$  et  $Q$  :

$$\nabla P = \frac{Q}{KA} \left[ \left[ 1 + \left( \frac{\lambda\beta}{A\sqrt{K\varepsilon}} Q \right)^2 \right]^{\frac{n-1}{2}} (\mu_{0app} - \mu_{\infty app}) + \mu_{\infty app} \right] \quad (22)$$

La relation précédente a été utilisée pour ajuster les données  $(Q_i, \nabla P_i)$  de nos expériences et cet ajustement capture bien la tendance des mesures. Ensuite, le gradient de pression correspondant à chaque  $Q_i$  a été évalué avec cette fonction. Il en résulte un nouveau jeu de données  $(Q_i, \widetilde{\nabla P}_i)$  où  $\widetilde{\nabla P}_i$  est le gradient obtenu avec l'équation (22). L'exploitation de ces

données pour obtenir la DTP demande d'une étude spécifique qui ne sera présenté dans ce travail. Néanmoins des premiers résultats sont présentés dans l'Annexe B.



## 5. Comparaison de l'YSM avec d'autres méthodes de porosimétrie

Tel que l'on a expliqué dans le Chapitre 2, la DTP est une caractéristique élusive dont la définition dépend de la méthode utilisée pour sa détermination. Néanmoins, on présente ici une comparaison entre méthodes dans le but d'expliquer quelques différences dans l'interprétation des résultats et dans l'information que l'on peut tirer de chaque technique.

### Comparaison entre MIP et YSM

Des échantillons analogues à ceux utilisés dans les manipulations précédentes ont été caractérisés par la MIP. Les résultats bruts de la MIP sont des courbes de pression capillaire qui peuvent être interprétées en termes de DTP de façon simple moyennant l'équation (2). Les résultats sont présentés dans la Figure 10. Un aspect important dont il faut tenir compte quand on représente des DTPs est la distance entre les différentes classes de taille de pores. Dû à la façon d'imposer les pressions lors des tests de MIP, il y a souvent une grande densité de mesures correspondant aux faibles tailles de pores. Ceci entraîne une fragmentation des probabilités calculées dans de classes de taille très proches et cache l'importance totale des petits pores. Un autre aspect important est l'influence sur la DTPs de l'angle de contact choisi pour le couple mercure/air. Dans l'intervalle usuel des angles de contact utilisés, les tailles de pores peuvent différer de 30% en fonction du choix, qui reste arbitraire dans la plupart des cas.

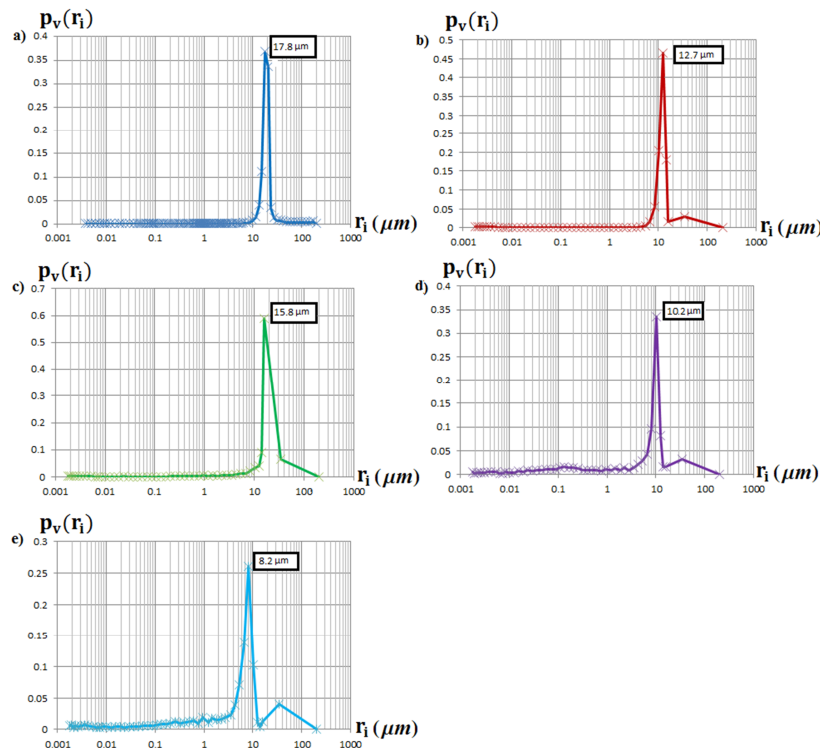


Figure 10: DTPs obtenues par la MIP pour les 5 matériaux analysés dans ce travail. a) Echantillon 1 ; b) Echantillon 2 ; c) Echantillon 3 ; d) Echantillon 4 ; e) Echantillon 5.

Les DTPs obtenues par de différentes techniques ne peuvent pas être directement comparées pour deux raisons principales. La première est que les dimensions de pore représentées dépendent de la technique. La deuxième est que les classes de taille de pore obtenues dans chaque cas ne sont pas les mêmes et il faut les regrouper pour qu'elles soient égales avant de les comparer. Les DTPs obtenues par l'YSM ont été regroupées pour les faire correspondre avec celles du MIP. Ensuite elles ont été comparées avec les DTPs déduites à partir de la MIP comme présenté dans la Figure 11.

En plus, la taille moyenne donnée par les deux techniques a été comparée avec les prédictions de l'équation (1), basées sur un modèle de faisceau de tubes (Figure 12). On peut observer que les tailles de pore obtenues par l'YSM sont plus petites que celles de la MIP et plus proches des prédictions de l'équation(1). La raison est la même qui a été expliquée précédemment : les mesures de perte de charge de l'YSM sont dominées par la taille des constrictions tandis que pour la MIP la dimension caractéristique est celle de la première entrée vers une certaine proportion du volume de pores.

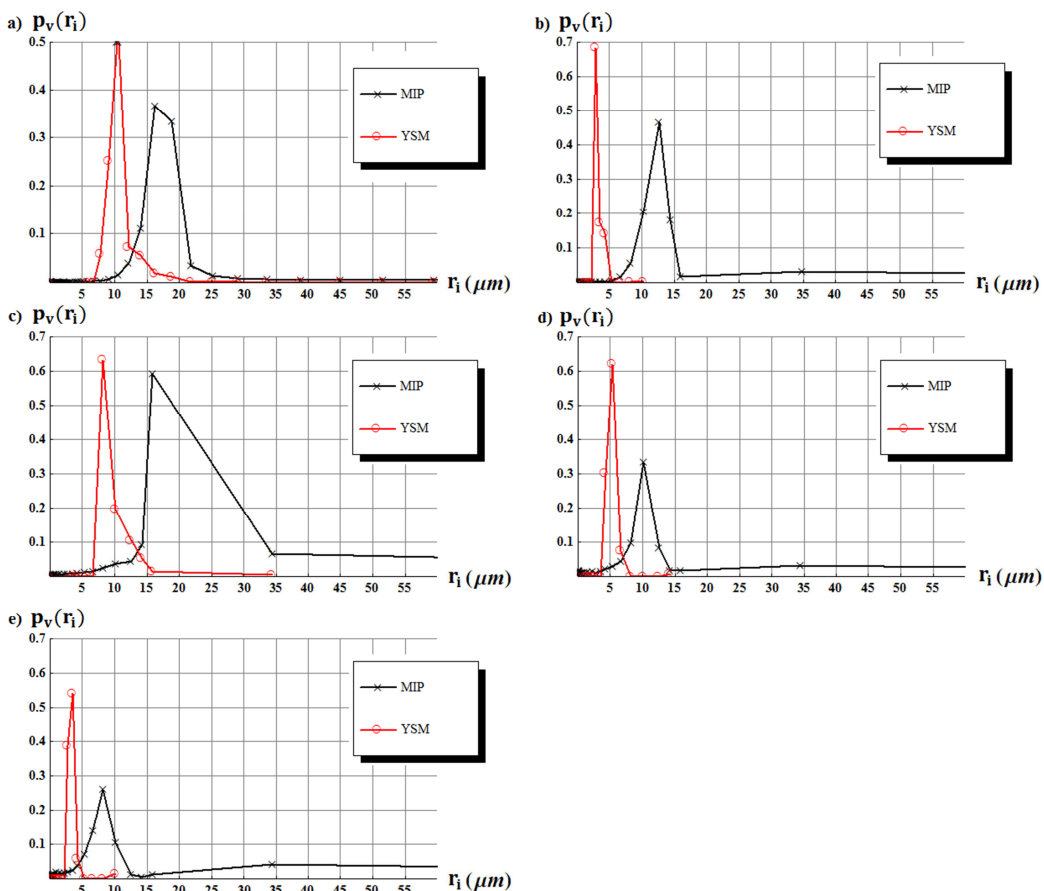


Figure 11: DTPs obtenues avec l'YSM comparées avec celles obtenues par la MIP pour les 5 matériaux. a) Echantillon 1 ; b) Echantillon 2 ; c) Echantillon 3 ; d) Echantillon 4 ; e) Echantillon 5.

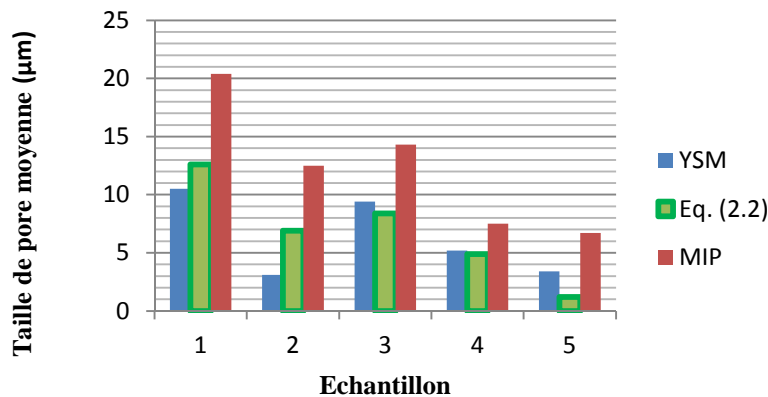


Figure 12 Comparaison entre les prédictions de l'équation (1) et les rayons moyens calculés par la MIP et YSM.

Par ailleurs, la courbe de pression capillaire est de grande importance dans l'industrie pétrolière entre autres. Elle représente la saturation d'un milieu poreux en phase non-mouillante en fonction de la pression appliquée. Avec la porosimétrie à mercure, on mesure directement cette courbe, ce qui n'est pas le cas de l'YSM. En effet, l'obtention d'une courbe de pression capillaire mercure/air dans le cas de l'YSM entraîne une transformation de la DTP fournie par cette méthode. La procédure consiste à associer une pression capillaire  $P_c$  à chaque classe de taille de pore avec l'équation (23). Ensuite, la saturation  $S$  est calculée comme étant la probabilité cumulée en volume pour chaque classe de taille de pore (équation 24).

$$P_{ci} = -\frac{2\sigma \cos \theta}{r_i} \quad (23)$$

$$S(P_{ci}) = \sum_{\forall r_i \geq -\frac{2\sigma \cos \theta}{P_{ci}}} p_v(r_i) \quad (24)$$

$\Theta$  (angle de contact mercure/air) est considéré comme étant de  $140^\circ$ , et  $\sigma$  est la tension de surface du couple mercure/air ( $0.485 \text{ N m}^{-1}$  à  $25^\circ\text{C}$ ).

En considérant les conséquences de la transformation directe des DTPs obtenues avec l'YSM en  $P_c$  avec cette procédure, on peut tirer les conclusions suivantes :

- Les classes de taille de pore  $r_i$  calculées par l'YSM sont intimement liées aux constrictions de milieux poreux. En effet, la méthode est basée sur la mesure de  $\nabla P$ , laquelle est dominée par les étranglements de pores. Dès lors, nous considérons ici en première approximation que l'écoulement d'un fluide à seuil à travers un pore ne se produit que lorsque le gradient de pression est suffisamment élevé pour produire un écoulement à travers un cylindre ayant la même longueur que le pore et le même rayon que la constriction.

- Il est donc implicitement supposé que tout le volume d'un pore sera saturé seulement une fois que la pression appliquée soit supérieure à celle requise pour pénétrer la constriction la plus étroite.
- Par conséquent, la pression capillaire correspondant à une saturation donnée doit être plus grande dans le cas de l'YSM que dans le cas du MIP. Ceci est représenté schématiquement dans la Figure 13, dans laquelle on considère un milieu poreux idéalisé avec seulement trois pores. Pour les mêmes raisons, les DTP calculées à partir de la MIP présentent des pores plus grands que celles obtenues par l'YSM.

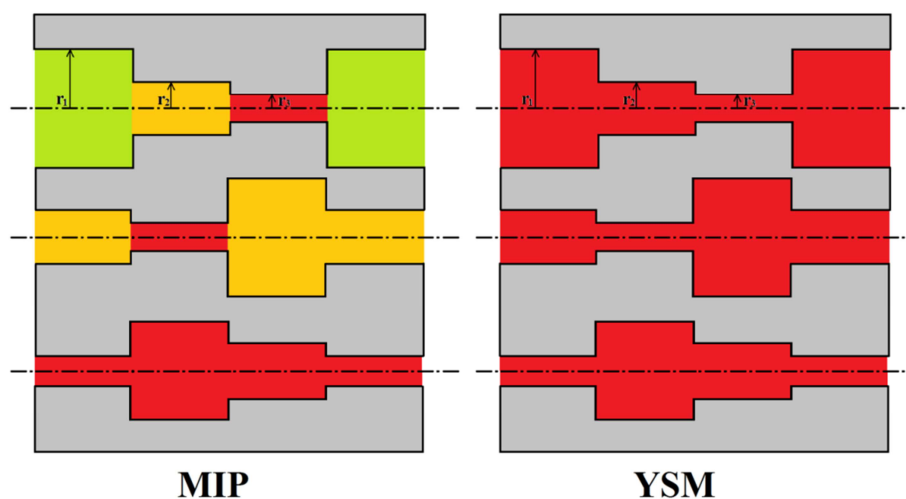
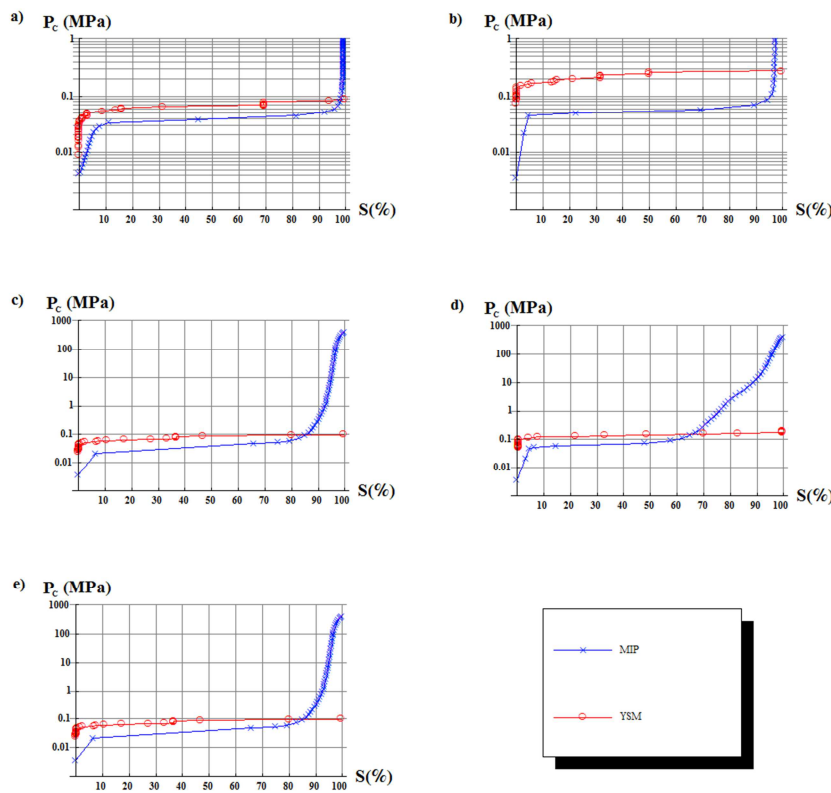


Figure 13: Milieu poreux idéalisé avec seulement 3 pores pour montrer l'interprétation de la saturation avec les deux méthodes. Les régions grises représentent le volume solide. Les régions non grises représentent le volume des pores saturés aux pressions capillaires  $P_{c1} = -\frac{2\sigma\cos\theta}{r_1}$  (vert),  $P_{c2} = -\frac{2\sigma\cos\theta}{r_2}$  (orange) et  $P_{c3} = -\frac{2\sigma\cos\theta}{r_3}$  (rouge) respectivement.

Le comparatif entre les courbes de pression capillaire obtenues par les deux techniques est présenté dans la Figure 14. On remarque que pour tous ces matériaux, il existe une valeur critique de  $P_c$  au-delà de laquelle  $S$  augmente brusquement. Cette valeur critique mesurée par la MIP est du même ordre, bien que plus faible, que celle calculée à partir des DTPs déduites par l'YSM. Ceci est cohérent avec les arguments ci-dessus. En outre, alors que dans les courbes de pression capillaire de la méthode MIP il y a une augmentation de  $P_c$  supplémentaire nécessaire pour atteindre les plus fortes saturations après le plateau, ce n'est pas le cas pour l'YSM. Ces hautes pressions capillaires sont dues aux plus petits pores, qui ne sont pas analysés avec YSM. La raison en est que leur analyse avec YSM exigerait l'imposition de pressions et de débits très élevés qui ne sont pas possibles avec le dispositif expérimental actuel. En fait, les prosimètres à mercure comportent un certain nombre de capteurs de pression adaptés aux plusieurs ordres de magnitude des pressions imposées lors d'un test type.



**Figure 14:** Pression capillaire en fonction de la saturation en mercure mesurée par la MIP comparée avec celles calculées à partir des DTPs obtenues par l'YSM.  $\theta = 140^\circ$ , and  $\sigma = 0.485 \text{ N m}^{-1}$ .

Compte tenu de l'objectif de remplacer la MIP, il est important d'obtenir des rapports entre la DTP délivrée par l'YSM et la courbe de  $P_c$ . Ceci implique la recherche d'un lien entre les classes de rayon de pore obtenues avec l'YSM et celles associées aux pressions nécessaires pour saturer un milieu poreux avec un fluide non mouillant. Une première approche visant à atteindre cet objectif est présentée ici.

Commençons par faire l'hypothèse que la chute de pression le long d'un chemin de percolation se produit exclusivement dans sa plus petite constriction. Dans ce cas-là, nous pouvons remarquer que la DTP (en nombre et non pas en volume) délivrée par l'YSM représente le nombre  $n_i$  de chemins percolants dont la plus petite constriction est  $r_i$ . Le nombre total de chemins percolants est  $\sum_i n_i$ . Cependant, le volume de ces constrictions n'est pas représentatif du volume total des chemins percolants et par conséquent  $\sum_i n_i \pi r_i^2 \ll \varepsilon \pi R^2$ . Supposons maintenant que tous les chemins percolants ont le même volume, qui est entièrement contenu dans les « volumes de pore » de longueur  $L$  dont le volume est  $\varepsilon L \pi R^2 / \sum_i n_i$ . Alors, le rayon des « volumes de pore » est  $r_{body} = \sqrt{\varepsilon R^2 / \sum_i n_i}$ .

Un chemin de percolation dont le rayon de pore est  $r_{body}$  et dont la constriction minimum a un rayon de  $r_i$  sera saturé en fluide non mouillant à des pressions allant de  $\left(-\frac{2\sigma \cos \theta}{r_{body}}\right)$  à  $\left(-\frac{2\sigma \cos \theta}{r_i}\right)$ . En première approximation, on considère qu'un chemin percolant sera

saturé en fluide non mouillant lorsqu'une pression  $-\frac{2\sigma\cos\theta}{(\frac{r_{body}+r_i}{2})}$  est appliquée. En tenant compte de ces considérations, on peut transformer les DTPs obtenues avec l'YSM en leurs « DTPs de pression capillaire » équivalentes moyennant les expressions suivantes:

$$\tilde{r}_i = \frac{r_{body} + r_i}{2} \quad (25)$$

$$\tilde{p(r_i)} = \frac{n_i}{\sum_i n_i} \quad (26)$$

où  $\tilde{r}_i$  est la classe de rayon de pore « équivalente pour la pression capillaire » et  $\tilde{p(r_i)}$  est sa probabilité équivalente en volume ou fréquence. Les « DTPs de pression capillaire » correspondant aux expériences réalisées dans avec les différents milieux poreux et leurs courbes de  $P_c$  associées sont présentées dans la Figure 15 et la Figure 16 ainsi que les résultats de la MIP. Un bon accord est trouvé entre les deux méthodes, surtout pour les milieux naturels (échantillons 3 à 5). En particulier, le plateau horizontal de  $P_c$ , est bien prédit.

De plus amples informations peuvent être obtenues grâce à l'interprétation des DTPs obtenues par l'YSM. En effet,  $\sum_i n_i$  est une estimation du nombre total de chemins percolants à travers le milieu poreux et  $r_1 = \frac{2\tau_0}{\nabla P_1}$  correspond au rayon de la constriction du chemin percolant au plus faible gradient de pression. Une valeur de  $r_1$  proche de  $r_{body}$  signifie qu'aucune constriction n'existe dans le chemin de percolation premièrement mobilisé.

Par ailleurs,  $\bar{r} = \frac{\sum_i n_i r_i}{\sum_i n_i}$  est le rayon moyen des constrictions. Par conséquent  $r_{body}/\bar{r}$  peut être utilisé comme un estimateur du ratio rayon de volume de pore – rayon de constriction. Nos hypothèses seront plus réalistes dans le cas où ce ratio est élevé parce que nous avons supposé que la totalité du volume est contenu dans les volumes de pore et toute la chute de pression est produite dans les constrictions. Un meilleur accord entre la MIP et l'YSM est effectivement obtenu quand le ratio rayon de volume de pore – rayon de constriction est élevé. En tout cas, ce n'est qu'une interprétation de base et d'autres analyses seront nécessaires afin d'assurer des relations plus fiables en utilisant d'autres moyens.

Enfin, un test consistant à caractériser deux échantillons poreux analogues, l'un avant et l'autre après réalisation des mesures de l'YSM, a été effectué. Les matériaux utilisés sont du Berea Sandstone et de l'Aerolith A10. Dans les deux cas, aucun changement important de la DTP n'est observé après réalisation des tests YSM. Cela pourrait indiquer que les échantillons sont réutilisables dans d'autres essais visant à caractériser les DTPs.

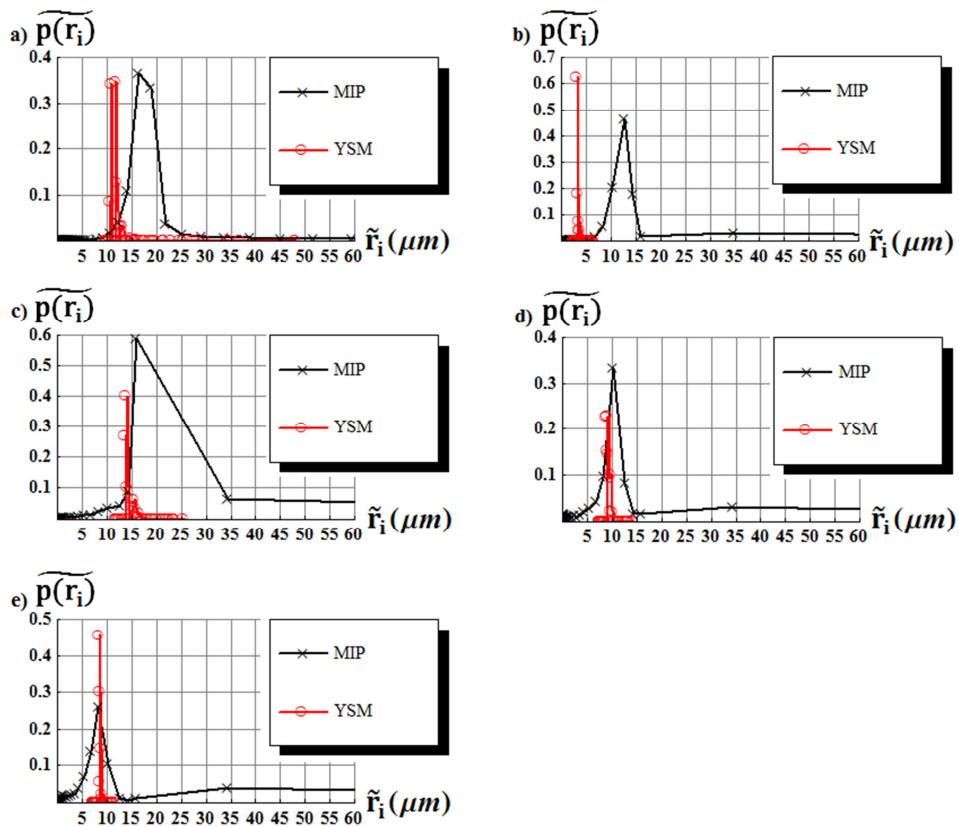


Figure 15: « DTPs de pression capillaire »équivalentes déduites avec l'YSM correspondant aux différents milieux poreux. a) Echantillon 1 ; b) Echantillon 2 ; c) Echantillon 3 ; d) Echantillon 4 ; e) Echantillon 5.

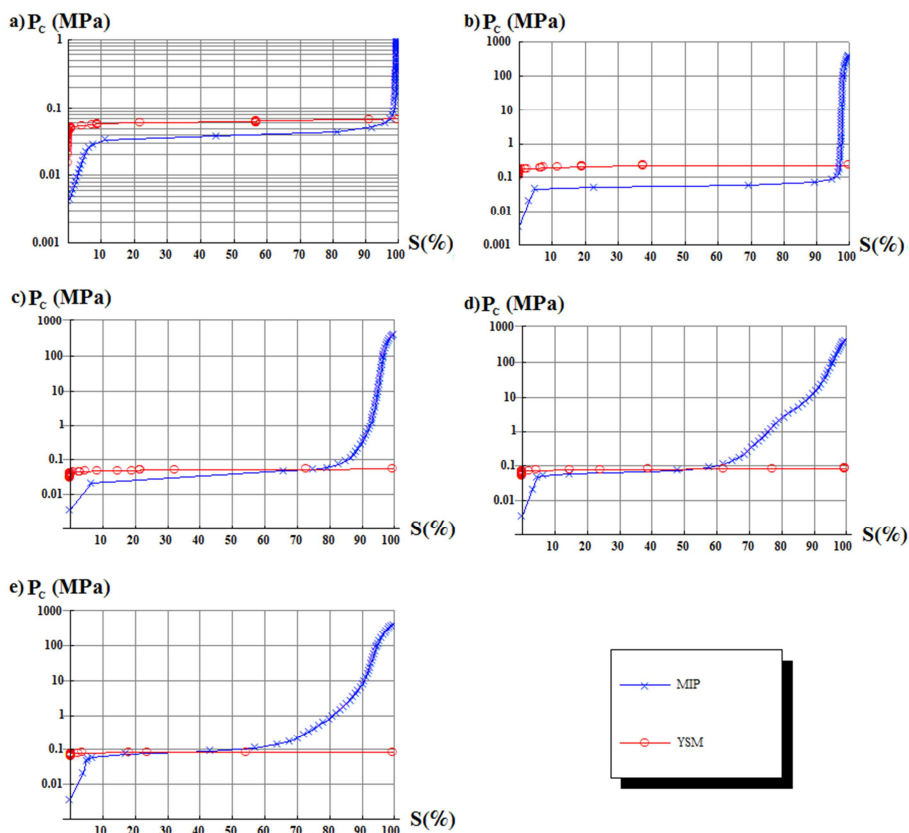


Figure 16: Comparatif entre la pression capillaire en fonction de la saturation en mercure mesurée par la MIP et celle calculée à partir des « DTPs de pression capillaire »équivalentes avec l'YSM.

### **Comparaison entre YSM et Microtomographie 3D**

Deux des matériaux analysés avec l'YSM dans le chapitre précédent ont également été étudiés par microtomographie 3D au CSTJF (TOTAL SA). Ici, nous allons présenter quelques images correspondant à ces matériaux, ainsi qu'une première analyse visant à déduire leurs DTPs. Toutefois, il est rappelé que l'obtention de DTP à partir des microtomographies est une tâche complexe. Par conséquent, seule une exploitation basique sera présentée ici dans le but de tirer des conclusions générales sur les avantages et les inconvénients de cette technique. En outre, les résultats obtenus seront comparés à ceux provenant de la MIP et de l'YSM en termes des DTPs et des courbes de pression capillaire.

Les milieux poreux analysés sont un silicate fritté A10 et un Berea Sandstone. Les dimensions des échantillons étaient d'environ 8 mm de diamètre et 15 mm de longueur. Pendant les expériences, un grand jeu d'images 2D correspondant à différentes tranches le long de l'axe de symétrie de l'échantillon a été obtenu avec un microscope à rayons X (520 Versa, Carl Zeiss X-ray Microscopy). Il faut rappeler ici que ces images correspondent à un volume (avec une profondeur de 1 pixel), même si elles sont appelées images 2D pour simplicité. Ensuite, des images 3D ont également été reconstruites par combinaison de ces vues 2D dans les deux cas.

Une analyse de l'image 2D présentée dans la Figure 17a a été effectuée. La première étape est la segmentation de l'image pour obtenir une nouvelle image binaire. Ceci entraîne le choix subjectif d'un seuil de gris. En fait, des porosités complètement différentes ont été calculées à partir des images segmentées avec deux seuils de gris divers (8% ou 17% en fonction du seuil choisi). Les régions noires de l'image segmentée se correspondent avec l'espace occupé par

les pores. Dans cette analyse basique, les rayons de pore  $r_p$  ont été calculés avec  $r_p = \sqrt{\frac{A_p}{\pi}}$  où  $A_p$  est l'aire de chaque région noire isolée, ce qui permet d'obtenir la DTP. On a remarqué que la taille de pores la plus fréquente est celle qui se correspond avec la résolution de l'image, ce qui suggère qu'une proportion importante des pores n'a pas été observée. La DTP en volume relatif obtenue à partir de cette image est présentée dans la Figure 18 et comparée avec les résultats fournis par la MIP. Des DTPs complètement différentes sont obtenues par chaque méthode, ce qui est expliqué par les dimensions de pore considérées dans chaque cas. Dans notre analyse de l'image, nous avons considéré non seulement les constrictions mais aussi les volumes de pore, ce qui n'est pas le cas du MIP.

Par ailleurs, les images 3D des deux milieux poreux analysés ont été exploitées par TOTAL S.A. suivant une méthode similaire à celle de Sheppard *et al.* (2005). Ainsi, la distribution de taille de constrictions, la distribution de taille de volumes de pores et la distribution de tortuosités ont été calculées. La distribution de tailles des constrictions obtenue par cette procédure (Figure 19) est en excellent accord avec celle obtenue par la MIP dans les régions observées par microtomographie (non limitées par la résolution des images). Cela veut dire qu'une définition convenable de la géométrie des pores dans l'étape d'analyse des images segmentées peut mener à l'obtention d'une DTP qui reproduise les résultats du MIP. Néanmoins, celle-ci est précisément la question sans réponse (malgré les progrès récents):

comment définir les pores afin de calculer de manière fiable les propriétés pétrophysiques d'intérêt (perméabilité,  $P_c(S)$ , etc.) ?

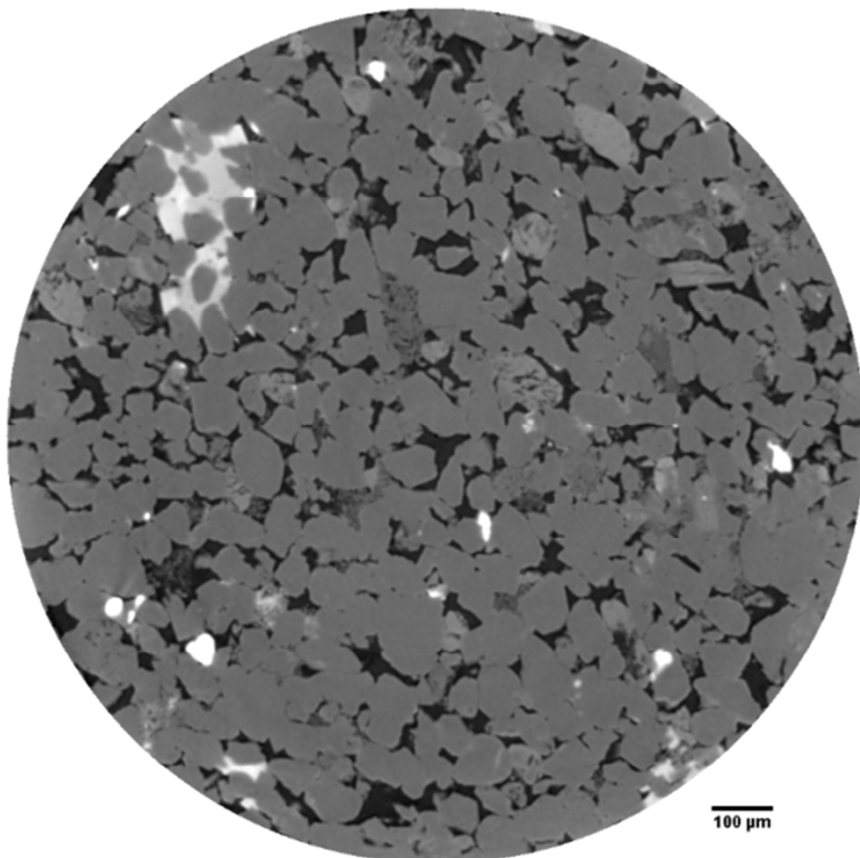


Figure 17: Microtomographie du Berea Sandstone avec une résolution de 1,5  $\mu\text{m}/\text{pixel}$ .

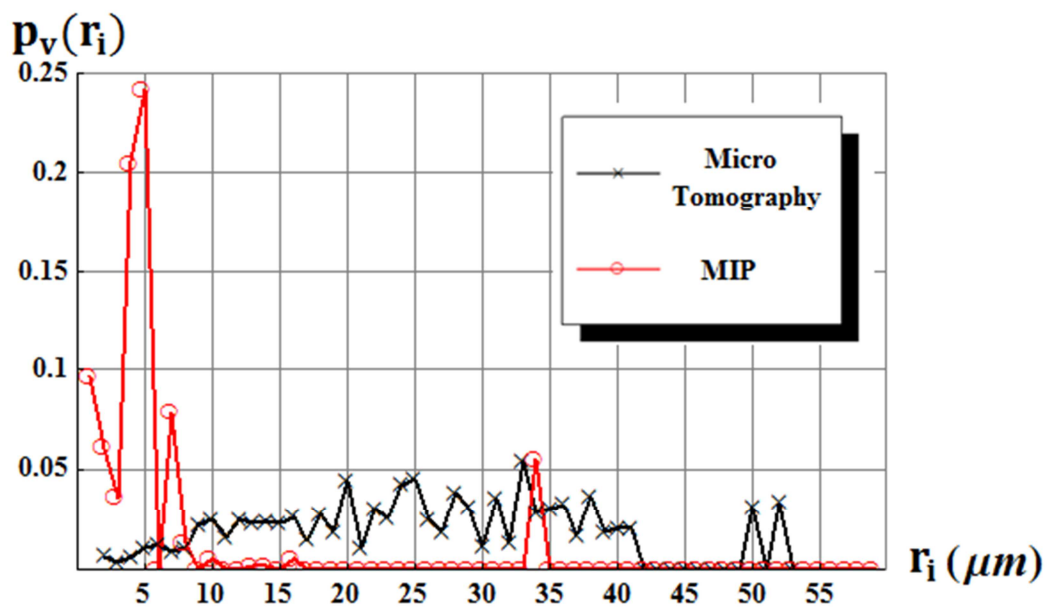


Figure 18 : DTPs obtenues à partir de l'image 2D (microtomographie) du Berea Sandstone comparée avec la DTP obtenue par la MIP.

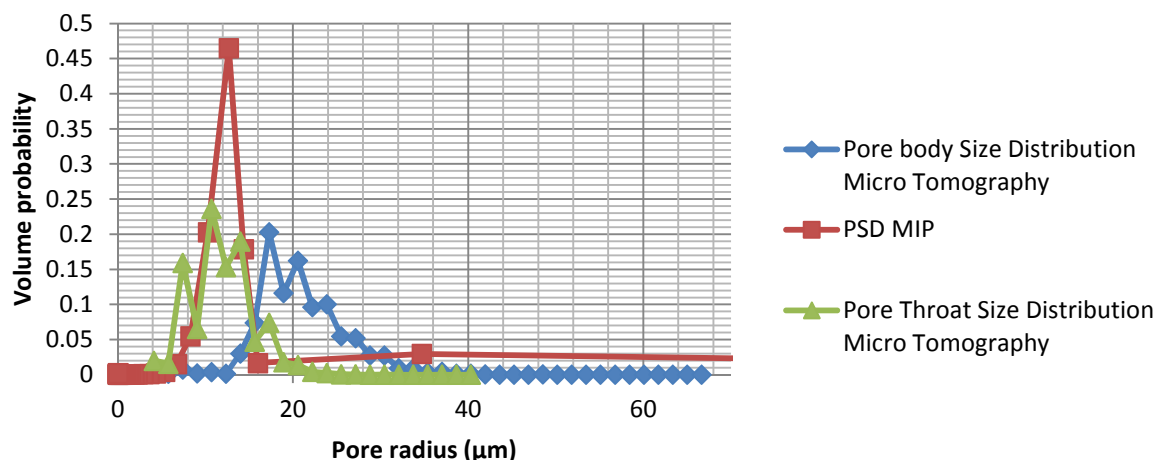


Figure 19: DTPs du silicate A10 obtenues avec MIP et avec microtomographie 3D.

## 6. Discussion, conclusions et perspectives

---

L'YSM inclue certaines hypothèses et modélisations qui n'ont pas encore été entièrement examinées. Ce dernier chapitre offre l'occasion d'aborder à nouveau de façon plus large certaines questions précédemment posées. En outre, nous tirerons aussi les conclusions finales des résultats présentés dans cette thèse et dans la dernière section nous proposerons des lignes directrices pour les futurs travaux dans ce sujet.

### **Discussion**

Trois questions principales seront traitées ici: la pertinence du modèle de faisceau de capillaires dans l'YSM, la pertinence du modèle d'Herschel-Bulkley pour approcher la rhéologie des fluides à seuil réels et la définition de la dimension de pore impliquée dans chaque méthode de porosimétrie. Cette discussion reprend certaines des idées présentées dans un article récent de Rodriguez de Castro *et al.* (2014).

Commençons par rappeler que la géométrie de l'espace poreux est si complexe que toute description implique l'introduction d'hypothèses et de simplifications. En effet, les milieux poreux réels ne sont pas des faisceaux de capillaires et il est évident que ce modèle n'est pas le plus réaliste. En plus, il ne prend pas en compte les non linéarités dans l'apparition des chemins percolants aux alentours du gradient de pression de seuil de l'écoulement. L'utilisation de modèles plus complexes tels que les réseaux de pores impliquerait la nécessité de connaître plus de détails concernant la géométrie des pores et de leur connectivité (nombre de coordination, ratio rayon de volume de pore – rayon de constriction, etc.). Cette information n'est pas disponible à moins que d'autres techniques telles que la microtomographie soient utilisées.

Une voie pour étendre la présente méthode à des modèles plus représentatifs de l'espace des pores est d'établir une relation entre le gradient de pression appliqué et le rayon critique des pores qui rejoignent l'écoulement à ce gradient de pression. Dans le cas d'un faisceau de capillaires, cette relation est donnée par l'équation (4). L'objectif de ce travail était de proposer une méthode simple qui permette la détermination de DTP représentatives des milieux poreux réels sans l'introduction de paramètres topologiques provenant d'autres techniques. Enfin, et comme expliqué précédemment, le faisceau de capillaires est également utilisé dans la porosimétrie à mercure, de sorte que la présente méthode sera au pire "seulement" aussi mauvaise que la porosimétrie à mercure concernant la représentativité de la morphologie des pores.

Comme présenté dans le Chapitre 2, certains auteurs affirment que la contrainte de seuil n'existe pas vraiment et qu'elle est simplement une idéalisation due aux temps de mesure limités et à la basse résolution expérimentale. Des temps de mesure très longs permettent

d'observer une augmentation continue de la viscosité aux taux de cisaillement plus faibles. La rhéologie des solutions de xanthane qui ont été utilisées dans nos expériences est mieux représentée par un modèle du type Carreau. Malheureusement aucun rapport analytique rigoureux exprimant Q en fonction de  $\nabla P$  dans un capillaire ne peut être obtenu pour ce type de fluides. Par conséquent, l'utilisation d'une loi rhéologique asymptotique (loi de puissance tronquée) devrait entraîner des erreurs du même ordre ou plus grandes que ceux introduites par l'utilisation du modèle d'Herschel-Bulkley pour ajuster les données rhéologiques. De plus, pour appliquer ce modèle dans la présente méthode, il serait nécessaire de définir une viscosité "critique" au-delà de laquelle une classe particulière de tailles de pore ne contribue que de façon négligeable à l'écoulement total, et cette viscosité "critique" serait analogue à une pseudo-contrainte de seuil. De toutes manières, il est important que le caractère rhéofluidifiant du fluide utilisé soit suffisamment prononcé pour que le fluide puisse être assimilé à un fluide à seuil. Ceci est le cas des solutions de polymères rigides. Par ailleurs, d'autres fluides à seuils devront être utilisés avec des milieux poreux dont la dimension des pores soit du même ordre que celle des molécules de xanthane.

Dans ce travail comme dans la littérature, il a été établi que la viscosité apparente des solutions de gomme xanthane s'écoulant dans les milieux poreux est analogue à celle effective si l'on introduit un facteur de décalage empirique  $\beta$  pour le taux de cisaillement. B a été calculé dans chaque cas comme étant la valeur qui produit le même taux de cisaillement critique pour le comportement rhéofluidifiant dans le milieu poreux et dans le rhéomètre. Cependant, deux questions importantes n'ont pas encore été formulées: 1) Existe-t-il vraiment un taux de cisaillement critique pour le comportement rhéofluidifiant dans le milieu poreux? 2) Et est la viscosité apparente définie comme dans la littérature réellement représentative de la viscosité dans le milieu poreux?

Dans la plupart de nos expériences, aucun plateau newtonien de viscosité apparente n'a été retrouvé aux faibles taux de cisaillement. En conséquence, il n'est pas strictement correct d'ajuster la viscosité apparente à un modèle de Carreau, étant donné que la viscosité aux taux de cisaillement faibles peut être affectée par la rétention de polymère. En effet, la viscosité apparente "extra" à des taux de cisaillement faibles provient des pertes de charge induites par un gâteau de filtration au lieu de la viscosité du fluide. Cela est prouvé par le fait que, même si la viscosité du fluide sortant à la fin des expériences est inférieure à celle du fluide avant l'injection,  $\mu_{app}$  était encore plus élevée aux débits plus faibles.

En ce qui concerne la deuxième question, compte tenu des possibles réductions de perméabilité pendant l'écoulement de polymère à faible débit, il est plus convenable d'utiliser le facteur de résistance (ratio de mobilités eau-polymère) plutôt que l'équation (20) pour représenter le comportement du fluide dans le milieu poreux.

D'un point de vue fondamental, on peut se demander quelle taille caractéristique des pores réels est déterminée en utilisant la méthode actuelle et quelle est la pertinence de l'utilisation de la DTP déduite par la MIP ou microtomographie comme DTP de référence. Pour répondre à ces questions, il est tout d'abord rappelé que les expériences effectuées ici sont

essentiellement des expériences de transport fluide et, par conséquent, la perte de charge est principalement sensible à la taille hydrodynamique de la constriction des pores plutôt qu'à la dimension des volumes de pores. En conséquence, la présente méthode n'est pas appropriée lorsque l'on s'intéresse à la détermination des caractéristiques telles que la surface spécifique. En outre, les DTP obtenues à partir de mesures d'intrusion de mercure sont dominées par les constrictions de pore, tandis que les volumes de pore dominant dans les DTP calculées à partir de mesures d'extrusion de mercure. Il n'est donc pas surprenant que les DTP calculées avec la présente méthode soient plus proches de celles provenant de l'intrusion du mercure.

En général, les DTP obtenues par différentes méthodes ne peuvent pas être directement comparées. L'utilisation de la MIP comme méthode de référence est justifiée lorsque les DTP sont consacrées au calcul de  $P_c(S)$ , parce que  $P_c(S)$  est mesurée directement avec cette technique. Cependant, la MIP ne doit pas être considérée comme la méthode de référence pour toutes les applications, même si c'est souvent le cas tout simplement par tradition ou parce que c'est une technique de routine. A d'autres égards, il est important de souligner que la gamme de tailles de pores qui peuvent être scannées avec chaque technique de porosimétrie est limitée. Pour une même gamme de tailles de pore, les pressions mises en jeu par la MIP et par l'YSM sont du même ordre de grandeur.

## **Conclusions**

Dans un contexte de consensus international sur la nécessité de développer des alternatives face à la toxique porosimétrie à mercure, une nouvelle méthode de porosimétrie pour caractériser les DTP des milieux poreux a été présentée dans cette thèse. Elle est basée sur des expériences d'écoulement des fluides à seuil à travers les milieux poreux.

Une procédure qui permet de calculer les DTP à partir de  $Q(\nabla P)$  a été développée et validée numériquement grâce à des expériences "*in silico*". De plus, l'influence de plusieurs paramètres sur la "qualité" de la DTP obtenue a été étudiée. De cette manière, il a été démontré que le bruit aléatoire dans les mesures de  $Q(\nabla P)$  semble être la source d'erreur plus importante.

Un protocole approprié pour la mise en œuvre expérimentale de l'YSM a été déterminé sur la base des conclusions tirées des expériences préliminaires. Les solutions aqueuses de xanthane ont été sélectionnées comme fluide à seuil utilisé. Ensuite, une série d'expériences ont été réalisées afin d'analyser l'effet de la concentration de polymère sur la DTP calculée. Il a été démontré que plus les solutions sont concentrées, plus le comportement des fluides à seuil est approximé et plus les DTPs obtenues sont proches de celles provenant du MIP.

Ensuite, d'autres séries d'expériences ont été réalisées avec les mêmes milieux poreux et fluides différents en vue d'étudier l'influence du type de milieu poreux obtenu sur la DTP. Les DTP calculées sont ordonnées de façon cohérente par rapport à la taille de pore moyenne donnée par l'équation (1)

Par ailleurs, la viscosité apparente des fluides à seuil dans les milieux poreux a été caractérisée et comparée à la viscosité effective mesurée avec le rhéomètre. Le facteur  $\beta$ , qui a été traditionnellement associé à la géométrie des pores, a été prouvé dépendant de la gamme de taux de cisaillement apparents expérimentée par le fluide dans le milieu poreux. En outre, il a été observé que le comportement apparent du fluide dans le milieu poreux est moins rhéofluidifiant que dans le rhéomètre. Ces observations ont été attribuées en partie aux larges gammes de débits imposées au cours des expériences.

L'importance de l'adsorption du polymère, de la rétention de polymère et la dégradation mécanique a été également évaluée par des mesures complémentaires de la densité et de la viscosité du fluide entrant et des effluents du milieu poreux. Tandis qu'aucun signe d'adsorption ni dégradation mécanique importante n'a été observé, la rétention de polymère aux plus bas débits est très notable en raison de l'orientation aléatoire des molécules de polymère. Cela pose un problème pour la caractérisation de petits pores, et d'autres procédures tel que des balayages intermédiaires à fort débit devront être évaluées. En outre, une YSM modifiée visant à obtenir des données Q ( $\nabla P$ ) lisses, réduire l'effet du bruit aléatoire et augmenter la précision aux faibles débits a été proposée.

L'YSM a été comparée à d'autres méthodes de porosimétrie, MIP et microtomographie. Les DTPs obtenues par ces méthodes ne sont pas les mêmes comme prévu et les principales raisons de ce fait ont été expliquées. En raison de son intérêt industriel, les courbes  $P_c$  ( $S$ ) correspondant à chaque méthode ont été obtenues grâce à une procédure simple. Une bonne définition de la correspondance entre les dimensions de pores caractérisées par chaque technique doit conduire à de bonnes estimations de  $P_c$  ( $S$ ) par autres méthodes que la MIP. Les résultats de microtomographie 3D ont également été utilisés pour illustrer le fait que les dimensions de pores observées "optiquement" peuvent être très différentes de celles caractérisées par d'autres méthodes.

En résumé, on peut conclure qu'un travail exploratoire exhaustif sur la faisabilité expérimentale d'une nouvelle méthode de porosimétrie basée sur l'injection de fluides à seuil a été présenté. De nombreux aspects de cette méthode ont été abordés et les points les plus délicats de la méthode ont été identifiés et ont soulevé des questions encore non résolues.

Cependant, l'YSM a un grand potentiel en tant que méthode de porosimétrie, non seulement pour calculer des DTP liées à la perméabilité, mais aussi pour obtenir des courbes de  $P_c$  pourvu que une bonne relation entre les dimensions des pores involucrées soit utilisée. En outre, un avantage indéniable de l'YSM est la simplicité des expériences et le fait qu'elle soit peu coûteuse et facile à mettre en place. De plus, l'YSM est polyvalente et peut être utilisée pour caractériser de différents types de milieux poreux. Par exemple, l'YSM serait utile pour caractériser des milieux poreux non consolidés pour lesquels la MIP n'est pas efficace.

## **Perspectives**

Comme on a déjà expliqué précédemment, même s'il a été démontré que la méthode présentée dans cette thèse possède un grand potentiel, elle doit encore être consolidée, et sa fiabilité doit être améliorée. Plusieurs lignes directrices pour les travaux futurs sont proposées ici.

La modification de l'YSM proposée pour obtenir des données  $Q(\nabla P)$  lises n'a pas été complètement développée. L'effet de l'augmentation du nombre de données grâce à l'évaluation des fonctions d'ajustement peut être exploré, ainsi que l'extrapolation de données à des débits inatteignables. Cela peut se traduire par une augmentation de la robustesse de la méthode.

Par ailleurs, l'YSM suppose qu'il n'y a pas de glissement sur les parois des pores et que le cisaillement est simple. Dès lors, il est nécessaire de vérifier la validité de ces hypothèses avec les fluides utilisés. D'autres aspects qui doivent être examinés à l'aide de milieux poreux modèles sont l'effet de la forme irrégulière des pores et leur connectivité. Quelques possibilités en cours d'évaluation sont les expériences en micro-modèles et les expériences en milieu poreux fabriqués par impression3D.

Les solutions aqueuses de gomme xanthane ont été sélectionnées parmi plusieurs candidats en raison de leur comportement plus simple dans les milieux poreux: viscoélasticité réduite, non thixotrope, adsorption limitée, etc. Néanmoins, d'autres fluides sont nécessaires dans les cas où la taille de la molécule de xanthane n'est pas négligeable par rapport à la taille des pores. Un protocole pour produire des émulsions monodispersées d'huile dans l'eau avec une taille de gouttelettes de  $1\mu\text{m}$  a été élaboré et la rhéologie de ces fluides a été caractérisée. Toutefois, la taille des gouttelettes que l'on peut obtenir n'est pas aussi faible que nécessaire. Par conséquent, d'autres types de fluides doivent être également considérés.

Étant donné que les courbes de  $P_c(S)$  sont d'un grand intérêt industriel, il est important d'étudier leur lien avec la dimension des pores caractérisée par l'YSM. Un paramètre clé qui pourrait aider à atteindre cet objectif est le ratio rayon de volume de pore – rayon de constriction. Une procédure qui n'a pas été encore complètement explorée est l'estimation de ce paramètre à partir du rapport entre la porosité mesurée et celle calculée à partir de la DTP obtenue par l'YSM. Le rapport entre les perméabilités mesurées et calculées pourrait être également analysé.

Un protocole expérimental modifié doit être adopté afin de réduire l'impact de la rétention de polymère aux faibles débits. Une possibilité consiste à inclure des balayages intermédiaires à débits élevés. En outre, l'installation de prises de pression supplémentaires pour mesurer la chute de pression entre les sections intermédiaires tout au long de l'échantillon permettra de localiser la rétention de polymère et d'identifier la nature du gâteau de filtration.



# EXPERIENCES D'ECOULEMENT DE FLUIDES A SEUIL EN MILIEU POREUX COMME NOUVELLE METHODE DE POROSIMETRIE

**RESUME :** À l'heure actuelle, la porosimétrie à mercure est la technique la plus répandue pour déterminer les distributions de taille des pores (DTPs) des milieux poreux. Cependant, cette technique présente plusieurs inconvénients tels que la toxicité du fluide utilisé. Malgré l'existence d'autres méthodes de porosimétrie moins toxiques, aucune parmi elles n'est suffisamment performante pour remplacer la porosimétrie à mercure. Dans ce contexte, l'objectif de la présente thèse est de répondre à la question suivante : est-il possible de développer une méthode simple, performante et non toxique pour caractériser les milieux poreux en termes de leur DTP ? Pour répondre à cette question, le point de départ est la base théorique d'une nouvelle méthode présentée dans la littérature. L'idée principale est d'obtenir la DTP d'un milieu poreux à partir des mesures des débits Q correspondant à différents gradients de pression  $\nabla P$  lors de l'injection de fluides à seuil. Sur la base de ces considérations théoriques, une procédure intuitive pour calculer les DTPs à partir de  $Q(\nabla P)$  est présentée dans ce travail. Elle consiste à considérer l'augmentation additionnelle de Q quand  $\nabla P$  est augmenté, comme conséquence des pores plus petits qui s'incorporent à l'écoulement. Le principe sous-jacent de ce comportement est la rhéologie des fluides à seuil en milieu poreux. La procédure est d'abord testée et validée numériquement. Ensuite, elle est appliquée à l'exploitation des données provenant d'expériences de laboratoire et les résultats obtenus sont comparés avec ceux fournis par porosimétrie à mercure et par microtomographie 3D.

**Mots clés :** contrainte de seuil, milieux poreux, porosimétrie, méthode expérimentale, distribution de taille des pores.

## FLOW EXPERIMENTS OF YIELD STRESS FLUIDS IN POROUS MEDIA AS A NEW POROSIMETRY METHOD

**ABSTRACT :** Nowadays, mercury porosimetry is the most widespread technique to determine pore size distributions (PSD) of porous media. However, this technique presents several drawbacks including toxicity of the employed fluid. Despite the existence of other less toxic porosimetry methods, none of them is efficient enough to replace mercury porosimetry. In this context, the objective of the present thesis is to answer the following question: is it possible to develop a simple, efficient and nontoxic method to characterize porous media in terms of their Pore Size Distribution? To answer this question, the starting point is the theoretical basis of a new method presented in the literature. The main idea is to obtain the PSD of a porous medium from the measurement of the flow rate Q at several pressure gradients  $\nabla P$  using yield stress fluids. On the grounds of these theoretical considerations, an intuitive approach to calculate PSD from  $Q(\nabla P)$  is presented in this work. It relies on considering the extra increment of Q when  $\nabla P$  is increased, as a consequence of the pores of smaller radius newly incorporated to the flow. The underlying principle of such behavior is the rheology of yield stress fluids in porous media. The procedure is first tested and validated on numerically generated experiments. Then, it is applied to exploit data coming from laboratory experiments and the obtained results are compared with those provided by mercury porosimetry and 3D micro tomographies.

**Keywords :** yield stress, porous media, porosimetry, experimental method, pore size distribution.

